NORTHWESTERN UNIVERSITY

Fundamental Studies and Applications of Multi-photon Transition induced Dispersion in Atomic Media

A DISSERTATION

SUBMITTED TO THE GRADUATE SCHOOL

IN PARTIAL FULFILLMENT OF THE REQUIREMENTS

for the degree

DOCTOR OF PHILOSOPHY

Field of Electrical Engineering and Computer Science

BY

Ye Wang

EVANSTON, ILLINOIS

December 2015

ABSTRACT

Fundamental Studies and Applications of Multi-photon Transition induced Dispersion in Atomic Media

Ye Wang

Multi-photon transition induced dispersion in atomic media can be tailored for many important applications. In this thesis, I have investigated, theoretically as well experimentally, several such applications: ultra-low power optical modulation, development of optically controlled waveplate and polarizer for realizing an all optical switch, an optical logic gate, and high-speed Stokes-metric imaging, and development of a superluminal ring laser for a range of applications, including ultra-sensitive rotation sensing and vibrometry.

All-optical modulation and switching are important for optical communication and quantum information processing. Conventional techniques of non-linear optics typically require relatively high power, and are not well suited for these applications. Our study has demonstrated an all-optical modulator, which can operate at a power level much lower than any other technique demonstrated so far. Specifically, a tapered nano-fiber (TNF) embedded in Rubidium (Rb) vapor has been used to produce ultra-low power modulation.

In order to develop an accurate model for the interaction of multi-photon laser fields with Rb atoms, an N-Level algorithm has been developed. This algorithm can be used to generate automatically the density matrix equations of motion for a system with an arbitrary number of

energy levels, such as the Zeeman sublevels within the hyperfine energy levels in Rb atoms. It has been used to design, analyze, and optimize many processes of interest using Rb atoms, including the study of ladder transitions, high speed modulation, optically controlled polarizer and waveplate, and double Raman gain for realizing a superluminal laser.

Study of all-optical modulation has been further extended to an Rb cascade system. With the Rb 5S-5P-6S ladder transition, optical modulation is demonstrated at a telecommunication band wavelength. With the use of a high pressure buffer gas, a 100-fold increase in modulation bandwidth has been observed.

An optically controlled polarizer and an optically controlled waveplate have also been demonstrated using the Rb ladder system. A combination of both can be used for realizing all optical switching and all optical logic gates. These devices can also be used to realize a high-speed Stokes-metric imaging system. The optically controlled polarizer is demonstrated using ^{87}Rb $5S_{1/2}$, F = 1->$5P_{1/2}$, F = 1, 2 -> $6S_{1/2}$, F = 1, 2 transition, where 795 nm light is used as the control beam and 1323 nm light is used as the probe beam. The optically controlled waveplate is demonstrated using the same transition. Specifically, a differential phase retardance of ~180 degrees between the two circularly polarized components of a linearly polarized signal beam is demonstrated. The optical activity responsible for the phase retardation process is explained in terms of selection rules involving the Zeeman sublevels. Both the optically controlled polarizer and waveplate can be potentially implemented using the TNF in Rb vapor system and be used to realize an ultra-low power all optical switch as well as an all-optical logic gate.

I have also investigated the feasibility of realizing a superluminal ring laser (SRL). An SRL

contains a gain medium with a tuned negative dispersion, for which the group velocity of light becomes superluminal. For the SRL, the mirror displacement sensitivity is enhanced very significantly. As such, the SRL has many potential applications, including vibrometry and rotation sensing. Using a double Raman pumped gain medium within Rb system, the enhancement factor is shown to be as large as 10^7. This system requires two strong pumps that are closely spaced in frequency. Accurate modeling of this system requires taking into account interference between the two pumps. An analysis is presented where we allow for an arbitrary number of harmonics that result from this interference, and investigate the behavior of the gain profile under a wide range of conditions. An experimental study of double-Raman gain in an Rb vapor cell is also described which is found to be in close agreement with the theoretical model. A double-Raman laser with a linear cavity is built using this gain media. Furthermore, a numerical algorithm designed to simulate a double Raman superluminal laser is also presented. As an extension of the study of the SRL, I have also investigated the properties of a subluminal laser (SLL), inside which the group velocity of light is much slower than the vacuum speed of light. It makes use of a composite gain spectrum consisting of a broad background along with a narrow peak. Since the group index can be very high, the frequency of such a laser is highly insensitive to a change in the cavity length, thus making it extremely stable. A similar study is applied to another version of SRL, where the gain profile is a combination of a broad gain from diode pumped alkali laser (DPAL) and a narrow absorption from Raman depletion.

ACKNOWLEDGEMENTS

There are some people played important roles in my PhD study, without whom this thesis would not be put in place. I would like to extend my gratitude to

My advisor, Professor Selim Shahriar, who was standing behind me and providing the greatest supports through my studies and research. He had been inspiring me with his enthusiasm, rigorous scholarship, and intelligence, and showed me the essential way to pursuit truth.

My lab mates, Shih Tseng, Mary Salit, Honam Yum, Subramanian Krishnamurthy, Joshua Yablon, Zifan Zhou, for their great helps in different phases of my research.

Jeffery Pritchard, a technician from Coherent, Inc. who had helped us installing and maintaining all of our Ti-Sapphire laser systems, passed on tremendous details of laser, and showed a great example of professionalism.

Jeffrey Sundwall, the manager of Northwestern University Scientific Instrument Shop, who helped me design and build fine elements for our experiments.

Dean Bruce Lindvall, Dean Ajit Tamhane, and Paula Straaton from Deans Office of McCormick School, for their kindness and supports through my years.

Dianne Kay Siekmann, Kamilah McCoy, and Kate Veraldi from Graduate School, who provided great helps on my career development.

My committee members, Professor Selim Shahriar, Professor Horace Yuen, and Professor Koray Aydin for their time and revise opinions on my dissertation.

Most important, to my lovely wife, Panrong Yin, for her sacrifices and supports through my PhD study. It is wordless to express how grateful I am to have her in my life.

In loving memory of my grandma, Huimin Song. (1927 – 2013)

TABLE OF CONTENTS

LIST OF FIGURES

It shows smooth single mode operation. (b) 1323 nm absorption signal detected using chopper and lock-in amplifier

Figure 4.2 Spectroscopic details of ladder transition in ^{85}Rb (a) Schematic of various hyperfine levels used, along with the transition frequencies. (b) Expected spectrum if both hyperfine states of intermediate level are occupied by zero velocity atoms. (c) Shift of spectrum in (b) due to F=3 state at the intermediate level being occupied by negative velocity atoms.

Figure 4.3 Typical absorption profiles for the ladder transitions (at 1323nm) that are observed in ^{85}Rb. (a) Corresponds to 795 nm laser power ~ 2mW, data taken in AC mode. The hyperfine transitions corresponding to the absorption dips are α: 3→2, β: 3→3, γ: 2→2, δ: 2→3. The repeat scan has been shown due to the asymmetry of the signal (b) Corresponds to 795 nm laser power ~ 200mW, we see near 100% absorption and the lines are highly power broadened. Note that the null value of the probe detuning is defined arbitrarily to be at the turnaround point of the scan in each case.

Figure 4.4 Spectroscopic details of ladder transition in ^{87}Rb (a) Schematic of various hyperfine levels used along with the transition frequencies. (b) Absorption corresponding to 795 nm laser power ~ 50mW; all four transitions can be clearly seen. The hyperfine transitions corresponding to the absorption dips are A: 2→1, B: 1→1, C: 2→2, D: 1→2. (c) Corresponds to 795 nm laser power ~ 0.5mW; two of the four lines are suppressed and only transitions from F=1 are observed.

Figure 4.5 Absorption spectrum for ^{87}Rb with ~400mW of pump power

Figure 4.6 Typical absorption profile for co- and counter-propagating geometries. $\Omega p = 5$.

Figure 4.7 Dressed state picture of 3-level cascade system for different velocity groups.

Figure 4.8 Contribution to absorption from 3 sample velocity groups (-vzero, 0, + vzero) for a 3-level cascade system when the control beam and signal beam are a) Co-propagating b)

pressure is ~6 psi and the pump and probe powers are ~800 mW and ~0.5 mW.

Figure 5.6 5S-5P-5D modulation data without buffer gas. (a) 2 KHz (b) 10 KHz (c) Modulation amplitude vs modulation speed. We have indicated the vertical axes in (a) and (b) as having arbitrary units, since the relevant parameter is the modulation depth, which is about 95% in both cases. In (a), the peak pump signal corresponds to an un-attenuated pump power of ~760 mW, and the peak probe transmission corresponds to an un-attenuated probe power of 0.5 mW. Similarly, in (b), the peak probe transmission corresponds to an un-attenuated probe power of 0.5 mW. Since this is an absorptive modulation, the degree of absorption can in principle be increased by increasing the optical density.

Figure 5.7 Modulation data in the presence of buffer gas (Ethane) at pressure of ~6 psi. (a) 1 MHz (b) 5 MHz (c) Modulation amplitude vs modulation speed. We have indicated the vertical axes in (a) and (b) as having arbitrary units, since the relevant parameter is the modulation depth, which is about 90% in both cases. The peak probe transmission at both 1 MHz and 5 MHz corresponds to an un-attenuated probe power of 0.5 mW.

Figure 5.8 Increase in modulation amplitude for two different modulation frequencies (1 MHz and 10 MHZ) with increase in pump power. Just as in Figure 5.6 and Figure 5.7, the vertical axis is shown in arbitrary units, since the relevant parameter is the modulation depth, which can be increased to be near 100% by increasing the optical depth, since it is an absorptive modulator. The data shown in Figure 5.7 correspond to the maximum power employed for the pump beams (760 mW), thus corresponding to the right-most data points in this figure.

Figure 6.1[A] Quantum Zeno Effect in an atomic V-system. [B] Evolution of the quantum state of a photon via passage through a series of waveplates. [C] In the presence of interleaved polarizers acting as measurement devices, the evolution to the horizontally polarized state is inhibited.

Figure 6.2 Schematic illustration of an optically controlled polarizer using a ladder transition in ^{87}Rb atoms

Figure 8.5 Illustration of the change in the gain profile when the first Raman pump Rabi frequency is varied, while keeping the second Raman pump Rabi frequency fixed.

Figure 8.6 Comparison between double Raman gain model and single Raman gain model by setting one Raman pump Rabi frequency to be zero. The plots show the gain (left axis) and phase delay (right axis) changes as a function of probe detuning δ. Plot (a) show the single Raman model with $\Delta p = 199\Gamma 3$. Plot (b) shows the single Raman model with $\Delta p = 201\Gamma 3$. Plot (c) shows the double Raman model with the second Raman pump turned off. Plot (d) shows the double Raman model with the first Raman pump turned off.

Figure 8.7 Comparison between double Raman gain model and single Raman gain model by setting Δ to be zero. Plot (a) to (g) are generated by the double Raman model with order number of 1,2,3,6,13,20 and 30 respectively, while plot (h) is generated by the single Raman model with the same parameters.

Figure 8.8 Comparison between velocity averaging model and non-averaging model.

Figure 8.9 Comparison between co-propagating and counter-propagating cases.

Figure 8.10 Gain suppressed by increasement of Ωs in Single Raman model. Dashed line in plot (d) shows the theoretical value of gain saturation.

Figure 8.11 Gain suppressed by increasement of Ωs in double Raman model. Dashed line in plot (d) shows the theoretical value of gain saturation.

Figure 8.12 ^{85}Rb transitions. Plot (a) shows the experiment scheme. Plot(b) is a linear absorption spectrum of ^{85}Rb and ^{87}Rb. The dashed line indicates the frequency of $f_{p1.}$

Figure 8.13 The experimental setup of double Raman Gain. Laser 1 is a Ti-Sapphire Laser operating at 795nm. Laser 2 is a Diode Laser with Tapered Amplifier operating at 780nm. See text for details.

coherence between state $|3$ and $|4$, i.e., $\rho 34$. (d) Same as figure (c), but for ^{87}Rb.

Figure 8.25 In the narrow gain model: (a) transitions, (b) effective 3-level model. Here Ωop, Ωs, and ΩRp are the Rabi frequencies for the optical pump, the signal field, and the Raman pump field, respectively. $\delta s(\delta Rp)$ is the detuing of the signal (Raman pump) from the $|1-|3$ $(|2-|3)$ transiton, ν is the frequency of the signal, and $\nu 0$ is defined as the value of the signal frequency corresponding to two photon resonance (i.e. $\delta s = \delta Rp$).

Figure 8.26 A typical gain spectrum produced by the Raman cell.

Figure 8.27 Flow-chart of the algorithm for solving the model for an actual SLL.

Figure 8.28 Relationship between cavity length and lasing detuning for the practical SLL for (a) extremely high stability enhancement and (b) relatively low stability enhancement.

Figure 8.29 Output power as a function of (a) length change and (b) laser frequency, for the model for a practical SLL.

Figure 8.30 Desired region of operation in the model for a practical SLL: (a) laser frequency as a function of cavity length and (b) stability as a function of laser frequency.

Figure 8.31 Real part of the effective dispersion in steady state of the model for a practical SLL.

Figure 8.32 Real part of the steady-state susceptibility for the combined absorbing and amplifying media (solid line), and the conventional gain medium (dashed line). The inset shows an expanded view of the solid line in the main figure

Figure 8.33 Sensitivity enhancement associated with Eqn.8.54. The inset (a) shows R in Eqn.8.54 in an expanded view (solid line), and its value in the linear limit (dotted line). The inset (b) is an expanded view of R with a linear vertical scale.

Figure 8.34 Illustration of relation between $L-L0$ and $\nu-\nu 0$ for $|\nu-\nu 0|/2\pi < 80MHz$.

Dotted line shows the behavior for an empty cavity. The inset shows an expanded view for $|\nu - \nu 0|/2\pi < 100kHz$.

Figure 8.35 Energy levels for (a) 795-nm Rb laser to produce broadband gain, (b) Raman depletion to induce narrowband absorption dip. (c) Schematics of the experimental set-up to realize a superluminal laser: PBS, polarizing beam splitter; BS, beam splitter; AOM, acousto-optic modulator. Note that the superluminal laser is the same as the Raman pump. The scheme shown is for ^{85}Rb atoms. The broadband gain is produced by side-pumping with a diode laser array.

Figure 8.36 Experiment Setup of a superluminal ring laser using double Raman pumped gain.

Figure 8.37 Comparison between double peak gain profiles built by double Lorentz function and double Raman gain model. Plot (a) (b) shows the image part and real part of susceptibility calculated by the double Lorentz function as signal Rabi frequency and signal frequency are scanned. Plot(c) shows the corresponding case where susceptibility is calculated by the double Raman gain model. Red and green surfaces represents the χ" and χ' respectively.

Figure 8.38 An example of using our algorithm to get two set of numerical solutions to a single Raman laser. See text for more details.

CHAPTER 1 INTRODUCTION

Multi-photon transition induced dispersion in atomic media can be tailored for many important applications. In this thesis, I have investigated several such applications: ultra-low power optical modulation, development of optically controlled waveplate and polarizer for realizing all optical switch, optical logic gate, and high-speed Stokes-metric imaging, and development of a superluminal ring laser for a range of applications, including ultra-sensitive rotation sensing and vibrometry.

All-optical modulation and switching are important for optical communication and quantum information processing [1,2,3,4,5,6]. Conventional techniques of non-linear optics typically require relatively high power, and are not well suited for these applications. In recent years, several innovative techniques for modulation and switching have been demonstrated at very low power. These include, for example, techniques based on instability-induced processes in atomic vapor [3], silicon micro ring resonators [4], and hollow-core fibers [5,6]. Our study demonstrated an all-optical modulator that can operate at a power level much lower than any other technique demonstrated so far [7]. Specifically, a tapered nano fiber (TNF) [8,9,10] embedded in Rb vapor is used to produce ultra-low power modulation[11,12,13]. The fact that many such modulators may be realizable on a chip-scale vapor cell makes this an attractive technology for optical communication. Two important factors have come together to produce such an efficient modulator. First, the TNF provides a unique combination of extremely small effective mode area of ~0.2 μm^2 [8] and interaction length of ~5 mm. In contrast, the hollow-core fiber [14] and the Arrow waveguide [15] have mode areas of about 100 μm^2 and

6.7 μm^2, respectively, but allow for large interaction lengths. However, the TNF is long enough to produce complete absorption in a vapor at a temperature of about 100° C, thus making high-contrast modulation feasible. Second, we make use of the quantum Zeno effect, which controls the absorption of a signal beam via pump-induced modification of absorption, rather than refraction, thus making it inherently very efficient.

During the study of all-optical modulation, an N-Level algorithm has been developed in order to take into account the transitions among Zeeman sublevels in Rubidium (Rb) atoms [16]. This algorithm can be used to generate automatically the density matrix equations of motion for a system with an arbitrary number of energy levels. A velocity-averaging model has been added to this algorithm in order to account for the effect of Doppler broadening. The algorithm has been further optimized using parallel computing techniques. It has been used to design, analyze, and optimize many processes of interest using Rb atoms, including the study of ladder transitions, high-speed modulation, optically controlled polarizer and waveplate, and double Raman gain for realizing a superluminal laser.

Study of all-optical modulation has been further extended to an Rb cascade system. With the Rb 5S-5P-6S ladder transition, optical modulation is demonstrated at a telecommunication band wavelength. With the use of a high-pressure buffer gas, a 100-fold increase in modulation bandwidth has been observed.

An optically controlled polarizer and an optically controlled waveplate have also been demonstrated using the Rb ladder system [17,18]. A combination of both can be used for realizing all optical switching and all optical logic gates [1,17]. These devices can also be used to realize an all optical switch, an optical logic gate, and a high-speed Stokes-metric imaging

system. The optically controlled polarizer is demonstrated using ^{87}Rb $5S_{1/2}$, F = 1->$5P_{1/2}$, F = 1,2 -> $6S_{1/2}$, F = 1,2 transition, where 795 nm light is used as the control beam and 1323 nm light is used as the probe beam. When the control beam is linearly polarized, it produces an excitation of the intermediate level with a particular orientation of the angular momentum. Under ideal conditions, this orientation is transparent to the signal beam if it has the same polarization as the control beam and is absorbed when it is polarized orthogonally. The optically controlled waveplate is demonstrated using the same transition. It is shown that the signal beam can be placed in any arbitrary polarization state with a suitable choice of polarization of the control beam. Specifically, a differential phase retardance of ~180 degrees between the two circularly polarized components of a linearly polarized signal beam is demonstrated. It is also demonstrated that the system can act as a Quarter Wave plate. The optical activity responsible for the phase retardation process is explained in terms of selection rules involving the Zeeman sublevels. Both the optically controlled polarizer and waveplate can be potentially implemented using the TNF in Rb vapor system and be used to realize an ultra-low power all optical switch as well as an all optical logic gate.

I have also investigated the feasibility of realizing a superluminal ring laser (SRL). An SRL contains a gain medium with a tuned negative dispersion, for which the group velocity of light becomes superluminal. For the SRL, the mirror displacement sensitivity is enhanced very significantly. As such, the SRL has many potential applications, including vibrometry, gravitational wave detection and rotation sensing [19,20,21,22,23,24,25,26,27,28]. The sensitivity can be defined broadly as $S \equiv \partial f / \partial L$, where f is the resonance frequency and L is the length of the cavity. In general, $S_{SRL} = \xi S_{EC}$, where S_{EC} is the sensitivity of the empty cavity,

and S_{SRL} is that of the superluminal ring laser. Under ideal conditions, the enhancement factor $\xi = 1/n_g$, where n_g is the group index. Using a double Raman pumped gain medium within Rb system, ξ is demonstrated to be as large as 10^7[20]. This system requires two strong pumps that are closely spaced in frequency. Accurate modeling of this system requires taking into account interference between the two pumps [19]. An analysis is presented in this thesis where we allow for an arbitrary number of harmonics that result from this interference, and investigate the behavior of the gain profile under a wide range of conditions. An experimental study of double-Raman gain in a Rb vapor cell is also described, which is found to be in close agreement with the theoretical model. The technique reported here can be used in developing a quantitative model of a superluminal laser under wide-ranging conditions. A linear cavity is built around this double-Raman gain media which demonstrates a double-Raman laser. Furthermore, a numerical algorithm designed to simulate a double Raman superluminal laser is also presented. The algorithm first uses the bicep method to locate the ranges where the gain function is monotonically increasing or decreasing and then uses the Illinois algorithm [29,30] to find the solution within each range. As an extension of the study of the SRL, I have also investigated the properties of a subluminal laser (SLL), inside which the group velocity of light is much slower than the vacuum speed of light. It makes use of a composite gain spectrum consisting of a broad background along with a narrow peak. Since the group index can be very high, the frequency of such a laser is extremely insensitive to a change in the cavity length, thus making it highly stable. Same study is extended to another version of SRL, where the gain profile is generated by a diode pumped alkali laser (DPAL) and a Raman depletion.

The thesis is organized in the following way. In Chapter 2, a tapered nano-fiber (TNF) in

rubidium (Rb) system is introduced. The processes of TNF fabrication, installation, and maintenance are described. Experimental results of absorption and all-optical modulation achieved by using the TNF embedded in a Rb vapor cell are presented. A two-layer slab waveguide design is presented which is considered to be a substitute of the TNF. In Chapter 3, the N-level algorithm is introduced. This algorithm is first applied to a simple two level system and is then applied to more complicated atomic systems. A Doppler shift model is then added to this algorithm. Towards the end of this chapter, parallel computing techniques for enhancing the speed of this algorithm are presented. Chapter 4 discusses a Rb cascade system. Spectroscopy results are shown first. Absorption spectra under co-propagating and counter-propagating setups are compared. Results of all optical modulation using this system are presented. Chapter 5, 6, and 7 discuss applications of this Rb cascade system, namely high speed modulation, optically controlled polarizer, and optically controlled waveplate. Simulations and experimental results are shown. Chapter 9 presents a study of the superluminal ring laser (SRL). A double Raman pumped gain media is first introduced. I present the algorithm used for modeling the gain produced in such a system, taking into account the effect of an arbitrarily large number of harmonics that result from the interference between the two pumps. I also describe the experimental setup for studying the gain properties of such a medium, along with the results obtained. A subluminal laser (SLL) is then discussed as a counterpart of the SRL. Another version of SRL is studied where a Raman depletion absorption is induced into a broad DPAL gain profile. Finally, I describe an iterative algorithm for getting single mode numerical solution to the laser equation efficiently. A summary is presented at the end of the thesis.

CHAPTER 2 TAPERED NANO FIBER (TNF) IN RUBIDIUM

2.1 Introduction

The interaction of light with atomic ensembles [31,32] has created a number of advancements in generating and controlling classical and quantum states of light [1,33,34]. In order to enable optical interactions with few photons (as desired in some quantum information processing studies [2]), much effort has been invested into increasing the interaction between atoms and photons. This is often done by employing high finesse optical microcavities, where quantum effects are readily observed between a single atom and a single photon [35,36,37,38]. However, these systems are extremely complicated. For applications where single-photon interactions are not needed, atomic ensembles in a simple non-resonant geometry are used to observe quantum optic effects. Previously, most work was performed with optical beams focused into an alkali vapor, where the use of a bulk, free-space geometry fundamentally limited the interaction strength and/or length [34]. Recent experiments have resulted in significant increases in both interaction strength and interaction length by encasing an atomic vapor into a waveguide [14,15], with V-system electromagnetically induced transparency (EIT) demonstrated in a photonic crystal fiber (PCF) with approximately 3 nW of pulsed power [14]. In both of these cases, the enhanced interaction comes from reducing the optical mode area. Here we explore the use of tapered optical nanofibers (TNF) with optical mode areas smaller than in previous experiments, and demonstrate low light level nonlinear interactions with a rubidium atomic vapor.

A TNF consists of a single-mode silica optical fiber where the original fiber diameter is

reduced to the submicron range. In this system, the optical mode which was initially guided by the core (cladding) interface is adiabatically converted with negligible loss [9] into a mode guided by the cladding (environment) interface. The evanescent field extends into the surrounding environment, which for the purposes of this work consists of a rubidium atom vapor. The use of an evanescent interaction maintains the benefit of independently controlling the interaction strength (through cross-sectional geometry) and length (due to the invariance of the evanescent field along the waveguide), and allows an increase of interaction strength over previous waveguide approaches [14,15]. This system has been previously used to study evanescent interactions with Cs atoms, such as probing atom fluorescence [39，40]. In principle the interaction length can be arbitrary long, just as in any waveguide, with a limit due to intrinsic optical waveguide loss. For a TNF of diameter 400 nm, approximately 10% of the optical field interacts with the rubidium vapor. For this diameter, we estimate that the total number of atoms interacting with the TNF as 1400 = cm, which for the typical taper length of 3 mm in this work gives a total number of atoms of ~450 (assuming a Rb atomic density of 6×10^{12} atoms/cm^3 for a vapor at 100℃).

2.2 Fabrication

The TNF fabrication system contains four major parts, e.g. the pulling stage, the fire arm, the microscope system, and the transmission monitor, which are shown in Figure 2.1. The pulling stage is used to pull the fiber apart and control the fire arm during fabrication. It is built with a Newport 3-axis motion controller, which is controlled by a customized Matlab program. Axis 1 & 2 of the controller control two magnetic fiber clips and drive them apart in fabricating.

Axis 3 controls the fire arm and scan the flame along with the fiber during the pulling process. Parameters such as moving speed and acceleration of each axis is adjustable through Matlab. Changes of these parameters will change the widths and lengths of the TNF. High degree purified hydrogen and oxygen are used in the fire system. Each gas goes through two regulators sequentially and gets its pressure controlled. The gases mix at a T connector and release from a tapered outlet notch, which is assembled onto Axis 3 of the motion controller. A sapphire crystal is placed in the center of the outlet with a small gap between its side surface and the inside wall of the notch, which ensures the gas releases evenly and forms a nice cone-shape air flow. The microscope system is used to monitor the shape of the tapered fiber. This system contains an internal illumination light source, a microscope, and a display. As light comes out of the illumination source, it is forced by the microscope and shoots on the fiber. The reflection will be received by the microscope and send to the display. For a regular single mode fiber (SMF) with even diameter, the image on display is a bright white rectangle with a light grey border, which are corresponding to the core and cladding. For a TNF fiber, a rainbow pattern with will be seen on the display (Figure 2.2). This is because the TNF's diameter is gradually reduced from the outside to the center (tapered part). As white light shoots on the fiber, beam refracts on its way back. Similar phenomenon is commonly seen from a prism. The refraction pattern helps us to determine the width of TNF, which will be explained later. The transmission monitor is used to monitor the TNF's transmission. It contains a 780nm diode laser, a photo detector, and a digital scope. A laser beam from the diode laser is coupled into the fiber from one end. It transmits through the TNF and received by the detector. By monitoring the output intensity and comparing it with its original value (before pulling), we can tell the transmission

of the TNF.

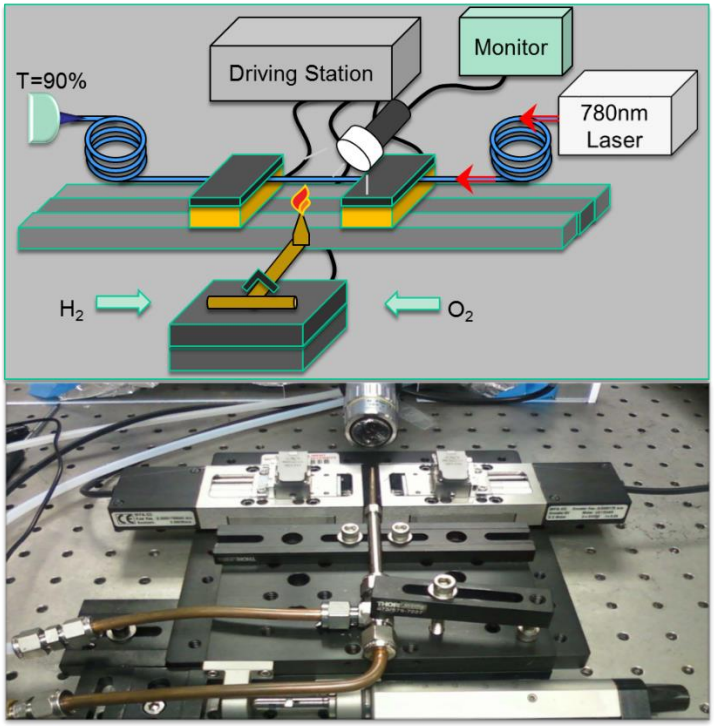

Figure 2.1 Tapered nano-fiber (TNF) fabrication system

TNF is built from a single mode fiber (SMF). Considering the resonant frequency of Rb system is in the 780nm range, we use Thorlabs 780HP fiber as the raw fiber, which has a 125μm thick cladding and a 250 μm coating. The coating, which is made by acrylic polymer, has to be removed before pulling. The stripped section is then cleaned by methanol. After the fiber is prepared, the Matlab code will be started. It will firstly initialize the motion controller by moving all three axes to their original positions. The pulling stage will then go into a one-minute idle before it starts pulling. Meanwhile, the prepared fiber will be loaded onto the pulling stage and firmly held by two magnetic clips. Its stripped section will be kept in the center of two clips. The fire will be lit once the pulling starts. The fiber gets heated by the flame and is pulled apart by axis 1 & 2. The pulling process will end when axis 1 & 2 reaches a

pre-defined position. And the flame will be turned off by closing the valves on two gas tubes. Pulling can also be terminated early by pressing a stop button on the motion controller if a desired TNF width has been observed through the monitoring system. The microscope system is used to monitor the width of tapered fiber. Unfortunately, due to the resolution limit of the microscope, the TNF image on display becomes very blur as the width of TNF's width gets smaller than 1 μm, which makes it hard to measure the width accurately. To precisely measure the width of the TNF, a high vacuum scanning electron microscope (SEM) is used. However, SEM requires its sample to be stick onto an isolating black tape. This operation will kill the transmission and make the TNF useless after measurement. To overcome this problem, it is found that the refraction pattern of the TNF can help to determine the fiber width without destroying fiber's transmission. As the tapered session gets thinner, the refraction pattern tends to show different color. A map is built to link the refraction pattern to the SEM test results (Figure 2.3). This map is used as an empirical matching engineer. After pulling is done, the refraction pattern will be looked up in the map to find the best matching width. Error of this estimation is around $\pm$100nm. The estimation can be improved after combined with the fiber transmission result. TNF's transmission is monitored by the transmission monitoring system. As TNF gets thinner, less energy is confined inside the fiber, which reduces the transmission [8]. Relation between energy fraction outside fiber and fiber diameter is shown in Figure 2.3. Combined the real transmission with dispersion pattern, the fiber width can be measured with an error about 50nm. Another usage of the transmission monitor is to make sure the TNF is fabricated properly. In a proper fabrication process, transmission will gradually reduce. Several factors, such as air flow and dust, can affect pulling quality. In such cases, abnormal volatility

will be captured by the transmission monitor. Fabrication has to be redone. After the pulling is finished, the TNF is glued onto a copper holder.

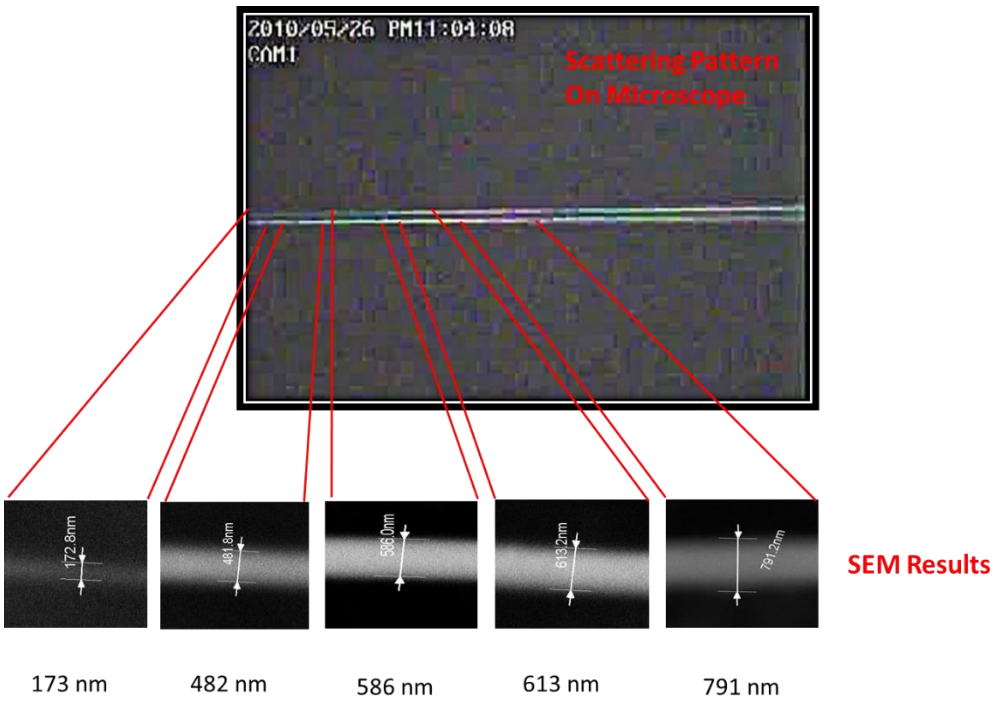

Figure 2.2 Map TNF scattering pattern with SEM test result.

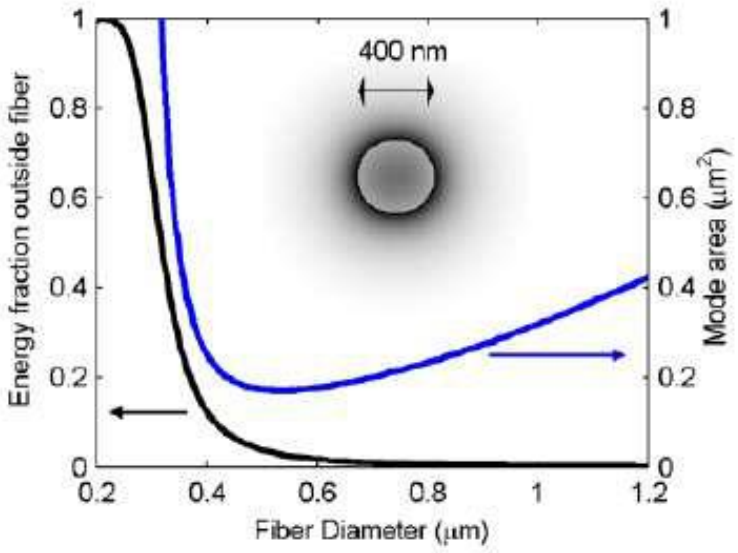

Figure 2.3 Fraction of mode energy outside fiber (black) and Mode area (blue) vs. fiber diameter.

2.3 Absorption in Rb vapor

Study of evanescent interaction is carried in a vacuum system. The vacuum system has two sections, e.g. a Rb reservoir and an interaction section. These sections are separated by a valve, and are continuously pumped by a mechanical pump to a pressure of 10 mTorr. The fiber is first attached to a custom made copper chuck using UV curable epoxy. The chuck is then inserted into the vapor cell from the top. Custom made Teflon ferrules mounted into Swagelok connectors are drilled through the center with a number 80 drill bit so that the fiber slips through. When the Swagelok connector is tightened, the ferrules are forced down and compressed to form a tight seal around the input and output of the fiber in order to keep air out of the system. To vaporize the Rb, the reservoir holding the Rb is heated to a temperature of 150 °C. In order to minimize the amount of Rb condensing on the cell and the fiber both are heated to about 100 °C. If Rb condenses on the fiber, transmission through the fiber will decrease. Light may be coupled into the fiber, and monitored at the output with an APD. A detailed schematic of the TNF system is shown in Figure 2.4.

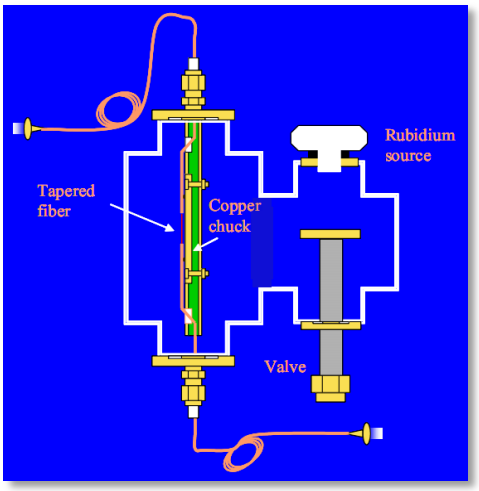

Figure 2.4 RB Vacuum System for evanescent interaction study.

Rb Linear Absorption with a Tapered Nano-fiber

A weak probe beam (approximately 10 nW) obtained from a Ti-Sapphire laser was transmitted through the TNF, and the optical transmission was monitored with an avalanche photodiode (APD), as shown in Figure 2.5(a). The frequency of the probe was scanned over the Doppler broadened spectrum of the D2 manifold. Figure 2.5(b) shows the transmission spectrum through the TNF (lower spectrum) and a reference Rb vapor cell kept at 100 °C (upper spectrum). The atomic density is estimated to be 6×10^{12} /cm^3.

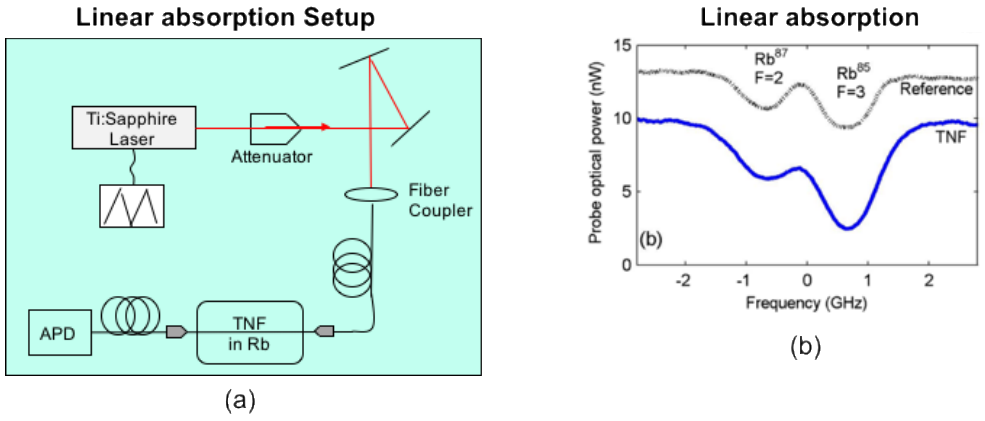

Figure 2.5 Linear absorption in a Rb vapor embedded TNF (blue) and reference cell (black)

The dip on the left corresponds to the F =2 transitions in the D2 manifold of ^{87}Rb, while the dip on the right corresponds to the F =3 transitions in the same manifold of ^{85}Rb. Far away from resonance, the probe was found to be attenuated by about 20% due to a combination of losses at the input couplers and by TNF absorption. The data clearly show transmission dips representative of Rubidium vapor absorption, with peak locations similar to that of the reference cell. However, the shape of the transmission dips for the Rb-TNF system is slightly

different than that for the reference cell, which is due to both differences in Doppler broadening and transit time dephasing present in this experimental measurement.

2.4 V-system modulation

We also performed a modulation experiment in the TNF system using counter-propagating and orthogonally polarized pump and probe. The experimental setup is summarized in Figure 2.6. The output of a Ti:Sapphire laser was split by a 50/50 non-polarizing beam splitter. The beam reflected by the splitter was shifted up by 80 MHz with an acousto-optic modulator (AOM), to produce the S-polarized probe beam. The beam passing through the splitter was upshifted by a second AOM, also at 80 MHz, to produce the pump beam, which was P-polarized by passing through a half-wave plate. Attenuators (not shown) were then used to reduce the power in both beams independently. The pump and probe were combined on a polarizing beam-splitter (PBS), and coupled into the TNF. The output was passed through another PBS, separating out the pump and the probe. The probe was then detected with an avalanche photo-diode (APD). Using another non-polarizing beam splitter, 10% of the probe beam (before attenuation) was diverted to a vapor cell for saturated absorption spectroscopy. Signal from this cell was used to lock the laser to a hyperfine transition.

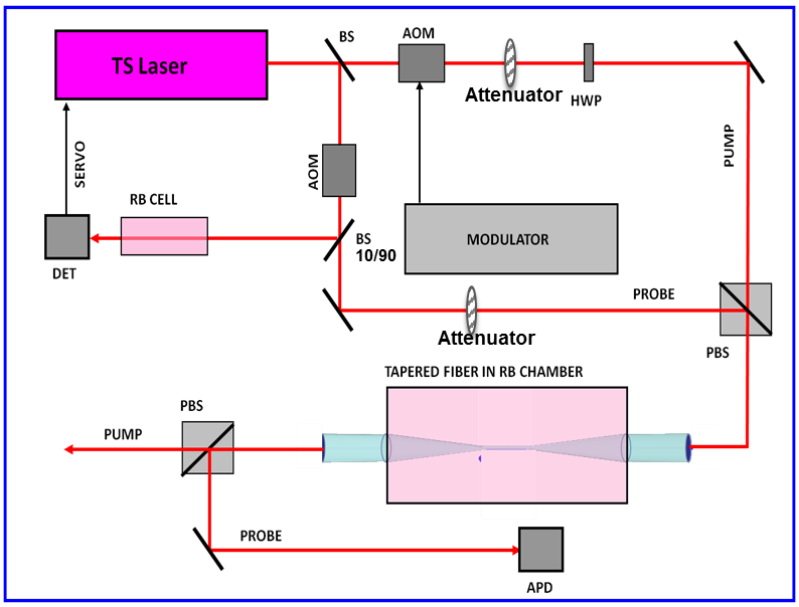

Figure 2.6 Experimental setup for demonstrating degenerate V-system modulation. Both AOMs are operated at the same frequency (80 MHz). The pump and the probe are each linearly polarized and orthogonal to each other.

A saturated absorption measurement was also performed using this setup and it showed the expected transparencies along with the cross-over peaks. Figure 2.7 illustrates the probe transmission spectrum (power ~1 nW) for counter- propagating pump powers of 10 nW (middle, green) and 30 nW (lower, red), for a TNF with a waist diameter of approximately 400 nm. For comparison, a reference trace is also shown for a conventional vapor cell (upper, blue). Here, the transparencies correspond to the F =3→ F'=2 and F= 3→F'= 3 transitions and the corresponding cross-over peak.

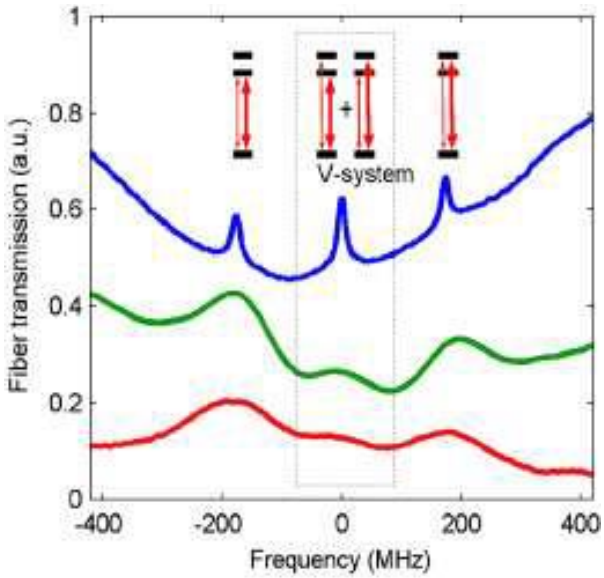

Figure 2.7 Saturated absorption observed in TNF with a probe power of 1 nW and a pump power of 10 nW (green) and 30 nW (red). Also plotted is saturated absorption in a reference cell (blue)

For the conventional vapor cell, the transparency seen at the cross-over resonance is larger than that at the hyperfine resonance peaks due to the larger number of atoms in the combined 180 MHz Doppler-shifted groups (there is approximately 1.5 times the number of atoms in an isotropic vapor cell, which arises from the width of the Doppler distribution) than the individual zero axial velocity groups. Furthermore, the peak widths are the power-broadened individual hyperfine transitions (~6 MHz power broadened to ~18 MHz). However, for the TNF signal, there is a noticeable difference between the linewidths and relative amplitudes of the two peaks. Here, the line broadening for the lower (middle) power curve is due primarily to the transit-time effect. The transit-time broadening is about 110 MHz, close to the theoretical prediction. The dramatically smaller amplitude of the cross-over resonance in the TNF measurement is likely due to a non-isotropic atomic velocity distribution in the Rb-TNF cell,

which leads to a smaller population of atoms with the correct longitudinal Doppler shifted velocity component. The relative magnitude of the three absorption peaks is consistent with a 210 MHz wide effective Doppler distribution. The effective reduction of the Doppler width may be attributable to the geometry of the cell and the relative position of the TNF and the vacuum pump. Further investigation will be carried out in the future to study this effect.

Figure 2.8 shows Rb linear absorption data taken using this setup. The probe (pump) power was 100 pW (40 nW). First, the red trace shows the probe transmission when the pump beam is turned off. As the probe frequency was scanned across the D1 manifold, three dips were observed. The biggest dip corresponds to the transition from the $5S_{1/2}$, F=3 ground-state in ^{85}Rb to the $5P_{3/2}$ hyperfine levels, which are not resolved because of Doppler broadening. The small dip on its left corresponds to a transition in ^{87}Rb, from $5S_{1/2}$, F=2 ground-state to the $5P_{3/2}$ hyperfine levels. The dip on its right corresponds to the transition from the $5S_{1/2}$, F=2 ground-state in ^{85}Rb to the $5P_{3/2}$ hyperfine levels. The scan range was not long enough to see the other transition in ^{87}Rb, from $5S_{1/2}$, F=1 ground-state to the $5P_{3/2}$ hyperfine levels.

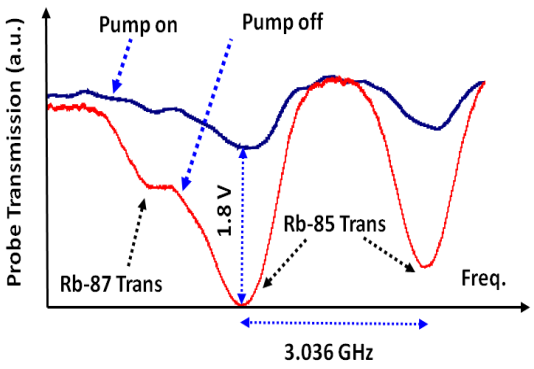

Figure 2.8 Absorption of D1 line in the absence (red) and presence (blue) of the pump.

The blue trace shows the probe absorption when the pump is turned on. There is a strong increase in the probe transmission at the center of the F=3 transition (the middle one in Figure 2.8). The physical mechanism behind the strong modulation of the probe transmission caused by the pump can be explained as follows. Consider first the Zeeman sublevel of the $m_F = 0$ in the F=3 ground-state, and how it is coupled to the F" = 2 excited state. The probe, which is a superposition of left and right circularly polarized light, with a relative phase Ψ, would couple this state to $m_F = -1$ and $m_F = 1$ sublevels in the F" = 2 state. The pump is also a superposition of left and right circularly polarized light, with a relative phase Φ, and would excite the same pair of transitions. However, the phases Ψ and Φ differ by π. As such, the net interaction can be represented as a V-system, with one leg excited by the probe and the other by the pump. This is illustrated in Figure 2.9. Here, the in-phase superposition state (|p>) is coupled to the ground state |a> by the P-polarized pump beam only, and the out-of-phase superposition state (|n>) is coupled to the ground state |a> by the S-polarized probe beam only. Thus, the net interaction is equivalent to the V-system and the mechanism can be understood in terms of the Autler Townes splitting or the Quantum Zeno effect, as explained in the previous chapter. Specifically, when the pump is turned on, the ground state gets split into two dressed states, each out of resonance for the probe if the pump intensity is greater than the saturation intensity of the isolated atom (i.e., $\Omega > \Gamma$, where Ω is the pump Rabi frequency, and Γ is the natural linewidth). When the Doppler broadening is taken into account, the condition for probe transparency is that $\Omega > \sqrt{\Gamma * \Gamma_D}$, where Γ_D is the half-width of the Doppler broadening. This condition is satisfied by the pump power (~40 nW) used. The same model applies to transitions to the F' = 3 and F' = 4

excited states as well. Of course, for some values of mF, only left (right) circular transition is allowed; in that case, the system behaves as a pure two level transition, excited by identically polarized parts of the pump and the probe. The reduction in probe transmission for these sublevels is due to the conventional saturation based transparency.

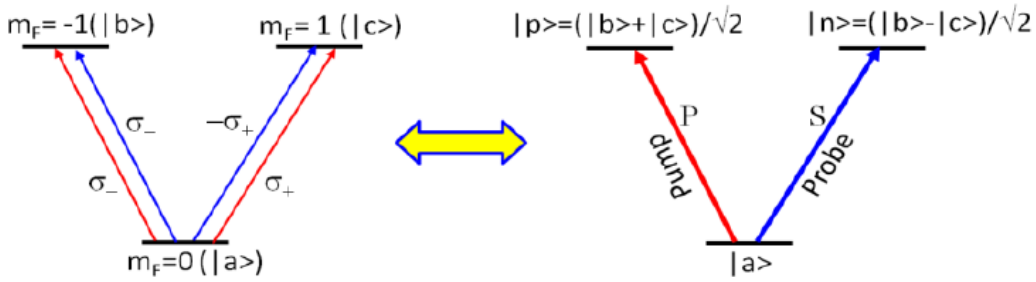

Figure 2.9 Schematic illustration of the Autler Townes splitting (AC Stark splitting) induced transparency.

It should be noted that when the pump is turned on, the residual probe absorption develops some asymmetry, and the centroid of each dip appears to be slightly shifted. Further investigation is required to elucidate the origin of these effects - for the purpose of modulation, these effects may not be very important.

Figure 2.10 shows results of pulsed modulation, with the laser locked at the center of the F=3 transition. The probe is kept constant at 100 pW, while the pump intensity is modulated by using the pump AOM. The top left panel shows the probe transmission when this modulation is at 10 Hz. The other three panels show the same for increasing modulation frequencies. At 10 KHz, the probe transmission deviates from the square profile, due to the limited bandwidth (~50kHz) of the APD.

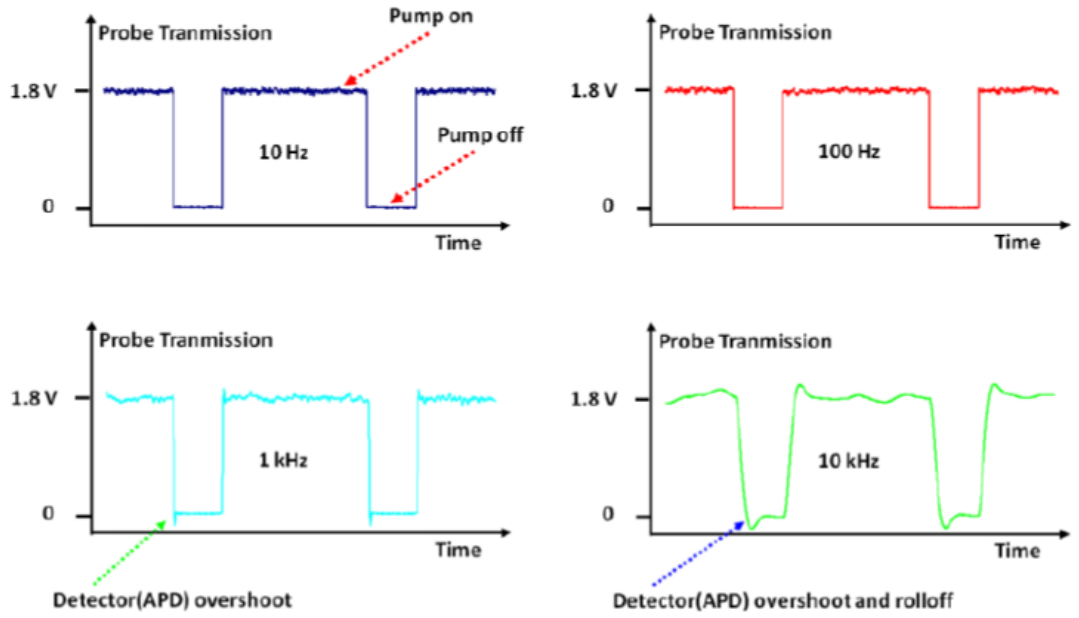

Figure 2.10 Low-frequency modulation results for a duty cycle of 70% (on-state), for four different frequencies. At 10 kHz, the signal is limited by the APD bandwidth.

A careful consideration of the physical mechanism behind this modulation reveals that the modulation speed is fundamentally limited by the time needed for the atoms to repopulate the ground state, |a>, after the pump is turned off, so that they can absorb the probe again. This means that the modulation bandwidth cannot exceed the homogeneous linewidth (HL). The HL can be increased very significantly by adding a buffer gas, such as ^{4}He. In a series of studies carried out in the context of the development of diode pumped alkali lasers (DPALs), it has been shown that the atoms excited to the $5P_{3/2}$ state relaxes very rapidly to the $5P_{1/2}$ state. The rate of relaxation from the 5P1/2 state to the ground state can be augmented by adding an auxiliary, strong beam that would be turned on and at the same time as the pump is turned off, and turned off before turning on the pump again. For buffer gas pressure of 1 atm, the HL is

about 20 GHz. A HL as large as 500 GHz is possible in the presence of a buffer gas pressure of 25 atm. This is discussed in greater detail in a later chapter.

In order to take advantage of this, one has to employ cascade transitions as the rapid fine structure mixing happens between the spin-3/2 and spin-1/2 state. Further, we would like to operate at a telecommunication wavelength. Hence, we decided to employ the $5S_{1/2}$-$5P_{1/2}$-$6S_{1/2}$ transition where the lower leg is excited by a pump optical field at 795 nm, while the upper leg is probed using a weak optical field at 1323 nm. We will discuss some spectroscopic details of the system before moving on to the actual experiments.

2.5 Enhancing TNF's Life Time

It is found that the TNF's transmission drops gradually over time and is believed that the fundamental reason for the transmission dying down was because of Rb atoms sticking to the relatively cooler surface of the fiber, thereby preventing transmission and breaking the symmetry of the evanescent field around the TNF. I tried four approaches to overcome this problem. First, a sandwich structure fiber holder is designed, which is composed by two layers of copper (Figure 2.11). The TNF is placed between two layers and is held tightly by the rubber cushions on both sides of the holder. The TNF received better heating in this way. Second, a tungsten filament is placed around the TNF. After the TNF's transmission drops, this filament will heat the TNF and bring the transmission back. The configuration is shown in Figure 2.12. Third, a laser cleaning system is built with a 25W CO_2 laser, as shown in Figure 2.13. The laser beam, coming out from the CO_2 laser, is focused on the TNF. The focus spot can be moved by turning the tilt mirror. The TNF gets heated by the laser beam and transmission will be resumed

in some degree. However, this setup can only clean one side of the TNF which is facing toward the incoming lase beam. Also, it is very hard to perfectly align and focus the beam since beam is invisible. Forth, we tried to replace the Rb cell with several Rb getters [REF]. The Rb getter, as shown in Figure 2.14, is a semiconductor device, which is designed to release Rb vapor by a desired precise amount. The release rate is controlled by the voltage applied to the device. However, after a series tests, it is found that the release rate is too low to match our experiment requirement.

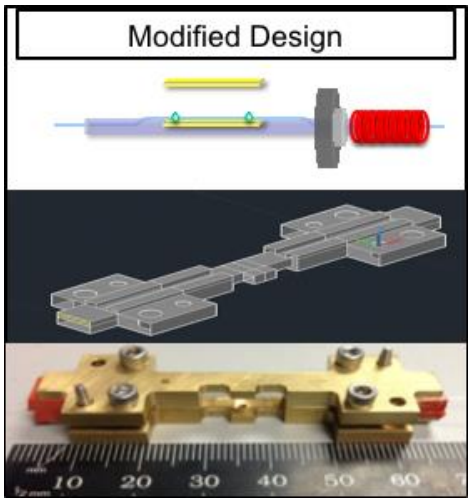

Figure 2.11 Sandwich structure fiber holder for enhancing TNF's life time.

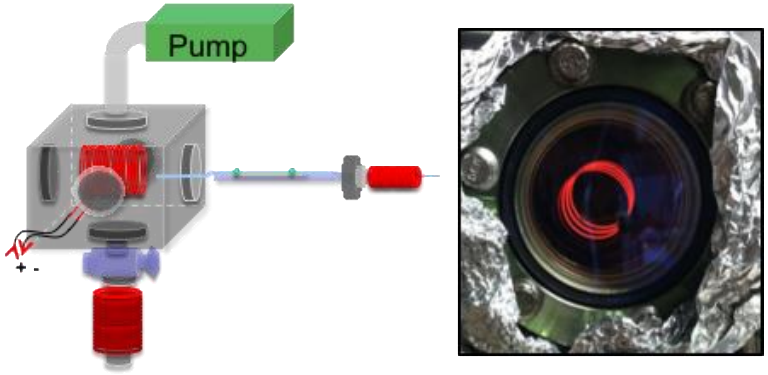

Figure 2.12 a tungsten filament placed around the TNF for enhancing TNF's life time.

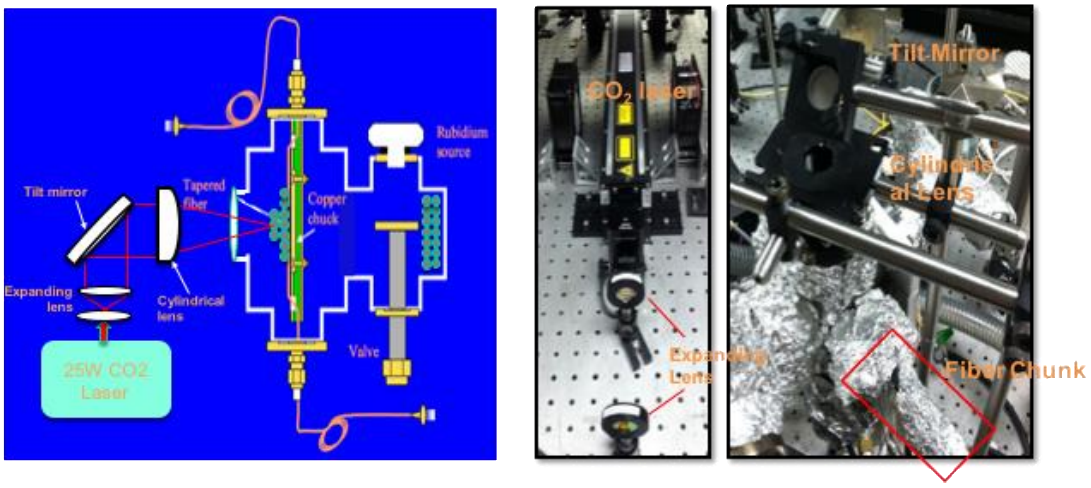

Figure 2.13 A CO2 Laser Cleaning System for enhancing TNF's life time.

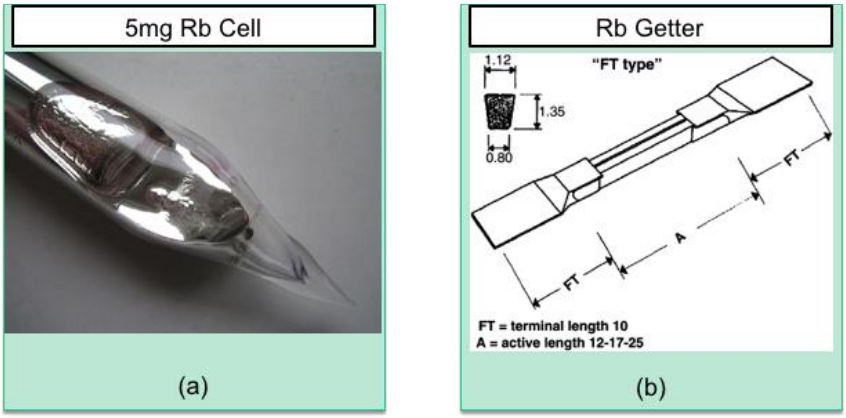

Figure 2.14 Replace Rb Cell with Rb Getter.

2.6 Substitute: A Two-Layer Slab Waveguide

Considering TNF's high maintaining cost and relatively short lift time, we considered to use a customized slab waveguide to replace the TNF. To make a waveguide, we need to provide the materials and dimensions of the waveguide. Effective index approximation [41] is used here.

Traditional slab waveguide contains three layers of materials with different dielectric constants. Light may be confined in the middle layer by total internal reflection if the dielectric

index of the middle layer is larger than that of the surrounding layers [42]. In our case, the waveguide is designed to be a two-layer slab and the top layer is removed so that the evanescent field on top of the waveguide can interact with its surrounding environment. Silicon nitride and silicon dioxide are used as the middle and base layers respectively. The refractive index of silicon nitride (n2) and silicon dioxide (n3) is a function of wavelength. They are given by ref. 43

$$n_2(\lambda) = \sqrt{\frac{B_1 \times \lambda^2}{\lambda^2 - {B_2}^2} + 1} \qquad 2.1\ (a)$$

$$n_3(\lambda) = \sqrt{C_1 + \frac{C_2 \times \lambda^2}{\lambda^2 - C_3} + \frac{C_4 \times \lambda^2}{\lambda^2 - C_5}} \qquad 2.1\ (b)$$

where $B_1 = 2.8939$, $B_2 = 0.13967$, $C_1 = 1.28604141$, $C_2 = 1.07044083$, $C_3 = 1.00585997 \times 10^{-2}$, $C_4 = 1.10202242$, $C_5 = 100$, and λ is in micro-meter. For $\lambda = 795\text{nm}$, n2 = 1.9965, n3 = 1.5384. For $\lambda = 1323\text{nm}$, n2 = 1.9815, n3 = 1.5307. These values are used to calculate the power distribution and effective refractive index which will be discussed.

Figure 2.15 shows the schematic of using effective index approximation to simulate power distribution of such a slab waveguide. Figure 2.15(a) shows a 3D view of this slab waveguide. A horizontally polarized light is coupled into the waveguide and propagates along the z direction. The waveguide is placed on the x-z plane and its vertical axis is defined as y. The thickness of silicon nitride layer is t nm. The width of silicon nitride layer is w nm. Width of the silicon dioxide layer is the same. Considering the power fraction within the base layer won't be able to interact with the environment, we set the thickness of the silicon dioxide to be infinite to simplify the calculation. To study the power distribution of this waveguide, we use effective refractive index approximation. The first step is to calculate the power distribution on top of the

waveguide in 2D, where we assume the slab has an infinite width, as shown in Figure 2.15(b). The effective refractive index is also calculated here. A slab waveguide is now considered to be an effective media with a unique refractive index, which is equal to the effective refractive index. We then assume the thickness of the media is infinite and calculate the power distribution on two sides of the media by plugging the effective refractive index into Maxwell Equation, as shown in Figure 2.15(c). Figure 2.16 shows the power distribution and effective refractive index calculated in the asymmetric case. Figure 2.17 shows the power distribution in the symmetric case.

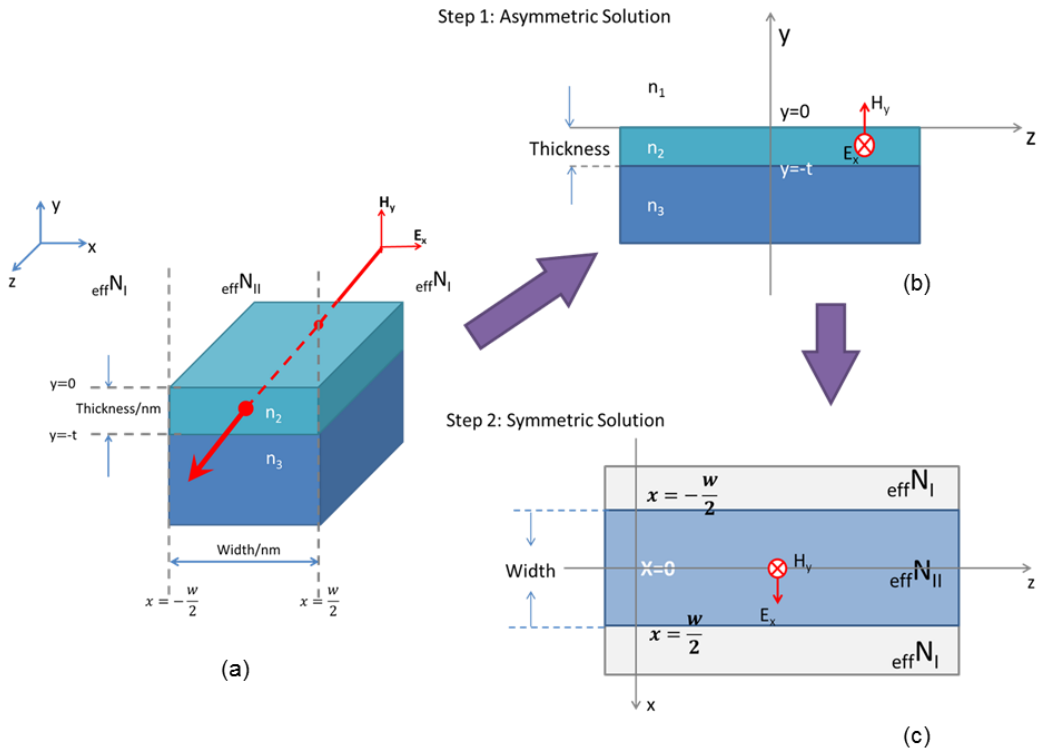

Figure 2.15 Schematic of using effective index approximation to simulate power distribution of such a slab waveguide. See text for more details.

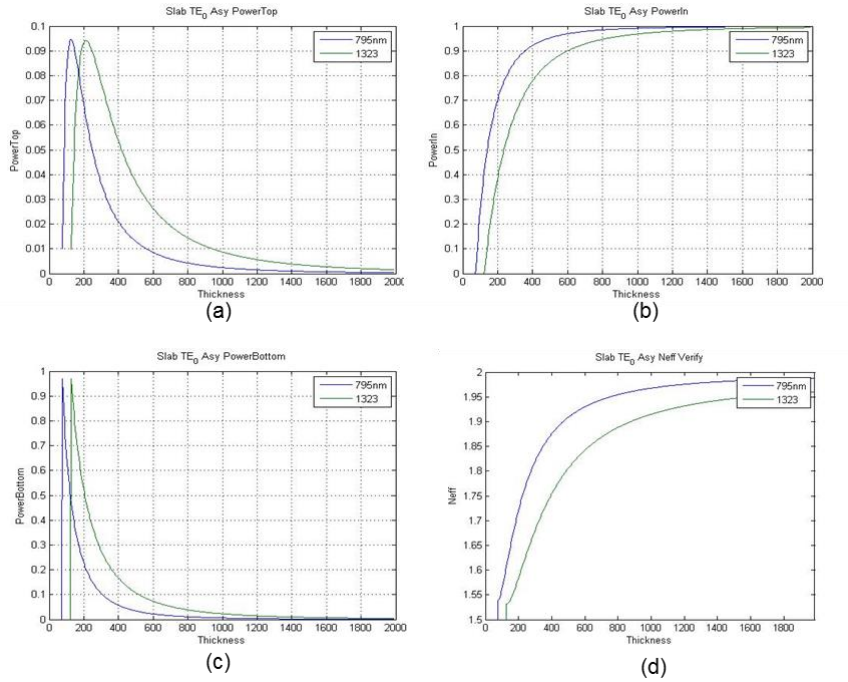

Figure 2.16 Two-layer slab waveguide power distribution and effective refractive index in asymmetric case, assuming slab width is infinite. Plot (a - c) shows the power fraction as a function of waveguide thickness at the top, inside, and bottom of the silicon nitride layer respectively. Plot (d) shows the effective refractive index as a function of waveguide thickness. The blue and green lines represent the values for 795nm and 1323nm beam respectively.

Remember in the TNF session, a 10% power leakage was observed within a 450nm nano-fiber. We would like to obtain the same power distribution using this waveguide. However, due to manufacture limits, the smallest thickness achievable was 250nm. Considering the power leakage on top of the waveguide (shown in Figure 2.16 (a)) is monotonically decreasing when thickness goes larger than 250nm. We choose t = 250nm as the desired thickness. Power distribution of a two-layer slab waveguide with infinite width and

250nm thickness is shown in Table 2.1.

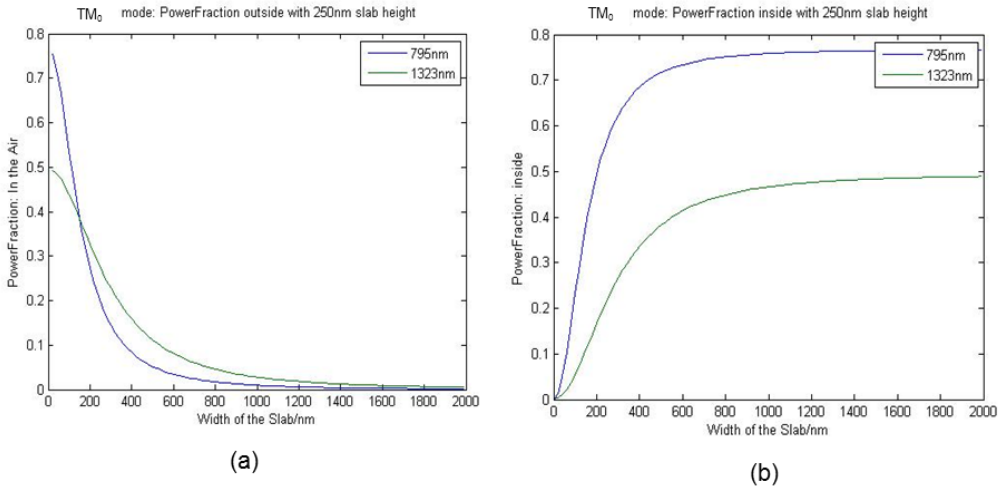

Figure 2.17 Power distribution of two-layer slab waveguide in symmetric case. Effective refractive approximation is used here. Plot (a) shows the power fraction on the sides of the effective media changes as a function of media width. Plot (b) shows the power fraction within the media.

Combining results of asymmetric solution and symmetric solution, we designed a waveguide with 250nm thickness and 400nm width. The total power distribution is given in Table 2.2.

	780nm	**1323nm**
Top	~5%	~9%
Inside	~80%	~55%
Bottom	~15%	~36%

Table 2.1 Power distribution in and out of the top layer of a two-layer slab waveguide

with infinite width and 250nm thickness.

	780nm	**1323nm**
Top	~5%	~9%
Sides	~8%	~16%
Outside total	~13%	~25%
in waveguide	~68%	~33%

Table 2.2 Power distribution of the two-layer slab waveguide with 250nm thickness and 400nm width.

CHAPTER 3 N-LEVEL ALGORITHM

3.1 Introduction

For some situations in atomic and molecular physics, it is necessary to consider a system with many energy levels, such as excitation involving many hyperfine levels and/or Zeeman sublevels. The Liouville's equation that describes the evolution of the density matrix, is expressed in terms of a commutator between the density matrix and the Hamiltonian, as well as additional terms that account for decay and redistribution [16, 44, 45, 46, 47]. To find solutions to this equation in steady-state or as a function of time, it is convenient first to reformulate the Liouville's equation by defining a vector corresponding to the elements of the density operator, and determining the corresponding time evolution matrix. To find the steady-state solution in a closed system, it is also necessary to eliminate one of the diagonal elements of the density matrix from these equations, because of redundancy. For a system of N atoms, the size of the evolution matrix is $N^2 \times N^2$, and the size of the reduced matrix is $(N^2 - 1) \times (N^2 - 1)$. When N is very large, evaluating the elements of these matrices becomes very cumbersome. In this section, we describe an algorithm that can produce the evolution matrix in an automated fashion, for an arbitrary value of N.

This Algorithm has been proven greatly helpful and extended to all my future researches. Usage of N-Level algorithm will be revisited in later chapters of this thesis.

3.2 A Two Level System

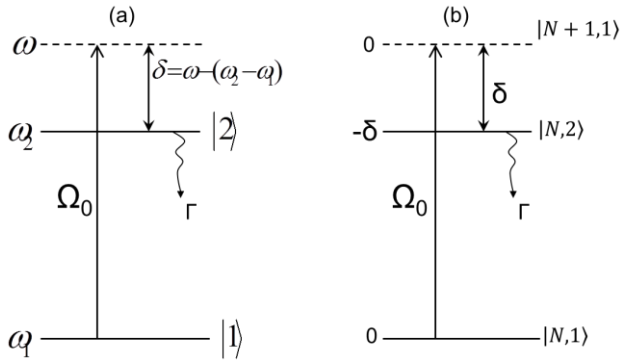

Figure 3.1 Schematic diagram showing a two-level system. (a) two-level system with eigenvector |1> and |2> ; (b) considering photon numbers, where |N,1> and |N+1,1> have the same energy, and the energy difference between |N+1,1> and |N,2> is ħδ

To illustrate the basic idea behind the algorithm, we first consider the simplest case: a two-level system of atoms excited by a monochromatic field [46], as illustrated in Figure 3.1. Here, $\hbar\omega_1$ and $\hbar\omega_2$ are the energies of levels $|1>$ and $|2>$, and ω is the frequency of the laser, with a Rabi frequency of Ω_0 [48]. The Hamiltonian, under electric dipole and rotating wave approximations, is given as

$$H=\hbar\begin{pmatrix} \omega_1 & \frac{\Omega_0}{2}e^{i(\omega t-kz_0+\phi)} \\ \frac{\Omega_0}{2}e^{-i(\omega t-kz_0+\phi)} & \omega_2 \end{pmatrix} \qquad (3.1)$$

where k is the wavenumber of the laser, z_0 is the position of the atom, and ϕ is the phase of the field. Without loss of generality, we set $z_0=0$ and $\phi=0$ in what follows. The corresponding two-level state vector for each atom is

$$|\psi\rangle = \begin{bmatrix} C_1(t) \\ C_2(t) \end{bmatrix} \tag{3.2}$$

which obeys the Schrodinger Equation

$$\mathrm{i}\hbar \frac{\partial |\psi\rangle}{\partial t} = \mathrm{H}\,|\psi\rangle \tag{3.3}$$

To simplify the calculation, we convert the wave function to the rotating wave frame by carrying out the following transformation into an interaction picture:

$$|\tilde{\psi}\rangle \equiv \begin{bmatrix} \tilde{C}_1(t) \\ \tilde{C}_2(t) \end{bmatrix} = R|\psi\rangle \tag{3.4}$$

where

$$R = \begin{bmatrix} \mathrm{e}^{\mathrm{i}\omega_1 \mathrm{t}} & 0 \\ 0 & \mathrm{e}^{\mathrm{i}\omega_2 \mathrm{t}} \end{bmatrix}$$

The Schrödinger equation now can be written as

$$\mathrm{i}\hbar \frac{\partial |\tilde{\psi}\rangle}{\partial t} = \tilde{\mathrm{H}}\,|\tilde{\psi}\rangle \tag{3.5a}$$

where

$$\tilde{\mathrm{H}} = \hbar \begin{pmatrix} 0 & \frac{\Omega_0}{2} \\ \frac{\Omega_0}{2} & -\delta \end{pmatrix} \tag{3.5b}$$

$$\delta = \omega - (\omega_2 - \omega_1) \tag{3.5c}$$

The time independent Hamiltonian shown in Eqn. 3.5b can also be derived easily without any algebraic manipulation. To see how, consider the diagram shown in Figure 3.1(b), where we have added the number of photons as a quantum number in designating the quantum states. Thus, for example, |N,1> represents a joint quantum system where the number of photons in the laser field is N, and the atom is in state 1, and so on. Of course, a laser, being in a coherent

state, is a linear superposition of number states, with a mean photon number <N>, assumed to be much larger than unity. In the presence of such a field, the interaction takes place between near-degenerate states, namely |N,2> and |N+1,1>, for example, with a coupling rate of $\Omega_0/2$, where $\Omega_N \propto \sqrt{N}$. Since the mean value of N is assumed to be very large, and much larger than its variance, one can assume the mean value of Ω_N, defined as Ω_0 to be proportional to $\sqrt{\langle N \rangle}$. Under this approximation, we see that the coupling between any neighboring, near-degenerate pair of states is Ω_0, and the energies of these states differ by δ. If we choose the energy of |N+1,1> to be 0, arbitrarily, then the energy of |N,2> is –ħδ. The interaction is contained within a given manifold, so that a difference in energy (by ħω) between neighboring manifold is of no consequence in determining the evolution. These considerations directly lead to the Hamiltonian in Eqn.3.5(b). For a system involving more than two levels, a similar observation can be employed to write down the time-independent Hamiltonian by inspection, as we will show later.

The decay of the excited state amplitude, at the rate of $\Gamma/2$, can be taken into account by adding a complex term to the Hamiltonian, as follows:

$$\widetilde{\mathcal{H}}' = \hbar \begin{bmatrix} 0 & \frac{\Omega_0}{2} \\ \frac{\Omega_0}{2} & -\frac{i\Gamma}{2} - \delta \end{bmatrix}$$

(3.6)

For this modified Hamiltonian, the equation of evolution for the interaction picture density operator can be expressed as

$$\frac{\partial}{\partial t}\tilde{\rho} = \frac{\partial}{\partial t}\tilde{\rho}_{ham} + \frac{\partial}{\partial t}\tilde{\rho}_{source} + \frac{\partial}{\partial t}\tilde{\rho}_{transverce-decay} \equiv Q$$

(3.7)

where the 2nd term in the middle accounts for the influx of atoms into a state due to decay from another state, and the 3rd term stands for the dephasing decay. In the case of a two level system, we have:

$$\frac{\partial}{\partial t}\tilde{\rho}_{ham} = -\frac{i}{\hbar}\left[\tilde{\mathcal{H}}'\tilde{\rho} - \tilde{\rho}\tilde{\mathcal{H}}'^{*}\right]$$

(3.8.a)

$$\frac{\partial}{\partial t}\tilde{\rho}_{source} = \begin{bmatrix} \Gamma\tilde{\rho}_{22} & 0 \\ 0 & 0 \end{bmatrix} \tag{3.8.b}$$

$$\frac{\partial}{\partial t}\tilde{\rho}_{transverce-decay} = \begin{bmatrix} 0 & -\gamma_d\tilde{\rho}_{12} \\ -\gamma_d\tilde{\rho}_{21} & 0 \end{bmatrix} \tag{3.8.c}$$

For simplicity, later in this thesis, we ignore the dephasing term in Eqn. 3.8(c). Substituting Eqn.3.6 into Eqn. 3.8a, we get:

$$\frac{\partial}{\partial t}\tilde{\rho}_{\text{ham}} = \begin{pmatrix} \frac{1}{2}i\Omega_0\left(\tilde{\rho}_{12} - \tilde{\rho}_{21}\right) & \frac{1}{2}i\left((i\Gamma - 2\delta)\tilde{\rho}_{12} + \Omega_0\left(\tilde{\rho}_{11} - \tilde{\rho}_{22}\right)\right) \\ -\frac{1}{2}i\left((-i\Gamma - 2\delta)\tilde{\rho}_{21} + \Omega_0\left(\tilde{\rho}_{11} - \tilde{\rho}_{22}\right)\right) & \frac{1}{2}\left(-i\Omega_0\left(\tilde{\rho}_{12} - \tilde{\rho}_{21}\right) - 2\Gamma\tilde{\rho}_{22}\right) \end{pmatrix}$$

(3.9)

Substituting Eqn. 3.8 into 3.7, we get

$$\frac{\partial}{\partial t}\tilde{\rho} = \frac{\partial}{\partial t}\begin{pmatrix} \tilde{\rho}_{11} & \tilde{\rho}_{12} \\ \tilde{\rho}_{21} & \tilde{\rho}_{22} \end{pmatrix} = \begin{pmatrix} \frac{1}{2}\mathrm{i}\Omega_0\left(\tilde{\rho}_{12} - \tilde{\rho}_{21}\right) + \Gamma\tilde{\rho}_{22} & \frac{1}{2}\mathrm{i}\left(\mathrm{i}(\Gamma + 2\mathrm{i}\delta)\tilde{\rho}_{12} + \Omega_0\left(\tilde{\rho}_{11} - \tilde{\rho}_{22}\right)\right) \\ -\frac{1}{2}\mathrm{i}\left((-\mathrm{i}\Gamma - 2\delta)\tilde{\rho}_{21} + \Omega_0\left(\tilde{\rho}_{11} - \tilde{\rho}_{22}\right)\right) & \frac{1}{2}\left(-\mathrm{i}\Omega_0\left(\tilde{\rho}_{12} - \tilde{\rho}_{21}\right) - 2\Gamma\tilde{\rho}_{22}\right) \end{pmatrix}$$
$$= Q \equiv \begin{pmatrix} Q_{11} & Q_{12} \\ Q_{21} & Q_{22} \end{pmatrix}$$

(3.10)

To solve these equations, it is convenient to construct the following vector

$$A = \begin{bmatrix} \tilde{\rho}_{11} \\ \tilde{\rho}_{12} \\ \tilde{\rho}_{21} \\ \tilde{\rho}_{22} \end{bmatrix} \tag{3.11}$$

Eqn.3.10 can now be expressed as a matrix equation

$$\frac{\partial}{\partial t} A = MA \tag{3.12}$$

where M is a (4×4) matrix, represented formally as:

$$M = \begin{bmatrix} M_{11} & M_{12} & M_{13} & M_{14} \\ M_{21} & M_{22} & M_{23} & M_{24} \\ M_{31} & M_{32} & M_{33} & M_{34} \\ M_{41} & M_{42} & M_{43} & M_{44} \end{bmatrix}$$

Of course, the elements of this matrix can be read-off from Eqn.3.10. However, this task is quite cumbersome for an N-level system. Thus, it is useful to seek a general rule for finding this element without having to write down Eqn. 3.10 explicitly. Later on in this paper, we establish such a rule, and specify the algorithm for implementing it. Here, we can illustrate this rule with some explicit examples:

$M_{11} = Q_{11}$, if we set $\tilde{\rho}_{11} = 1$ and $\tilde{\rho}_{ij(ij \neq 11)} = 0$ in Eqn.3.7;

$M_{12} = Q_{11}$, if we set $\tilde{\rho}_{12} = 1$ and $\tilde{\rho}_{ij(ij \neq 12)} = 0$ in Eqn.3.7;

$M_{13} = Q_{11}$, if we set $\tilde{\rho}_{21} = 1$ and $\tilde{\rho}_{ij(ij \neq 21)} = 0$ in Eqn.3.7;

$M_{14} = Q_{11}$, if we set $\tilde{\rho}_{22} = 1$ and $\tilde{\rho}_{ij(ij \neq 22)} = 0$ in Eqn. 3.7;

$M_{21} = Q_{12}$, if we set $\tilde{\rho}_{11} = 1$ and $\tilde{\rho}_{ij(ij \neq 11)} = 0$ in Eqn.3.7;

$M_{22} = Q_{12}$, if we set $\tilde{\rho}_{12} = 1$ and $\tilde{\rho}_{ij(ij \neq 12)} = 0$ in Eqn. 3.7;

$M_{23} = Q_{12}$, if we set $\tilde{\rho}_{21} = 1$ and $\tilde{\rho}_{ij(ij \neq 21)} = 0$ in Eqn. 3.7;

$M_{24} = Q_{12}$, if we set $\tilde{\rho}_{22} = 1$ and $\tilde{\rho}_{ij(ij \neq 22)} = 0$ in Eqn. 3.7;

Etc. ... *(3.13)*

This is the key element of the algorithm presented in this paper. Explicitly, in a computer program, such as the one in Appendix A, every time a parameter is changed, the elements of the M matrix are evaluated by repeating Eqn.3.7, while setting all but one of the elements of the density matrix to zero. For numerical integration as a function of time, one can then use a Taylor expansion, for example, to solve Eqn. 3.12.

To find the steady-state solution, we set $\frac{\partial}{\partial t} A = 0$, so that:

$$\begin{bmatrix} M_{11} & M_{12} & M_{13} & M_{14} \\ M_{21} & M_{22} & M_{23} & M_{24} \\ M_{31} & M_{32} & M_{33} & M_{34} \\ M_{41} & M_{42} & M_{43} & M_{44} \end{bmatrix} \begin{bmatrix} \tilde{\rho}_{11} \\ \tilde{\rho}_{12} \\ \tilde{\rho}_{21} \\ \tilde{\rho}_{22} \end{bmatrix} = 0 \qquad (3.14)$$

Expanding this equation, we get:

$$\begin{cases} M_{11}\tilde{\rho}_{11} + M_{12}\tilde{\rho}_{12} + M_{13}\tilde{\rho}_{21} = -M_{14}\tilde{\rho}_{22} \\ M_{21}\tilde{\rho}_{11} + M_{22}\tilde{\rho}_{12} + M_{23}\tilde{\rho}_{21} = -M_{24}\tilde{\rho}_{22} \\ M_{31}\tilde{\rho}_{11} + M_{32}\tilde{\rho}_{12} + M_{33}\tilde{\rho}_{21} = -M_{34}\tilde{\rho}_{22} \\ M_{41}\tilde{\rho}_{11} + M_{42}\tilde{\rho}_{12} + M_{43}\tilde{\rho}_{21} = -M_{44}\tilde{\rho}_{22} \end{cases} \qquad (3.15)$$

For a closed system, the sum of the diagonal elements of the density matrix equals unity. In the case of the two level system, we thus have $\tilde{\rho}_{11} + \tilde{\rho}_{22} = 1$. Since we have five equations for four variables, one of the equations in Eqn.3.15 is redundant. We can thus choose to eliminate the last equation, for example, and replace $\tilde{\rho}_{22}$ with $(1 - \tilde{\rho}_{11})$ in the remaining three equations, to get

$$\begin{bmatrix} M_{11} & M_{12} & M_{13} \\ M_{21} & M_{22} & M_{23} \\ M_{31} & M_{32} & M_{33} \end{bmatrix} \begin{bmatrix} \tilde{\rho}_{11} \\ \tilde{\rho}_{12} \\ \tilde{\rho}_{21} \end{bmatrix} \equiv M' \begin{bmatrix} \tilde{\rho}_{11} \\ \tilde{\rho}_{12} \\ \tilde{\rho}_{21} \end{bmatrix} = \begin{bmatrix} M_{14} \\ M_{24} \\ M_{34} \end{bmatrix} \tilde{\rho}_{11} - \begin{bmatrix} M_{14} \\ M_{24} \\ M_{34} \end{bmatrix} \qquad (3.16.a)$$

so that

$$\begin{bmatrix} (M_{11} - M_{14}) & M_{12} & M_{13} \\ (M_{21} - M_{24}) & M_{22} & M_{23} \\ (M_{31} - M_{34}) & M_{32} & M_{33} \end{bmatrix} \begin{bmatrix} \tilde{\rho}_{11} \\ \tilde{\rho}_{12} \\ \tilde{\rho}_{21} \end{bmatrix} = - \begin{bmatrix} M_{14} \\ M_{24} \\ M_{34} \end{bmatrix} \qquad (3.16.b)$$

Here, we have defined M' as the reduced matrix resulting from M after eliminating the last row and column, for convenience of discussion during the presentation of the general algorithm later on.

To simplify the notation further, we define:

$$B \equiv \begin{bmatrix} \tilde{\rho}_{11} \\ \tilde{\rho}_{12} \\ \tilde{\rho}_{21} \end{bmatrix}, \; S \equiv \begin{bmatrix} M_{14} \\ M_{24} \\ M_{34} \end{bmatrix}, \; W \equiv \begin{bmatrix} (M_{11} - M_{14}) & M_{12} & M_{13} \\ (M_{21} - M_{24}) & M_{22} & M_{23} \\ (M_{31} - M_{34}) & M_{32} & M_{33} \end{bmatrix} \tag{3.17}$$

Using these definitions in Eqn. 3.16, we get:

$$WB = -S$$

Multiply both side by W^{-1}, we get

$$B = -W^{-1}S \tag{3.18}$$

In a computer code, such as the one in Appendix A, the elements of W and S can be determined in an automated fashion by using a simple algorithm based on a generalization of this example. We get the values of $\tilde{\rho}_{11}$, $\tilde{\rho}_{12}$, and $\tilde{\rho}_{21}$ by using Eqn.3.17. Using the condition $\tilde{\rho}_{11} + \tilde{\rho}_{22} = 1$, we can find the value of $\tilde{\rho}_{22}$.

For the 2-level system, the elements of M, W and S can be worked out by hand, without employing the general rules, with relative ease. However, for arbitrarily large systems, it can become exceedingly cumbersome. In what follows, we describe a compact algorithm for determining the elements of M, W and S for a system with N energy levels.

To start with, determine the elements of the complex effective Hamiltonian of Eqn.3.6, as well as the elements of $\tilde{\rho}_{source}$ for the N-level system. These matrices can be used to calculate the elements of Q, as defined in Eqn. 3.7 and 3.10. The elements of M can then be found by

using the following algorithm. Let M_{np} denote the element corresponding to the n-th row and p-th column of the M matrix. Similarly, let $Q_{\alpha\beta}$ denote the element corresponding to the α-th row and β-th column of the Q matrix, and $\tilde{\rho}_{\varepsilon\sigma}$ denote the elements corresponding to the ε-th row and σ-th column of the $\tilde{\rho}$ matrix. Then use the following prescription to obtain $M_{np} = Q_{\alpha\beta}$ if we set $\tilde{\rho}_{\varepsilon\sigma}=1$ and $\tilde{\rho}_{ij(ij\neq\varepsilon\sigma)}=0$ in Eqn.3.7.

Thus, the crux of the algorithm is to obtain a way of finding α,β,ε and γ efficiently, for a given set of values of {n,p}. These indices are obtained as follows:

$$\beta = \; nzrem[n/N]; \quad \alpha = 1+(n-\beta)/N; \quad \sigma = nzrem[p/N]; \quad \varepsilon = 1+(p-\sigma)/N \qquad (3.19)$$

where *nzrem* is a user-defined function prescribed as follows: *nzrem*[A/B]= *remainder*[A/B] if the remainder is non-zero; otherwise *nzrem*[A/B]=B. As an example, consider the case of the last line in Eqn.3.13. Here, n=2, p=4 and N=2. Thus, applying Eqn.3.19, we get: $\beta=2$, $\alpha=1$, $\sigma=2$, $\varepsilon=2$, in agreement with the last line of Eqn.3.13. We should note that there are other ways to determine these coefficients as well, using the greatest integer function, for example.

Once (α,β) and (ε,σ) have been obtained, set $\tilde{\rho}_{\varepsilon\sigma}$ to be 1 while setting the other elements to 0, evaluate the Q matrix using Eqn.3.7 and then pick out $Q_{\alpha\beta}$ and assign it to M_{np}. Then repeat this procedure of evaluating the Q matrix every time with different element of the $\tilde{\rho}$ matrix set to 1 sequentially, until all elements of the M matrix have been calculated.

The steps for finding S and W, as defined in Eqn.3.17 for the case of a two level system, are rather simple. The last column of the M matrix barring the very last element is the S matrix. In order to determine the elements of W, find first the M' matrix, which is obtained

from M by eliminating the last row and the last column, as illustrated in Eqn.3.16 for a two level system. Define C_i as the i-th column of the M' matrix, and D_i as the *i*-th column of the W matrix. Initialize the W matrix by setting $D_i=C_i$ for each value of *i*, ranging from 1 to (N^2-1). Then, update a selected set of D_i, using an index k running from 1 to (N-1), as follows:

$$D_{(k-1)N+k} = C_{(k-1)N+k} - S \tag{3.20}$$

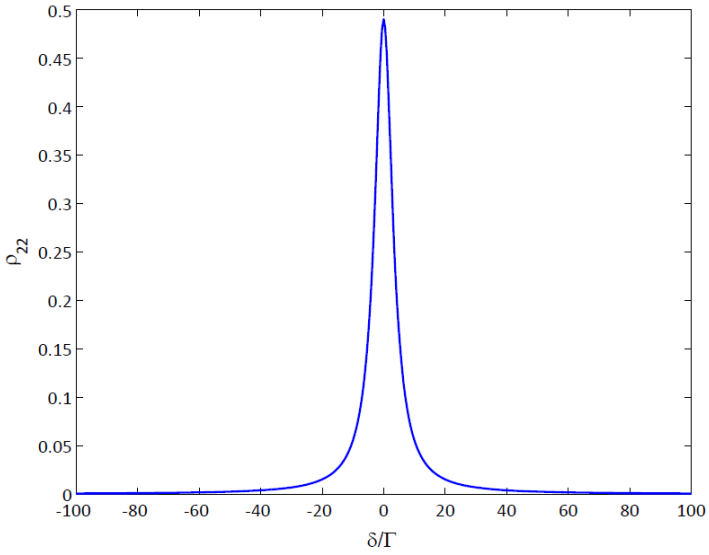

Figure 3.2 Population of excited state for a two-level system calculated using this algorithm.

To illustrate this rule, consider, for example, the case where N=3. In this case, $D_1=C_1-S$ (for k=1) and $D_5=C_5-S$ (for k=2), and $D_i=C_i$ for the other six columns. With S and W thus determined, Eqn.3.20 is used to find the steady-state solution vector: B. A particular element of the density matrix, $\tilde{\rho}_{jk}$ (excluding $\tilde{\rho}_{NN}$), corresponds to the ((j-1)*N+k)-th element of the B vector. The population in the N-th level, $\tilde{\rho}_{NN}$ is simply obtained from the knowledge of

the steady- state populations in all other levels and the constraint $\sum_{i=1}^{N} \tilde{\rho}_{ii} = 1$. Explicitly, we can write:

$$\tilde{\rho}_{NN} = 1 - \sum_{j=1}^{(N-1)} B((j-1)N + j) \tag{3.21}$$

where we have used the notation that B(k) represents the k-th element of the B vector.

A Matlab code for an N-level system, applied to the case of two-levels, is shown in Appendix A. The code is valid for a general system, by changing N to any integer value, and modifying the effective, complex Hamiltonian (Eqn.3.6) and the source terms (Eqn. 3.7) only. The rest of the program does not have to be changed. Of course, the plotting commands would have to be defined by the user based on the information being sought. As an example, the population of the excited state as a function of the detuning, δ, produced by this code, is plotted in Figure 3.2.

3.3 A Three Level System

The two-level problem discussed above is somewhat trivial, and may mask the generality of the algorithm. Therefore, we include here the specific steps for a three-level Λ system [49, 50, 51, 52, 53, 54], shown in Figure 3.3, in order to elucidate how the algorithm is completely transparent to the number of energy levels involved.

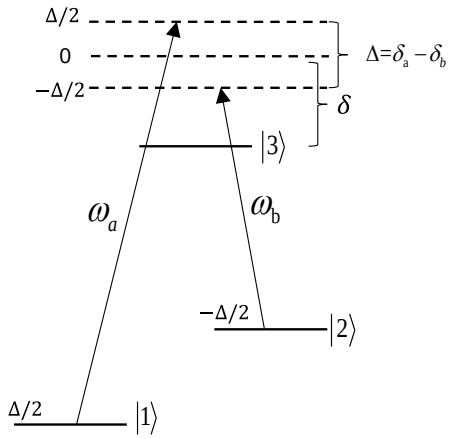

Figure 3.3 Schematic illustration of a three level system

In this case, the Hamiltonian under electric dipole and rotating wave approximations is given by

$$H=\hbar\begin{pmatrix} \omega_1 & 0 & \frac{\Omega_a}{2}e^{i\omega_a t} \\ 0 & \omega_2 & \frac{\Omega_b}{2}e^{i\omega_b t} \\ \frac{\Omega_a}{2}e^{i\omega_a t} & \frac{\Omega_b}{2}e^{i\omega_b t} & \omega_3 \end{pmatrix} \tag{3.22}$$

where $\hbar\omega_1$, $\hbar\omega_2$, and $\hbar\omega_3$ are the energies of the three levels, and ω_a and ω_b are the frequencies of the laser fields.

After applying the interaction picture transformation using the following matrix

$$R=\begin{bmatrix} e^{i\theta t} & 0 & 0 \\ 0 & e^{i\beta t} & 0 \\ 0 & 0 & e^{i\alpha t} \end{bmatrix} \tag{3.23}$$

where $\theta = \omega_1 - \frac{\Delta}{2}, \beta = \omega_2 + \frac{\Delta}{2}, \Delta = \delta_a - \delta_b, \delta = (\delta_a + \delta_b)/2, \delta_a = \omega_a - (\omega_3 - \omega_1),\ \delta_b = \omega_b - (\omega_3 - \omega_2)$ the Hamiltonian can be expressed as

$$\tilde{H}=\frac{\hbar}{2}\begin{pmatrix} \Delta & 0 & \Omega_a \\ 0 & -\Delta & \Omega_b \\ \Omega_a & \Omega_b & -2\delta \end{pmatrix}. \tag{3.24}$$

The transformed state vector for each atom can be written as

$$|\tilde{\psi}\rangle = \mathrm{R}|\psi\rangle = \begin{bmatrix} \tilde{C}_1(t) \\ \tilde{C}_2(t) \\ \tilde{C}_3(t) \end{bmatrix} \tag{3.25}$$

The time independent Hamiltonian $\tilde{\mathrm{H}}$ of Eqn.3.24 can be written down by inspection, following the discussion presented earlier for the two-level system. First, we observe that the energy difference between |1> and |3> ($\tilde{\mathrm{H}}_{11} - \tilde{\mathrm{H}}_{33}$) is $\hbar\delta_a$, and the energy difference between |2> and |3> ($\tilde{\mathrm{H}}_{22} - \tilde{\mathrm{H}}_{33}$) is $\hbar\delta_b$. Next, we make a judicious but arbitrary choice that $\tilde{\mathrm{H}}_{11} = \frac{\hbar}{2}\Delta$. We then get that $\tilde{\mathrm{H}}_{33} = -\hbar\delta$, which in turn implies that $\tilde{\mathrm{H}}_{22} = -\frac{\hbar}{2}\Delta$. The off diagonal terms are, of course, obvious, with non-zero elements for transitions excited by fields. This approach is generic, and can be used to find the time independent Hamiltonian by inspection for an arbitrary number of levels. We should note that a complication exists when closed-loop excitations are present. In that case, it is wiser to work out the Hamiltonian explicitly using the transformation matrix approach outlined here.

We now add the decay term to get the complex Hamiltonian

$$\tilde{\mathrm{H}}' = \frac{\hbar}{2}\begin{pmatrix} \Delta & 0 & \Omega_a \\ 0 & -\Delta & \Omega_b \\ \Omega_a & \Omega_b & -i\Gamma - 2\delta \end{pmatrix} \tag{3.26}$$

We assume that the population of the excited state decays at the same rate ($\Gamma/2$) from $|3\rangle$ to $|1\rangle$ and from $|3\rangle$ to $|2\rangle$. Now we construct the M matrix for the three-level system which satisfies the following equation under the steady-state condition:

$$\begin{bmatrix} M_{11} & M_{12} & M_{13} & M_{14} & M_{15} & M_{16} & M_{17} & M_{18} & M_{19} \\ M_{21} & M_{22} & M_{23} & M_{24} & M_{25} & M_{26} & M_{27} & M_{28} & M_{29} \\ M_{31} & M_{32} & M_{33} & M_{34} & M_{35} & M_{36} & M_{37} & M_{38} & M_{39} \\ M_{41} & M_{42} & M_{43} & M_{44} & M_{45} & M_{46} & M_{47} & M_{48} & M_{49} \\ M_{51} & M_{52} & M_{53} & M_{54} & M_{55} & M_{56} & M_{57} & M_{58} & M_{59} \\ M_{61} & M_{62} & M_{63} & M_{64} & M_{65} & M_{66} & M_{67} & M_{68} & M_{69} \\ M_{71} & M_{72} & M_{73} & M_{74} & M_{75} & M_{76} & M_{77} & M_{78} & M_{79} \\ M_{81} & M_{82} & M_{83} & M_{84} & M_{85} & M_{86} & M_{87} & M_{88} & M_{89} \\ M_{91} & M_{92} & M_{93} & M_{94} & M_{95} & M_{96} & M_{97} & M_{98} & M_{99} \end{bmatrix} \begin{bmatrix} \tilde{\rho}_{11} \\ \tilde{\rho}_{12} \\ \tilde{\rho}_{13} \\ \tilde{\rho}_{21} \\ \tilde{\rho}_{22} \\ \tilde{\rho}_{23} \\ \tilde{\rho}_{31} \\ \tilde{\rho}_{32} \\ \tilde{\rho}_{33} \end{bmatrix} = 0 \qquad (3.27)$$

The elements of the M matrix can be found explicitly by following the same steps as shown in Eqn.3.7 through 3.12 for the two-level system. Alternatively, these can be found by using a generalization of the rule shown in Eqn.3.13, and implemented by a computer code.

Substituting $\tilde{\rho}_{11}+\tilde{\rho}_{22}+\tilde{\rho}_{33}=1$ into Eqn.3.27, we get

$$\begin{bmatrix} M_{11} & M_{12} & M_{13} & M_{14} & M_{15} & M_{16} & M_{17} & M_{18} \\ M_{21} & M_{22} & M_{23} & M_{24} & M_{25} & M_{26} & M_{27} & M_{28} \\ M_{31} & M_{32} & M_{33} & M_{34} & M_{35} & M_{36} & M_{37} & M_{38} \\ M_{41} & M_{42} & M_{43} & M_{44} & M_{45} & M_{46} & M_{47} & M_{48} \\ M_{51} & M_{52} & M_{53} & M_{54} & M_{55} & M_{56} & M_{57} & M_{58} \\ M_{61} & M_{62} & M_{63} & M_{64} & M_{65} & M_{66} & M_{67} & M_{68} \\ M_{71} & M_{72} & M_{73} & M_{74} & M_{75} & M_{76} & M_{77} & M_{78} \\ M_{81} & M_{82} & M_{83} & M_{84} & M_{85} & M_{86} & M_{87} & M_{88} \end{bmatrix} \begin{bmatrix} \tilde{\rho}_{11} \\ \tilde{\rho}_{12} \\ \tilde{\rho}_{13} \\ \tilde{\rho}_{21} \\ \tilde{\rho}_{22} \\ \tilde{\rho}_{23} \\ \tilde{\rho}_{31} \\ \tilde{\rho}_{32} \end{bmatrix} = \begin{bmatrix} M_{19} \\ M_{29} \\ M_{39} \\ M_{49} \\ M_{59} \\ M_{69} \\ M_{79} \\ M_{89} \end{bmatrix} \tilde{\rho}_{11} + \begin{bmatrix} M_{19} \\ M_{29} \\ M_{39} \\ M_{49} \\ M_{59} \\ M_{69} \\ M_{79} \\ M_{89} \end{bmatrix} \tilde{\rho}_{22} - \begin{bmatrix} M_{19} \\ M_{29} \\ M_{39} \\ M_{49} \\ M_{59} \\ M_{69} \\ M_{79} \\ M_{89} \end{bmatrix}$$

(3.28.a)

Or

$$\begin{bmatrix} (M_{11}-M_{19}) & M_{12} & M_{13} & M_{14} & (M_{15}-M_{19}) & M_{16} & M_{17} & M_{18} \\ (M_{21}-M_{29}) & M_{22} & M_{23} & M_{24} & (M_{25}-M_{29}) & M_{26} & M_{27} & M_{28} \\ (M_{31}-M_{39}) & M_{32} & M_{33} & M_{34} & (M_{35}-M_{39}) & M_{36} & M_{37} & M_{38} \\ (M_{41}-M_{49}) & M_{42} & M_{43} & M_{44} & (M_{45}-M_{49}) & M_{46} & M_{47} & M_{48} \\ (M_{51}-M_{59}) & M_{52} & M_{53} & M_{54} & (M_{55}-M_{59}) & M_{56} & M_{57} & M_{58} \\ (M_{61}-M_{69}) & M_{62} & M_{63} & M_{64} & (M_{65}-M_{69}) & M_{66} & M_{67} & M_{68} \\ (M_{71}-M_{79}) & M_{72} & M_{73} & M_{74} & (M_{75}-M_{79}) & M_{76} & M_{77} & M_{78} \\ (M_{81}-M_{89}) & M_{82} & M_{83} & M_{84} & (M_{85}-M_{89}) & M_{86} & M_{87} & M_{88} \end{bmatrix} \begin{bmatrix} \tilde{\rho}_{11} \\ \tilde{\rho}_{12} \\ \tilde{\rho}_{13} \\ \tilde{\rho}_{21} \\ \tilde{\rho}_{22} \\ \tilde{\rho}_{23} \\ \tilde{\rho}_{31} \\ \tilde{\rho}_{32} \end{bmatrix} = -\begin{bmatrix} M_{19} \\ M_{29} \\ M_{39} \\ M_{49} \\ M_{59} \\ M_{69} \\ M_{79} \\ M_{89} \end{bmatrix}$$

(3.28.b)

To simplify the above expression, we define the following objects as before

$$B=\begin{bmatrix}\tilde{\rho}_{11}\\ \tilde{\rho}_{12}\\ \tilde{\rho}_{13}\\ \tilde{\rho}_{21}\\ \tilde{\rho}_{22}\\ \tilde{\rho}_{23}\\ \tilde{\rho}_{31}\\ \tilde{\rho}_{32}\end{bmatrix} \qquad S=\begin{bmatrix}M_{19}\\ M_{29}\\ M_{39}\\ M_{49}\\ M_{59}\\ M_{69}\\ M_{79}\\ M_{89}\end{bmatrix} \qquad W=\begin{bmatrix}(M_{11}-M_{19}) & M_{12} & M_{13} & M_{14} & (M_{15}-M_{19}) & M_{16} & M_{17} & M_{18}\\ (M_{21}-M_{29}) & M_{22} & M_{23} & M_{24} & (M_{25}-M_{29}) & M_{26} & M_{27} & M_{28}\\ (M_{31}-M_{39}) & M_{32} & M_{33} & M_{34} & (M_{35}-M_{39}) & M_{36} & M_{37} & M_{38}\\ (M_{41}-M_{49}) & M_{42} & M_{43} & M_{44} & (M_{45}-M_{49}) & M_{46} & M_{47} & M_{48}\\ (M_{51}-M_{59}) & M_{52} & M_{53} & M_{54} & (M_{55}-M_{59}) & M_{56} & M_{57} & M_{58}\\ (M_{61}-M_{69}) & M_{62} & M_{63} & M_{64} & (M_{65}-M_{69}) & M_{66} & M_{67} & M_{68}\\ (M_{71}-M_{79}) & M_{72} & M_{73} & M_{74} & (M_{75}-M_{79}) & M_{76} & M_{77} & M_{78}\\ (M_{81}-M_{89}) & M_{82} & M_{83} & M_{84} & (M_{85}-M_{89}) & M_{86} & M_{87} & M_{88}\end{bmatrix}$$

Substituting them into Eqn.3.28.b, we get $WB=-S$, or $B=-W^{-1}S$.

The Matlab program shown in Appendix B implements our algorithm for the three level system. Note that this program is essentially the same as the program for the two-level case with the following modifications: we have (a) defined additional parameters relevant to this system, (b) entered proper elements in the Hamiltonian, and (c) added appropriate source terms for the populations. As an example, we have shown in Figure 3.4 a plot of the population of the excited state, produced using this code, displaying the well-known coherent population trapping dip.

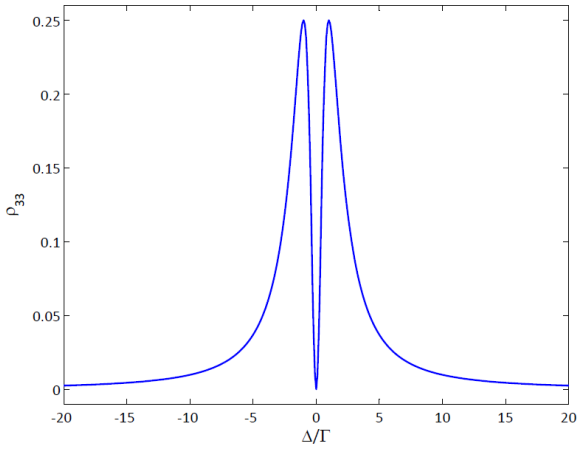

Figure 3.4 Population of the excited state for a three-level system calculated with this algorithm.

3.4 Applying the code to a system with an arbitrary number of energy levels

There are many examples in atomic and molecular physics where it is necessary to include a large number of energy levels. One example is an atomic clock employing coherent population trapping [55]. The basic process employs only three Zeeman sublevels. However, the other Zeeman sublevels have to be taken into account in order to describe the behavior of the clock accurately. Using alkali atoms for other applications such as atomic interferometry, magnetometry and Zeno-effect based switching also requires taking into account a large number of Zeeman sublevels [56,57,58,59]. Another example is the cooling of molecules using lasers. In this case, many rotational and vibrational levels have to be considered [60]. The code presented here can be applied readily to these problems, with the following modifications: (a) define additional parameters to characterize the problem, (b) develop the time independent Hamiltonian (possibly by inspection using the technique described earlier, if no closed-loop excitation is present), (c) enter proper elements in the Hamiltonian, (d) add proper decay terms to the Hamiltonian, (e) add appropriate source terms for the populations, and (f) add plotting instructions for components of interest from the solution vector. Of course, if numerical techniques are to be employed for finding time-dependent solutions, the code can be truncated after the M matrix is determined, followed by application of Eqn.3.12 along with a proper choice of initial conditions.

3.5 Consider Doppler Effect

Due to Doppler Effect, atoms moving at different velocity experience different detuning

(frequency shift) when interact with photons emitted from the same light source. A velocity averaging model is introduced here to take Doppler Effect into account.

Assuming the atoms moves within a small distance range when interacting with photons and the beam size is large enough to cover this range, only the velocity components of the atoms that aligned with the direction of laser beam would contribute to the frequency shift. According to Maxwell-Boltzmann distribution[61], atoms are moving at the velocity which follows a Gaussian distribution ~$N(0, \sigma^2)$, where $\sigma = \sqrt{k_b T/m}$, k_b is Boltzmann constant, T is Temperature in Kelvins, m is the molar mass, and N is the normal distribution function. Suppose we have a laser beam with frequency f_0 shining on an atom, which moving away from the laser source at velocity v, the laser frequency the atom experience is $f = f_0 - kv$, where k is the wave number of the laser beam. One way to simulate the velocity averaging model is to use Monte Carlo simulation [62], which requires a large number of velocity samples and high computation complexity. Another way is to divide the atoms into finite number of different groups. In each group, the atoms are assumed to moving at a constant velocity. The probability of an atom to be found at velocity v_i follows normal distribution, e.g. $P(v_i) = N(v_i + \Delta v) - N(v_i)$, where Δv is the velocity difference between each contiguous group, and $N(v_i)$ is the cumulative distribution function of the normal distribution~$N(0, \sigma^2)$. Suppose there are 2m+1 groups of velocity, the susceptibility χ follows $\chi = \sum_{i=-m}^{m} \chi(v_i) P(v_i)$. The smaller the Δv is, the more accurate the result is. Simulations use this model will be introduced in Chapter 5, 7, 8, and 9.

3.6 Parallel Computing

Our simulations usually require scanning of one or two parameters, for instance detuning or / and Rabi frequency, in order to understand the change of density matrix as a function of a certain set of parameters. One example is shown in Figure 3.4. Each time the parameters are changed, the N-level algorithm needs to be called. For a complicated atomic system, such as a Rb cascade system (Chapter 5), an optically controlled polarizer (Chapter 6), an optically controller waveplate (Chapter 7), and a double Raman gain system (Chapter 8), the calculation using N-level algorithm becomes complicated., since the size of W matrix in Eqn.3.17 can be as large as 125 by 125 elements. If Doppler Effect needs to be included, the calculate becomes more complicated and takes days to run. In order to reduce the calculation time, parallel computing using multiple CPU is introduced here.

The idea of parallel computing using multiply CPU is to divide a complex calculation, usually contains multiple iterations, into several tasks. Each task is ran by a CPU. During the parallel computing process, CPUs do their calculations simultaneously. When all tasks are finished, the results will be combined and passed to the shared memory. The speed up scale depends on the number of tasks the calculation can be divided into and the number of CPUs.

Our calculation uses Matlab parallel computing toolbox. At the beginning of a parallel computation, number of workers has to be assigned. A worker is a combination of a CPU and a pre-allocated memory. Then a scheduler will be created to allocate CPU and memory for calculation. This scheduler will also monitor the progress of calculation, take charge of communication between tasks if needed, and combine results when all tasks are finished, as

shown in Figure 3.5. The calculation will then start to run as indicated by the code. There are several ways to divide a calculation into different tasks in Matlab. “Parfor” is used here. Calculation is wrapped by a function, and parameters are passed into this function as arguments. Within each parfor iteration, this function is called and ran by the scheduler. The tasks are guaranteed independent with each other. With a 8-core PC, a 5~6X speed up is observed.

To further reduce the calculation time, more CPUs are needed. Northwestern Quest computing cluster is used [63]. There are 450 nodes with nearly ~5000 CPUs in Quest. Each time of using Quest, a request need to be submitted through Unix Shell. Quest system will then allocate resource (CPU, memory, disk) based on the request. The more resources needed, the longer the waiting time will be. 64 CPUs are found to be the optimal number for our calculation, which balances the Quest waiting time and Matlab computing time. A ~40X speed up is observed.

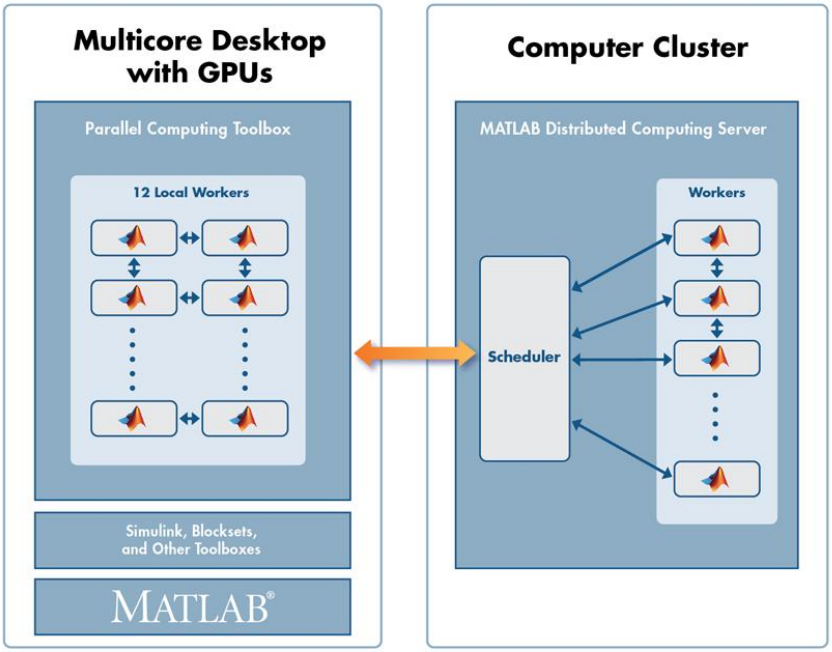

Figure 3.5 Matlab Parallel Computing Toolbox.

CHAPTER 4 RUBIDIUM CASCADE SYSTEM

4.7 Spectroscopy

We chose to primarily use the $5S_{1/2} \rightarrow 5P_{1/2} \rightarrow 6S_{1/2}$ ladder transition in Rb for our experiment, dictated in part by lasers readily available to us and also due to the interest in operating it in one of the telecommunication bands. In order to observe the spectrum, we locked the pump laser (795 nm) to one of the resonances of the $5S_{1/2} \rightarrow 5P_{1/2}$ manifold using the reference saturated absorption cell and the probe laser (at 1323nm) was then scanned across the $6S_{1/2}$ manifold over a few 5-6 GHz. Our pump beam was obtained from a Ti-Sapphire laser while the probe beam was obtained from a tunable semiconductor laser. There was no clear spectral experimental data available in the literature for these transitions and the display for the semiconductor laser wavelength was not very accurate. Also, when its frequency was scanned using an external voltage source, the display did not change to reflect the change in wavelength. Thus, we had to first test whether the laser was scanning properly when an external voltage was applied. For this, we put the laser beam through a Fabry-Perot cavity to make sure that the laser was operating in single mode and scanning smoothly. Further, there was inherent slow variation of the probe signal as the laser was scanned, probably due to reflection from the windows of the cell. Hence, it was not easy to observe the spectrum directly. Instead, we used a chopper to modulate the intensity of the pump signal at a frequency of ~1 KHz. The same pulse sequence was sent it as the reference to a lock-in amplifier, which was then used to demodulate the probe. Thus, only the part of the probe which was modulated at the chopping frequency, or in other words, the part that was affected by the pump modulation (i.e. absorption signal of

interest) was detected, eliminating other sources of noise, which were unaffected by the pump modulation. Figure 4.1 (a) and Figure 4.1 (b) show the result of the Fabry-Perot scan and the absorption signal as seen using a lock-in amplifier, respectively.

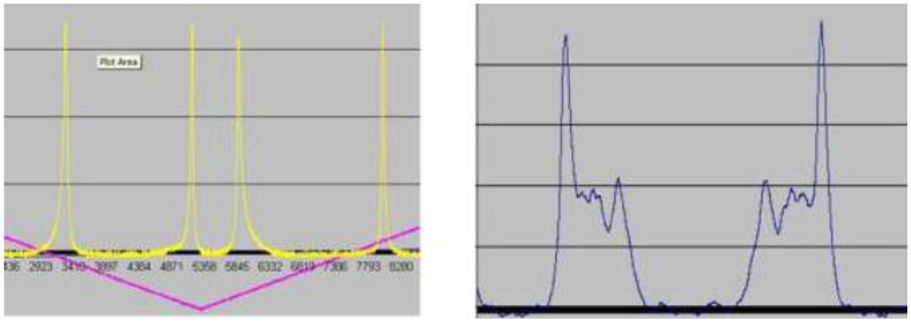

Figure 4.1 (a) Transmission through Fabry-Perot cavity as 1323nm laser is scanned externally. It shows smooth single mode operation. (b) 1323 nm absorption signal detected using chopper and lock-in amplifier

Figure 4.2(a) shows the spectroscopic details of the ladder transition for ^{85}Rb. The probe beam was scanned over the $6S_{1/2}$ manifold while the control beam was locked to the F=2→F'=2 transition on the lower leg. The separation between the hyperfine levels in the $5P_{1/2}$ manifold (~360 MHz) is less than the Doppler linewidth (~600 MHz). Hence, atoms are excited to both hyperfine levels of the $5P_{1/2}$ manifold even if the 795nm laser is locked to only the F=2 →F'=2 transition. As a result, it is expected that 4 lines would be observed for the 1323nm absorption (upper leg) as this laser is scanned over a few GHz (Figure 4.2(b)). However, it is to be noted that, due to Doppler shift, the atoms excited to the F'=3 state of the intermediate level correspond to negative velocity (with respect to the direction of propagation of the 795 nm laser beam) atoms, and not zero velocity atoms. Thus, the transitions from this state to the $6S_{1/2}$ manifold are shifted to lower frequencies by an amount equal to the separation

between the hyperfine states in the $5P_{1/2}$ manifold (~360 MHz). In the case of ^{85}Rb, the frequency difference between the hyperfine states in the $6S_{1/2}$ manifold (~710 MHz) is such that this shift causes the F=2→F'=2 transition almost to overlap the F=3→F'=3 transition, for the 1323 nm beam. As a result, only 3 lines are expected to be observed distinctly (see Figure 4.2(c)). It is to be noted that Figure 4.2 (b) and Figure 4.2 (c) only illustrate the expected relative positions of the ^{85}Rb absorption lines (at 1323nm), and not the actual observed data, which are described next.

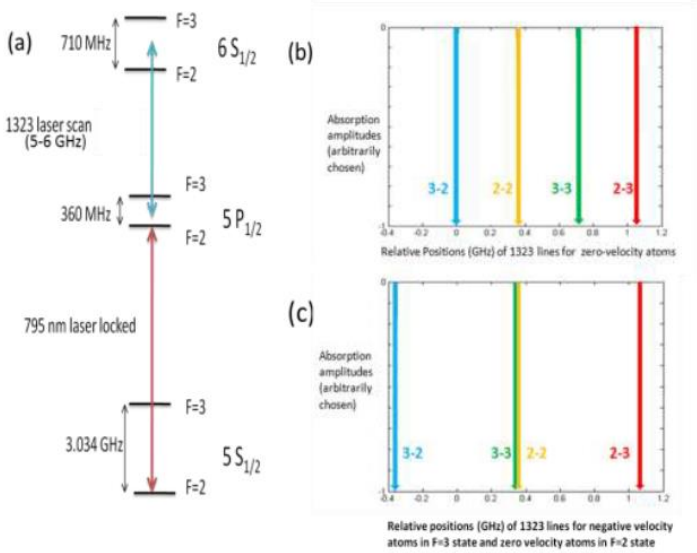

Figure 4.2 Spectroscopic details of ladder transition in ^{85}Rb (a) Schematic of various hyperfine levels used, along with the transition frequencies. (b) Expected spectrum if both hyperfine states of intermediate level are occupied by zero velocity atoms. (c) Shift of spectrum in (b) due to F=3 state at the intermediate level being occupied by negative velocity atoms.

Figure 4.3(a) and Figure 4.3(b) show a couple of typical absorption profiles that were observed for ^{85}Rb. The data in Figure 4.3 (a) corresponds to a relatively low power (~2 mW) of

the control beam, and only three absorption lines are observed, in keeping with the explanation provided in Figure 4.2 above. The relative separation between the lines is in good agreement with the expected spectrum. This data has been taken in AC mode (on a standard digital oscilloscope) and hence shows negative values. The slow background modulation seen in the signal is most likely due to the etalon effect from the windows of the cell. The data in Figure 4.3(b), taken in DC mode, corresponds to a much higher power (~200 mW) of the control beam, and we see almost complete absorption of the probe while the lines are strongly power broadened. Of course, the amount of 1323nm absorption increases with the number of atoms excited to the intermediate leg, which in turn is determined by the power of the control beam. Thus at sufficiently high power of the control beam, the upper transition is completely saturated.

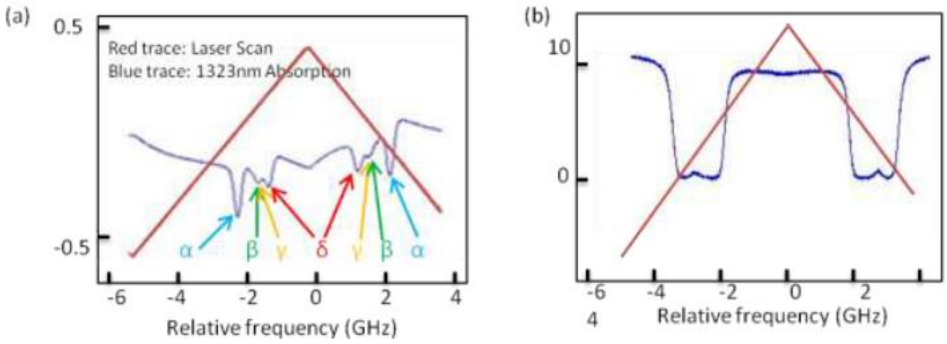

Figure 4.3 Typical absorption profiles for the ladder transitions (at 1323nm) that are observed in ^{85}Rb. (a) Corresponds to 795 nm laser power ~ 2mW, data taken in AC mode. The hyperfine transitions corresponding to the absorption dips are α: 3→2, β: 3→3, γ: 2→2, δ: 2→3. The repeat scan has been shown due to the asymmetry of the signal (b) Corresponds to 795 nm laser power ~ 200mW, we see near 100% absorption and the lines are highly power broadened. Note that the null value of the probe detuning is

defined arbitrarily to be at the turnaround point of the scan in each case.

Figure 4.4 shows the spectroscopic details for ^{87}Rb and a few typical absorption profiles that were observed at 1323nm. The control laser was locked to the F=1→F'=1 transition on the lower leg as shown in Figure 4.4 (a). For moderately high powers (~50mW) of the control beam, atoms get excited to both hyperfine levels of the $5P_{1/2}$ manifold, due to power broadening of the $5S_{1/2} \rightarrow 5P_{1/2}$ transition. At these powers, we can clearly resolve 4 absorption lines, as shown in Figure 4.4 (b). It is worth noting that each of the lines is control-power-broadened because of the fact that a significant number of velocity groups are excited to both hyperfine states of the intermediate level due to the relatively high power of the control beam. At sufficiently low powers of the control beam (~0.5mW), two of the four lines are almost completely suppressed, and each individual line can be seen as a narrow sharp line, as illustrated in Figure 4.4 (c).

As before, these data have been captured in AC mode on a standard digital oscilloscope, and hence show negative values. The slow background modulation observed in both figures is again most likely due to the etalon effect of the Rb cell window, as mentioned previously. It should be noted that ladder transitions of this type have been studied previously, theoretically as well as experimentally [64,65,66] in different contexts. The hyperfine splitting frequencies we have observed for the $5P_{1/2}$ to $6S_{1/2}$ transition for both ^{85}Rb and ^{87}Rb are in agreement with those reported in Ref. 64. However, the experiment reported therein did not show any absorption lines for this transition; therefore, a quantitative comparison of the spectral response is not possible. Further, the accidental near-degeneracy we have observed between the

F=3→F'=2 and F=2→F'=2 transitions on the upper leg in the case of ^{85}Rb due to contributions from different velocity groups has not been reported in any of these references.

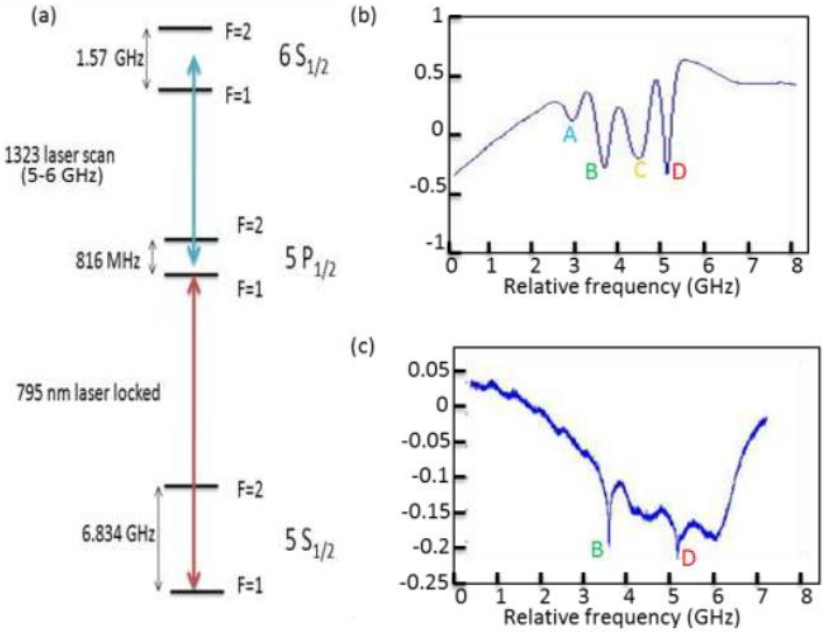

Figure 4.4 Spectroscopic details of ladder transition in ^{87}Rb (a) Schematic of various hyperfine levels used along with the transition frequencies. (b) Absorption corresponding to 795 nm laser power ~ 50mW; all four transitions can be clearly seen. The hyperfine transitions corresponding to the absorption dips are A: 2→1, B: 1→1, C: 2→2, D: 1→2. (c) Corresponds to 795 nm laser power ~ 0.5mW; two of the four lines are suppressed and only transitions from F=1 are observed.

Figure 4.5 shows the spectral data for ^{87}Rb with a pump power of ~400 mW. At this power level, some of the transitions begin to saturate. Of course, absorption spectrum observed depends critically on the temperature as the density of Rb atoms increases with increasing temperature. As a thumb rule, the density doubles for every 10℃ rise in temperature. Here, all the spectral data reported are at a temperature of ~120℃.

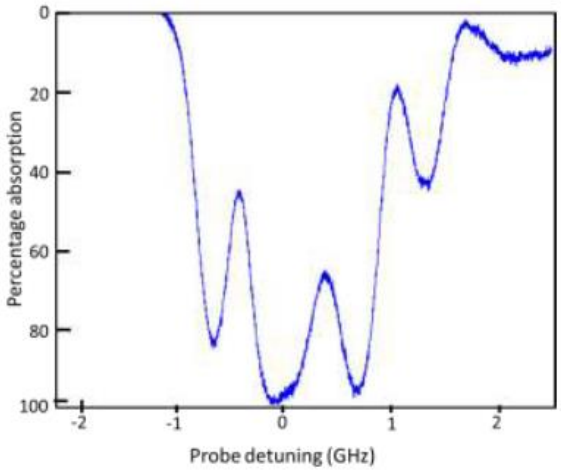

Figure 4.5 Absorption spectrum for ^{87}Rb with ~400mW of pump power

4.8 Co-propagation vs Counter-propagation

It is useful to note a couple of differences in the observed signals between the co-propagating and the counter-propagating cases. Since we do not have experimental data under identical conditions (powers of the pump and the probe, temperature etc.) for the two geometries and our theoretical results are fairly consistent with our experimental data, we would present these differences using our simulation results. Figure 4.6 shows the simulation results for both geometries for a pump Rabi frequency of 5 (in units of the natural linewidth of the 5P manifold ~5.7 MHz) when both the control and the signal beams have the same polarization. As seen in the figure, the counter propagating geometry produces narrower (and deeper) absorption lines as compared to the co-propagating case. In addition, there is also an apparent splitting in the counter-propagating geometry which is absent in the co-propagating case. These differences based on geometry are due to what we refer to as pump power limited Doppler broadening (PPLDB).

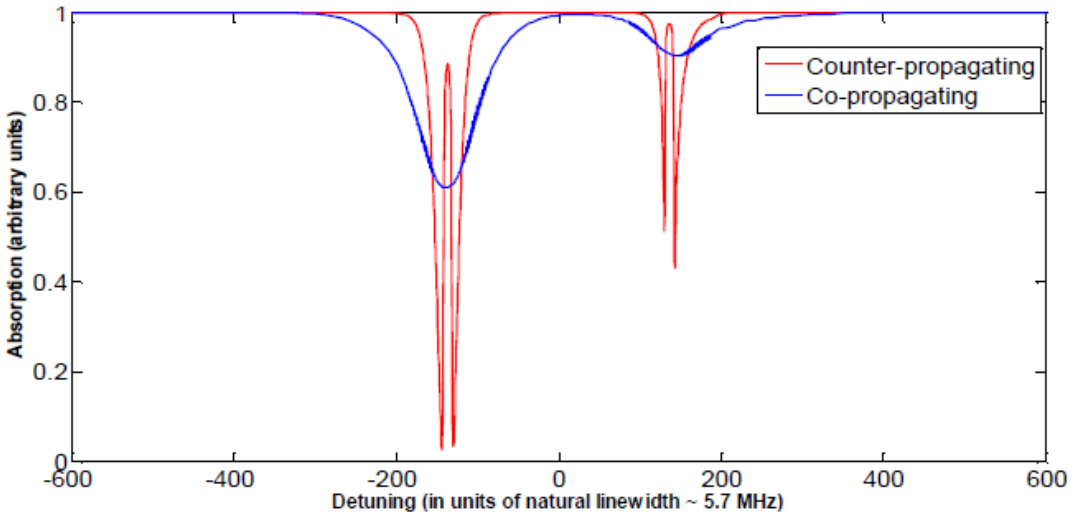

Figure 4.6 Typical absorption profile for co- and counter-propagating geometries. Ωp = 5.

For the purpose of understanding, it suffices to consider a 3-level cascade system with similar energy difference between the levels as in our original system i.e. $k_2 \sim 0.6\ k_1$. Figure 4.7(a) shows such a system where the pump is on resonance with the intermediate level and the probe is scanned across the upper level. Figure 4.7(b) shows the (partial) dressed picture of the interactions for the zero velocity atoms. Here |1'> and |2'> are shown to be degenerate (with δp = 0), while we show |3> to be higher in energy by an amount equal to probe field energy (for δs = 0). This picture is valid for a weak probe and enables us to understand clearly the dynamics of the probe absorption. On the right-side of Figure 4.7(b), we show the two split states that result from diagonalization of the interaction between |1'> and |2'>. Similar diagrams are shown in Figure 4.7(c) and Figure 4.7(d) for a positive velocity (same direction of propagation as pump) for the co-propagating and counter-propagating configurations, respectively.

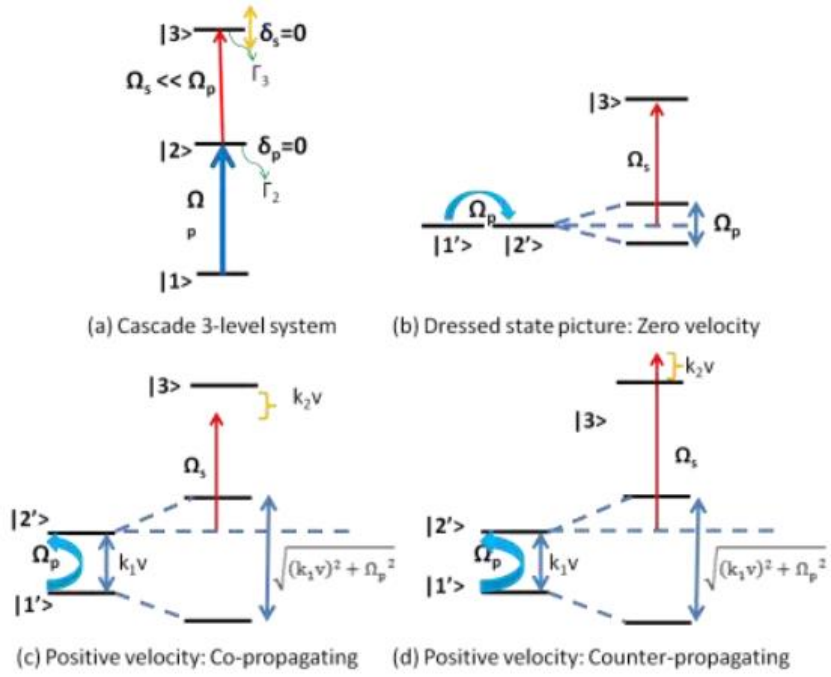

Figure 4.7 Dressed state picture of 3-level cascade system for different velocity groups.

For an arbitrary velocity group v, the energies of the partially diagonalized states can be easily calculated to be $\lambda = (-k_1 v \pm \sqrt{(k_1 v)^2 + \Omega_p^2})/2$, where k_1 is the wavenumber of the pump optical field and Ω_p is the pump Rabi frequency. Thus, for the zero-velocity group of atoms, these atomic states would have energies $\pm\Omega_p/2$ and hence would produce absorption at probe detunings of $\mp\Omega_p/2$, as shown in Figure 4.7(b). This is a manifestation of the well-known Autler Townes splitting (ATS). For any non-zero velocity group, the probe would be further Doppler shifted by $k_2 v$, with the direction of shift depending on whether the probe is co-propagating or counter-propagating, as shown in Figure 4.7(c) and Figure 4.7(d) respectively. Thus, the resonances would occur at $(k_2 + k_1/2\,)v \mp (\sqrt{(k_1 v)^2 + \Omega_p^2})/2$ for a co-propagating probe and at $(k_2 - k_1/2\,)v \mp (\sqrt{(k_1 v)^2 + \Omega_p^2})/2$ a counter-propagating probe. We also note that the velocity spread of atoms that contribute significantly to the

absorption can be estimated to be of the order of $kv_{FWHM} \sim \sqrt{\Gamma_2^2 + 2\Omega_2^2}$, where Γ_2 is the decay rate of the intermediate level. From these expressions, we can make the following observations:

For a vanishingly weak pump, the spread of the velocity groups that contribute significantly to the absorption of the probe is very small ($kv_{FWHM} \sim \Gamma_2$). Thus, both geometries would produce narrow lines (although co-propagating is still slightly broader) with linewidths that are essentially Doppler free and primarily determined by the decay rates of the intermediate and upper level. We can roughly estimate the minimum observable linewidth to be $\sqrt{\Gamma_2^2 + \Gamma_3^2}$, where Γ3 is the decay rate of the upper level.

There are some differences that arise for a pump Rabi frequency that is much larger than the minimum observable linewidth. We first note that in the co-propagating case, for any given pump Rabi frequency Ω_p we can always find a velocity group, $v_{zero} = \Omega_p/2\sqrt{k_2^2 + k_1 k_2}$ that produces resonance at zero probe detuning. If we carry out a similar exercise for the counter-propagating case, we find that the velocity group that produces resonance at zero probe detuning would have $v_{zero} = \Omega_p/2\sqrt{k_2^2 - k_1 k_2}$ and this has no valid solution if k2 < k1, as is the case for our system. As a consequence, in a co-propagating geometry, ATS is generally washed out while it is preserved to some extent in the counter-propagating geometry, the specific details of which depend on the exact value of Ω_p.

Finally, we also note that $(k_2 + k_1/2)v$ is much larger than $(k_2 + k_1/2)v$. Thus, the resonances for the co-propagating geometry occur at much larger detunings, resulting in broader (and consequently shallower) lines as compared to the counter-propagating geometry.

Similar conclusions can be reached for the negative velocity group of atoms. We refer to

this phenomenon of line broadening in a cascade system for a strong pump as Pump power limited Doppler broadening (PPLDB) since the number of velocity groups that contribute significantly to the absorption signal is proportional to the pump power. In Figure 4.8, the contribution to the absorption (not normalized over the Doppler profile) from three velocity groups (-Vzero, 0, +Vzero) are presented for both co-propagating and counter-propagating geometries for our simplified system. As seen in Figure 4.8, in the co-propagating case, the nonzero velocity groups contribute significantly to the absorption at zero detuning, while in the counter-propagating case, the contributions from non-zero velocity groups tend to align with the zero-velocity group contribution.

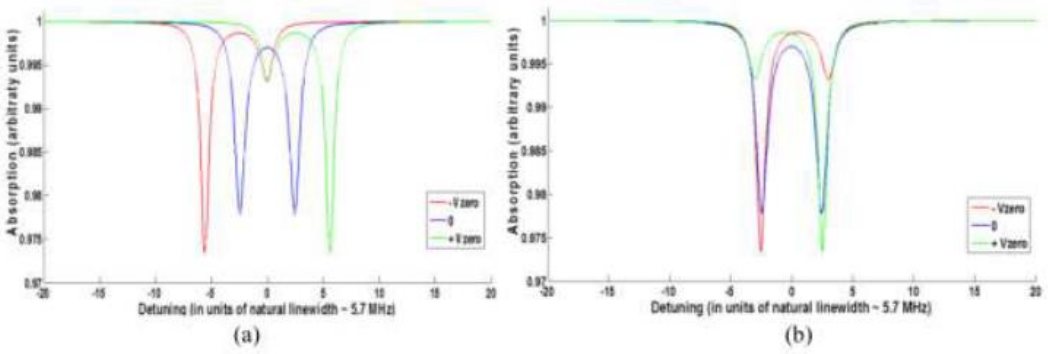

Figure 4.8 Contribution to absorption from 3 sample velocity groups (-vzero, 0, + vzero) for a 3-level cascade system when the control beam and signal beam are a) Co-propagating b) Counter-propagating.

We primarily used ^{87}Rb for most of our experiments due to the relatively simpler hyperfine structure. The modulator experiment should work just as well if the ladder transition is of the type $5S_{1/2} \rightarrow X \rightarrow Y$, where X is $5P_{1/2}$ or $5P_{3/2}$, and Y can be one of many states that are coupled to the X states via optical dipole transitions and has a higher energy than that of X. For example

Y can be $7S_{1/2}$, $4D_{3/2}$, $4D_{5/2}$, $5D_{3/2}$, $5D_{5/2}$, and so on.

4.9 Optical modulation

As shown in Figure 4.9 the basic modulator system consists of three states: a ground state (|1>), a strongly-damped intermediate state (|2>), and a third state (|3>) which may or may not be strongly damped. The control beam couples |1> to |2>, and the probe beam couples |2> to |3>. For resonant excitation, the corresponding dressed states (defined as products of photon number states and atomic states) are degenerate, as shown in Figure 4.9(b). When the coupling between |1> and |2> is strong, the resulting states, upon diagonalization (|+> and |->) are split by an amount equaling the Rabi frequency of the |1> to |2> transition, which is much larger than the natural linewidth of |3>, as illustrated in Figure 4.9(c).

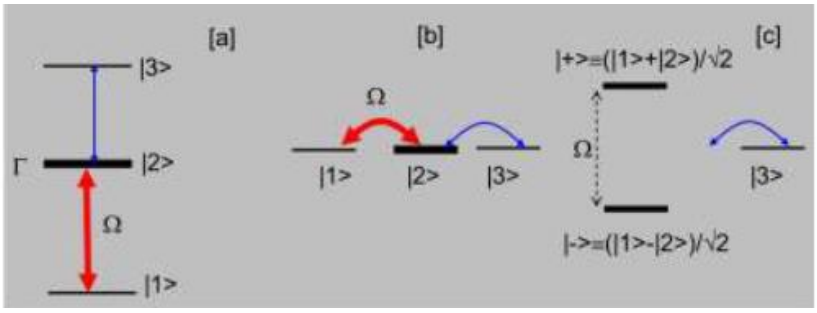

Figure 4.9 AC-Stark effect in a Ladder Transition: (a) The control beam couples |1> to |2>, and the probe beam couples |2> to |3>; (b) For resonant excitation, the corresponding dressed states are degenerate; (c) When the strong control beam coupling is diagonalized, the resulting states are split by an amount much larger than the natural linewidth of |2>.

There are several combinations of parameters that can be considered for controlling the

probe absorption. Consider first Case I, where the probe is resonant for the |2> to |3> transition, but the pump is relatively weak, so that the two diagonalized states (|+> and |->) are not resolved. In this case, the probe is transparent when the pump is not present (since the atoms remain in state |1>), and is absorbed when the pump is turned on. Consider next Case II where the pump is strong so that the two diagonalized states are clearly resolved, but the probe is detuned from the |2> to |3> transition (positively or negatively) by half the separation between the two diagonalized states. In this case, the probe is absorbed in the presence of the pump, but is transparent when the pump is not present. This is the same as what happens for Case I, but for different reasons. Finally, consider Case III, where again the pump is strong so that the two diagonalized states are clearly resolved, but the probe is resonant for the |2> to |3> transition (as shown in Figure 4.9). In this case, the probe is transparent both in the presence and in the absence of the pump. We describe experimental results based on Case I, while the scheme we describe for high speed modulation in the next chapter in the presence of buffer gas is based on Case II. The experimental configuration is illustrated schematically in Figure 4.10. Briefly, beams from two tunable lasers (Ti-Sapphire laser at 795 nm, and a fiber laser at 1323 nm) are combined with a dichroic mirror (DCM). Both the control and the signal beams are co-propagating, and linearly polarized in the same direction. A part of the 795 light is sent to a reference vapor cell for saturated absorption spectroscopy and locking. The combined beams are sent through a vapor cell, shielded from magnetic fields with μ-metal. The cell is heated to temperatures of about 150℃ using bifilarly wounded wires that do not add any magnetic fields. After passing through the cell, another DCM is used to split the light into two parts, and the signal at each frequency is monitored with a separate detector. An Acousto-Optic modulator

(AOM) or an Electro-Optic modulator (EOM) were used as intensity modulators for turning the pump on and off.

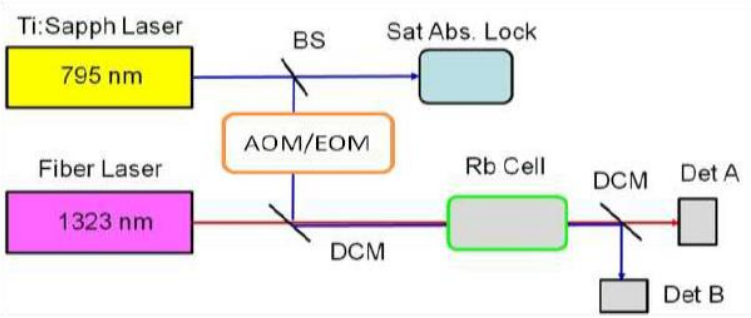

Figure 4.10 Schematic illustration of the experimental setup for observing the ladder-transition based modulator. DCM: Dichroic mirror, AOM: Acousto-Optic modulator, EOM: Electro-Optic modulator, BS: Beam Splitter.

The acousto-optic modulator (AOM) and the electro-optic modulator (EOM) shown in Figure 4.10 are used only while performing the actual modulation, and are removed while characterizing the absorption profile at 1323nm. While performing spectroscopic measurements and switching at low frequencies (up to ~5MHz), we used Thorlabs PDA55 and Thorlabs PDA400 for detecting light at 795nm and 1323nm respectively. For high frequency switching, (where the use of EOM necessitated low control beam power), an APD was used for detection of 1323nm light while the 795nm light was not monitored on a detector-the switching input applied to the EOM was used as reference.

In order to demonstrate modulation, we chose to use the strongest absorption line at the upper leg of transitions, which in our case was the F=3 →F'=2 resonance for ^{85}Rb (due in part to the fact that in a natural mixture of Rb, 72.15 % is ^{85}Rb, and 27.85% is ^{87}Rb). Keeping the probe laser (1323 nm) parked on this resonance, we then modulated the amplitude of the pump

beam (795 nm). At low frequencies, switching of the control beam was accomplished using an AOM while for higher frequencies, an EOM configured for intensity modulation was used.

A typical modulation signal is shown in Figure 4.11. For low frequencies, we used a pump power of ~200mW and we see a strong modulation, in phase with the pump modulation, with a modulation depth of essentially 100% up to a speed of 1MHz. The modulation depths obtained while using the EOM were smaller because of the low control beam power (~2mW) used. This was necessitated by the damage threshold (~20mW) of the EOM used to switch the pump beam and the relatively low efficiency of the EOM (~20%). We have tested the modulation up to a speed of 75 MHz, and determined a 3dB bandwidth of approximately 3 MHz, as shown in Figure 4.12. We have plotted the modulation amplitude at various frequencies (obtained using the EOM), normalized to the amplitude at 1MHz, where the modulation depth was essentially 100%, when obtained with the AOM.

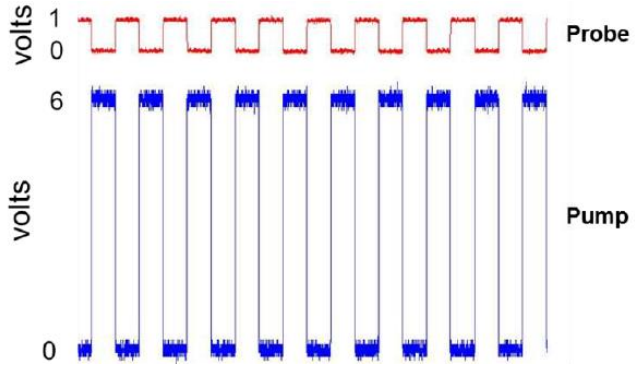

Figure 4.11 Probe and pump signals (top and bottom respectively) up to a frequency of 1 MHz.

A consideration of the physical mechanism behind this modulation reveals that the modulation speed is fundamentally limited by the time needed for the atoms to leave the

intermediate state for the probe to be transparent again. This happens at a time scale which is inversely proportional to the decay rate of the atoms or the homogeneous linewidth (HL~ 6 MHz). Hence, the speed of operation is more or less constrained to a few MHz. In the next chapter, I will discuss a technique adopted by us to develop a high speed modulator.

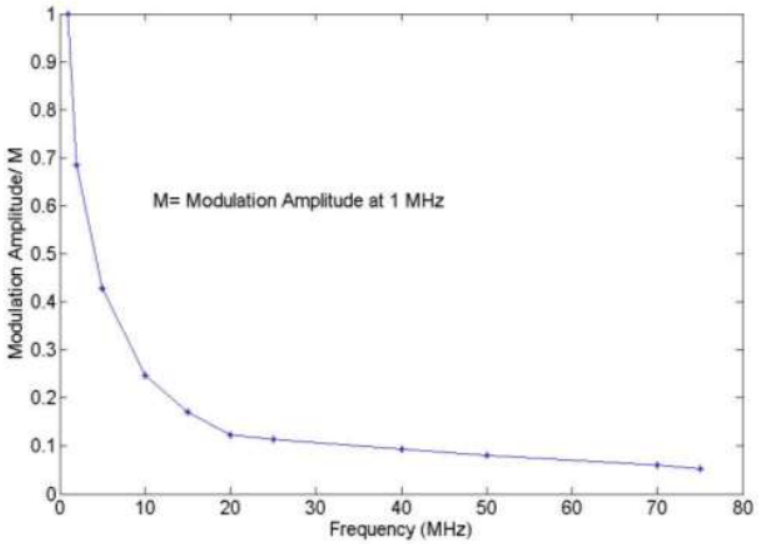

Figure 4.12 Modulation amplitude (normalized to the amplitude at 1 MHz) vs. frequency.

CHAPTER 5 HIGH SPEED MODULATION

5.1 Introduction

All-optical modulation and switching are important for optical communication and quantum information processing [1,2,3,5,6]. We have already demonstrated a cascade system all-optical modulator, polarizer and waveplate at a telecommunication wavelength using the $5S_{1/2}$-$5P_{1/2}$-$6S_{1/2}$ system, where the lower leg, at 795 nm, controls the transmission and absorption of the upper leg at 1323 nm [86,17,18]. We verified experimentally that the bandwidth for the modulator is limited by the decay rate (~6 MHz) of the intermediate level. We also proposed a novel scheme for increasing the modulation bandwidth using buffer gas induced rapid fine structure mixing. In this paper, we present experimental results for such a modulator using the $5S_{1/2}$-$5P_{3/2}$-$5D_{3/2}$ system, where the lower leg is at 780 nm and the upper leg is at ~776 nm. The process is aided by the presence of the $5P_{1/2}$ level. The choice of these particular transitions is primarily determined by the operational wavelength of the devices at our disposal. The principle of operation is the same for any cascade system with two intermediate fine structure levels, and thus can be used at a wavelength corresponding to the telecommunication band, for example. In combination with a tapered nano fiber (TNF) system [7,8,9,10], the system has the potential to be used for low-power high-speed all-optical switching.

The rest of the session is organized as follows. In section 5.2, we briefly review the effects of buffer gas on alkali atoms. In section 5.3, we present a detailed model for our system and show simulation results. The details of the experimental set-up and the spectral information

corresponding to the 5S-5P-5D system are presented in section 5.4. In section 5.5, we present the experimental results, including spectral data and modulation data with and without buffer gas. We discuss means to improve the system performance in section 5.6.

5.2 Effect of high-pressure buffer gas on alkali metals

It is well known that in the presence of high pressure buffer gas, there is rapid inter-mixing and dephasing of atoms in the $5P_{3/2}$ and the $5P_{1/2}$ states of alkali metals [67,68,69,70,71]. For concreteness, we restrict our discussion to the case where the buffer gas used is Ethane, and the alkali atom of interest is ^{85}Rb. The behavior of ^{87}Rb as well as other alkali atoms, and under the presence of different buffer gases, is qualitatively similar, while differing in details. Relevant parameters for ^{87}Rb as well as other alkali atoms can be found in [68,98,88].

Consider a vapor cell loaded with ^{85}Rb and Ethane buffer gas at 300 Torr, and a temperature of about 150° C. These parameters are close to those used in the experiment. We consider first the three lowest energy manifolds: $5S_{1/2}$, $5P_{1/2}$ and $5P_{3/2}$, indicated as states |A>, |B> and |C>, respectively, as shown in Figure 5.1. Since the buffer gas induced width of the absorption spectrum under such conditions will be much broader than the hyperfine splitting within each of these three manifolds, we can treat each of them as a single energy level. When excited by a pump at the D2 line (i.e., the A-C transition), the presence of the buffer gas causes the following two effects.

First, the coherence generated between states |A> and |C> dephases rapidly, without affecting the rate at which atoms in state |A> decay radiatively to level |C> via spontaneous emission. The radiative decay rate, denoted by Γ_R, is the inverse of the radiative lifetime of

~27 nsec, so that $\Gamma_R \approx 37 * 10^6\,\mathrm{sec}^1$ [75, 72]. The dephasing rate, denoted by Γ_D, is determined by the pressure of the buffer gas. For Ethane, this dephasing rate is about $2\pi \times 2 \times 10^7\,\mathrm{sec}^{-1}$ /Torr (20 MHz/Torr) [85,97], so that the rate at 300 Torr is $\Gamma_D \approx 2\pi \times 6 \times 10^9\,\mathrm{sec}^{-1}$ (6 GHz). Taking into account the fact that the Doppler width is about 0.6 GHz, and that the $5S_{1/2}$ manifold has a hyperfine splitting of about 3 GHz, this dephasing would produce an absorption profile on the A-C leg with a width of at least 9.6 GHz, in the limit of a weak pump. Of course, essentially the same effect is present on the A-B leg. The state |B> decays radiatively at almost the same rate (~$37 \times 10^6\,\mathrm{sec}^{-1}$) as that of state |C>, while the A-B coherence decays at the same dephasing rate (Γ_D) as that of the A-C coherence. As such, the absorption profile on the A-B leg also has a width of about 9.6 GHz at this pressure of Ethane. It should be noted that the absorption profile on each of these legs would be widened further due to additional dephasing attributed to the radiative and collisional relaxation of populations in states |B> and |C>, as discussed later.

Second, states |B> and |C> decay into each other at a rate determined by the pressure of the buffer gas. The rate of decay from |C> to |B>, denoted as Γ_{CB}, is about $1.07 \times 10^7\,\mathrm{sec}^{-1}$ / $Torr$ [14]. Thus, for a pressure of 300 Torr, we have $\Gamma_{CB} \approx 3.21 \times 10^9\,\mathrm{sec}^{-1}$ (~0.51 GHz). This is nearly a factor of 87 times faster than the rate of radiative decay from |C> to |A>. The rate of decay from |B> to |C> is determined by assuming that, in the limit of vanishingly small optical excitation applied on the A-C leg, the populations of all the energy levels will correspond to a thermal equilibrium, obeying Boltzmann statistics. Given that the number of Zeeman sublevels in the $5P_{3/2}$ manifold is twice as large as the number of Zeeman sublevels in the $5P_{1/2}$ manifold, we thus get $\Gamma_{BC}/\Gamma_{CB} = 2\,exp(-\Delta E\,/\,kT)$, where ΔE is the energy

difference between states |C> and |B>, k_B is the Boltzmann constant, and T is the temperature in Kelvin [68]. For ^{85}Rb, we have $\Delta E/kB \approx 341.1\, Kelvin$. Thus, at 150℃, we get that $\Gamma_{BC}/\Gamma_{CB} \approx 0.89$, so that $\Gamma_{BC} \approx 2.86 \times 10^9\ \mathrm{sec}^{-1}$ (~0.46 GHz). Of course, the actual ratio of populations between state |C> and state |B> will differ from the thermal equilibrium value of Γ_{BC}/Γ_{CB} due to the presence of the (typically strong) pump along the A-C transition (as well as possibly other optical fields that may be present or generated).

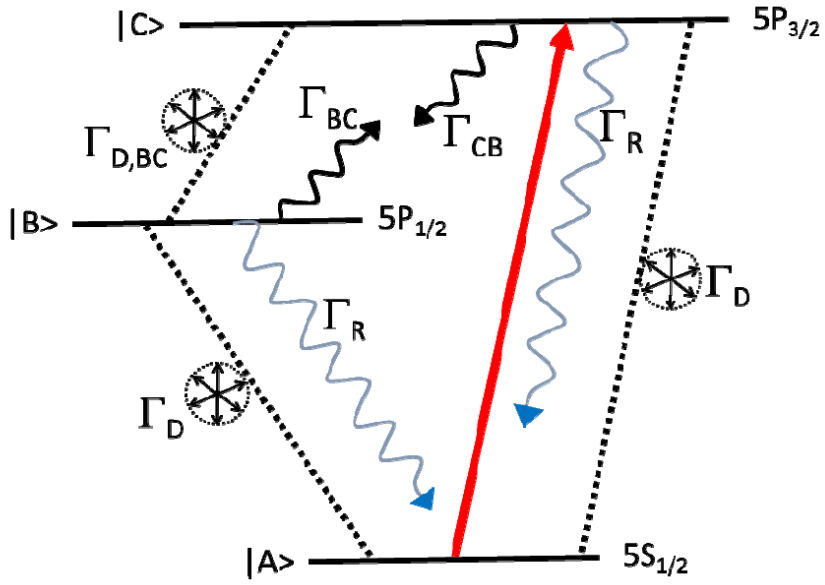

Figure 5.1 Schematic illustration of the population and coherence dynamics in an alkali atom in the presence of a high-pressure buffer gas.

It should be noted that the exchange of populations between states |B> and |C> automatically implies that any coherence that could possibly be generated between states |B> and |C> (e.g., in the presence of another pump acting along the A-B leg which is phase coherent with the pump along the A-C leg) would decay as well. We denote this decay rate as $\Gamma_{D,BC}$. The minimum value of the decay rate is $\Gamma_{D,BC,MIN} = (\Gamma_{BC} + \Gamma_{CB})/2$, which in this

case corresponds to a rate of ~$3.04 \times 10^9\ \mathrm{sec}^{-1}$ [73]. In principle, the actual dephasing rate of the BC coherence could be much larger, given the fact that the collision-induced dephasing rate Γ_D of the A-B (as well as the A-C) coherence is nearly a factor of 12.4 larger. Thus, we can write $\Gamma_{D,BC} = \Gamma_{D,BC,MIN} + \alpha\Gamma_D$, where α is a parameter the value of which depends on the details of the collision process that generates the dephasing of the A-B and A-C transition. Theoretical studies carried out so far [68,70,96] do not provide any clear indication regarding the value of α. Furthermore, to the best of our knowledge, no experimental study to determine the value of α has been carried out yet. Fortunately, for the experiment described in this paper, no coherence is generated between states |B> and |C>. As such, the value of α as well as the value of $\Gamma_{D,BC}$ does not affect the experimental results, nor the outcome of the simulations thereof.

Along the same line, we denote by $\Gamma_{D,AC}$ ($\Gamma_{D,AB}$) the net rate at which the A-C (A-B) coherence would dephase. Accounting for the additional dephasing caused by the decay of populations from state |C>, we thus get that $\Gamma_{D,AC} = \Gamma_D + (\Gamma_R + \Gamma_{CB})/2$. Similarly, we get that $\Gamma_{D,AB} = \Gamma_D + (\Gamma_R + \Gamma_{BC})/2$. Since the value of Γ_R is much smaller than the other rates, we see that $\Gamma_{D,AC} \approx \Gamma_D + \Gamma_{CB}/2$ and $\Gamma_{D,AB} \approx \Gamma_D + \Gamma_{BC}/2$. Thus, the spectrum profile on the A-C (A-B) leg will be broadened further by $\Gamma_{CB}/2$ ($\Gamma_{BC}/2$), in addition to the 9.6 GHz estimated above.

Finally, we note that all the decay and dephasing timescales for ^{87}Rb are very similar to those described above for ^{85}Rb. Thus, even though the experiment described here makes use of a natural mixture of both of these isotopes (72.16% of ^{85}Rb and 27.84% of ^{87}Rb), we treat our system, in simulations, as if it is made entirely of ^{85}Rb.

5.3 Modeling and simulation results

For realizing a high-speed optical modulator, we make use of the system described above, augmented by another transition coupling the $5P_{3/2}$ state to the $5D_{3/2}$ state. The control beam is applied on the $5S_{1/2}$-$5P_{3/2}$ leg, and the signal beam is applied on the $5P_{3/2}$-$5D_{3/2}$ leg. This system is illustrated schematically in Figure 5.2. On the left, we show only the population decay rates. On the right, we show additional dephasing of the coherences among the various states, without corresponding decays of the populations of these states. The exact meaning of these various dephasing rates can be deciphered from the density matrix equations for these states and is described later.

As shown in Figure 5.2(a), the population of state |2> decays to level |1> radiatively at the rate of γ_a, which is the same as Γ_R shown in Figure 5.1. In addition, it decays to state |4>, via collision with Ethane atoms, at the rate of γ_{down}, which is the same as Γ_{CB} shown in Figure 5.1. Similarly, population of state |4> decays radiatively to state |1> at the rate of γ_a ($= \Gamma_R$), and to state |2> collisionally at the rate of γ_{up} ($= \Gamma_{BC}$). Finally, state |3> decays radiatively to each of states |2> and |4>. For simplicity, we have ignored the small difference in the branching ratios of these, and assumed that these two decay rates are the same, indicated as $\gamma_b/2$, where $\gamma_b \approx 2\pi \times 10^6\,\mathrm{sec}^{-1}$ (1 MHz). The decay of these populations also causes corresponding decays of the coherences among these states. Specifically, if the population of state |i> has a net decay rate of γ_I, then the decay rate of the co**h**erence between states |i> and |j> is given by $(\gamma_i + \gamma_j)/2$ [18].

Figure 5.2(b) shows the rates of additional decays for the coherences among these states, caused by collisions with Ethane atoms. For the 1-2 coherence, this rate, indicated as γ_d, is the same as Γ_D shown in Figure 5.1. Similarly, for the 1-4 coherence, this rate is also γ_d $(= \Gamma_D)$. For the 2-4 coherence, the rate is $\alpha\gamma_d$ $(= \alpha\Gamma_D)$, where the precise value of the parameter α is not known, as discussed earlier while describing the model presented in Figure 5.1. Consider next the coherences involving state |3>, the uppermost state. We denote by $\beta\gamma_d$ $(= \beta\Gamma_D)$ the dephasing rate for the 2-3 as well as the 4-3 coherence, and by $\xi\gamma_d$ $(= \xi\Gamma_D)$ the dephasing rate of the 1-3 coherence, since these dephasing rates are expected to be closely related to that of the 1-2 coherence. This is because these dephasing rates are not due to population excitation or relaxation, but rather due to phase changing collisions, which should affect all coherences in a similar fashion. To the best of our knowledge, no experimental study has been carried out, nor any explicit theoretical model developed, to establish the values of the parameters β and ξ. In principle, the value of β can be established by determining the absorption profile of the 2-3 transition, as described in more detail later. However, since the 2-3 absorption can only be seen when a pump is also present on the 1-2 transition, any inference regarding the 2-3 dephasing rate would depend on the parameters of the 1-2 pump, including its power, spectrum, temporal profile, as well as correlation between its frequency and the frequency of the 2-3 probe. Thus, a systematic and extensive experimental study, aided by a theoretical model, has to be carried out to determine accurately the values of $\alpha, \beta \; and \; \xi$. We will carry out, and report the findings of such a study in the near future.

For the purpose of the experiment and the simulation thereof reported here, we instead

rely on a physical argument to estimate the values of these parameters. The dephasing of the 1-2 and 1-4 coherences are caused by collisions (between a ^{85}Rb atom and an Ethane molecule) that changes the optical transition frequencies in a random fashion. Since this can happen when the ^{85}Rb atom is any of the states, a plausible value of each of these parameters (α, β and ξ) is unity. We have used these values in the simulations, which show that the behavior of the optical modulation is completely insensitive to the value of α (since the 2-4 coherence is always zero, as explained earlier), and relatively robust against variations in β and ξ away from the unity values.

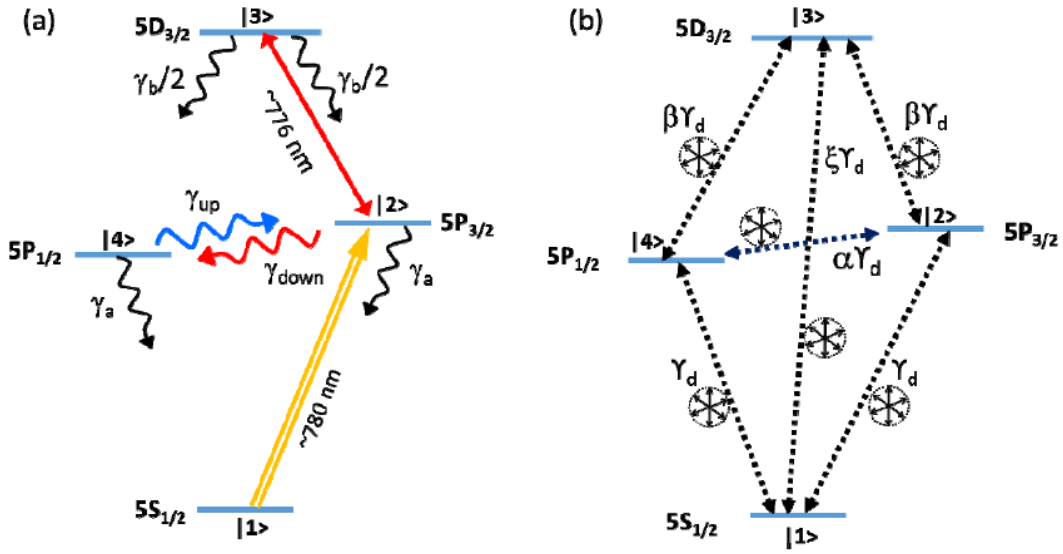

Figure 5.2 Model used for numerical simulation (a) Optical fields and decay rates-radiative and collisional. (b) Transverse decay (dephasing) terms.

For our numerical simulations, we used the Liouville equation, which describes the evolution of the density matrix, given the Hamiltonian. We follow the prescription described in [73] and accordingly, the density matrix evolution is represented by

$$\frac{\partial}{\partial t}\tilde{\rho} = \frac{\partial}{\partial t}\tilde{\rho}_{ham} + \frac{\partial}{\partial t}\tilde{\rho}_{source} + \frac{\partial}{\partial t}\tilde{\rho}_{trans-decay} \tag{5.1}$$

where

$$\frac{\partial}{\partial t}\tilde{\rho}_{ham} = -\frac{i}{\hbar}\left[H'\tilde{\rho} - \tilde{\rho}H'^{*}\right] \tag{5.2}$$

and *H'* is the Hamiltonian under the Rotating Wave Approximation and in a basis which is rotating at the optical frequency. In our case, it is given by

$$H' = \begin{pmatrix} 0 & \Omega_a/2 & 0 & 0 \\ \Omega_a/2 & -i\gamma_2/2 & \Omega_b/2 & 0 \\ 0 & \Omega_b/2 & -i\gamma_3/2 & 0 \\ 0 & 0 & 0 & -i\gamma_4/2 \end{pmatrix} \tag{5.3}$$

Here, γ_2 is the sum of the radiative decay and buffer gas induced collisional decay i.e. $\gamma_2 = \gamma_a + \gamma_{down}$. Similarly, $\gamma_4 = \gamma_a + \gamma_{up}$. The addition of the decay terms to the diagonal elements of the Hamiltonian is a convenient way of taking into account the decay of atomic populations, and the corresponding decay of the relevant coherences [73]. Finally, following the convention in [73], the source terms and transverse decay terms in Eqn.5.1 can be represented in matrix forms by Eqn.5.4 and 5.5 respectively:

$$\frac{\partial}{\partial t}\tilde{\rho}_{source} = \begin{pmatrix} \gamma_a(\tilde{\rho}_{22} + \tilde{\rho}_{44}) & 0 & 0 & 0 \\ 0 & (\gamma_b\,\tilde{\rho}_{33}/2 + \gamma_{up}\,\tilde{\rho}_{44}) & 0 & 0 \\ 0 & 0 & 0 & 0 \\ 0 & 0 & 0 & (\gamma_b\,\tilde{\rho}_{33}/2 + \gamma_{down}\,\tilde{\rho}_{22}) \end{pmatrix} \tag{5.4}$$

$$\frac{\partial}{\partial t}\tilde{\rho}_{trans-decay} = \begin{pmatrix} 0 & -\gamma_d\tilde{\rho}_{12} & -\xi\gamma_d\tilde{\rho}_{13} & -\gamma_d\tilde{\rho}_{14} \\ -\gamma_d\tilde{\rho}_{21} & 0 & -\beta\gamma_d\tilde{\rho}_{23} & -\alpha\gamma_d\tilde{\rho}_{24} \\ -\xi\gamma_d\tilde{\rho}_{31} & -\beta\gamma_d\tilde{\rho}_{32} & 0 & -\beta\gamma_d\tilde{\rho}_{34} \\ -\gamma_d\tilde{\rho}_{41} & -\alpha\gamma_d\tilde{\rho}_{42} & -\beta\gamma_d\tilde{\rho}_{43} & 0 \end{pmatrix} \tag{5.5}$$

A typical result of the simulation using this model is presented in Figure 5.3, for a square

modulation at 1 GHz. The red trace represents the pump while the blue trace is the probe. Here, we have used the values of the relevant parameters for temperature of $150℃$, and an Ethane pressure of 300 Torr, and have used $\alpha = \beta = \xi = 1$. The pump Rabi frequency was chosen to be $\Omega_p = 8000\gamma_a$. The probe Rabi frequency was chosen to be $0.1\gamma_a$. While we have indicated the vertical axis as having arbitrary units, it should be noted that the Rabi frequencies, which correspond to the square root of the intensities, are specified above. Since this is an absorptive modulation, the degree of absorption can be increased by increasing the optical density, via using either a longer cell length or a larger density. The modulation depth, which is about 90% as shown, can easily be made to be essentially 100%, as is the case for virtually any absorptive modulator.

Such a modulator can exhibit a wide range of behavior, depending on the choice of parameters. In [89], where we first proposed the concept of realizing a high-speed modulator using a ladder transition and a buffer gas, we discussed in great detail, in section 5.6, the range of behavior that can be expected, and the physical explanations thereof. We also considered, in [89], the case where a re-shelving pump is employed to depopulate level |4> rapidly, following the turning off of the pump, and showed that the modulation works with or without the re-shelving pulses, albeit with differing modulation depths for a given optical density (in this context, it should again be noted that for an absorptive modulator, any desired modulation depth can be achieved by increasing the optical density). It should also be noted that in [89], we considered a model system, while, in this paper, we are considering a specific system. In what follows, we summarize the most salient features of the behavior of this modulator.

First, the modulation bandwidth is determined primarily by the decay rate of |2> to state |4>, which is indicated as γ_{down} in Figure 5.2. In the case considered here, this rate is 0.51 GHz. Second, the collisional dephasing rate of the 1-2 coherence (which, in this case, is $\gamma_d = 9.6\,GHz$), does not determine, nor affect significantly, the bandwidth of the modulation. However, a large value of this rate allows more efficient absorption of a high bandwidth pump pulse. Third, for most efficient modulation for a given optical density, the pump Rabi frequency should be close to γ_d. However, this is not a fundamental constraint. Since this is an absorptive modulator, any degree of modulation amplitude at a given optical density can be increased to a modulation depth of near 100% by increasing the optical density. This can be achieved by increasing the temperature of the cell, or by increasing the interaction length. Fourth, the transient response (i.e., the ringing) of the probe is affected by two parameters. As explained in detail in [89], the ringing that occurs after the pump is turned on, happens at the rate of the pump Rabi frequency. For the pump Rabi frequency used here ($\Omega_p = 8000\gamma_a$), this corresponds to a time scale of about 0.02 nanoseconds, which is roughly the time scale of these oscillation seen in Figure 5.3. On the other hand, the ringing that is seen to occur after the pump is turned off is due to the fact that we have used rectangular profiles for the pump pulses, which has spectral components that exceed the bandwidth of the homogeneous absorption (~9.6 GHz) along the 1-2 transition. In a real experiment, the applied pulses would be smooth, and these ringing would be suppressed strongly if the rise and fall times of the applied pulses are slower than the inverse of this bandwidth.

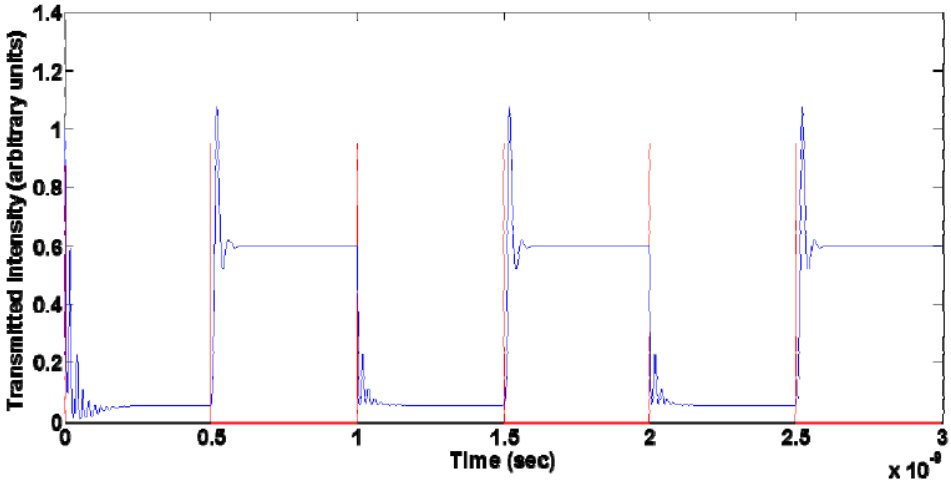

Figure 5.3 Simulation results for high speed modulator at 1 GHz. Red trace: pump; Blue trace: Probe. While we have indicate the vertical axis as having arbitrary units, it should be noted that the Rabi frequencies, which correspond to the square root of the intensities, are specified (pump Rabi frequency is $800\gamma_a$*, and probe Rabi frequency is* $0.1\gamma_a$*). Since this is an absorptive modulation, the degree of absorption can be increased by raising the optical density. The modulation depth, which is about 90% as shown, can be made to be essentially 100% with higher optical density.*

5.4 Experimental set-up

Figure 5.4 Experimental set-up for high speed modulator. shows the set-up for the experiment. The 780 nm and the 776 nm beams were obtained from two different continuous-wave tunable Ti-Sapphire lasers. They were cross polarized, and combined and separated using polarizing beam splitters. Both beams were focused to a spot size of about 50μm in diameter. We used an acousto-optic modulator (AOM) or an electro-optic modulator (EOM) for modulating the pump beams. In either case, the power at the output of these modulators is very small and is not sufficient to saturate the buffer gas broadened

absorption profile. This necessitated the use of an optical amplifier. However, since our particular amplifier (a tapered amplifier) works only for a certain input polarization, a half wave plate was added before it. Furthermore, an optical isolator was added after the output of the modulator to prevent feedback from the amplifier. The cell was constructed using conflat flanges with a 4-way cross at the center, providing for two windows for the beam paths, and one each for connecting the Rb reservoir and the Ethane gas tank. A valve, placed between the chamber and the Ethane tank, was closed during the use of the cell as a modulator. Connections were also provided for a mechanical pump, which achieved a pressure of 10−3 Torr in the absence of any buffer gas. The Rb cell was heated to approximately 150° C. A buffer gas pressure of typically ~300 Torr (~6 psi) was used during the experiment. A separate, sealed Rb vapor cell was used to lock the frequency of the pump laser to the D2 transition.

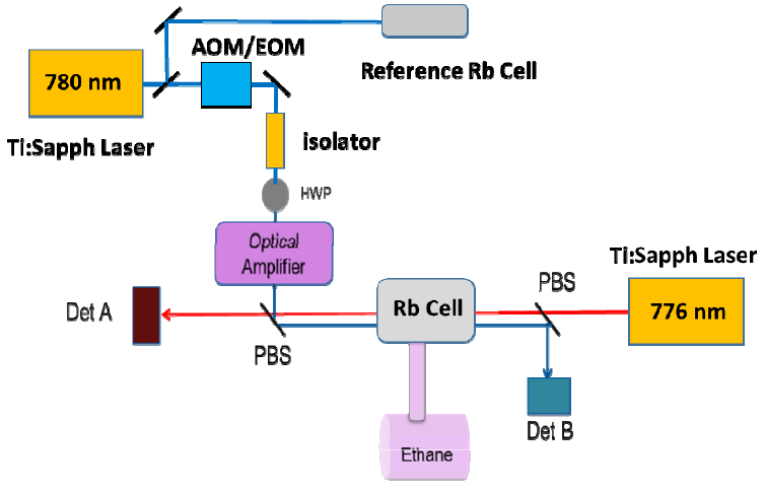

Figure 5.4 Experimental set-up for high speed modulator.

5.5 Results

The spectroscopic details and the absorption line shapes for the 5S-5P-5D transitions can be found in several publications [10,74,75,76,77]. In the absence of the Ethane buffer gas, and for a counter-propagating geometry (as employed in our experiment), the linewidth of the 2-3 transition is expected to be essentially Doppler-free [66]. Of course, the actual spectrum observed depends on the exact frequency of the pump applied on the 1-2 transition, as well as the power of this pump [89,17]. In the presence of the high-pressure Ethane buffer gas, however, all the individual hyperfine transitions are washed out, resulting in a single, broad absorption peak. For example, for an Ethane gas pressure of ~250 Torr (~5 psi), and pump and probe powers of ~760 mW and ~0.5 mW respectively, the observed linewidth of the 776 nm probe absorption was found to be ~2 GHz, as shown in Fig. 5. The value of Γ_D (= γ_d) for this pressure is ~5 GHz. If the width of this spectrum were to be attributed solely to the collisional dephasing rate ($\beta\gamma_d$), it would imply that the value of β is ~0.4. However, as we discussed earlier, the width of the absorption profile of the 2-3 transition under this condition cannot be ascribed necessarily to this dephasing rate ($\beta\gamma_d$); rather, it is expected to depend on the degree and nature of excitation produced in state 2, which in turn depends on the spectrum, frequency and power of the pump applied on the 1-2 transition. As mentioned earlier, a detailed and systematic experimental study of the absorption processes in this system in the presence of high-pressure buffer gas, augmented by a theoretical model, is necessary to determine the precise value of β (as well as α and ξ). Such as study is underway, and will be reported on in the future. Nonetheless, the significant broadening

observed is consistent with our assumption, in the theoretical simulation, that the values of these parameters (α, β, and ξ) are of the order of unity.

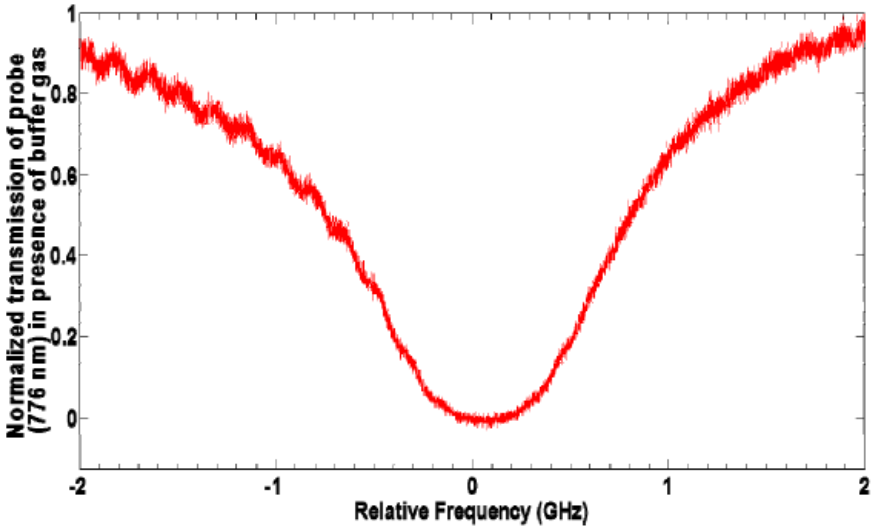

Figure 5.5 Probe (776 nm) absorption lineshape in the presence of buffer Ethane. Here, Ethane pressure is ~6 psi and the pump and probe powers are ~800 mW and ~0.5 mW.

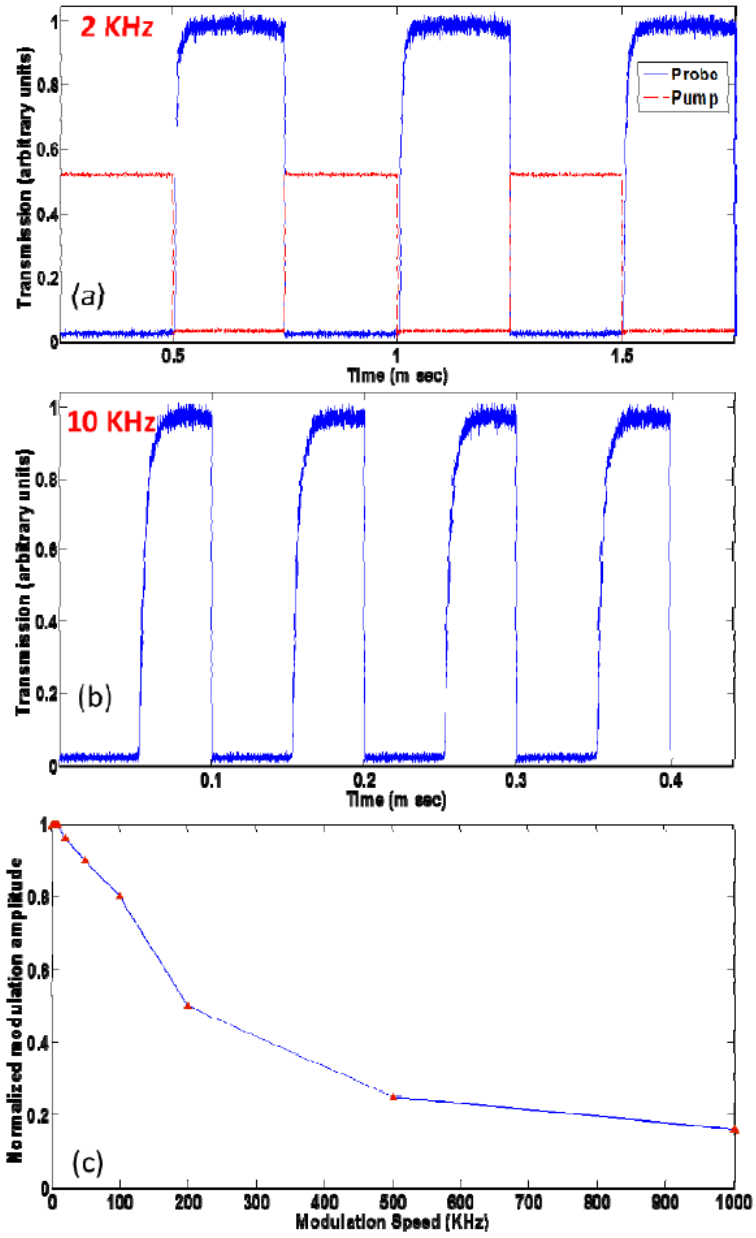

Figure 5.6 5S-5P-5D modulation data without buffer gas. (a) 2 KHz (b) 10 KHz (c) Modulation amplitude vs modulation speed. We have indicated the vertical axes in (a) and (b) as having arbitrary units, since the relevant parameter is the modulation depth, which is about 95% in both cases. In (a), the peak pump signal corresponds to an un-attenuated pump power of ~760 mW, and the peak probe transmission corresponds to an un-attenuated probe power of 0.5 mW. Similarly, in (b), the peak probe transmission

corresponds to an un-attenuated probe power of 0.5 mW. Since this is an absorptive modulation, the degree of absorption can in principle be increased by increasing the optical density.

Figure 5.6 shows the results of modulation without buffer gas. The system shows almost perfect square modulation at 2 KHz, as shown in Figure 5.6 (a). Here, the red trace represents a scaled version of the pump signal. It is not shown in other figures. As is evident from Figure 5.6 (b), the signal starts to roll off at a frequency of 10 KHz. Indeed, as can be from Figure 5.6 (c), where we have plotted the modulation amplitude vs. the speed, the bandwidth is about 200 KHz. However, it should be noted that the data shown here is for square modulation. Since a square pulse consists of many harmonics, it is conceivable that the actual bandwidth (for sinusoidal modulation) is 8-10 times larger, i.e. about 2MHz, consistent with the earlier observation for the 5S-5P-6S system [89]. The power output from the EOMs was too small to produce the desired modulation even with the optical amplifier. Hence, we had to use exclusively the AOMs for our experiments which in turn restricted us to square modulation.

Figure 5.7 shows the result of the modulation in the presence of buffer gas. With the rest of the conditions remaining identical, we obtained a 100- fold increase in the bandwidth. The rapid decay from state |2> to state |4> caused by the buffer gas results in the probe becoming transparent on a very short time scale, as is evident from Figure 5.7. Once again, the data shown is for square modulation and the actual bandwidth is about 200 MHz.

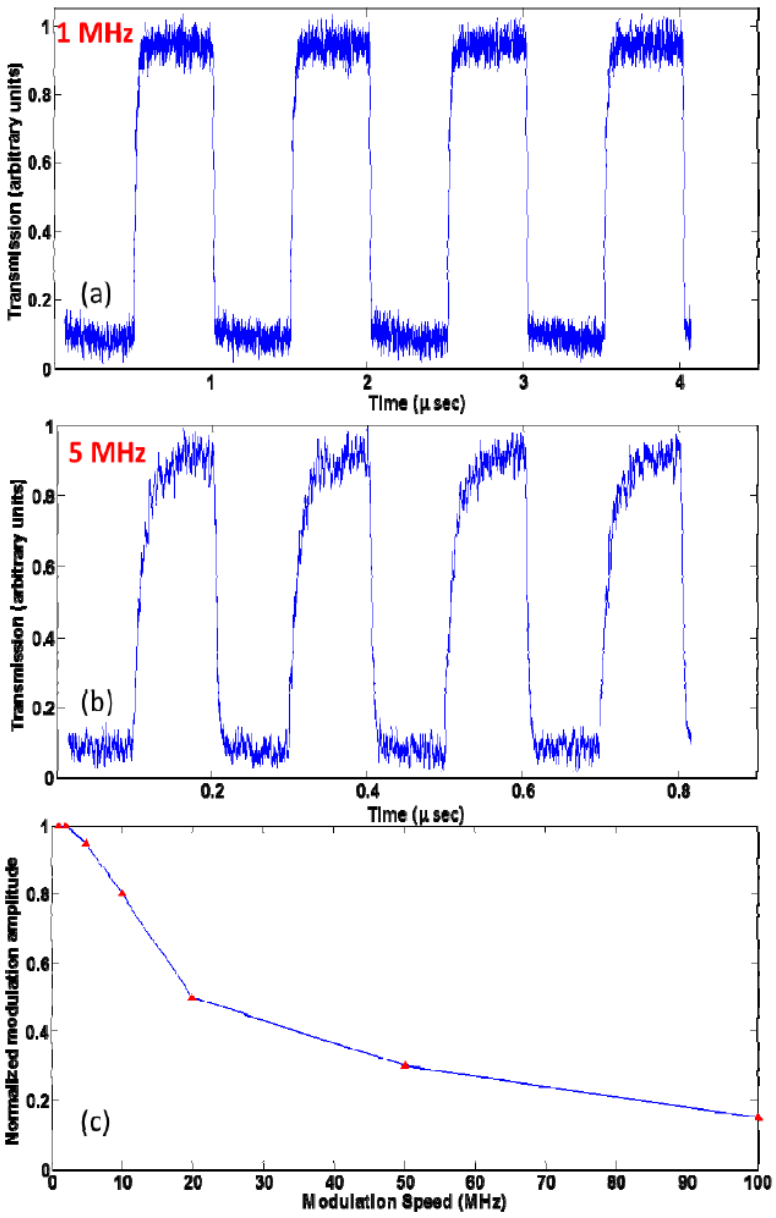

Figure 5.7 Modulation data in the presence of buffer gas (Ethane) at pressure of ~6 psi. (a) 1 MHz (b) 5 MHz (c) Modulation amplitude vs modulation speed. We have indicated the vertical axes in (a) and (b) as having arbitrary units, since the relevant parameter is the modulation depth, which is about 90% in both cases. The peak probe transmission at both 1 MHz and 5 MHz corresponds to an un-attenuated probe power of 0.5 mW.

5.6 Improvements to system and future outlook

As noted above, we observed a 100-fold increase in the bandwidth after the addition of buffer gas, reaching a bandwidth of ~0.2 GHz. This is consistent with our model that shows that the bandwidth is bounded by the rate of collisional decay from |2> to |4>, which, for the parameters employed here, is $\gamma_{down} = 0.51\, GHz$. Given that it is an absorptive modulator, the bandwidth of the modulation could be increased further (but within the bound set by γ_{down}) by increasing the optical density. One way to do so is to increase the temperature. However, for Ethane buffer gas, a temperature much higher than 150 degrees tends to cause degradation of the windows. The other way to do so is to increase the effective interaction length. For a free space system, this cannot be done without reducing the pump intensity, since the effective interaction length is the Rayleigh length, which depends on the spot size.

On the other hand, it should be possible to increase the bandwidth (up to the limit set by the value of γ_{down}) by using higher pump power. However, our current set up did not allow us to increase the pump power beyond the 760 mW used. Instead, we studied the dependence of the modulation amplitude on the pump power, as shown in Figure 5.8. As can be seen, the modulation amplitude keeps increasing monotonically with increasing pumps power, at two different modulation frequencies. From this data, it can be inferred that higher bandwidth would have been observed if we were able to increase the pump power well beyond 760 mW. We did not try to increase the intensity (which, rather than the power, is the relevant parameter) by focusing the beam to a smaller spot, since this process would reduce the Rayleigh length to be much smaller than the current value of ~1 cm (for a focused spot size

of 50 μm), which in turn would reduce the modulation amplitude, thus potentially offsetting any enhancement due to increased intensity.

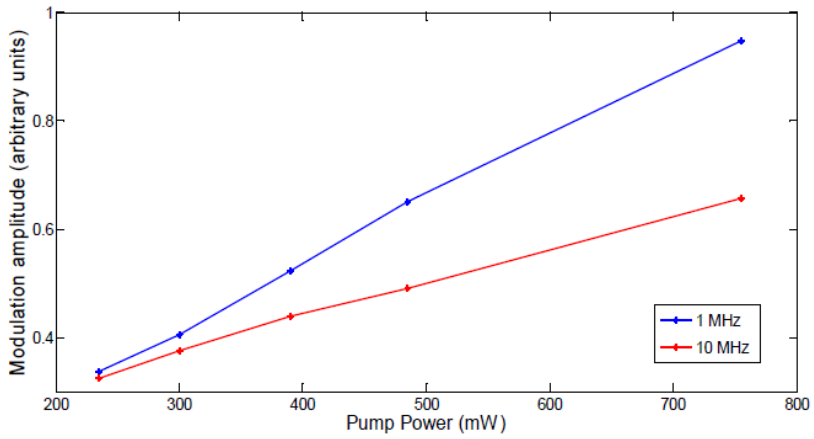

Figure 5.8 Increase in modulation amplitude for two different modulation frequencies (1 MHz and 10 MHZ) with increase in pump power. Just as in Figure 5.6 and Figure 5.7, the vertical axis is shown in arbitrary units, since the relevant parameter is the modulation depth, which can be increased to be near 100% by increasing the optical depth, since it is an absorptive modulator. The data shown in Figure 5.7 correspond to the maximum power employed for the pump beams (760 mW), thus corresponding to the right-most data points in this figure.

Of course, the upper limit of the modulation bandwidth itself can be increased further by increasing the pressure of the buffer gas, thereby increasing the value of γ_{down}, which is expected to vary linearly with the buffer gas pressure up to a value of at least as high as 25 atmosphere [78, 95]. Using the fact that this decay rate varies as 1.07*107 sec−1/Torr for Ethane, for a pressure of 25 atmosphere (= 19000 Torr) the modulation bandwidth would be about 32 GHz. However, given the constraint of our current system on the maximum

intensity achievable without reducing the Rayleigh length to be significantly smaller, increasing the pressure beyond the 600 Torr we used would not allow us to observe a higher bandwidth. In the near future, we plan to use a different experimental system in order to demonstrate higher bandwidth. Specifically, we will use a Silicon Nitride waveguide, embedded in a cell containing Rb vapor as well as high pressure Ethan buffer gas. The core technology for such a system has already been demonstrated [79]. This system has the property that, just like in the case of the TNF, the evanescent field that interacts with the atoms can produce a very high intensity at a very low power. Furthermore, unlike in the case of the TNF, the interaction length can be made very long. One of the drawbacks of the system is that, in its current incarnation, the power throughput is very small due to inefficient input coupling. This problem can be circumvented by using a tapered section at the input, or using a photonic crystal based coupler.

It should be possible to realize this modulator at a telecommunication wavelength at very low control powers using the tapered nano fiber (TNF) set-up [8], employing the $5S_{1/2}$-$5P_{3/2}$-$6S_{1/2}$ system, for which the probe transition is at ~1367 nm. The TNF needs to be designed to operate as a single mode fiber for both wavelengths: 780 nm and 1367 nm. We have carried out designs of such a TNF, and have shown that there is a range of taper diameters for which it is possible to have a significant overlap between the evanescent modes at these two wavelengths. The TNF would be embedded in a Rb vapor cell, and pressurized with Ethane buffer gas. The pump and the probe will be combined using a dichroic mirror and launched into the TNF. As a figure of merit (FOM) for implementation in our TNF system, one can use the number of photons in the pump field that are needed to switch the state of the probe from

'off' to 'on'. In order to achieve an intensity equivalent to a free space pump power of 1W for a spot size of $50\mu m$, the TNF system with a mode area of $0.2\,\mu m^2$ would require a pump power of ~80 μW. Assuming a rise time of 2.5 nS for operation at a modulation speed of 200 MHz, the number of pump photons at 780 nm needed for switching would be $\sim 5 \times 10^5$. Of course, a telecom wavelength modulator of this type can also be realized using the SiN waveguide approach discussed above. Allowing for a near unity throughput using one of the configurations (e.g. tapered waveguide section or a photonic crystal at the input) mentioned above, a bandwidth of 32 GHz for the same power level would correspond to an FOM of $\sim 3 \times 10^3$. Of course, to achieve high modulation depth while using the same power, the interaction length (and hence the optical density) has to be much longer than that of the TNF (which is only about 1 cm). As mentioned above, this is easy to achieve for the waveguide, even within the constraint of a small chip, by using smoothly folded patterns. As a comparison with other techniques for low power all-optical modulation [5,92], we find that the instability induced switch has an FOM of 4×10^4 photons [81] while micro-ring resonators based switches have an FOM of 4×10^7 photons [80]. Thus, this approach is a potentially attractive option for low power all-optical modulation.

CHAPTER 6 OPTICALLY CONTROLLED POLARIZER

6.7 Schematic

6.7.1 Quantum Zeno effect (QZE)

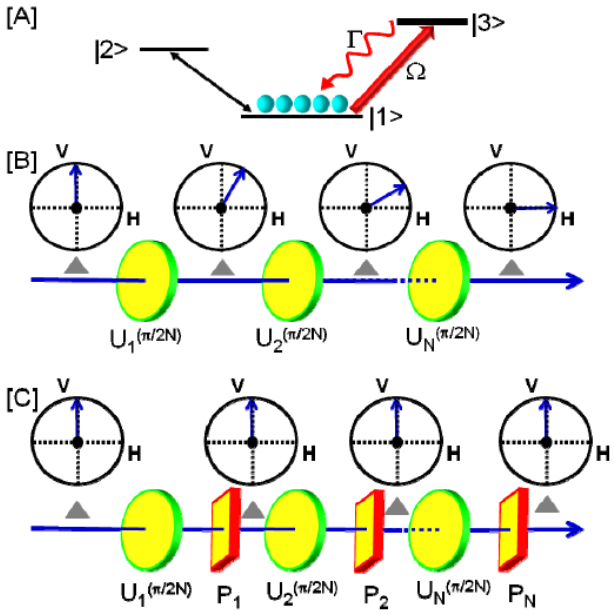

Figure 6.1[A] Quantum Zeno Effect in an atomic V-system. [B] Evolution of the quantum state of a photon via passage through a series of waveplates. [C] In the presence of interleaved polarizers acting as measurement devices, the evolution to the horizontally polarized state is inhibited.

The quantum Zeno effect (QZE) [11,12,13] is the suppression of the evolution of a quantum state through the quantum measurement process. Figure 6.1[A] shows the energy level diagram of a three level system that illustrates this process. Here, states |1> and |2> are assumed long-lived, while state |3> decays rapidly, at a rate Γ, into state |1> only. The QZE in

this configuration can be described as follows. In the absence of any coupling to state |3>, state |1> will undergo Rabi oscillation, thus getting excited to state |2> at a rate determined by the 1↔2 coupling strength. When coupled to state |3>, the spontaneous emission emulates a measurement process, which resets the quantum state of the system to state |1>. As such, evolution of state |1> into state |2> is inhibited.

The phenomenon described above, although initially investigated in the context of atomic transitions, is in fact a general quantum mechanical effect occurring in any system where periodic quantum measurement and quantum state evolution occur. In particular, it is instructive to analyze a bulk-optic model for this effect, as illustrated in Figure 6.1[B]. Here, we consider the evolution of the polarization state of a photon. The polarization degree of freedom for the photon spans two orthogonal states: |V> and |H> representing vertical and horizontal polarizations, respectively. The general quantum state can thus be written as $\alpha|V\rangle + \beta|H\rangle$, with $|\alpha|^2 + |\beta|^2 = 1$. Consider now a specific situation where input quantum state is $|V\rangle$. When it passes through a wave plate with its fast/slow axis at an angle of 45° with respect to the vertical axis, the polarization state of the photon can be expressed as (ignoring an overall phase factor) $|\Psi\rangle = \cos(\Delta n\omega t/2)|V\rangle + i\sin(\Delta\omega t/2)|H\rangle$, where Δn is the difference in refractive index between the fast and slow axis of the waveplate, t is the time of propagation and ω is the optical frequency. We can describe this process by an unitary evolution operator U_ϕ such that $U_\phi|V\rangle = cos\phi|V\rangle + sin\phi|H\rangle$, where ϕ = Δnωt/2. When N such plates are placed in series, each causing a unitary evolution U_ϕ with ϕ = π/2N, the polarization state of the photon at the output become |H>, aside from an overall but inconsequential phase factor. Consider next a situation where these waveplates are interleaved with polarizers oriented along

the vertical axis, as shown in Figure 6.1[C]. The polarizers act as a measurement device, collapsing the state to be |V> with probability $\cos^2\phi$. In the limit N→∞, corresponding to continuous measurement, the final state will be the same as the initial state.

It is also instructive to analyze this process without invoking a quantum description of light. Specifically, we consider a classical light beam polarized in the $\hat{x}$ (vertical) direction at the input. After passing through a waveplate, the polarization state can be expressed as $\alpha\hat{x} + \beta\hat{y}$, with $|\alpha|^2 + |\beta|^2 = 1$, and α = cos(π / 2N) . It is now easy to see that after a series of N waveplates and polarizers, the output intensity can be expressed as $I_{out} = I_0[\cos^2(\pi/2N)]^N$ and in the limit N→∞, it can be verified that I_{out}→I_0, where I_0 is the initial intensity. This result seems to imply that there is a so-called "classical Zeno effect". This is erroneous, since the concept of a measurement induced reduction of a state is absent in the classical World. Instead, the process can be understood via the Quantum Zeno effect by considering a quantum model of a classical laser field (by which we mean a field with intensity much stronger than that of a single photon). Any such field (including, but not limited to the coherent state) can be expressed as a superposition of the Fock states: $|V\rangle = \sum_n \alpha\,|n\rangle$. Now, the analysis we presented above for a single photon can be applied to each Fock state. Thus, after passing though the series of N polarizers and waveplates, the polarization state remains the same. Therefore, QZE applies even if one does not explicitly consider the optical field quantum mechanically.

6.7.2 Optically controlled polarizer

It is well known that the polarization state of an optical field gets modified after propagating through an optically dense vapor medium, a manifestation of optical activity. In an atomic system involving ladder type transitions, the presence of two different frequencies open up the possibility of controlling the behavior of the probe (upper leg) polarization by careful design of the pump parameters (lower leg). In particular, it is possible to make the vapor cell act as a polarizer, oriented either vertically or horizontally depending on the polarization of the pump.

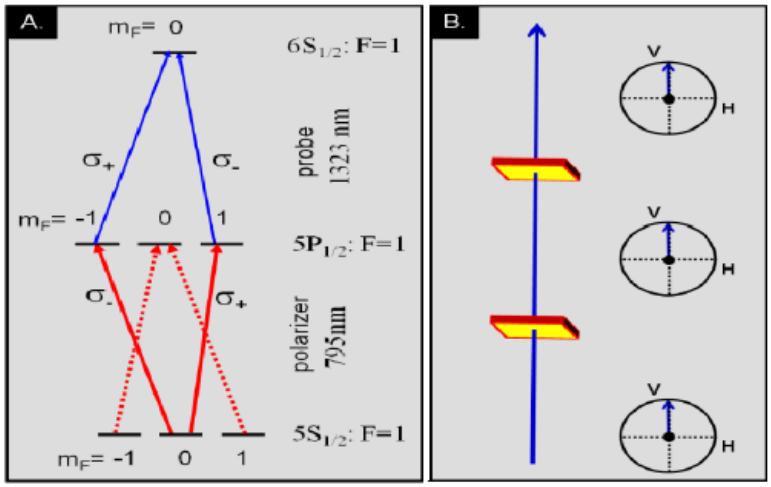

Figure 6.2 Schematic illustration of an optically controlled polarizer using a ladder transition in ^{87}Rb atoms

In Figure 6.2(a), we illustrate the basic mechanism for realizing such a polarizer, using a simplified set of transitions. We assume here that the atomic population is optically pumped into $5S_{1/2}$, F = 1, m_F = 0 Zeeman sublevel. Here, the control beam at 795 nm is resonant, and linearly polarized, in the horizontal direction, for example. This means that the two circular

components of the control beam, σ_+ and σ_-, are out of phase with each other. As such, these components will produce an out-of-phase superposition of the $m_F = -1$ and $m_F = 1$ Zeeman sublevels. Such a superposition would act as a non-absorbing (dark) state for the 1323 nm probe that is vertically polarized, since it has two circular polarization components (σ_+ and σ_-) that are in phase with each other. By the same token, this superposition will act as a strong absorber for a 1323 nm probe that is horizontally polarized. Thus, the presence of this control beam would make the system an ideal polarizer. Of course, experimental conditions result in non-ideal behavior and these are discussed in later sections.

6.7.3 QZE based all-optical logic gate

A QZE based optical logic gate can be realized if the polarizing effect generator is augmented by a wave-plate effect generator, as shown in Figure 6.3. Before we understand the working of the logic gate, it is instructive to understand how the waveplate effect is generated. Consider first the case where the lower leg is excited by the field which is detuned from resonance, and the fields on resonance arrows are turned off. The control field is now a right-circularly polarized (σ_+) beam at around 795 nm, tuned a few GHz below the $5S_{1/2}$, F = 1→ $5P_{1/2}$, F = 1 transition. We assume here that the atomic population is optically pumped into the $5S_{1/2}$, F = 1,m_F = 0 Zeeman sublevel. The control beam, therefore, produces an off-resonant excitations to only the $5P_{1/2}$, F = 1,m_F = 1 Zeeman sublevel in the intermediate state. The probe, at around 1323 nm, is chosen to be linearly polarized; therefore, it has two components: σ+ and σ-. As shown in the diagram, the σ- component sees the effect of the atoms (because of the

detuning, it sees only a real susceptibility, with virtually no absorption), while the σ+ component does not. The parameters of the control beam can be tuned to achieve the condition for a π phase-shift for the σ- component only, so that the polarization of the signal beam is rotated by 90 degrees. Theoretical and experimental investigations of controlled polarization rotation of a probe field using another optical field (pump) and employing ladder transitions in Rb have been carried out previously [81,82]. However, both of these employ the EIT effect where the upper leg is excited by a strong control field while the lower leg is probed by a weak optical field, and thus has fundamentally different characteristics than the system we have considered.

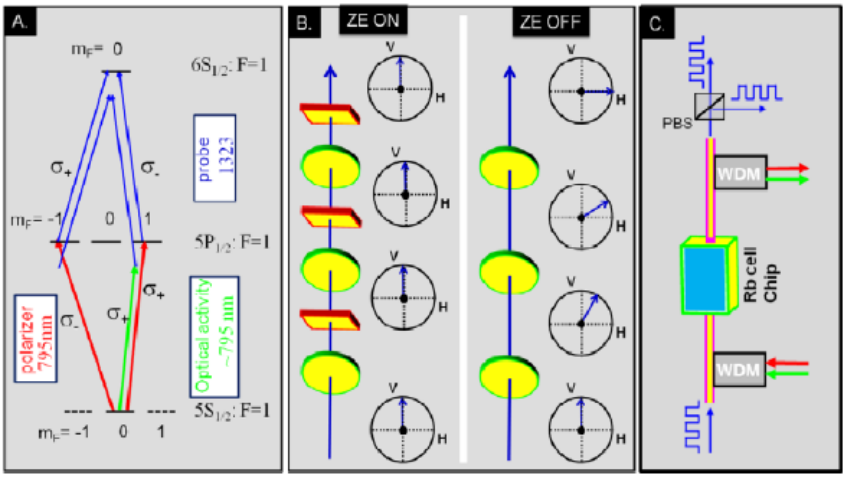

Figure 6.3 Schematic illustration of an optical logic gate using a ladder-transition based polarizer and optical activity in Rb atoms.

The red beams on the lower leg represent the control signal for the polarizer. The presence of this control beam results in selective transmission of one particular polarization of the signal beam (blue) and complete suppression of the orthogonal polarization, as explained previously. In order to understand the effect of applying both the green and red control beams

simultaneously, one should recall the model presented in Figure 6.1 for the QZE and the discussion that followed, where we considered N pairs of polarizers and polarization rotators, and showed that the polarization does not change as $N \rightarrow \infty$. The physical implementation described here operates in this limit. Even though both processes are occurring simultaneously, the net result is equivalent to infinitesimal evolutions where the processes alternate after each time step. When the polarizing effect generator is turned off, the polarization of the probe beam rotates by 90 degrees; when it is left on, the Zeno effect induced by the measurement due to the polarizer prevents the polarization of the probe beam from rotating, without any attenuation. This is illustrated in Figure 6.3(b). On the other hand, when the waveplate effect generator is turned off, the polarization state does not change at all. In Figure 6.3 (c), we show how this process can be used as an optical logic gate for a probe data stream. Briefly, using WDM couplers, all the control beams and the probe at 1323 nm are made to propagate through a Rb vapor cell. Another WDM coupler is used to filter out the beams at 795 before the final polarizing beam splitter (PBS) placed at the output. The two ports of the PBS serve as the two output channels of the gate. If the control beams represent a data stream with their presence and absence denoting the '1' and '0' state respectively, then it is easy to construct a truth table for the outputs at port 1 and 2 respectively as shown in Table 6.1.

Table 1. Truth table for QZE based logic gate

Polarizer	Waveplate	O/P at Port 1	O/P at Port 2
0	0	1	0
0	1	0	1
1	0	1	0
1	1	1	0
X	Y	X + Y'	X'Y

Table 6.1 Truth table for QZE based logic gate.

Thus, if the sense of the ‘1’ and ‘0’ states of the waveplate effect generator beam are reversed, output at port 1 simply implements an OR operation on the 2 inputs while if the same is done for the polarizer effect generator, output at port 2 implements an AND gate. Of course, the output at ports 1 and 2 are complementary, as expected for a PBS. Full implementation of such a logic gate requires the realization of both the polarizer effect and the waveplate effect in the same medium. However, given the complexity offered by an actual atomic system, we decided to investigate and optimize these two effects separately. In another paper, we present the details of our study of the waveplate effect. In this paper, we describe the details of our study of the optically controlled polarizer.

6.7.4 Stokesmetric imaging

It is well documented that in many situations of interest, features indiscernible via conventional imaging become highly resolved under Stokesmetric Imaging (SI) [83,84,85,86]. In a typical SI scenario, a target is illuminated by fully or partially polarized light. The light scattered or reflected by the target is then analyzed using a Stokesmeter, which determines the magnitude of each of the four Stokes parameter components. Stokesmeters, in their simplest form, are comprised of a combination of polarizers and wave-plates with different orientations. A key problem with the existing SI systems is that the polarizers and waveplates cannot be turned on or off or reoriented rapidly. The free space versions of the optically controlled

polarizers and waveplates that are described in this paper have the potential to operate at speeds of few MHz (limited by the decay rate of the intermediate level) and thus hold the promise of making very high speed SI practical.

6.8 Experiment

The experimental configuration we used to realize an optically controlled polarizer is shown is shown schematically in Figure 6.4. We used a conventional vapor cell, containing a natural mixture of both the isotopes of Rb. However, we used only ^{87}Rb for our experiment. Here, the control beam and signal beam are co-propagating. A similar set-up was used when the control beam and the signal beam were counter-propagating.

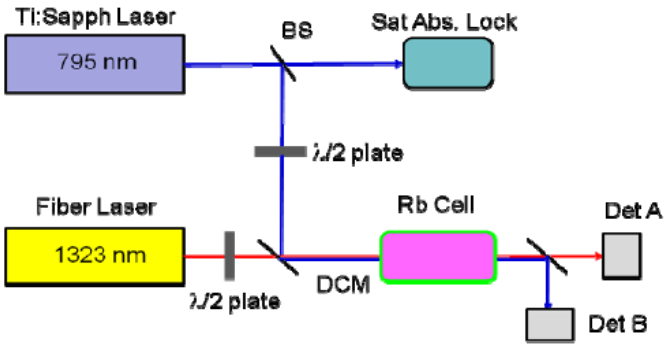

Figure 6.4 Experimental setup used to realize the ladder-system polarizer.

Briefly, beams from two tunable lasers (one at 795 nm, and the other at 1323 nm) were combined with a dichroic mirror (DCM). A part of the 795 nm light was sent to a reference vapor cell for saturated absorption spectroscopy and locking. The combined beams were sent through a vapor cell, shielded from magnetic fields with μ-metal. The cell was heated using bifiliarly wounded wires that do not add any magnetic fields. After passing through the cell,

another DCM was used to split the light into two parts, and each frequency was detected with a separate detector. The polarization of each input beam was controlled separately with two half waveplates. The control laser was locked to one of the lines on the $5S_{1/2} \leftrightarrow 5P_{1/2}$ manifold, while the signal laser at 1323 was scanned over the $5P_{1/2} \leftrightarrow 6S_{1/2}$ manifold. For the remainder of the paper, the hyperfine levels in the ground state are indicated by unprimed alphabets (F), those in the $5P_{1/2}$ level are primed (F') and those in the $6S_{1/2}$ level are double-primed (F").

Previously, we showed a simplified set of energy levels in order to explain the basic process behind an optically controlled polarizer. In practice, however, it is extremely difficult to realize such an ideal system. For example, it is generally necessary to take into account both the hyperfine levels (F' = 1 and F' = 2) in the $5P_{1/2}$ manifold to account for Doppler broadening and power broadening. Furthermore, it is virtually impossible to eliminate all the atoms from the $m_F = \pm 1$, F = 1 Zeeman sublevels via optical pumping. Hence, all the Zeeman sub-levels at the $5P_{1/2}$ manifold also get coupled with the optical fields. The full set of relevant energy levels that need to be considered are shown in Figure 6.5. In our model, we considered all the Zeeman sub-levels which explicitly interact with an optical field (all sublevels of the F=1, F'=1,2 and F"=1,2 hyperfine levels), while the F = 2 hyperfine level and the $5P_{3/2}$ level were only considered as population transfer levels and hence all their sub-levels were lumped together as a single level. The transition strengths [87] indicated are expressed as multiples of the weakest transition, which in our case is the transition from the F = 1, m_F = 1 sub-level to the F' = 1, m_F = 0 sub-level. In order to avoid unnecessary clutter, the matrix elements for the F' = 1 to F" = 1, 2 transitions and for the F' = 2 to F" = 1 transition are not shown. More details regarding the model are presented in the section 6.9. Initially, we carried out our experiments

without employing optical pumping. Later in the paper, we will discuss in detail how to implement optical pumping properly in order to optimize the performance of the polarizer.

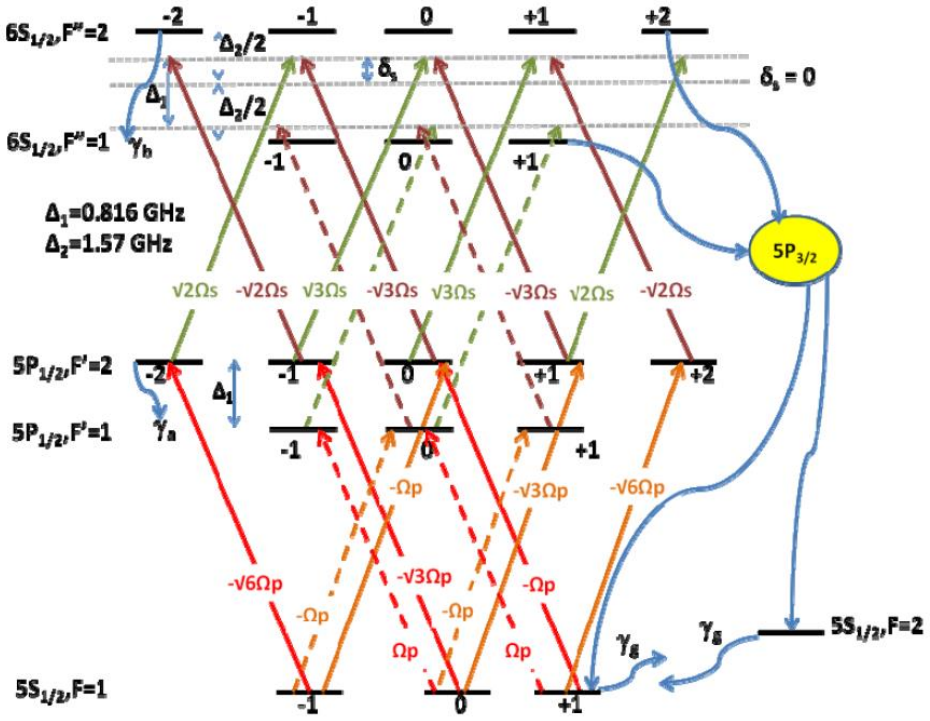

Figure 6.5 Model used for numerical computation. See text for more details.

Figure 6.6 (a) shows evidence of the polarizing property of the control beam as the signal beam was scanned across the $5P_{1/2} \leftrightarrow 6S_{1/2}$ manifold. The control beam was vertically polarized, co-propagating with the signal beam, had a power of ~5mW and was locked to the F = 1→F'= 2 line. The temperature of the cell was about ~200 Celsius. The blue (red) trace is the signal transmission when the signal beam is vertically (horizontally) polarized. The F" = 1 and F" = 2 labels indicate the transitions from the F' = 2 level, as the power of the control beam was not strong enough to produce excitations to the far detuned F' = 1 level. As is evident from Figure 6.6(a), signal transmission for the F' = 1 → F" = 1 increased significantly when the control beam and the signal beam are cross-polarized. The F' = 1 → F" = 2 transition showed

opposite behavior to the F'= 1→F"= 1 line in terms of the percentage of absorption. This is due to the fact that the matrix elements for the σ- transitions of the F' = 2 → F"= 2 line are of opposite sign as compared to the F'= 2 → F" = 1 line [87], and hence the σ- coherences pick up an additional phase difference of π, thus changing the sense of polarization from horizontal to vertical and vice-versa. The assumption in the preceding argument is that the significant contribution to the absorption of the signal beam is from the F' = 2 level, since the F' = 1 is highly detuned.

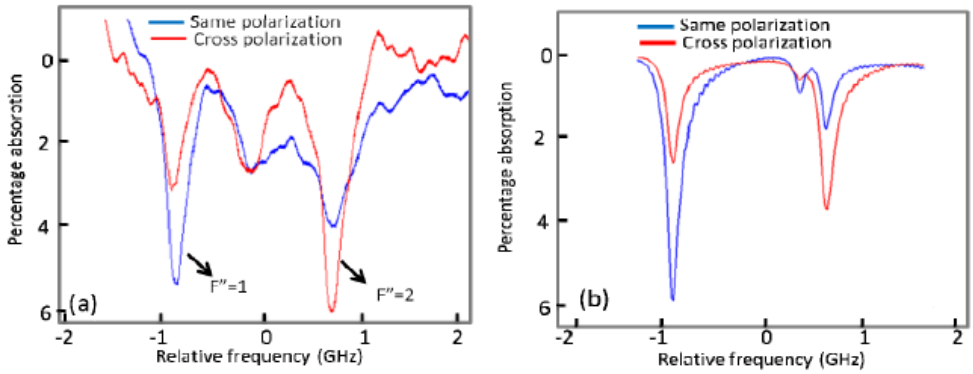

Figure 6.6 Polarizer effect for co-propagating geometry for pump power ~5mW a) Experiment b) Theory.

We obtain ~50% reduction in absorption for the F'= 2 → F"= 1 line and about ~70% reduction for the F" = 2 line. The background modulation is due to an etalon effect caused by the two windows of the cell, which were anti-reflection (AR) coated for 795 nm, but not for 1323 nm. In the future, the etalon effect could be eliminated by using a cell where the windows are not parallel to each other, along with AR-coating at 1323 nm. Figure 6.6(b) shows the corresponding numerical simulation and it is fairly consistent with our experimental result. For this particular simulation, the pump was slightly detuned below the F = 1→F'= 2 line and this

results in the appearance of an additional dip near the F" = 2 line, which is due to the F' = 1→F" = 2 line. Indeed, this feature does not appear if the pump laser is resonant with the F = 1→F' = 2 line or if the pump power is not sufficient to excite the atoms to the F'= 1 level. In the experimental data too there seems to be an additional dip in-between the two lines, which we believe may not be caused due to the etalon effect alone. As our simulations indicate, this additional feature might be due to a shift in the pump laser frequency resulting in excitations from the F' = 1 level, but a more thorough investigation is needed to resolve this apparent discrepancy. However, it should be noted that the device we propose would operate at one of the main absorption dips, rendering the central dip largely irrelevant.

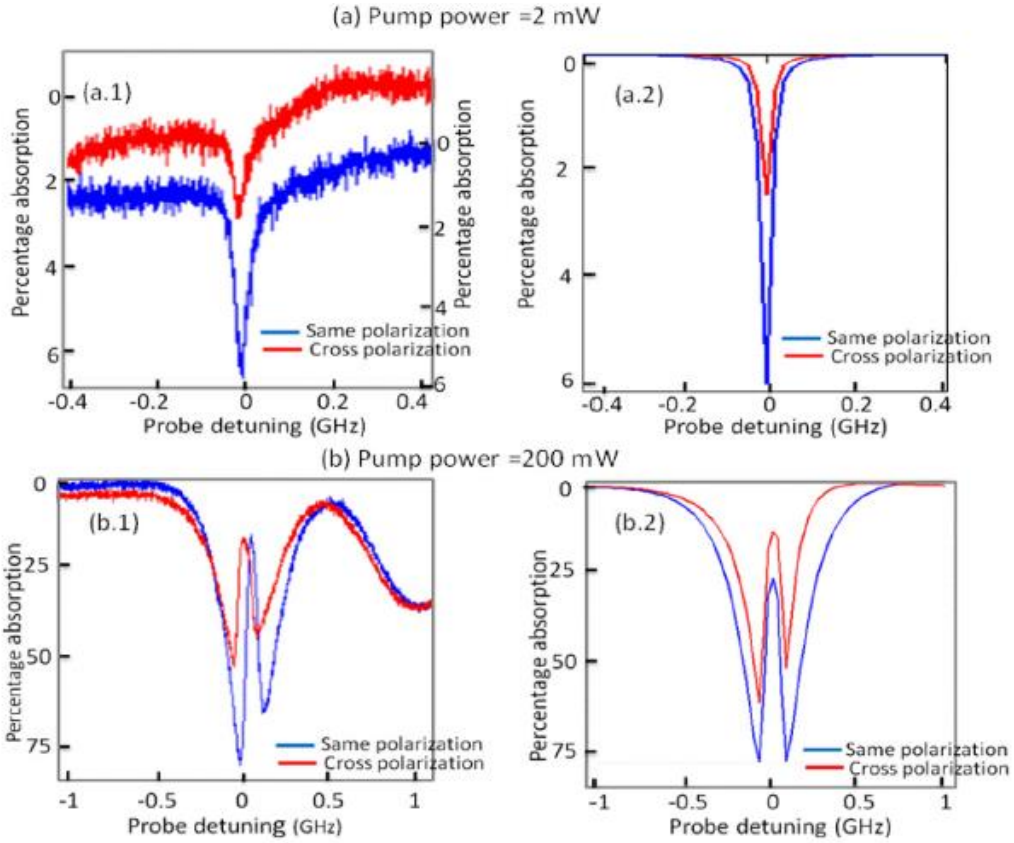

Figure 6.7 Polarizer effect for counter-propagating geometry for 2 different powers of the pump. a.1) Experiment a.2) Theory and b.1) Experiment b.2) Theory.

We also investigated the performance of the polarizer under a counter-propagating geometry. Figure 6.7 shows data for the F” = 1 transition obtained for two different power levels (~2mW and ~200mW) of the control beam and the corresponding numerical simulation. The F” = 2 transition also showed similar behavior and is not shown here for the sake of brevity.

It is useful to note a couple of differences in the observed signals between the co-propagating and the counter-propagating cases. Since we do not have experimental data under identical conditions (powers of the pump and the probe, temperature etc.) for the two geometries and our theoretical results are fairly consistent with our experimental data, we would present these differences using our simulation results. Figure 6.8 shows the simulation results for both geometries for a pump Rabi frequency of 5 (in units of the natural linewidth of the 5P manifold ~5.7 MHz) when both the control and the signal beams have the same polarization. As seen in Figure 6.8, the counter propagating geometry produces narrower (and deeper) absorption lines as compared to the co-propagating case. In addition, there is also an apparent splitting in the counter-propagating geometry which is absent in the co-propagating case. These differences based on geometry are due to what we refer to as pump power limited Doppler broadening (PPLDB) but we believe this issue is tangential to the focus of the work presented here and hence we discuss it in greater detail later.

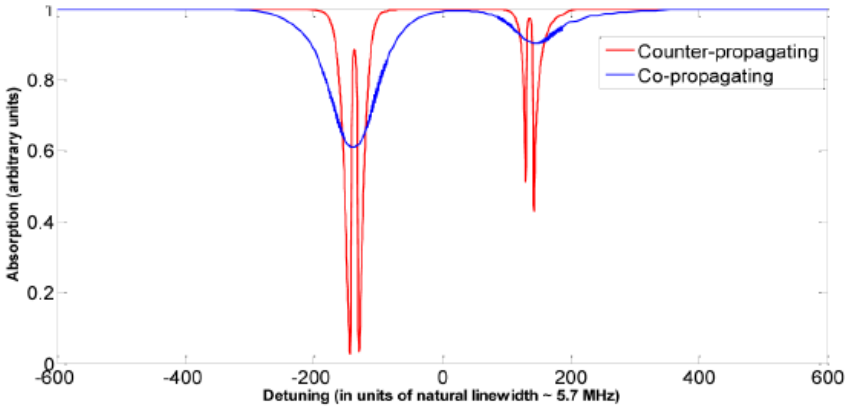

Figure 6.8 Typical absorption profile for co- and counter-propagating geometries. Here, $\Omega p = 5$.

Despite the significant differential absorption at virtually all power levels of the 795nm light, in order for our system to work as an ideal polarizer, we need nearly 100% suppression of one polarization versus nearly 100% transmission for the orthogonal polarization. Towards this end, we used our numerical model to identify the parameter space and experimental modifications needed to improve the contrast. We will first describe the model used before going to discuss the experimental modification necessary to achieve an acceptable contrast in probe absorption.

6.9 Simulation

Any analysis of the polarizer proposed above would require careful monitoring of the populations and coherences of the various Zeeman sub-levels involved in the system. A detailed diagram of all the relevant levels considered along with the relative transition strengths has been presented in Figure 6.5. Due to power broadening, the $5P_{1/2}$, F' = 1 hyperfine level

interacts with both the control and the signal optical fields (indicated by dashed lines), albeit at a large detuning, and these interactions have been taken into account in our model. However, we ignored the coherent coupling between F = 2 and the $5P_{1/2}$ manifold, because of the large frequency difference between F = 1 and F = 2 (~6.8GHz for ^{87}Rb). Also, while the control beam is shown to be resonant in Figure 6.5, ours is a general model where the control beam can be detuned from the F' = 2 level by an arbitrary value, say δ_p.

All the Zeeman sub-levels in the $5P_{1/2}$ ($6S_{1/2}$) manifold are assumed to decay at the same rate, γ_a~5.75 MHz (γ_b~3.45 MHz). We also assume a nominal cross-relaxation rate (γ_g ~0.1 MHz) between F = 1 and F = 2 hyperfine levels. Figure 6.9 shows the various decay channels and branching ratios in the system. Here, the individual decay rates between the Zeeman sublevels are not explicitly shown but only the branching ratios between the hyperfine levels, which were obtained by summing the decay rates of all possible transitions between the corresponding hyperfine levels. The decay rate between any two Zeeman sub-levels was calculated by assuming it to be proportional to the square of the matrix element of the corresponding transition, such that the sum of all such decays rates from the decaying level equaled the net decay from that level. For example, consider m_F = 0, F' = 2 sub-level which decays at a rate γ_a. The transition strengths for the σ+, σ-, and π-transitions to the F = 1 (F = 2) are in the ratio 1:1:2 (√3:√3:0). Thus, the net decay rate between the mF = 0, F'= 2 sub-level to the m_F = −1, + 1 and 0 states of the F = 1 level were computed to be γ_a/12, γ_a/12 and γ_a/3 respectively and the decay to the F = 2 level was computed to be γ_a/2, since all the hyperfine levels in the F = 2 state are lumped together as a single state in our model. We have also taken into account the sourcing of atoms into the ground states from the $6S_{1/2}$ state via the $5P_{3/2}$ state

(shown by dashed lines in Figure 6.9). For our computations, these additional source terms were modeled using an "effective decay rate" directly from the hyperfine levels in the $6S_{1/2}$ state to the $5S_{1/2}$ manifold. A detailed calculation, taking into account the various branching ratios into and from all the hyperfine levels of the $5P_{3/2}$ state was used to determine these rates. However, the decay rate of each of the individual Zeeman sub-level in the $6S_{1/2}$ state was not considered, rather it was assumed that all of them decayed equally to the Zeeman sub-levels of F = 1 and F = 2 levels at the respective "effective decay rates" previously determined. The ratio between the decay rates into the $5P_{1/2}$ and $5P_{3/2}$ state from the $6S_{1/2}$ state was simply decided by the ratio of the explicit values of the transition strength of the D1 and D2 lines [87].

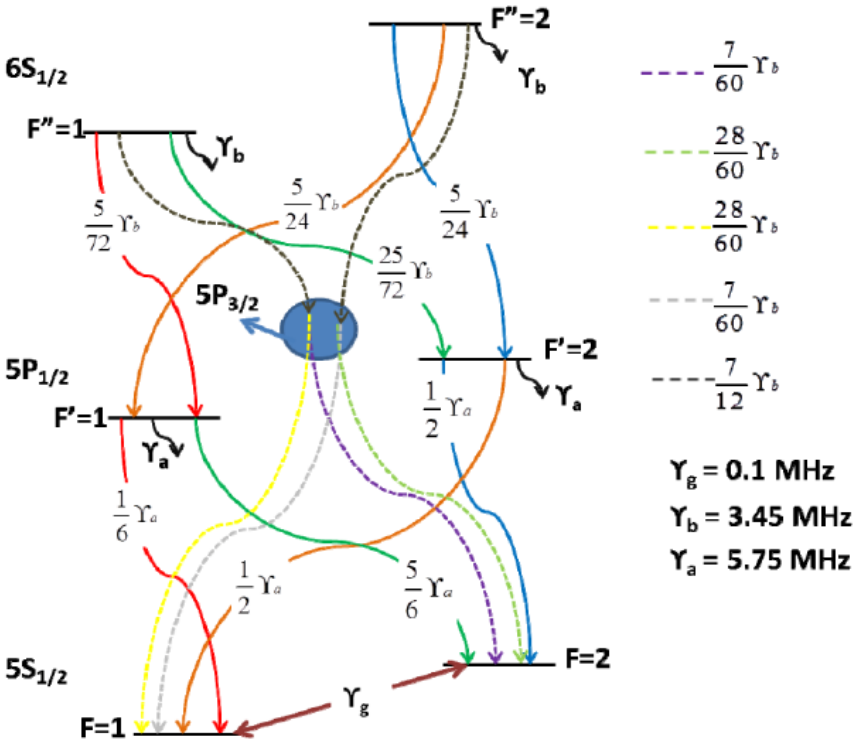

Figure 6.9 Decay rates and branching ratios between various levels in our model.

In addition to keeping track of the signs of the matrix elements involved in the transitions

between the Zeeman sub-levels, it is also important to keep track of the explicit phase associated with the optical fields. In most cases, this phase can be factored out while transforming the Hamiltonian to the rotating basis. However, if any level has multiple pathways for excitation such that the pathways form a closed loop architecture, it is not possible to transform all the phases out of the Hamiltonian. Upon transformation to the rotating basis, this results in the appearance of a so called "closed-loop phase" on one of the legs of the Hamiltonian which cannot be eliminated by any transformation, as shown in Figure 6.10. In fact, changing the polarization of either the signal beam or the control beam from horizontal to vertical results in changing this closed-loop phase by π and thus the study of the Polarizer effect essentially boils down to studying the behavior of the system as this closed-loop phase is switched between 0 and π.

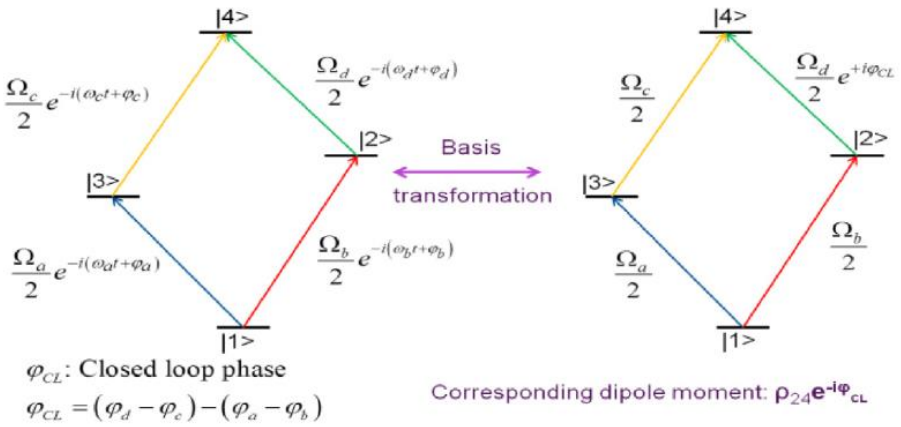

Figure 6.10 Effect of closed-loop architecture resulting from multiple excitation pathways between two levels.

In our model, we have up to a maximum of 20 levels. We used the Liouville equation, which describes the evolution of the density matrix in terms of a commutator between the

density matrix and the Hamiltonian, to obtain the steady-state solution. The usual method of vectorizing the density matrix and then inverting the coefficient matrix thus obtained, is not easy to handle as the size of the coefficient matrix is very large (400*400). In order to overcome this problem, we developed a novel algorithm which would compute the said coefficient matrix automatically, given the Hamiltonian and the source matrix. Briefly, we set each of the elements of the density matrix to unity one at a time while setting all the others to zero and repeatedly compute the commutator between the density matrix and the Hamiltonian. Once this procedure is repeated over all the elements of the density matrix, we would have computed the coefficient matrix. The source terms, as well as any other dephasing terms (such as collisional dephasing) are added in finally as a constant matrix. Details regarding the algorithm are to appear in a separate paper, which is currently under review [16].

While averaging over the Doppler profile, we used the supercomputing cluster at Northwestern (QUEST) to perform our computations. Using 64 cores and computing the steady state solution for 512 values of detuning, each averaged over 800 points of the Doppler profile, we obtained the steady-state solution for our 20-level system in 3-4 minutes. With a smaller system, say for a 15-level system, we obtained the solution in a few seconds. Some of the results, thus obtained, have already been reproduced in Section 6. For all the simulations, a temperature of 500 Kelvin was used and the density of atoms was taken to be ~$10^{11}/cm^3$.

6.10 Improvements to system and future work

In general, the quality of a polarizer is characterized by its extinction ratio, η, defined as

the ratio of the transmitted intensity of light with its state of polarization (SOP) parallel to the transmission axis to the transmitted intensity of the same beam of light with its SOP perpendicular to the transmission axis. The minimum value of η that might be acceptable depends on the signal to noise ratio (SNR) desired in a particular application. For the SI application, for example, an SNR of about 5 would suffice, according to the Rose criterion [88]. For the optical logic gate, the SNR requirement could be even lower. This would translate directly to the η that can be achieved in our polarizer, assuming other sources of noise are negligible. The best case, shown in Figure 6.7(b) corresponds to an η ~2.5. The value of η can be increased significantly by using higher optical densities of the Rb medium (resulting in very high absorption of light polarized perpendicular to the transmission axis) but this would also result in lowering of the transmission of light polarized along the transmission axis of the polarizer. Thus, the requirement of a high value of η needs to be balanced against maximum achievable transmission and this would again depend on the particular application at hand.

In order to increase the extinction ratio of our all-optical polarizer without sacrificing the maximum transmission achievable for a beam of light polarized along the transmission axis, it is necessary to make modifications to our system. One of the non-idealities in our system is that all the Zeeman sublevels in the F = 1 state are populated due to decay from various channels. Since the transition between the F = 1, $m_F = 0$ and the F' = 1, $m_F = 0$ Zeeman sublevels is forbidden, application of a π-polarized optical pumping beam between the F = 1 and F' = 1 states would pump the atoms into the F = 1, $m_F = 0$ state, as required. However, we note that a π-transition is allowed between the F = 1, $m_F = 0$ and F' = 2, $m_F = 0$ Zeeman sublevels. Hence, if the interaction of the π-beam with F' = 2 in considered, it is not possible to obtain a

time-independent Hamiltonian after switching to a rotating basis. In order to circumvent this complication, we made the simplifying assumption that the π-beam excites only the F = 1→F' = 1 transition. Although not necessary, we also assumed that the control beam only interacts with the F' = 2 level. Given the separation (0.816 GHz) between the F' =1 and F' = 2 levels, these assumptions are valid for the power levels used in our simulation, as detailed later. The π-beam, expanded using a cylindrical lens and locked to F = 1 → F' = 1 transition, needs to be brought in through a slot running parallel to the length of the Rb Cell. However, application of this pumping beam alone is not sufficient, as there is decay from the intermediate (5P) levels into the F = 2 state, which is another non-ideality in our system. This mandates the need for another optical pumping beam from the F = 2 state to the $5P_{3/2}$ state. The net effect of this additional pumping beam was modeled as an increased decay rate from the F = 2 to F = 1 state. The maximum decay rate obtainable by the application of such a beam is γ_a, the radiative decay rate of the $5P_{3/2}$ manifold. We further note that the ratio of steady-state populations in the F = 1 and F = 2 states (in the absence of any field) can be estimated to be ~γ_a/γ_g, where γ_a is the nominal decay rate from the F = 1 to F = 2 state. It is clear that we can increase the population in the F = 1 state by further decreasing γ_g, and this can be accomplished by using a buffer gas loaded cell. Figure 6.11 shows our model after the afore-mentioned changes are incorporated. As noted previously, to avoid unnecessary clutter, not all transition strengths are shown.

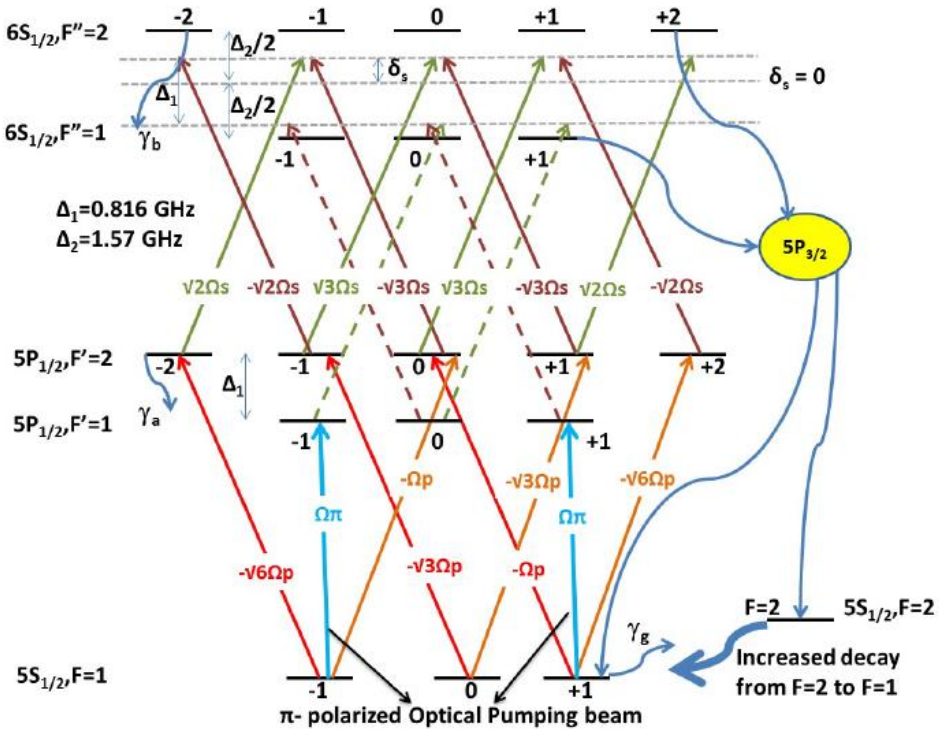

Figure 6.11 Modified model after addition of optical pumping beams and buffer gas.

A typical simulation result obtained by employing the modified system is shown in Figure 6.12. Again, only the F' = 2 → F" = 1 transition is shown for the sake of brevity. As is evident from Figure 6.12, at zero detuning, a signal beam with the same polarization as the control beam is almost completely absorbed (0.00001% transmission) while nearly 90% of an orthogonally polarized beam is transmitted, corresponding to an η~105, comparable to the best commercially available polarizers. For this particular simulation, we used the co-propagating geometry, the decay rate from the F = 2 to F = 1 state was set to be equal to the decay rate of the 5P manifold while the decay rate in the opposite direction was set (reduced due to buffer gas) to about 10 KHz. The Rabi frequencies of the control beam and the optical pumping beam were set to be 0.5 and 10 (in units of the natural linewidth of the 5P manifold γ_a~5.7 MHz), respectively. The density of atoms was taken to be 10^{11}/cm^3 and the temperature was set to

500K.

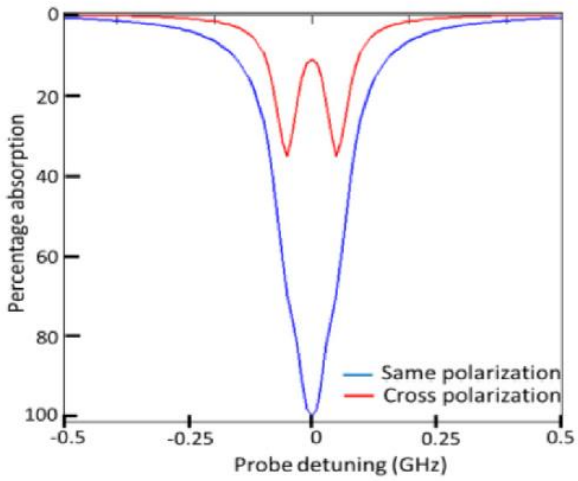

Figure 6.12 Numerical simulation of polarizer effect in the presence of two optical pumping beams and using a buffer gas loaded cell.

It should be possible to realize such a polarizer at a very low light level, using a tapered nanofiber (TNF) embedded in Rb vapor [7,8,9,10]. In a TNF, the typical mode area is ~0.2 μm^2. Thus, assuming a saturation intensity of 3mW/cm^2, a Rabi frequency of 10γ_a would correspond to a power of only ~1 nW. Unlike the free space case, the maximum speed of operation in the TNF system would be limited by the transit time broadening (~60 MHz) rather than the natural linewidth of the 5P manifold (~6 MHz). To see why, note that the speed is limited by the rate at which atoms in the intermediate state relax to the ground state [89] and for a TNF system, this rate is effectively determined by the transit time. Finally, we note that the TNF system may be suitable only for demonstrating an all-optical logic gate but not for SI, for which the free space version of the polarizer is better suited. Significant changes to the set-up are required in order to implement the improved scheme both in free space and in the TNF system. Efforts are

underway in our laboratory towards making these modifications and we intend to report on the progress and results in the near future.

CHAPTER 7 OPTICALLY CONTROLLED WAVEPLATE

7.7 Schematic

In an atomic system involving ladder type transitions, the presence of two different frequencies open up the possibility of controlling the behavior of the probe (upper leg) polarization by careful design of the pump parameters (lower leg). In particular, it is possible to make the vapor cell act as a waveplate. The mechanism for producing controlled polarization rotation, is illustrated schematically in Figure 7.1, using a cascaded atomic transition involving four levels where direct excitation to the upper level from the ground state is dipole forbidden. We consider the $m_F = 0$ Zeeman sublevel of a certain hyperfine level into which the atoms have been optically pumped, as the ground state. The lower leg is excited by a highly off-resonant right-circularly polarized beam (control/pump beam), that produces excitations to only the $m_F = 1$ Zeeman sublevel in the intermediate state. The signal beam (probe), applied between the intermediate level and the upper level, is linearly polarized with the polarization axis orthogonal to the quantization axis, and excites the $\sigma+$ and $\sigma-$ transitions on the upper leg. Here, we have assumed that (a) the light beams are propagating in the direction of quantization, and (b) that light is defined to be right (left) circularly polarized if, when looking along the direction of the Poynting vector, the electric field vector appears as rotating in the clock-wise (counter clock-wise) direction. It should be noted that some text books and papers follow the opposite convention, under which what we are calling right-circular polarization would be called left-circular polarization, while others follow the convention we are using here. Further, if the traveling wave laser field is propagating opposite to the direction of quantization, the m_F

= 0 → m_F = 1 transition is excited by a left circularly polarized light according the convention we have used. We assume that the frequency of the signal beam is very different from that of the control beam, so that the signal beam only couples to the upper leg, and the control beam only couples to the lower leg. The off-resonant control beam produces a light shift of the m_F = 1 Zeeman sublevel in the intermediate state. If the frequency of the signal beam is chosen to be such that its detuning (from the unperturbed frequency of the upper leg transition) is significantly different from this light shift, then the component of the probe which excites the σ- transitions sees the effect of the pump, and sees only a real susceptibility with virtually no absorption, while the component exciting the σ+ transitions does not see any effect of the pump. The parameters of the control beam can be tuned to achieve the condition for a π phase-shift for the σ- component only, so that at the output the linear polarization is rotated by 90 degrees.

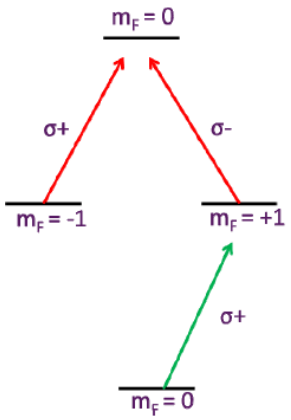

Figure 7.1 Schematic illustration of an optically controlled polarization rotator using circularly polarized control beam.

It should be noted that the above schematic can only be used as a polarization rotator for a linear polarization of the probe. For example, it can be seen that it is impossible to obtain a

purely circular polarization of the probe (without any loss), as it would require complete absorption on one of the legs of the upper transition. In fact, a simple Jones matrix analysis of the above system (in the absence of absorption) shows that the polarization state of the probe is $sin\phi\hat{x} + cos\phi\hat{y}$, where φ is the phase difference introduced between the two legs of the signal beam. In order for the system to behave as a quarter wave plate, for example, one needs to apply a linearly polarized pump. As shown in Figure 7.2, in this scenario, both the $m_F = +1$ (|2>) and $m_F = -1$ (|3>) states get coupled to the $m_F = 0$ (|1>) state and the effect produced is not transparent in the simple schematic discussed above. However, by a suitable rotation of the intermediate states, one can reduce the process to a similar scenario, where for any arbitrary polarization of the pump, only one of the intermediate states is coupled, while the other is decoupled. Explicitly, any arbitrary polarization of the pump can be represented as $\hat{\sigma}_+ + \beta\hat{\sigma}_-$, where α and β can be complex. This couples |1> to α*|2> + β*|3> (denoted as |+ >), where '*' denotes complex conjugation. The orthogonal state, |1> = α|3>-β|2>, is not coupled by the pump, as can be verified by explicit calculation. A similar analysis can be carried out for the probe field as shown in Figure 7.2. Now the situation is formally identical to the one presented in Figure 7.1, where one of the legs sees the effect of the pump while the other does not.

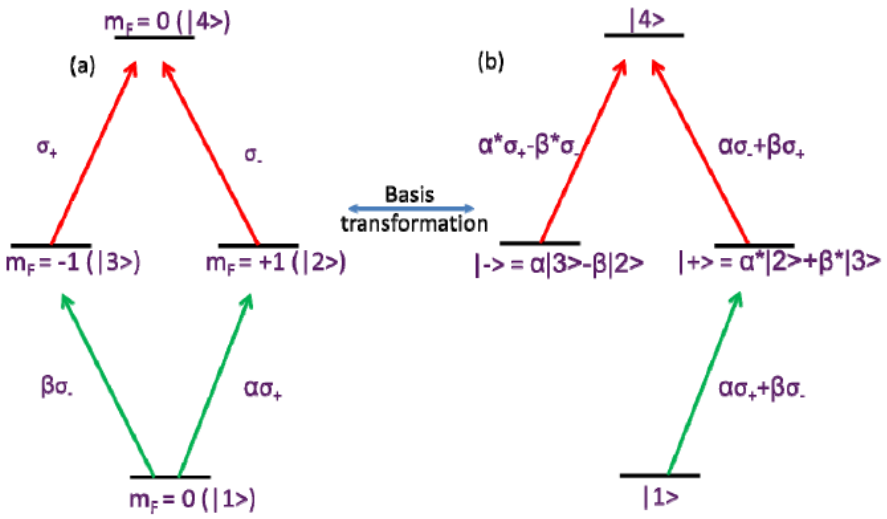

Figure 7.2 Generalized schematic of an optically controlled waveplate using control beam of arbitrary polarization.

For illustrative purposes, let us consider a probe polarized along the $\hat{y}$ direction. Denoting $\hat{\sigma}_- = \hat{x} - i\hat{y}/\sqrt{2}$ and $\hat{\sigma}_+ = -\hat{x} - i\hat{y}/\sqrt{2}$, one obtains $\hat{y} = i(\hat{\sigma}_- + \hat{\sigma}_+)/\sqrt{2}$. Decomposing $\hat{y}$ in terms of the rotated basis and introducing a phase shift φ on the field coupling the | + > state to |4>, one obtains the following expression for the polarization state $\hat{p}$ of the probe-

$$\hat{p} = i\left[\left(\alpha^* + \beta^*\right)\left(\alpha\hat{\sigma}_- + \beta\hat{\sigma}_+\right)e^{i\phi} + \left(\alpha - \beta\right)\left(\alpha^*\hat{\sigma}_+ + \beta^*\hat{\sigma}_-\right)\right]/\sqrt{2}$$
$$= i\left[\left(\left(|\alpha|^2 + \beta^*\alpha\right)e^{i\phi} + \left(|\beta|^2 - \beta^*\alpha\right)\right)\hat{\sigma}_- + \left(\left(|\beta|^2 + \alpha^*\beta\right)e^{i\phi} + \left(|\alpha|^2 - \alpha^*\beta\right)\right)\hat{\sigma}_+\right]/\sqrt{2} \quad (7.1)$$

Using appropriate values of α, β and φ, one can obtain circular polarization. For example, consider a pump polarized linearly at 45°, for which α = i/(i-1) and β = 1/(i-1). If we now set φ = π/2, one obtains $\hat{\sigma}_+$ polarization for the probe, as can be verified by explicit substitution in Eqn. 7.1. In its most general form, the probe can also be in some arbitrary polarization state. All one needs to do is to resolve it in terms of the new rotated orthogonal states and introduce a phase shift on one of the legs, leaving the other unaffected. By a suitable choice of the pump

polarization, one can place the probe in any desired polarization state.

In our set-up, we utilized the $5S_{1/2}$-$5P_{1/2}$-$6S_{1/2}$ cascade system in ^{87}Rb atoms, with F = 2 as the ground state. The pump and probe beams are at 795 nm and 1323nm respectively. The primary reason for choosing the upper leg as the probe is the need for an all-optical switch at a telecommunication wavelength. In Figure 7.1 and Figure 7.2, we showed a simplified set of energy levels in order to explain the basic process behind an optically controlled waveplate. In practice, however, it is extremely difficult to realize such an ideal system. We first note that it is virtually impossible to optically pump all the atoms into the , $5S_{1/2}$, F = 2, m_F = 0 Zeeman sublevel. Hence, Zeeman sub-levels other than $m_F = \pm 1$ at the $5P_{1/2}$ manifold also get coupled with the pump and probe optical fields. Furthermore, it is generally necessary to take into account both hyperfine levels (F' = 1 and F' = 2) in the $5P_{1/2}$ manifold to account for Doppler broadening and power broadening. Thus, the full set of energy levels that need to be considered is quite large, and the actual model employed for our system is discussed in the next section. For the remainder of the paper, the hyperfine levels in the ground state are indicated by unprimed alphabets (F), those in the $5P_{1/2}$ level are primed (F') and those in the $6S_{1/2}$ level are double-primed (F").

7.8 Simulation

In previous analyses of similar systems (CHAPTER 6), a simple model consisting of only the relevant hyperfine levels transitions was employed [81,82]. Other works [90,91] consider some of the Zeeman sub-levels, but make use of few assumptions to eliminate some of the

density matrix elements to arrive at a somewhat approximate result. In our model, we considered all the Zeeman sub-levels which explicitly interact with an optical field (all sub-levels of the F = 2, F' = 1, 2 and F'' = 1 hyperfine levels), while the F = 1 hyperfine level and the $5P_{3/2}$ level were only considered as population transfer levels and hence all their sub-levels were lumped together as a single level. The full set of energy levels that we have incorporated in our model are shown in Fig. 7.3. The transition strengths [87,64,92] indicated are expressed as multiples of the weakest transition, which in our case is the transition from the F = 2, $m_F = 0$ sub-level to the F' = 1, $m_F = 1$ sub-level, for example. We assume that the control beam is tuned below the F = 2→ F' = 1 transition while the signal beam is detuned by an amount δs from the F' = 1 → F'' = 1 transition. Due to the Doppler width and power broadening, the F' = 2 hyperfine level also interacts with both the control and the signal optical fields (indicated by dashed lines), albeit at a large detuning, and these interactions have been taken into account in our model. However, we ignored the coherent coupling between F = 1 and the $5P_{1/2}$ manifold, because of the large frequency difference between F = 1 and F = 2 (~6.8GHz for ^{87}Rb).

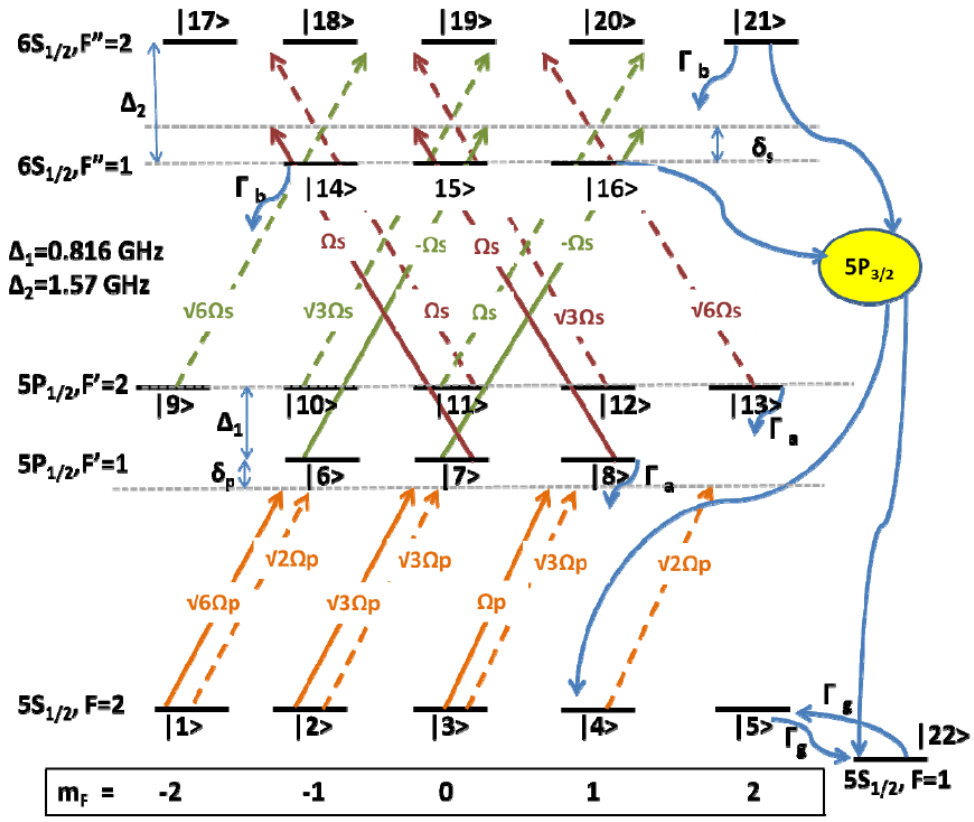

Figure 7.3 Model used for numerical computation. See text for more details.

All the Zeeman sub-levels in the $5P_{1/2}$ ($6S_{1/2}$) manifold are assumed to decay at the same rate, γ_a~5.75 MHz (γ_b~3.45 MHz). We also assume a nominal cross-relaxation rate (γ_g ~0.01 MHz) between the ground states. The decay rate between any two Zeeman sub-levels was calculated by using the fact that it is proportional to the square of the matrix element of the corresponding transition, and that the sum of all such decays rates from the decaying level must equal the net decay from that level. For example, consider m_F = 0, F' = 2 sub-level which decays at a rate γ_a. The transition strengths for the σ+, σ-, and π-transitions to the F = 2 (F = 1) are in the ratio√3:√3:0 (1:1:2). Thus, the net decay rate between the mF = 0, F'= 2 sub-level to the mF = −1, + 1 and 0 states of the F = 2 level were computed to be $\gamma_a/4$, $\gamma_a/4$ and 0

respectively and the decay to the F = 1 level was computed to be $\gamma_a/2$, since all the hyperfine levels in the F = 1 state are lumped together as a single state in our model. We have also considered the sourcing of atoms into the ground states from the $6S_{1/2}$ manifold via the $5P_{3/2}$ state. A detailed calculation, taking into account the various branching ratios into and from all the hyperfine levels of the $5P_{3/2}$ state was used to determine these "effective decay rates" directly from the $6S_{1/2}$ states to the ground states. Table 7.1 shows these "effective decay rates" from each of the Zeeman sub-levels in the $6S_{1/2}$ manifold to the ground states. The ratio between the rates of decay into the $5P_{1/2}$ and $5P_{3/2}$ states from a given upper level was decided by the ratio of the explicit values of the transition strength of the D1 and D2 lines.

Table 1. Effective Decay rates between excited states and ground states

		F" = 2					F" = 1		
	m_F	-2	-1	0	1	2	-1	0	1
	-2	0.68852	0.19426	0.05055	0	0	0.2361	0.09722	0
	-1	0.19426	0.47296	0.190277	0.07583	0	0.1667	0.11805	0.04861
F = 2	0	0.05055	0.190277	0.45166	0.190277	0.05055	0.104167	0.125	0.104167
	1	0	0.07583	0.190277	0.47296	0.19426	0.04861	0.11805	0.1667
	2	0	0	0.05055	0.19426	0.68852	0	0.09722	0.2361
	-1	0.04722	0.03333	0.02083	0.009722	0	0.21296	0.1226875	0.1088
F = 1	0	0.01944	0.023611	0.025	0.023611	0.01944	0.1226875	0.199	0.1226875
	1	0	0.009722	0.02083	0.03333	0.04722	0.1088	0.1226875	0.21296

Table 7.1Effective decay rates between excited states and ground stats.

It should be noted that in our model we have not taken into account the fact that the atoms spend a finite amount of time in the laser beam, which is the transit time effect. Given the size of the beam diameter (about 0.05 mm in the focused spot), the transit time for the atoms with a mean velocity of ~350 m/s is about 140 nanoseconds, corresponding to a transit time broadening of about 1 MHz. The transit time is thus much larger than the time needed for the system to reach steady state, which is of the order of the radiative decay times (~30 nsec) of the excited states. It is, therefore, reasonable to use a steady state solution, without taking into

account the transit time effect. The effect of the transit time broadening can be taken into account by increasing the natural linewidth (~6 MHz) via addition of the transit time linewidth (~1 MHz) to it. However, given that this broadening would change the linewidth by less than 20%, this is not likely to have a significant effect on the results. An elaborate model for a laser excitation of an atomic transition in a vapor cell where the effect of the transit time is taken into account via rate equations can be found in [93] and [94]. In the near future, we will carry out a more comprehensive analysis of our system by applying this formalism. We used the Liouville's equation, which describes the evolution of the density matrix in terms of a commutator between the density matrix and the Hamiltonian augmented by the phenomenological determined decay rates, to obtain the steady-state solution. The usual method of vectorizing the density matrix and then inverting the coefficient matrix thus obtained, is not easy to handle as the size of the coefficient matrix is very large (400*400). In order to overcome this problem, we made use of a novel algorithm, recently developed by us [16] which would compute the said coefficient matrix automatically in a very efficient manner, given the Hamiltonian and the source matrix. While averaging over the Doppler profile, we used the supercomputing cluster at Northwestern (QUEST) to perform our computations. Using 64 cores and computing the steady state solution for 512 values of detuning, each averaged over 800 points of the Doppler profile, we obtained the steady-state solution for our 22-level system in 3-4 minutes.

7.9 Experiment

We investigated the system when the pump and the probe are both co-propagating and

counter-propagating. The experimental configuration for the co-propagating geometry is illustrated schematically in Figure 7.4. Briefly, beams from two tunable lasers (one at 795 nm, and the other at 1323 nm) are combined with a dichroic mirror (DCM). A part of the 795 light is sent to a reference vapor cell for saturated absorption spectroscopy and locking. The combined beams are sent through a vapor cell, shielded from magnetic fields with μ-metal. The cell is heated using bifiliarly wounded wires that do not add any magnetic fields. After passing through the cell, the two beams are separated using another DCM, and each frequency is measured with a separate detector. The set-up for the counter-propagating version is similar (not shown). The control beam at 795 nm, which is polarized linearly initially, is passed through either a quarter-wave-plate or a half-wave plate in order to produce the desired polarization. The polarization of the signal beam, at 1323 nm, is controlled separately with a half-wave-plate. Ideally, the 1323 nm laser would also be locked at a particular frequency but this laser was found to be stable, so that locking it was not necessary.

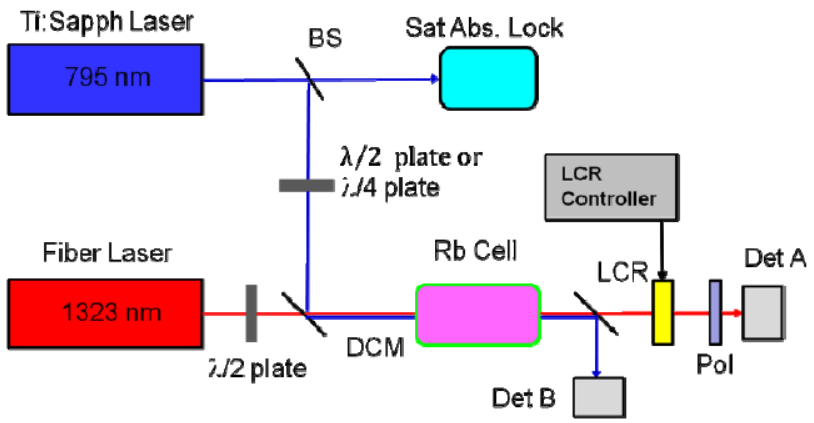

Figure 7.4 Experimental set-up.

In order to determine the polarization of the signal beam after passing through the cell, we inserted an analyzer before detector A, consisting of a voltage-controlled liquid crystal retarder (LCR), whose fast axis is placed at 45 degrees to the initial polarization direction (say $\hat{y}$) of the signal beam, followed by a polarizer with its axis orthogonal to initial polarization of the signal beam. Having only an orthogonal polarizer at the output is, in general, not enough, as one cannot determine if the observed signal is a manifestation of polarization rotation alone or a combination of both rotation and absorption, unless of course the detector signal is at least as large as the far off-resonant signal. However, it can serve as a diagnostic tool in identifying the regions of large phase shift as the probe is scanned across the $6S_{1/2}$ manifold. The LCR produces a phase retardance between its orthogonal axes that depends non-linearly on the amount of voltage applied to the LCR controller which can be determined from a calibration curve provided by the manufacturer and verified independently by us. During our experiment, the control voltage to the LCR is scanned linearly from 0 V to 10 V, with 2 V and 8V corresponding to a phase shifts of approximately π and 0, respectively for the wavelength that we are using. This particular arrangement of the analyzer provides us with a very large set of data points (corresponding to the LCR scan) from which to obtain the values of absorption coefficients and the phase rotation. The signal observed at the detector A can be ascertained by performing a Jones matrix analysis of the entire system, which is discussed next.

Jones matrix analysis

Let E_{in} be the signal field amplitude before the Rb cell and let $\hat{y}$ be its polarization direction. We assume the direction of propagation of the probe to be the quantization direction.

Let $\hat{\sigma}_+ = -(\hat{x} + i\hat{y})/\sqrt{2}$ and $\hat{\sigma}_- = (\hat{x} - i\hat{y})/\sqrt{2}$ be the unit vectors corresponding to right (RCP) and left circular polarizations (LCP) respectively. Then, E_{in} can be represented in the circular polarization basis as $\vec{E}_{in} = E_0\hat{y} = E_{in+}\hat{\sigma}_+ + E_{in-}\hat{\sigma}_-$, where $E_{in+} = E_{in-} = iE_0/\sqrt{2}$ and E_0 is some arbitrary value. The field amplitude after the cell can be represented, in its most general form as

$$\vec{E}_{out} = E_{in+}e^{(-\alpha_+ + j\phi_+)}\hat{\sigma}_+ + E_{in-}e^{(-\alpha_- + j\phi_-)}\hat{\sigma}_- \tag{7.2}$$

where (α_+, φ_+) and (α_-, φ_-) are the attenuations and phase rotations for the RCP and LCP part of the signal beam respectively after passing through the Rb vapor cell. With $\hat{x}$ and $\hat{y}$ as the basis for the Jones vector representation and after some algebraic manipulation, we find that the field amplitude after the cell can be represented as

$$\vec{E}_{out} = i\frac{E_0}{2}e^{(-\alpha_- + j\phi_-)}\begin{bmatrix} -e^{(-\alpha_d + j\phi_d)} + 1 \\ -i(e^{(-\alpha_d + j\phi_d)} + 1) \end{bmatrix} \tag{7.3}$$

where $\alpha_d = \alpha_+ - \alpha_-$ and $\Phi_d = \phi_+ - \phi_-$. Thus, α_d and ϕ_d d represent the differential absorption and phase rotation between the RCP and LCP parts of the signal beam. If θ represents the phase retardation produced by the LCR, then the Jones matrix for the LCR is given by

$$J_{LCR} = \begin{bmatrix} e^{i\theta/2} & 0 \\ 0 & e^{-i\theta/2} \end{bmatrix} \tag{7.4}$$

and the Jones matrix for the LCR whose axis is rotated by 45° is given by $J_{LCR45} = R^{-1}(45^o) * J_{LCR} * R(45^o)$ where R(45°) represents the rotation matrix for 45° and is given by

$$R(45^o) = \begin{bmatrix} 1/\sqrt{2} & 1/\sqrt{2} \\ -1/\sqrt{2} & 1/\sqrt{2} \end{bmatrix} \tag{7.5}$$

Finally, the polarizer with its axis parallel to the $\hat{y}$ axis has the Jones matrix representation

$$J_{YPol} = \begin{bmatrix} 0 & 0 \\ 0 & 1 \end{bmatrix} \tag{7.6}$$

Thus, the Jones vector for the signal observed at the detector A would be

$$J_{out} = J_{YPol} * J_{LCR45} * E_{out} \tag{7.7}$$

Performing the calculations, we find that the intensity as seen by the detector A is given by

$$I = \frac{E_0^{\,2}}{4} e^{-2\alpha_-} \left(1 + e^{-2\alpha_d} + \left(e^{-2\alpha_d} - 1\right)\sin\theta + 2e^{-\alpha_d}\cos\phi_d \cos\theta\right) \tag{7.8}$$

In Figure 7.5(a), I is plotted for different values of φ_d (in degrees) and $\alpha_d = 0$ as the LCR phase retardance θ varies from 0 (left-end) to π (center) and back to 0 (right-end). As is evident from the figure, the signature for increasing differential phase rotation is the upward shift of the minimum and downward shift of the maximum of the curve until $\varphi_d = 90°$, at which point the signal is perfectly flat. For greater values of φ_d, the shape of the curve gets inverted until $\varphi_d = \pi$. On the other hand, for non-zero values of αd and $\varphi_d = 0$, the minima of the curves get shifted inwards, the curves slope upward on either side of the minima and the central part of the curve is flattened out, as shown in Figure 7.5(b). For non-zero values of both α_d and φ_d, the interpretation is not so straightforward and one has to use 3 data points and invert the expression for I to obtain their values. The algebra is somewhat involved and we present only the final result

$$y = e^{\alpha_d} = \sqrt{\frac{I_2^2\left(C_1 - C_3 - S_{3-1}\right) + I_1 I_2\left(C_3 - C_2 - S_{2-3}\right) + I_2 I_3\left(C_2 - C_1 - S_{1-2}\right)}{I_2^2\left(C_3 - C_1 - S_{3-1}\right) + I_1 I_2\left(C_2 - C_3 - S_{2-3}\right) + I_2 I_3\left(C_1 - C_2 - S_{1-2}\right)}} \tag{7.9}$$

$$\cos\phi_d = \frac{\left(I_2 - I_1\right)\left(y + \frac{1}{y}\right) + \left(I_2 S_1 - I_1 S_2\right)\left(\frac{1}{y} - y\right)}{2\left(I_1 C_2 - I_2 C_1\right)} \tag{7.10}$$

where $C_j = \cos(\theta_j)$, $S_j = \sin(\theta_j)$, and $S_{j-k} = \sin(\theta_j - \theta_k)$, where θ_j is the phase rotations produced for some voltage, and I_j is the corresponding intensity seen by the detector.

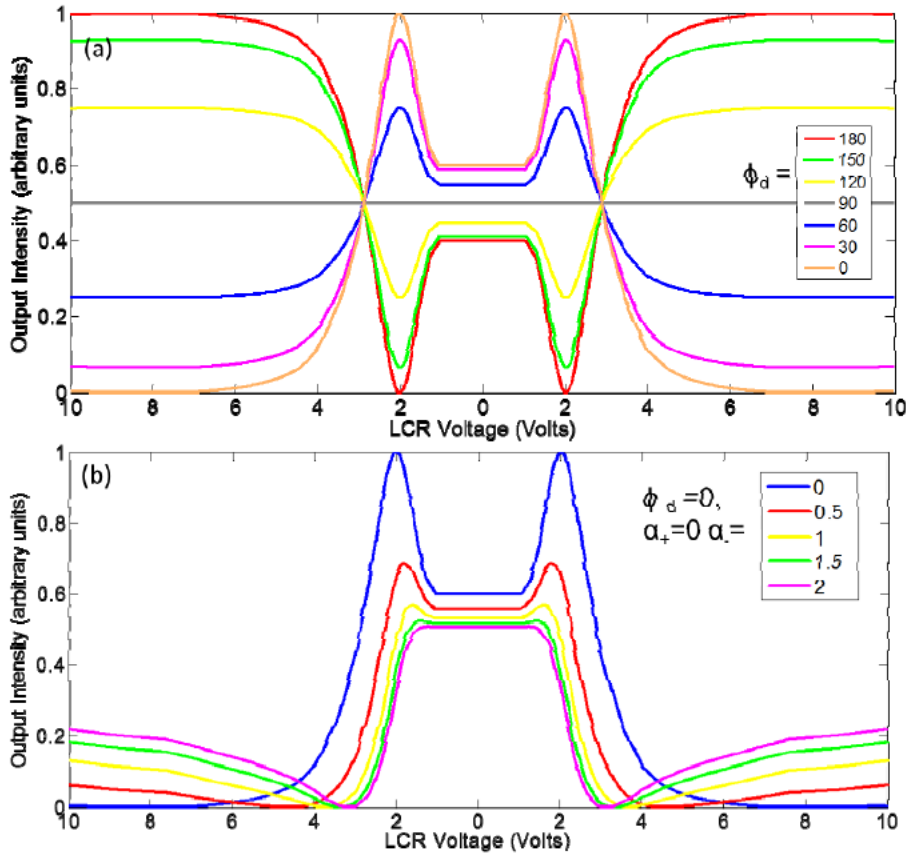

Figure 7.5 Ideal Output seen by detector for different values of a) φ_d with $\alpha_+ = \alpha_- = 0$ and b) α- with $\varphi_d = \alpha_+ = 0$.

The exact shape of the $5P_{1/2}$-$6S_{1/2}$ absorption lines depend critically on the control beam intensity and detuning, and the spread in atomic velocities (which in turn depends the temperature of the cell). The line shape is further complicated by the unequal transition strengths and hence, varying Autler Townes splittings or light shifts. As a result, each of the probe resonance peaks may be split as well as shifted significantly from the nominal positions. In addition, the structures from one resonance may overlap with other structures from a

neighboring resonance. As such, it is quite difficult to associate a feature observed at a certain detuning with a specific transition. Our model does a good job in predicting the line shapes for very low pump intensities. However, for strong pump intensities, such as those employed experimentally, a combination of a more accurate model which addresses all non-idealities, as well as an exact measurement of the velocity spread and the optical density would be needed to reproduce theoretically the line shapes observed. In the future, efforts will be made to improve the modeling in this way. Thus, for the somewhat approximate model we have at hand, and the qualitative estimate of the experimental parameters, it is difficult to predict precisely the probe detuning at which one expects to see large phase shifts in the experiment. Therefore, as a diagnostic tool to identify regions of high phase shift, the LCR was first removed. Rotation of polarization by 90°, which would enable us to use the device as an all-optical switch, corresponds to regions where the signal is at least as large as the signal with the polarizer placed parallel to the initial polarization direction of the signal beam. As the probe laser was scanned across the $6S_{1/2}$ manifold, the detuning of the control beam was varied in order to maximize the transmission through the orthogonal polarizer over the largest possible bandwidth. The best results were obtained when the pump and probe were counter-propagating and the results are shown in Figure 7.6.

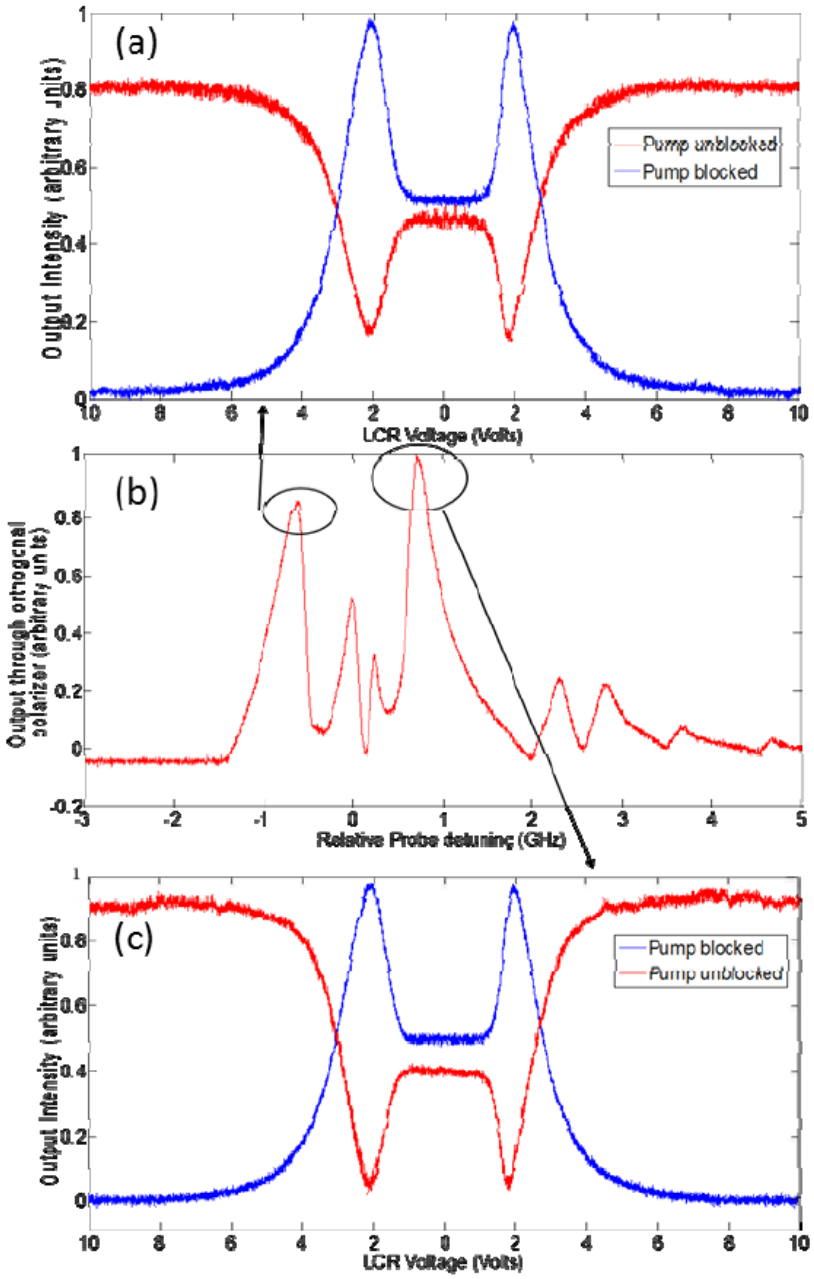

Figure 7.6 Observed experimental data showing differential phase rotation of (a) ~160° and (c) ~180° and almost no differential absorption at certain detunings. (b) transmission through orthogonal polarizer as probe is scanned.

Figure 7.6(b) shows the transmission through the orthogonal polarizer as the probe laser was scanned over ~5 GHz. The control beam was right circularly polarized and the signal beam

was vertically polarized. The pump was placed at a detuning of about 1.2 GHz. The temperature of the cell was maintained around 130° Celsius and the pump power was about 600 mW, obtained from a Ti-Sapphire laser. The probe laser was about 1 mW, obtained from a fiber coupled semiconductor laser. Both beams were focused to a spot size of about 50 μm near the center of the Rb cell. The probe frequency scan was then stopped and with the probe laser fixed at a frequency corresponding to a region of high phase shift, the LCR was inserted at 45° to the initial polarization direction of the probe and its control voltage was scanned linearly from 10V to 0V and back up to 10V. The blue trace (normalized from 0 to 1) corresponds to the situation when the control beam was blocked and can thus be treated as the reference signal, corresponding to 0 phase retardance. When the control beam is unblocked, the system acts as an optically controlled waveplate and the red trace is obtained. Comparing with the theoretical plots, one can see that the phase shifts in Figure 7.6 (a) and (c) correspond to $\varphi_d \sim 160°$ and $\varphi_d \sim 180°$, respectively with $\alpha_d \sim 0$. These values obtained are consistent with those obtained using the analytical expressions in Eqn.7.9 and 7.10. Figure 7.7 shows the result obtained from numerical simulations using the model presented in section 2. We perform our calculations by setting Γ_a to unity and rescaling all parameters in units of Γ_a. The pump is resonant with the F = 1 to F' = 2 transition and the probe detuning (δ_s) ranges from $-1200\Gamma_a$ to $1200\Gamma_a$. Figure 7.7 (a) and (b) show the phase shift of the RCP and LCP parts of the signal beam introduced by the Rb medium and Figure 7.7 (c) shows the difference between them. Figure 7.7 (d)- (f) show the corresponding figures for attenuation. The pump detuning is ~1.2 GHz (same as the experimental value), the Rb density is $10^{12}/cm^3$ and the cell length is 7.5 cm. Other relevant parameters used for this particular simulation are as follows- the decay rates Γ_a, Γ_b and Γ_g are

$2\pi*5.75\ \text{sec}^{-1}$, $2\pi*3.45\ \text{sec}^{-1}$ and $2\pi*0.1\ \text{sec}^{-1}$ respectively. The separation Δ, between F' = 1 and F' = 2 is $2\pi*814.5\ \text{sec}^{-1}$ ($=141.4\Gamma_a$) and the Rabi frequencies have been chosen to be $\Omega_p = 100\Gamma_a$, and $\Omega_s = 0.1\Gamma_a$. As is evident from Figure 7.7(c) and (f), around the data point indicated in the figure, for this set of parameters, we can produce a phase shift of about 180° with minimal differential absorption. For reasons explained earlier, it is not currently possible to ascertain whether the corresponding 180° phase shift observed experimentally occurs at precisely this frequency.

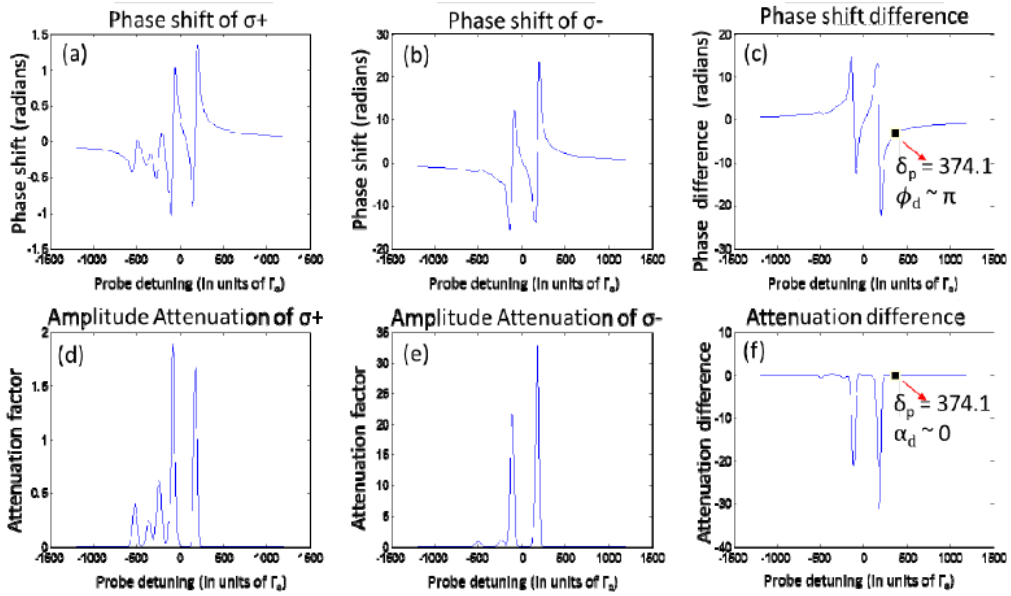

Figure 7.7 Numerical simulation of 15-level system showing phase shift and attenuation of the RCP and LCP parts of the probe beam as a function of probe detuning. Here $\delta_c \sim 1.2$ *GHz,* $n_{atom} \sim 10^{12}/cm^3$ *and* $\Omega_{min} = 100\Gamma_a$.

The expressions used to calculate the attenuation and additional phase retardance introduced by the Rb medium are given by

$$\phi_+ = kL\frac{\beta_+}{2}Re\left(a_{13,4}\rho_{13,4} + a_{14,5}\rho_{14,5} + a_{12,7}\rho_{12,7} + a_{13,8}\rho_{13,8} + a_{14,9}\rho_{14,9}\right) \tag{7.11}$$

$$\phi_{-} = kL\frac{\beta_{-}}{2}Re\left(a_{12,5}\rho_{12,5} + a_{13,6}\rho_{13,6} + a_{12,9}\rho_{12,9} + a_{13,10}\rho_{13,10} + a_{14,11}\rho_{14,11}\right) \quad (7.12)$$

$$\alpha_{+} = kL\beta_{+}Im\left(a_{13,4}\rho_{13,4} + a_{14,5}\rho_{14,5} + a_{12,7}\rho_{12,7} + a_{13,8}\rho_{13,8} + a_{14,9}\rho_{14,9}\right)/2 \quad (7.13)$$

$$\alpha_{-} = kL\beta_{-}Im\left(a_{12,5}\rho_{12,5} + a_{13,6}\rho_{13,6} + a_{12,9}\rho_{12,9} + a_{13,10}\rho_{13,10} + a_{14,11}\rho_{14,11}\right)/2 \quad (7.14)$$

And

$$\beta_{\pm} = b_{min}^{2}\frac{3n_{atom}\Gamma\lambda^{3}}{4\pi^{2}\Omega_{min}} \quad (7.15)$$

where k is the wavevector of the signal beam, L is the length of the cell, n_{atom} is the density of Rb atoms, Ω_{min} is the Rabi frequency for the weakest probe transition and the various a_{ij}'s are the ratios of the Rabi frequency (Ω_{ij}) of the |i> -> |j> transition to Ω_{min} For example, $a_{12,7} = \Omega_{12,7}/\Omega_{14,9} = \sqrt{6}$. b_{min}^{2} is the fraction of the atoms (<1) that decay along the transition corresponding to Ω_{min} , among all allowed decay channels from the decaying level. In our model, the amplitudes for all possible transitions from |14> are in the ratio $1:1:1:\sqrt{3}:\sqrt{6}$ and hence the fraction of atoms that decay along the different channels are in the ratio 1:1:1:3:6. Thus, $b_{min}^{2} = 1/(1+1+1+3+6) = 1/12$.

It is possible to produce arbitrarily large phase rotation by increasing the temperature and thus the density of Rb atoms. However, since the difference in phase rotation is so large, the bandwidth over which the device can operate as a half-wave plate, for example, becomes narrower. Thus, for wide bandwidth operation, we would need to operate in the parameter space where we not only have φ_d ~180°, but the slope should also be very small, as shown for the data point marked in Figure 7.7(c). We also investigated the waveplate effect under a co-propagating geometry. We found that the absorption line shapes for the co-propagating geometry are broader and shallower compared to the counter-propagating geometry, the

reasons for which have been clearly elucidated in [17]. As a consequence, under identical conditions, the phase rotation produced is smaller. This was confirmed experimentally, but the results have been omitted for the sake of brevity. The system can also be used as a quarter-wave plate by using a pump that is linearly polarized at 45° to the direction of polarization of a linearly polarized probe, as explained earlier. Figure 7.8(a) shows the result for such a situation with the polarizer in front of detector A parallel to the direction of polarization of the probe. Here, the probe is vertically polarized while the pump is linearly polarized at 45° and is at a detuning of δ_c~1 GHz and has a power of ~600 mW. Figure 7.8(b) shows the corresponding simulation results for a vertical and circularly polarized probe after passing through our analyzing system.

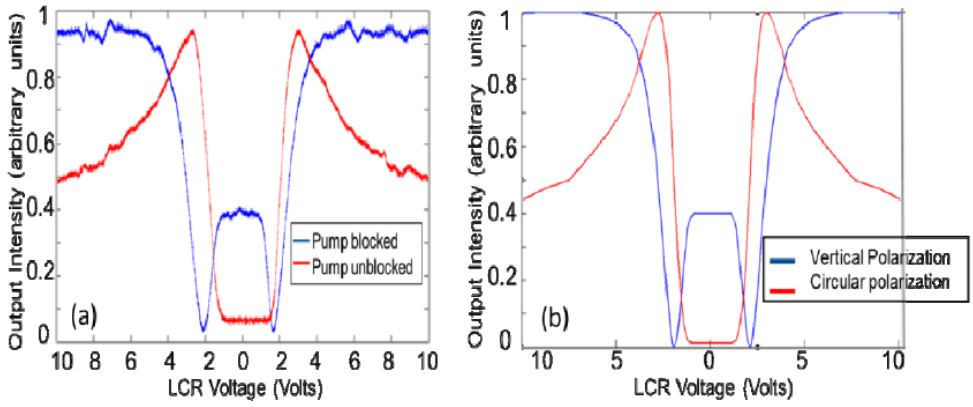

Figure 7.8 System behaving as Quarter Wave Plate using pump which is linearly polarized at 45° (a) Experimental result (b) Expected detector output for linear and circular polarization of the probe.

CHAPTER 8 DOUBLE RAMAN GAIN

8.1 Double Raman Gain Media

The basic system we consider for producing the double Raman gain peaks is illustrated schematically in Figure 8.1. Here, level $|1>$ and $|2>$ are assumed to be long-lived ground states, each coupled via electric dipolar transitions to the intermediate state $|3>$ and $|4>$, which are assumed to be far apart in energy. Since the energy difference between $|1>$ and $|2>$ is much less than the thermal energy, (k_BT, where k_B is the Boltzmann constant and T is the temperature) at room temperature, the population in these two levels are roughly equal under thermal equilibrium. An optical pumping beam, locked to the $|1>\rightarrow|4>$ transition, is tuned to create a population imbalance between these two states. The effect of this pump is modeled as a net decay rate of Γ_{12} from state $|1>$ to state $|2>$. (Decaying from $|4>\rightarrow|2>$ is included implicitly here.) The Raman pumps with frequencies ω_{p1} and ω_{p2} respectively, are applied to the $|2>\rightarrow|3>$ transition, each being highly detuned in order to avoid the effect of spontaneous emission. The Rabi frequencies of these two pumps are Ω_{p1} and Ω_{p2} respectively. The probe beam, at frequency ω_s, is applied to the $|1>\rightarrow|3>$ transition, also highly detuned. We indicate by $\hbar\omega_j$ the energy of the state $|j>$, for $j=\{1,2,3\}$. Δ_p is defined as the detuning of the central frequency of the two Raman pump fields, i.e., $\Delta_p=(\omega_{p1}+\omega_{p2})/2-(\omega_3-\omega_2)$. The frequency difference between the two Raman pumps is $\Delta\equiv\omega_{p2}-\omega_{p1}$. The detuning of the probe beam is $\delta=\omega_s-(\omega_3-\omega_1)$. When $\delta=\Delta_p\pm\Delta/2$, a two-photon transition condition is met. In that case, the Raman probe will experience a gain. In the experiment to be described later, we implemented the Λ system with ^{85}Rb D1 line,

with |1>, |2>, and |3> corresponding to the $5S_{1/2}$ F=2, $5S_{1/2}$ F=3, and $5P_{1/2}$ respectively, and the D2 transition is used for optical pumping (i.e., $|4>$ is the $5P_{3/2}$ manifold).

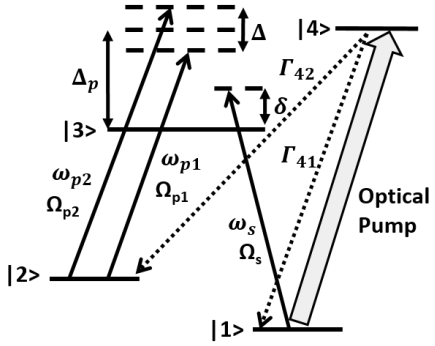

Figure 8.1 The double Raman Gain System. Ω_s is the Rabi frequency of Raman probe. Ω_{p1} and Ω_{p2} are Rabi frequencies of Raman pumps 1 and 2 respectively. Γ_{41} and Γ_{42} are the decay rates from |4> to |1> and |2> respectively.

Under the electric dipole and rotating wave approximation, the Hamiltonian for the system shown in figure 1 can be expressed in the basis of $|1>$, $|2>$, and $|3>$, as

$$\mathcal{H} = \hbar \begin{bmatrix} \omega_1 & 0 & \frac{1}{2}e^{i\omega_s t}\Omega_s \\ 0 & \omega_2 & (\frac{1}{2}e^{i\omega_{p1} t}\Omega_{p1} + \frac{1}{2}e^{i\omega_{p2} t}\Omega_{p2}) \\ \frac{1}{2}e^{-i\omega_s t}\Omega_s & (\frac{1}{2}e^{-i\omega_{p1} t}\Omega_{p1} + \frac{1}{2}e^{-i\omega_{p2} t}\Omega_{p2}) & \omega_3 \end{bmatrix} \quad (8.1)$$

Here, without loss of generality, we have assumed that the phase of each of three fields is zero. The gain experienced by the probe is not affected by the relative phases of these fields, since there is no closed loop involved in the interaction [16].

As can be seen, the term in the Hamiltonian that represents the coupling between $|2>$ and $|3>$ contains two different oscillatory terms. As such, there is no transformation that can convert this into a fully time-independent form. Thus, we choose arbitrarily to carry out a

transformation that eliminates the time dependence for only one of the terms. Specifically, the state vector $|\psi>$ is transformed to $|\tilde{\psi}\rangle \equiv Q|\psi\rangle$, where $Q \equiv \mathrm{e}^{\mathrm{i}\theta_1 t}|1><1| + \mathrm{e}^{\mathrm{i}\theta_2 t}|2><2| + \mathrm{e}^{\mathrm{i}\theta_3 t}|3><3|$, and choose $\theta_1 = -\omega_1$, $\theta_2 = -\delta - \frac{\Delta}{2} + \Delta_\mathrm{p} - \omega_2$, and $\theta_3 = -\delta - \omega_3$. The effective Hamiltonian for $|\tilde{\psi}\rangle$ is then given by Ref.16

$$\tilde{\mathcal{H}} = \hbar \begin{bmatrix} 0 & 0 & \frac{\Omega_\mathrm{s}}{2} \\ 0 & -\frac{1}{2}(2\delta + \Delta - 2\Delta\mathrm{p}) & \frac{1}{2}(\Omega_{\mathrm{p}1} + \mathrm{e}^{\mathrm{i}\Delta t}\Omega_{\mathrm{p}2}) \\ \frac{\Omega_\mathrm{s}}{2} & \frac{1}{2}(\Omega_{\mathrm{p}1} + \mathrm{e}^{-\mathrm{i}\Delta t}\Omega_{\mathrm{p}2}) & -\delta \end{bmatrix} \tag{8.2}$$

The Liouville's equation for the density matrix in this basis can be written as

$$\frac{d\tilde{\rho}}{dt} = -\frac{i}{\hbar}\left(\tilde{\tilde{\mathcal{H}}}\tilde{\rho} - \tilde{\rho}\tilde{\tilde{\mathcal{H}}}^{\dagger}\right) + M_{source} \tag{8.3}$$

Where $\tilde{\tilde{\mathcal{H}}}$ is a non-Hermitian Hamiltonian introduced for convenience[16], and is given by

$$\tilde{\tilde{\mathcal{H}}} = \tilde{\mathcal{H}} - i\frac{\hbar}{2}(\Gamma_1|\tilde{1}><\tilde{1}| + \Gamma_2|\tilde{2}><\tilde{2}| + \Gamma_3|\tilde{3}><\tilde{3}|) \tag{8.4}$$

And M_{source} accounts for the influx of population into the three states, which is expressed as

$$M_{source} = (\Gamma_{21}\tilde{\rho}_{22} + \Gamma_{31}\tilde{\rho}_{33})|\tilde{1}><\tilde{1}| + (\Gamma_{12}\tilde{\rho}_{11} + \Gamma_{32}\tilde{\rho}_{33})|\tilde{2}><\tilde{2}| + (\Gamma_{13}\tilde{\rho}11 + \Gamma_{23}\tilde{\rho}_{22})|\tilde{3}><\tilde{3}| \tag{8.5}$$

Here $\Gamma_i\ (i = 1,2,3)$ is the net decay rate of state $|\tilde{\imath}>$, $\Gamma_{ij}\ (i,j = 1,2,3)$ is the decay rate from level $|\tilde{\imath}>$ to level $|\tilde{\jmath}>$, and $\tilde{\rho}_{ij} \equiv <\tilde{\imath}|\tilde{\rho}|\tilde{\jmath}>$. In formulating (8.5, we have assumed a closed system, i.e., $\tilde{\rho}_{11} + \tilde{\rho}_{22} + \tilde{\rho}_{33} = 1$.

In general, all the decay rates in Eqn.8.4 and 8.5could be non-vanishing. However, for one particular system of inherence, we make the following assumptions about these rates. $\Gamma_3\ (= 2\pi \times 6 \times 10^6 sec^{-1})$ is the radiation decay rate from level |3>, and we assume

$\Gamma_{31} = \Gamma_{32} = \Gamma_3/2$. We also assume that $\Gamma_{13} = \Gamma_{23} = 0$. In the absence of optical pumping, $\Gamma_1 = \Gamma_{12}$ and $\Gamma_2 = \Gamma_{21}$ would account for the collisional exchange of populations between $|\tilde{1}>$ and $|\tilde{2}>$, with $\Gamma_1 \cong \Gamma_2$ (of the order of a few kHz) since the population of states $|\tilde{1}>$ and $|\tilde{2}>$ are roughly equal in thermal equilibrium at the operating temperature. However, the effect of the optical pumping via state |4> produced a net decay rate from $|\tilde{1}>$ to $|\tilde{2}>$ that is much stronger than these collisional ratios. Thus, we assume that $\Gamma_2 = \Gamma_{21} = 0$ and $\Gamma_1 = \Gamma_{12} \equiv \Gamma_{\mathrm{op}}$, where Γ_{op} is the rate of optical pumping.

Since some of the coupling terms in the Liouville equation have a periodicity of $(2\pi/\Delta)$, the general solution of the density matrix is an infinite sum which includes stationary components plus all the harmonies (positive + negative) of Δ

$$\tilde{\rho} = \tilde{\rho}^0 + \sum_{n=1}^{\infty}(\tilde{\rho}^{-\mathrm{n}}\mathrm{e}^{-\mathrm{in}\Delta t} + \tilde{\rho}^{\mathrm{n}}\mathrm{e}^{\mathrm{in}\Delta t}) \tag{8.6}$$

A characteristic parameter for the strength of the contribution of the n-th order is K_n, defined as the sum of the absolute values of all the elements:

$$K_n \equiv \sum_{i=1}^{3}\sum_{j=1}^{3}\{|\tilde{\rho}_{ij}^{n}| + |\tilde{\rho}_{ij}^{-n}|\}. \tag{8.7}$$

In general, $\mathrm{K_n}$ for a given n would increase monotonically with increasing pump Rabi frequencies. Furthermore, for a fixed set of parameters, $\mathrm{K_n}$would decrease monotonically with increasing n. These pattern can be used as a guide in deciding the maximum value of n to keep in the summation of Eqn.8.6. Specifically, we will use the convention that

$$\tilde{\rho} = \tilde{\rho}^0 + \sum_{n=1}^{M}(\tilde{\rho}^{-\mathrm{n}}\mathrm{e}^{-\mathrm{in}\Delta t} + \tilde{\rho}^{\mathrm{n}}\mathrm{e}^{\mathrm{in}\Delta t}),\ K_M < \varepsilon \tag{8.8}$$

where ε can be chosen to have a value that is sufficient for the required accuracy. We will use a value of $\varepsilon = 0.01$ in the results presented here.

It should be noted that Eqn.8.8 represents a relation for each element of the density matrix:

$$\tilde{\rho}_{ij} = \tilde{\rho}_{ij}{}^{0} + \sum_{n=1}^{M}(\tilde{\rho}_{ij}{}^{-\mathrm{n}}\mathrm{e}^{-\mathrm{in}\Delta t} + \tilde{\rho}_{ij}{}^{\mathrm{n}}\mathrm{e}^{\mathrm{in}\Delta t}),\ i = \{1,2,3\}, j = \{1,2,3\}, K_M < \varepsilon \qquad (8.9)$$

The Liouville Equation (Eqn.8.3), when applied to the density matrix of Eqn.8.8 (or equivalently 8.9), represents a set of coupled differential equations involving 9 variables $\tilde{\rho}_{ij}$ subject to the closed system constraints that $\tilde{\rho}_{11} + \tilde{\rho}_{22} + \tilde{\rho}_{33} = 1$. If we represent the 9 variables as a vector $\vec{A}$ (with the elements ordered in any chosen way), then the Liousville Equitation can be expressed as $\dot{\vec{A}} = M\vec{A}$, where the matrix M is time dependent. As such this system does not have a steady state solution, even when the closed system constraint is used.

In principle, one can determine the time evolution of $\vec{A}$ via simple numerical integration. However, we are interested in the limit where the system reaches a quasi steady state where the time evolution involves only the harmonics of Δ. In this limit, for all $i, j, and\ n \leq M$, the elements $\tilde{\rho}_{ij}{}^{0}$ and $\tilde{\rho}_{ij}{}^{\pm n}$ become constants. We can then equate terms with the same temporal coefficients in order to derive the values of these elements.

To illustrate this process explicitly, consider, for example, the case of M=1, and focus arbitrarily on $\tilde{\rho}_{12}$. The Liousville Equation implies that

$$\frac{d\tilde{\rho}_{12}}{dt} = -\frac{1}{2}\Gamma_1\tilde{\rho}_{12} - \frac{1}{2}\Gamma_2\tilde{\rho}_{12} - \mathrm{i}\delta\tilde{\rho}_{12} - \frac{\mathrm{i}}{2}\Delta\tilde{\rho}_{12} + \mathrm{i}\Delta_p\tilde{\rho}_{12} + \frac{\mathrm{i}}{2}\tilde{\rho}_{13}\Omega_{p1} + \frac{\mathrm{i}}{2}\mathrm{e}^{-\mathrm{i}t\Delta}\tilde{\rho}_{13}\Omega_{p2} - \frac{\mathrm{i}}{2}\tilde{\rho}_{32}\Omega_s \qquad (8.10)$$

where $\tilde{\rho}_{12} = \tilde{\rho}_{12}^{0} + \tilde{\rho}_{12}^{1}e^{i\Delta t} + \tilde{\rho}_{12}^{-1}e^{-i\Delta t}$. In quasi steady state, $\tilde{\rho}_{12}^{0}, \tilde{\rho}_{12}^{1}$, and $\tilde{\rho}_{12}^{-1}$ are constants. As such, the L.H.S. of Eqn.8.10 becomes:

$$\frac{d\tilde{\rho}_{12}}{dt} = 0 + i\Delta\tilde{\rho}_{12}^{1}e^{i\Delta t} - i\Delta\tilde{\rho}_{12}^{-1}e^{-i\Delta t} \qquad (8.11)$$

On the right hand side (R.H.S), we use the relation that $\tilde{\rho}_{ij} = \tilde{\rho}_{ij}^{0} + \tilde{\rho}_{ij}^{1}e^{i\Delta t} + \tilde{\rho}_{ij}^{-1}e^{-i\Delta t}$.

Furthermore, we use the closed-system constraint that $\tilde{\rho}_{11} + \tilde{\rho}_{22} + \tilde{\rho}_{33} = 1$ in order to eliminate $\tilde{\rho}_{33}$ everywhere. Now, equating the constant terms between the L.H.S and R.H.S, we get

$$0 = -\frac{1}{2}(\tilde{\rho}_{12}^{0}\Gamma_1) - \mathrm{i}\tilde{\rho}_{12}^{0}\delta + \mathrm{i}\Delta_p\tilde{\rho}_{12}^{0} + \frac{\mathrm{i}}{2}\Omega_{p1}\tilde{\rho}_{13}^{0} + \frac{\mathrm{i}}{2}\Omega_{p2}\tilde{\rho}_{13}^{1} - \frac{1}{2}\tilde{\rho}_{12}^{0}\Gamma_2 - \frac{\mathrm{i}}{2}\Delta\tilde{\rho}_{12}^{0} - \frac{\mathrm{i}}{2}\tilde{\rho}_{32}^{0}\Omega_s \tag{8.12}$$

Similarly, equating the coefficients of the $e^{i\Delta t}$ terms we get

$$\mathrm{i}\Delta\tilde{\rho}_{12}^{1} = -\frac{1}{2}(\tilde{\rho}_{12}^{1}\Gamma_1) - \mathrm{i}\delta\tilde{\rho}_{12}^{1} + \mathrm{i}\Delta_p\tilde{\rho}_{12}^{1} + \frac{\mathrm{i}}{2}\Omega_{p1}\tilde{\rho}_{13}^{1} - \frac{1}{2}\Gamma_2\tilde{\rho}_{12}^{1} - \frac{\mathrm{i}}{2}\Delta\tilde{\rho}_{12}^{1} - \frac{\mathrm{i}}{2}\Omega_s\tilde{\rho}_{32}^{1} \tag{8.13}$$

and by equating the coefficients of the $e^{-i\Delta t}$ terms we get

$$-\mathrm{i}\Delta\tilde{\rho}_{12}^{-1} = -\frac{1}{2}(\tilde{\rho}_{12}^{-1}\Gamma_1) - \mathrm{i}\delta\tilde{\rho}_{12}^{-1} + \mathrm{i}\Delta_{\mathrm{p}}\tilde{\rho}_{12}^{-1} + \frac{\mathrm{i}}{2}\tilde{\rho}_{13}^{-1}\Omega_{\mathrm{p1}} + \frac{\mathrm{i}}{2}\Omega_{\mathrm{p2}}\tilde{\rho}_{13}^{0} - \frac{1}{2}\Gamma_2\tilde{\rho}_{12}^{-1} - \frac{\mathrm{i}}{2}\Delta\tilde{\rho}_{12}^{-1} - \frac{\mathrm{i}}{2}\tilde{\rho}_{32}^{-1}\Omega_{\mathrm{s}} \tag{8.14}$$

The same process can be used to generate these questions corresponding to each element, $\tilde{\rho}_{\mathrm{ij}}$ of the density matrix. However, because of the closed system constraint, the equations resulting from $\tilde{\rho}_{33}$ are redundant. As such, we get 24 different equations, which can be easily solved via simple matrix inversion. For a general value of M, we set $8 \times (2M + 1)$ different equations, which can be solved in the same manner.

The solution of the density matrix is then used to determine the gain and dispersion experienced by the probe beam. To do so, we note first that the probe field can be expressed as

$$\vec{\mathrm{E}}_{\mathrm{signal}} = \hat{\epsilon}E_0\cos(kz - \omega_s t) \tag{8.15}$$

Where the polarization, $\hat{\epsilon}$, is chosen to be orthogonal to that of the pump, due to the selection rules for the Raman transition we have employed experimentally. The polarization density at the frequency of the probe can be expressed as (at z=0, for simplicity, without loss of generality):

$$\vec{\mathrm{P}}_{\mathrm{s(z=0)}} = \epsilon_0 \chi \vec{E}_{(z=0)} = \frac{1}{2}\hat{\epsilon}\epsilon_0 \chi E_0 (\mathrm{e}^{\mathrm{i}\omega_s t} + \mathrm{e}^{-\mathrm{i}\omega_s t}) \tag{8.16}$$

The total polarization density is given by

$$\vec{\mathrm{P}}_{\mathrm{total}} = -N|e|\langle \vec{r} \rangle \tag{8.17}$$

Where N is the density of the atoms, |e| is the electron charge (assuming that a single electron is responsible for the interaction, valid for alkali atoms), and $\vec{r}$ is the position of the electron with respect to the nucleus of the atom.

The polarization density responsible for the electric susceptibility of the probe, given in Eqn8.16, is the component at frequency ω_s of the following quantity:

$$\vec{\mathrm{P}}_{\epsilon} = -N|e|\langle r_{\epsilon} \rangle \hat{\epsilon} \ , \qquad r_{\epsilon} = \vec{r} \cdot \hat{\epsilon} \tag{8.18}$$

We assume that $\langle 1|r_{\epsilon}|3\rangle = \langle 3|r_{\epsilon}|1\rangle \equiv r_{13}$, $\langle 2|r_{\epsilon}|3\rangle = \langle 3|r_{\epsilon}|2\rangle \equiv r_{23}$, and $\langle 1|r_{\epsilon}|2\rangle = \langle 2|r_{\epsilon}|1\rangle \equiv 0$. The value of $\langle r_{\epsilon} \rangle$ is then given by:

$$\langle r_{\epsilon} \rangle = tr(\rho r_{\epsilon}) = r_{13}(\rho_{13} + \rho_{31}) + r_{23}(\rho_{23} + \rho_{32}) \tag{8.19}$$

For our system, ρ_{23} & ρ_{32} correspond to oscillation that are at frequencies far away from ω_s. As such, only ρ_{13} & ρ_{31} will contribute to the polarization density in Eqn.8.16. In the presence of dual Raman pumps, ρ_{13} & ρ_{31} will have components at ω_s, as well as at

$\omega_s \pm n\Delta$. However, only the components of ρ_{13} & ρ_{31} at ω_s will contribute to the polarization density of Eqn.8.16. Explicitly, we note that

$$\rho_{13} = \tilde{\rho}_{13} e^{-i\omega_s t} = \tilde{\rho}_{13}{}^{0} e^{-i\omega_s t} + \sum_{n=1}^{M} (\tilde{\rho}_{13}{}^{-n} e^{-i(\omega_s - n\Delta)t} + \tilde{\rho}_{13}{}^{n} e^{-i(\omega_s + n\Delta)t}) \tag{8.20.a}$$

$$\rho_{31} = \tilde{\rho}_{31} \mathrm{e}^{i\omega_s t} = \tilde{\rho}_{31}{}^{0} \mathrm{e}^{i\omega_s t} + \sum_{n=1}^{M} (\tilde{\rho}_{31}{}^{-\mathrm{n}} \mathrm{e}^{-\mathrm{i}(\omega_s - n\Delta)t} + \tilde{\rho}_{31}{}^{\mathrm{n}} \mathrm{e}^{-\mathrm{i}(\omega_s + n\Delta)t}) \tag{8.20.b}$$

Thus, the parameter χ in Eqn.8.16 can be expressed as:

$$\chi = -\frac{2r_{13}\tilde{\rho}_{13}{}^{0}}{\varepsilon_0 E_0} N|e| \tag{8.21}$$

Noting that $\Omega_s \equiv |e| r_{13} E_0/\hbar$, we get

$$\chi = \frac{2N\hbar\Omega_s}{\varepsilon_0 E_0^2} \tilde{\rho}_{13}{}^{0} \tag{8.22}$$

The gain experienced by the probe can be expressed as $\mathrm{G} = \mathrm{e}^{-\alpha \mathrm{L}}$, where $\alpha = \frac{1}{2} k_0 Im(\chi)$ and L is the length of the media. The phase delay experienced by the probe is $\Phi = \frac{1}{2} k_0 Re(\chi) L$.

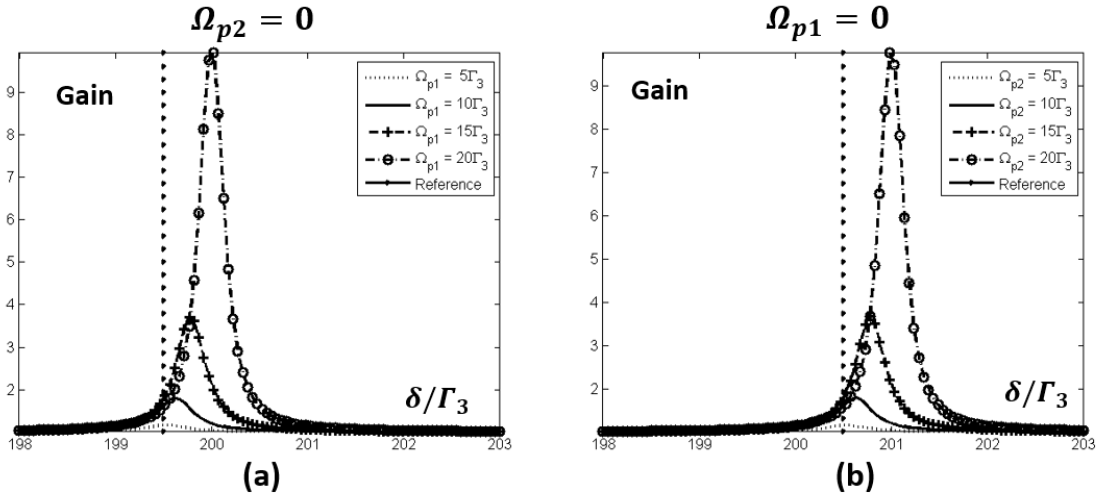

Figure 8.2 Illustration of individual Raman gain profiles and effects of light shift. In (a), the higher frequency Raman pump is turned off; in (b), the lower frequency Raman pump

is turned off. The location of the gain peaks moves with increasing pump power, due to light shift (or the ac-Stark shift). The reference line in both plots indicate the positions where the gain peak should be without considering light shift. See text for additional details.

Before showing the response of the complete system, we illustrate first the effect of each Raman pump individually on the gain seen by the probe. In Figure 8.2(a), we show the probe gain in the absence of the higher frequency Raman pump. For convenience, we have chosen $N = 2.5 \times 10^{16} m^{-3}$, $L = 0.1m$, $\Omega_s = 0.5\Gamma_3$, $\Gamma_{12} = 0.5\Gamma_3$ and $k_0 = 8.06 * 10^6 m^{-1}$, corresponding to the D2 manifold in Rb. For $\Omega_{p1} = 5\Gamma_3$, we see a peak gain of ~1.7. As the pump strength is increased to $20\Gamma_3$, gain is increased to ~9.8. It should be noted that the peak is slightly shifted to the right from the two photon resonant condition due to the light shift experienced by level 1. This shift becomes more prominent for higher pump power. The amount of light shift agrees with the expected value of $\Omega_{p1}^2/4\delta_1$, where $\delta_1 \equiv (\Delta_p - \Delta/2)$ is the detuning of this pump. Figure 8.2(b) shows the corresponding plots in the absence of the lower frequency Raman pump. The peak gain observed for both cases are the same for the same pump power as expected.

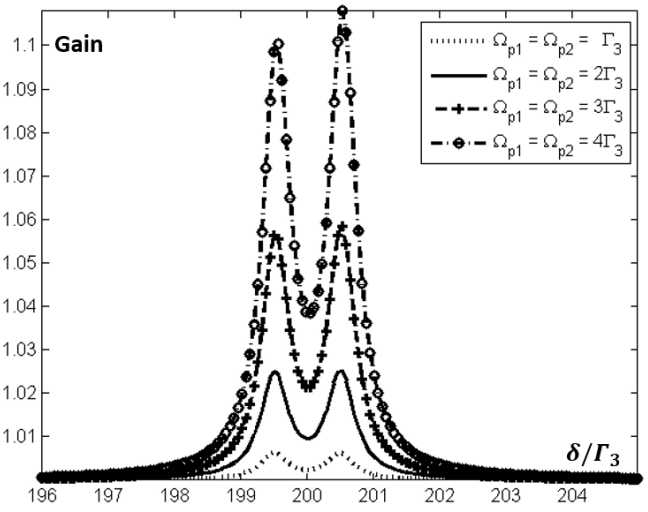

Figure 8.3 Illustration of the changes in the Raman gain profile while the pump Rabi frequencies, kept equal to each other, are increased.

Next, we consider the case where both pumps are present simultaneously. A typical set of probe gain plots are shown in Figure 8.3, as function of probe detuning. We set $\Delta = \Gamma_3$, $\Delta_p = 200\Gamma_3, \Omega_s = 0.5\Gamma_3$, N $= 2.5 \times 10^{16} m^{-3}$, L=0.1m, M =7. The figure shows the cases when $\Omega_{p1} = \Omega_{p2} = \Gamma_3, 2\Gamma_3, 3\Gamma_3, and\ 4\Gamma_3$ respectively. The gain profile shows equal peaks when $\Omega_{p1} = \Omega_{p2} = \Gamma_3$. As the Rabi frequency becomes stronger, the second gain peak becomes larger. The imbalance becomes more significant when Ω_p are further increased.

In Figure 8.4, we set $\Omega_{p1} = 5\Gamma_3$ and change the value of Ω_{p2}, while all the other parameters are kept the same as those in Figure 8.3. Plot (a) through (d) show the cases when $\Omega_{p2} = \Gamma_3, 3\Gamma_3, 4\Gamma_3,$ and $5\Gamma_3$ respectively. It should be noted that the peak corresponding to the second pump becomes larger (Figure 8.4(d)) than that corresponding to the first pump when $\Omega_{p2} = \Omega_{p1}$. Figure 8.5 shows the case where all the other parameters are the same as those in

Figure 8.4, but $\Omega_{p2} = 5\Gamma_3$ and Ω_{p1} is increased from Γ_3 to $5\Gamma_3$. As can be seen, the ratio of the peaks of the two gains follows a pattern that is similar to those in Figure 8.4.

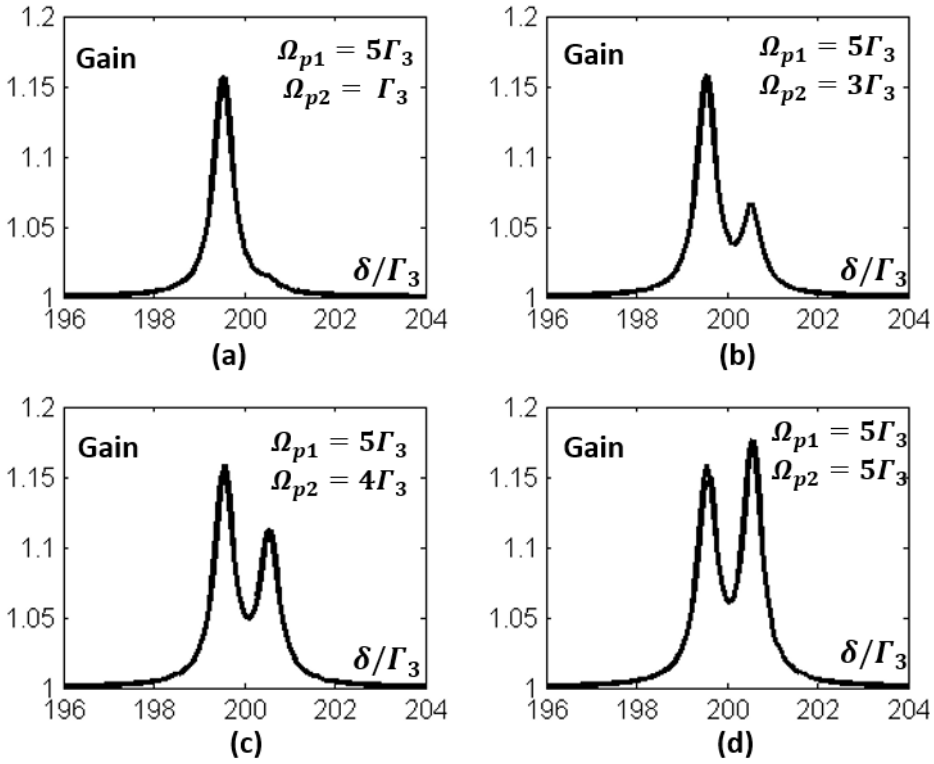

Figure 8.4 Illustration of the changes in the gain profile when the second Raman pump Rabi frequency is increased, while keeping the first Raman pump Rabi frequency fixed.

We have also verified that this imbalance is reproduced when pumps are detuned below resonance. Specifically, the pump that is further detuned from state |3> is more efficient in producing gain. Obviously, this exact native of this imbalance depends on the choice of parameters, such as the difference detuning Δ, the mean detuning Δ_p, and the absolute strengths of the pumps. This rather surprising result is due to the complicated interplay between the various higher order terms. It shows that the simple model generally used [25] for double Raman gain, where the gain spectrum is expressed simply as the sum of two independent

Lorentzians, is invalid. Rather, the more comprehensive model presented here must be used in determining the actual gain spectrum.

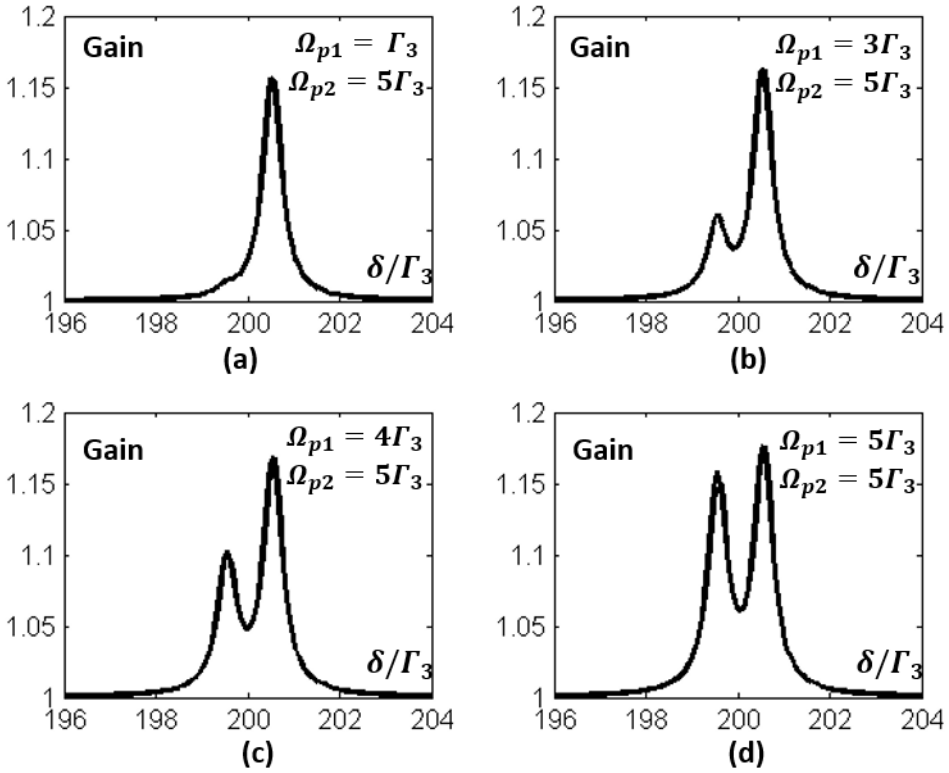

Figure 8.5 Illustration of the change in the gain profile when the first Raman pump Rabi frequency is varied, while keeping the second Raman pump Rabi frequency fixed.

Next, we compare the results obtained by the double Raman code with those produced by the single Raman pump model, which does not require expansion into many orders, since the Hamiltonian after the Q transformation become time independent. The first comparison we made is to compare single Raman result with double Raman result by setting one Raman pump Rabi frequency to be zero. This is illustrated in Figure 8.6, where we plot both the probe gain and the phase delay as function of the probe frequency. Plot (a) shows the result of the single Raman model. We set $\Omega_p = 20\Gamma_3$, $\Delta_p = 199\Gamma_3$, $\Gamma_{12} = 0.5\Gamma_3$, $\Omega_s = 0.5\Gamma_3$, $L = 0.1m$, and

$N = 2.5 \times 10^{16} m^{-3}$. Plot (b) shows the result of single Raman model by setting $\Delta_p = 201\Gamma_3$ while keeping all the other parameters the same. Plot (c) shows the result of double Raman model by setting $\Omega_{p1} = 20\Gamma_3$, $\Omega_{p2} = 0$, $\Delta_p = 200\Gamma_3$, $\Delta = 2\Gamma_3$ (recall that the two photo transition happens when $\delta = \Delta_p \pm \Delta/2$), and keep all the other parameters the same as plot (a) & (b). Plot (d) shows the result of double Raman model by setting$\Omega_{p1} = 0$, $\Omega_{p2} = 20\Gamma_3$, and keep all the other parameters the same as plot (c) . The plots demonstrate that the single Raman code and double Raman code returns the same result when one of the Raman pump Rabi frequency is set to be zero in the double Raman code.

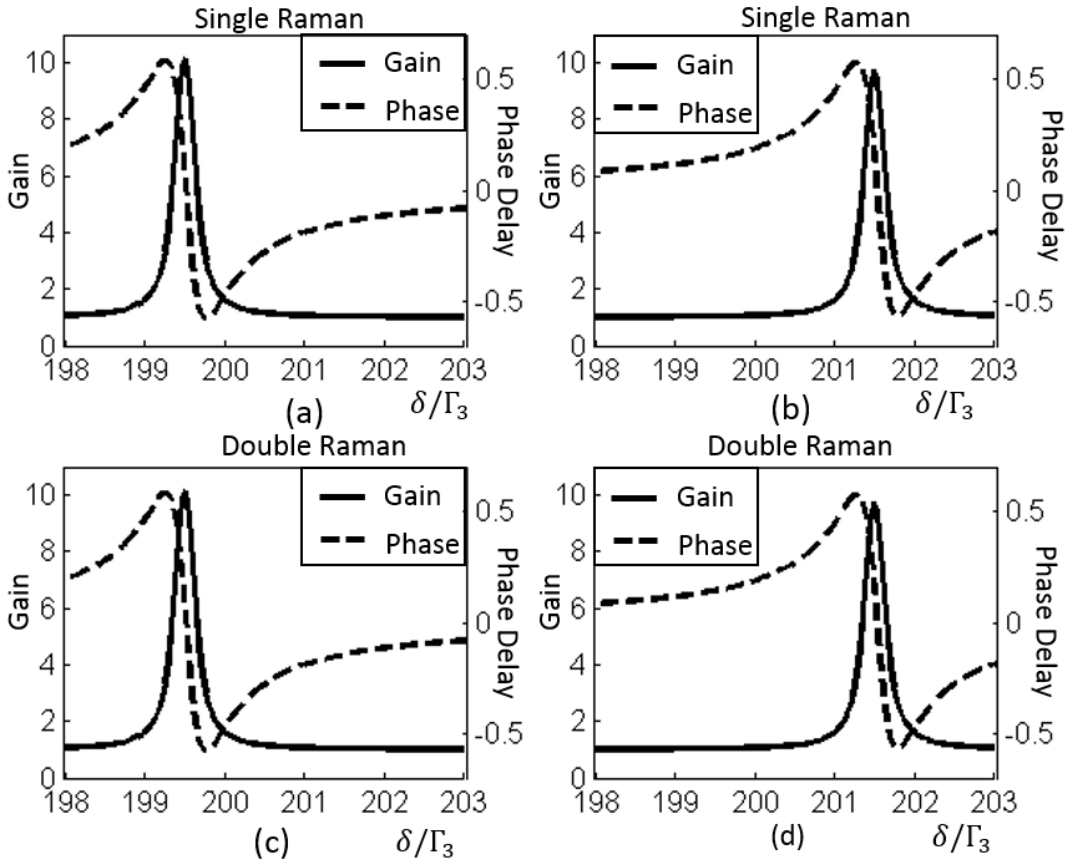

Figure 8.6 Comparison between double Raman gain model and single Raman gain model by setting one Raman pump Rabi frequency to be zero. The plots show the gain

(left axis) and phase delay (right axis) changes as a function of probe detuning δ. Plot (a) show the single Raman model with $\Delta_p = 199\Gamma_3$. Plot (b) shows the single Raman model with $\Delta_p = 201\Gamma_3$. Plot (c) shows the double Raman model with the second Raman pump turned off. Plot (d) shows the double Raman model with the first Raman pump turned off.

We also considered the limiting case where $\Delta \to 0$, and compared the result with those obtained using the single Raman model. As $\Delta \to 0$, (8.22 Eqn.8.22 is no more valid. All the harmonics and zero order term are at the same frequency. In this case, we set $\chi = \frac{2N\hbar\Omega_s}{\epsilon_0 E_0^2}[\,\tilde{\rho}_{13}^0 + \sum_{n=1}^{M}(\tilde{\rho}_{13}^{-n}e^{-in\Delta t} + \tilde{\rho}_{13}^{n}e^{in\Delta t})]$. This is illustrated in Figure 8.7 Comparison between double Raman gain model and single Raman gain model by setting Δ to be zero. Plot (a) to (g) are generated by the double Raman model with order number of 1,2,3,6,13,20 and 30 respectively, while plot (h) is generated by the single Raman model with the same parameters. In the double Raman model, we set$\Omega_{\mathrm{p1}} = \Omega_{\mathrm{p2}} = 20\Gamma_3$, $\Omega_{\mathrm{s}} = 0.01\Gamma_3$ $\Delta_{\mathrm{p}} = 110\Gamma_3$, $\Delta = 0$, $\Gamma_{12} = \Gamma_3$, $\mathrm{L} = 0.1\mathrm{m}$, $\mathrm{N} = 2.5 \times 10^{16} m^{-3}$. Plot (a) – (g) shows the results of double Raman simulation by setting M = 1,2,3,6,13,20, and 30 respectively. Plot (h) shows the single Raman case, where we keep all the other parameters the same but set $\Omega_{\mathrm{p}} = 40\Gamma_3$. Ripples are observed on the left side of the phase delay when M is small. As the orders M increases, the ripples diminishes and double Raman model shows closer results compared with single Raman model.

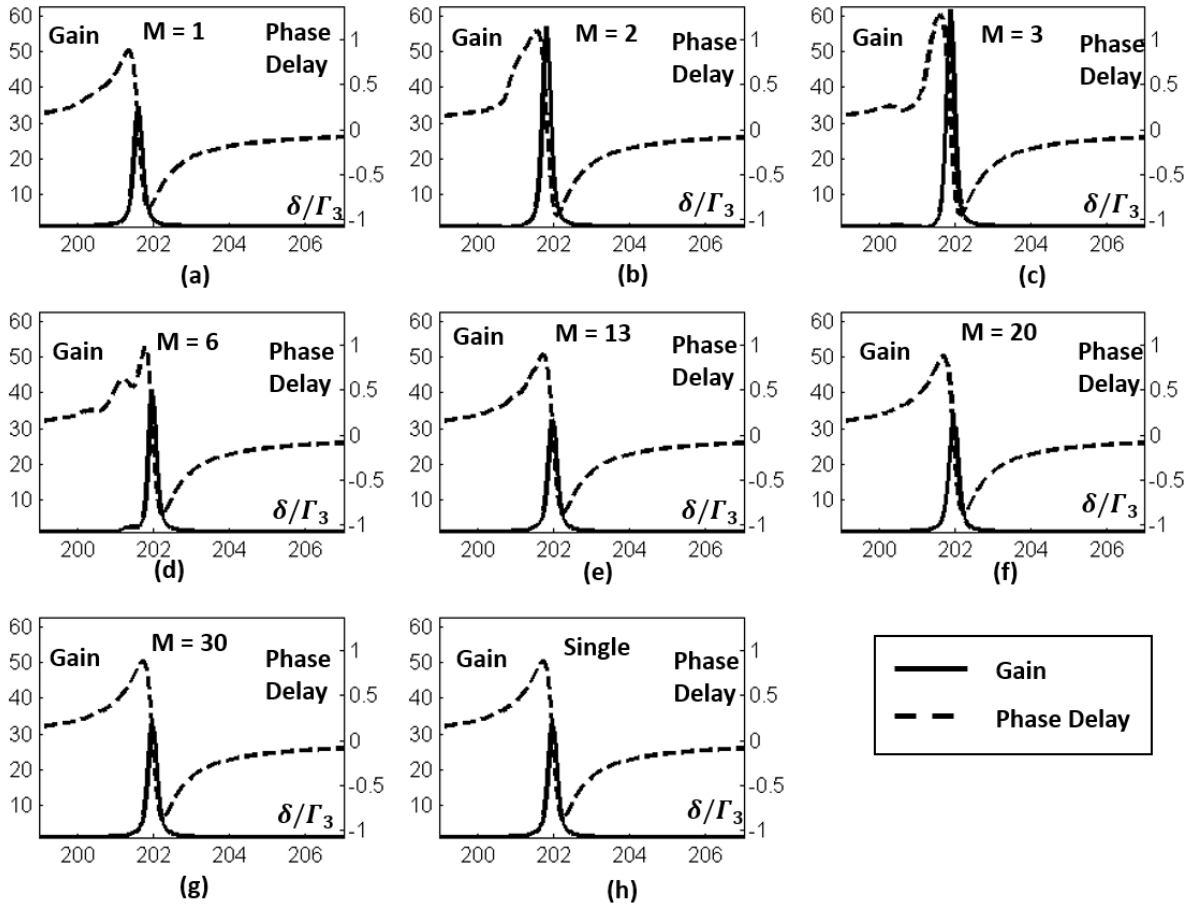

Figure 8.7 Comparison between double Raman gain model and single Raman gain model by setting Δ to be zero. Plot (a) to (g) are generated by the double Raman model with order number of 1,2,3,6,13,20 and 30 respectively, while plot (h) is generated by the single Raman model with the same parameters.

Effect of velocity averaging

Next, we consider the effect of velocity distribution, which is important for realizing the double Raman gain in a vapor cell. We consider first the case where the two pumps as well as the probe are propagating in the same direction. We assume a Maxwell – Boltzmann distribution for the velocities of the atoms. The temperature of the cell is assumed to be 373 Kelvin. The specific

atom we consider is ^{87}Rb. The length of the cell is assumed to be 0.1 m, at a density of $5 \times 10^{17} m^{-3}$.

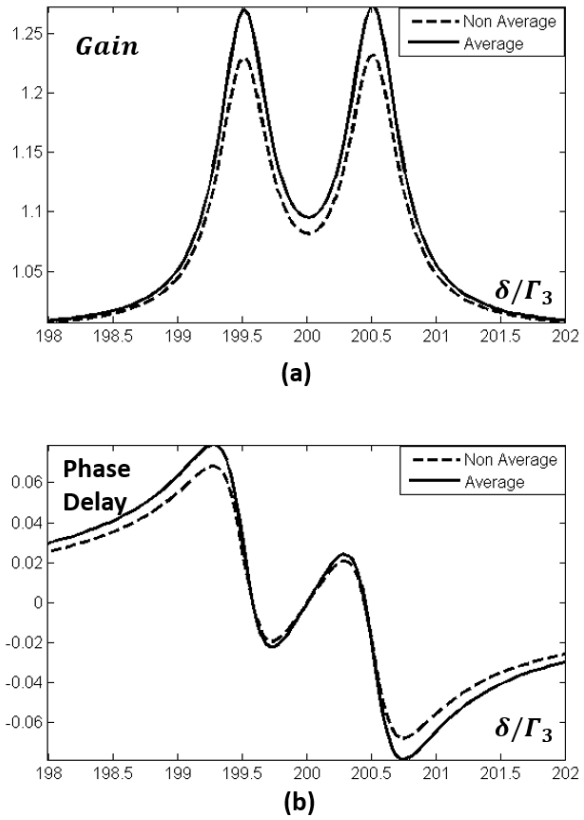

Figure 8.8 Comparison between velocity averaging model and non-averaging model.

Figure 8.8 shows the modification of the gain profile due to the velocity averaging, for $\Delta = \Gamma_3, \Omega_{p1} = \Omega_{p2} = 2\Gamma_3, \Omega_s = 0.01\Gamma_3, \Delta_p = 200\Gamma_3, \Gamma_{12} = 0.5\Gamma_3, N = 5 \times 10^{17} m^{-3}$, and L =0.1m, where we have used only the first order expansion (M=1). Plot (a) shows the gain as a function of δ/Γ_3. Plot (b) shows the phase delay as a function of δ/Γ_3. As can be seen, the averaging produces only a small reduction in the gain, is keeping with the well-known Doppler-shift insensitivity of co-propagating Raman interaction.

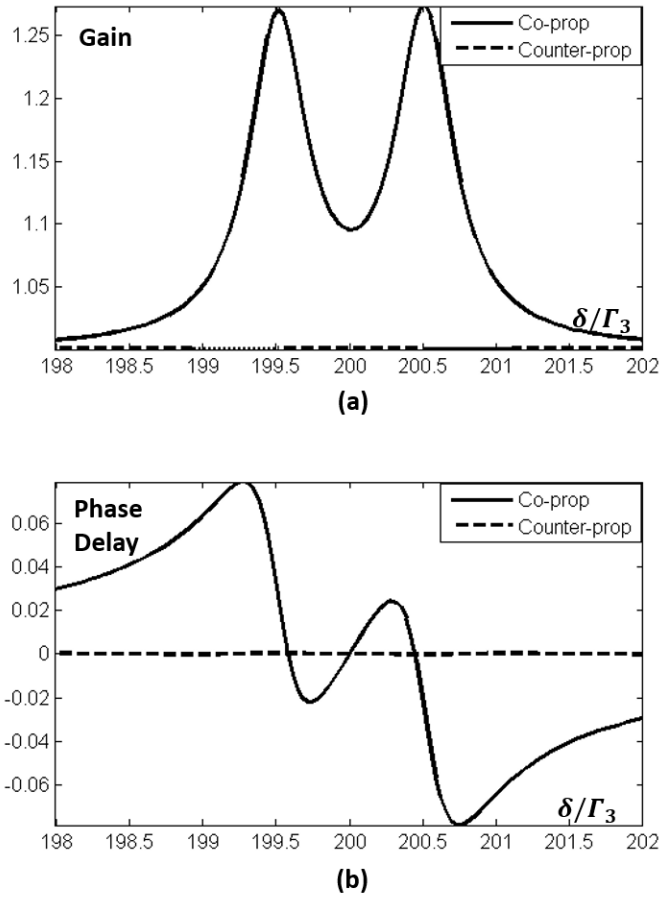

Figure 8.9 Comparison between co-propagating and counter-propagating cases.

Next, we consider the case where the two pumps are co-propagating, but the probe is propagating in the opposite direction. Physically, it is expected that the efficient gain in this case would come only for the zeros velocity band. Therefore, the next gain averaged over the velocity profile should be much smaller than that for the co-propagating case. This is indeed found to be the case, as shown in Figure 8.9.

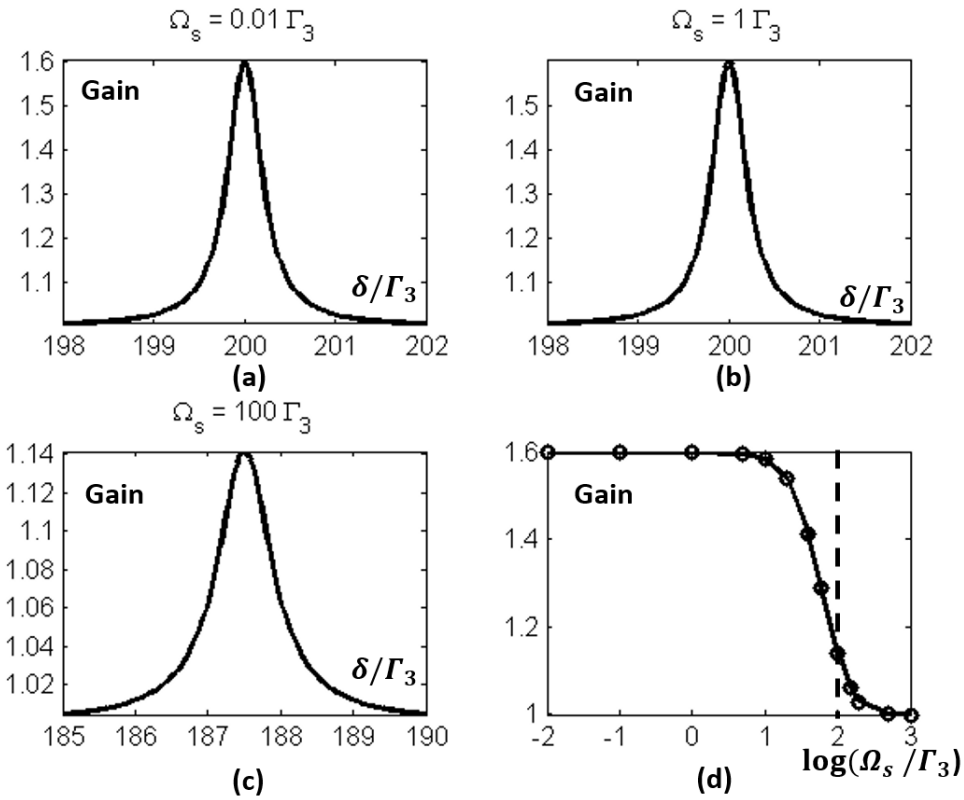

Figure 8.10 Gain suppressed by increasement of Ω_s in Single Raman model. Dashed line in plot (d) shows the theoretical value of gain saturation.

We consider next the saturation of the gain as a function of the probe power. Such a saturation is important in determining the steady-state property of a laser based on this gain profile. First, we consider the case where only a single Raman pump is present. This is illustrated in Figure 8.10. Here, we have used $\Omega_p = 2\Gamma_3$, $\Delta_p = 200\Gamma_3$, $N = 5 \times 10^{17} m^{-3}$, $L = 0.1m$, $\Gamma_{12} = 0.5\Gamma_3$. Figure 8.10. a-c show gain decreasing as the probe Rabi frequency is increased from $\Omega_s = 0.01\Gamma_3$ to $\Omega_s = 100\Gamma_3$. Figure 8.10.d shows the peak gain as a function of $\log(\Omega_s/\Gamma_3)$. The vertical line indicates the saturation point which occurs when the Raman

coupling rate matches the optical pumping rate $\Omega_s\Omega_p/(2\Delta_p) = \Gamma_{12}$, which correspond to $\Omega_s = 2\Gamma_3$.

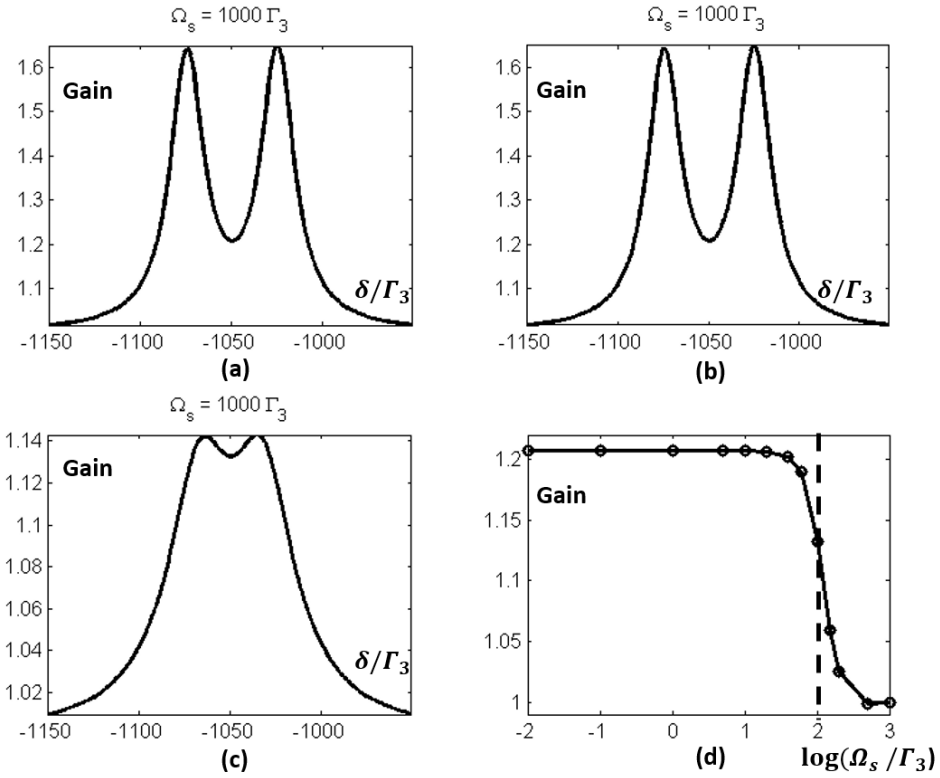

Figure 8.11 Gain suppressed by increasement of Ω_s in double Raman model. Dashed line in plot (d) shows the theoretical value of gain saturation.

Next, we show the gain saturation process for the case of double Raman pumps. Here, the gain value of most interest for realizing a superluminal laser is the one at the center. The results are shown in Figure 8.11, where we have used $\Omega_{p1} = \Omega_{p2} = 2\Gamma_3$, $\Delta = \Gamma_3$, $\Delta_p = 200\Gamma_3$, $N = 5 \times 10^{17} m^{-3}$, $L = 0.1m$, $M = 6$, and $\Gamma_{12} = 0.5\Gamma_3$. Figure 8.11. a-c show three cases where Ω_s is changed from $0.01\Gamma_3$ to $100\Gamma_3$. Figure 8.11.d shows the center gain as a function of Ω_s. Again, as expected, the gain saturates when $\Omega_s(\Omega_{p1} + \Omega_{p2})/(2\Delta_p) = \Gamma_{12}$, as indicated by the vertical line.

Comparison with experimental data

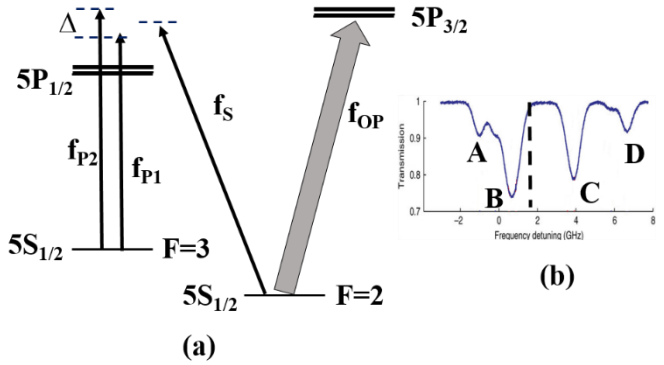

Figure 8.12 ^{85}Rb transitions. Plot (a) shows the experiment scheme. Plot(b) is a linear absorption spectrum of ^{85}Rb and ^{87}Rb. The dashed line indicates the frequency of $f_{p1.}$

We used a room-temperature cell of ^{85}Rb atom to carry out experimental investigation of the double-Raman gain. The transition used are illustrated schematically in Figure 8.12. As shown in Figure 8.12-a, the two Raman pumps, at frequencies f_{P1} and f_{P2}, are tuned slightly above the $5S_{1/2}$, F=3 → $5P_{1/2}$ transition. The frequency difference between these is denoted as $\Delta = f_{p2} - f_{p1}$. The probe beam, at frequency f_S, is applied along the $5S_{1/2}$, F=2 → $5P_{1/2}$ transition. The optical pumping is tuned to the $5S_{1/2}$, F=2 → $5P_{3/2}$ transition. Figure 8.12-b shows the selective position of the frequency f_{P1} with respect to a set of reference transitions in the D1 (~795nm) manifold, observed using a cell containing a natural mixture of ^{87}Rb and ^{85}Rb. Here, the A and D lines correspond to transition in ^{87}Rb, the B line corresponds to the $5S_{1/2}$, F=3 → $5P_{1/2}$ transition and the C line corresponds to the $5S_{1/2}$, F=2 → $5P_{1/2}$ transition in ^{85}Rb. As can be seen, the frequency f_{P1} is tuned just above the Doppler profile of the B line.

Figure 8.13 shows schematically the experimental setup. A Ti:Sapphire laser is used to generate the Raman pumps and the Raman probe. A part of the laser output is split off with a non-polarizing beam splitter (NPBS1), and passed through a reference vapor cell (Rb Cell 1). The laser frequency was scanned by applying a driving voltage $V_D = V_B + V_{SAW}$, where V_B is a bias voltage, and V_{SAW} is a sawtooth ramp, ranging from -|Vm| to |Vm|. The value of V_B was adjusted until the frequency of the laser at the zero-crossing point of V_{SAW} was found to be just above the $5S_{1/2}$, F=3 -> $5P_{1/2}$ transition in ^{85}Rb (as shown in Figure 8.12.b). The sawtooth ramp was then disconnected, thus parking the laser frequency at this point, denoted as f_{P2}. The Raman gain profile measurement was periodically interrupted, and the sawtooth was re-connected to ensure that the laser frequency remained at the same position. The Ti:Sapphire laser was stable enough so that only a minor adjustment of V_B was needed over the whole experimental period. The laser beam transmitted through NPBS1 was then passed through a Half-Wave Plat (HWP), followed by a Polarizing Beam Splitter (PBS1). The angle of the HWP was adjusted, as needed, to control the amount of light reflected by PBS1. The light transmitted through PBS1 was passed through NPBS2. The light transmitted through NPBS2 was passed through an Acousto-Optic Modulator (AOM3), driven by a VCO at frequency f_{AOM3}. The value of f_{AOM3} was set nominally at half the frequency difference (~3.034GHz) between the F=2 and F=3 states in the $5S_{1/2}$ manifold of ^{85}Rb. The light upshifted in frequency by f_{AOM3} was than reflected back and passed through the AOM3 again, thus producing light at frequency f_S, the Raman probe frequency. The value of f_S could be scanned across the two photon resonant condition for each Raman pump by tuning the value of f_{AOM3}. The field at f_S, emerging from AOM3 upon reflection, was then reflected partially

by NPBS2, and directed into the primary cell (Rb Cell 2) used for producing the Raman gain.

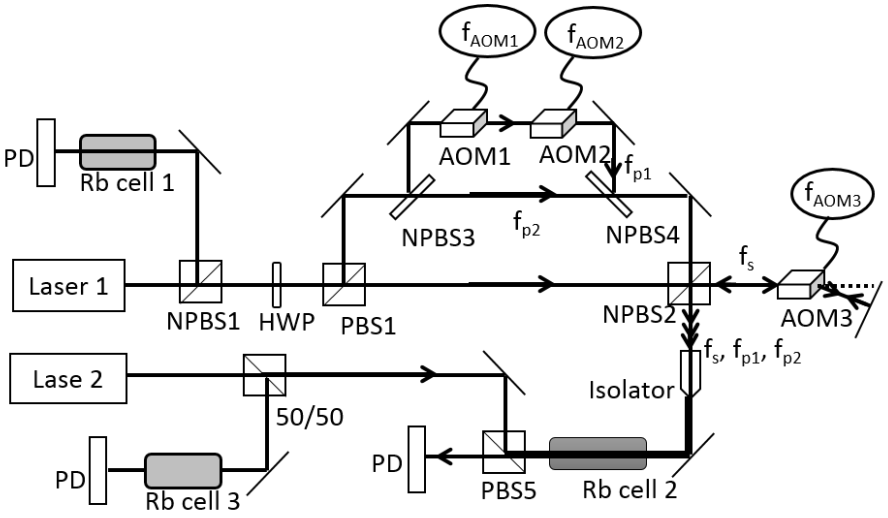

Figure 8.13 The experimental setup of double Raman Gain. Laser 1 is a Ti-Sapphire Laser operating at 795nm. Laser 2 is a Diode Laser with Tapered Amplifier operating at 780nm. See text for details.

The light reflected by PBS1 was passed through three consecutive beam splitters (NPBS3, NPBS4 and NPBS2) and also sent to the primary cell. This served as one of the Raman pumps at frequency f_{P2}. Light reflected by NPBS3 was passed through two sequential AOMs (AOM1 and AOM2), configured so that AOM1 shifted the frequency up by f_{AOM1}, and AOM2 shifted the frequency down by f_{AOM3}, thus producing the second Raman pump at frequency f_{P1}. Thus, we have $\Delta = f_{P1} - f_{P2} = f_{AOM1} - f_{AOM2}$. The value of Δ was tuned as necessary by changing both f_{AOM1} and f_{AOM2}. The beam at frequency f_{P1}, emerging from AOM2, was then reflected by NPBS4 and then passed through NPBS2, entering the primary cell (Rb Cell 2), while co-propagating with the other Raman pump as well as the probe. Note that the two Raman pumps have the same (linear) polarization, while the probe polarization is orthogonal to that of

the pumps. Upon exiting the primary cell, the beams were passed through another PBS (PBS2) thus separating the probe from the pumps. The transmitted probe power was monitored with a photodetector.

The beam necessary for the optical pumping, at frequency f_{OP}, was generated from a different laser system: a diode laser combined with a tapered amplifier. A part of the light from this laser was reflected by a beam-splitter (NPBS5), and passed through another reference Rb cell (Rb cell 3). The same technique as described above was used to ensure that this laser remained resonant with the $5S_{1/2}$, F=2 -> $5P_{3/2}$ transition in ^{85}Rb. The light passing through NPBS5 was then reflected by PBS2 into the primary cell.

The Solid line in Figure 8.14 shows a typical experimental result obtained with this setup. The vertical axis shows the gain experienced by the probe. The horizontal axis is the frequency of the probe, expressed in term of δ/Γ_3, where Δ_p is the mean detuning of the two Raman pumps (see Figure 8.12.a), δ is the detuning of the Raman probe, and Γ_3 is the radiative linewidth of the intermediate state, which is $\sim 2\pi * 6 * 10^6 \mathrm{sec}^{-1}$. For this data, we have $\Delta_p/\Gamma_3 \sim 200$ and $\Delta/\Gamma_3 = 1.365$. The cell was heated to ~90℃, corresponding to a density of ~2*10^{16}m^{-3}[95].The power in the first Raman (lower frequency) pump was 48.4mW, and that in the second Raman pump was 12.9mW. The power in the probe beam was $150\mu W$. The diameter of the probe was about the same as that of the first Raman pump ($d_{pump1}/d_{probe} \cong 1$), while the diameter of the second Raman pump was somewhat bigger ($d_{pump1}/d_{pump2} \cong 0.75$).

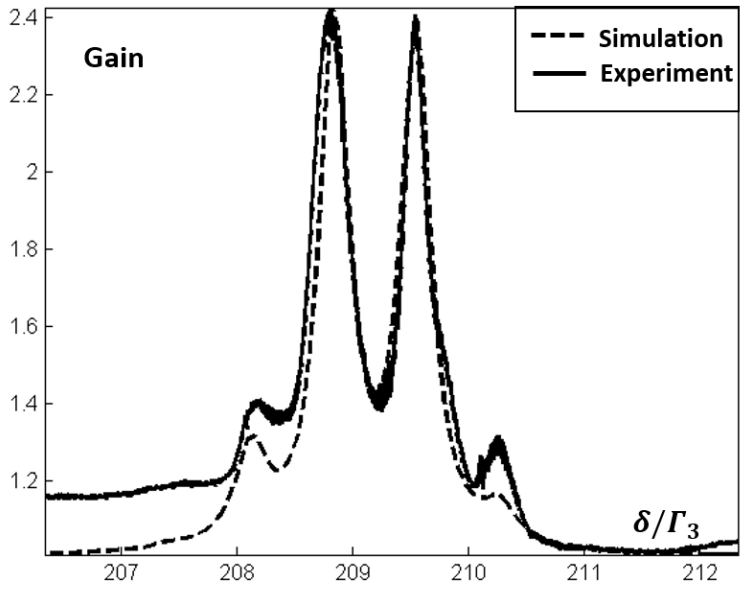

Figure 8.14 Experimental data vs simulation results. See text for details.

The dashed line in Figure 8.14 shows the result of the simulation, corresponding to this data. Here, we increased the value of M until a stable result was obtained for $M \geq 7$. The plot shown corresponds to M=7. For the simulation, we have used the pump and probe powers listed above, and used the same ratios for the beam diameter shown above. However, the actual size of the diameter for the first Raman pump was used as a fitting parameter. This was necessary became the absolute calibration of the beam profile used to measure the beam diameters was somewhat inaccurate. A value of $d_{pumps} \cong 1.4mm$ produced the plot shown here. We also assumed that the transition strength for each leg of the Raman transition is the same, with a saturation intensity that is 1.5 times larger than that for the strongest (cycling) transition in the D2-manifold of ^{85}Rb (i.e., the F=3, $m_F \rightarrow F' = 4, m_F = 4$ transition). This is an approximation based on considering all different Zeeman sublevels that actually

contribute to the Raman transition for the cross linear polarization used. A more accurate calculation would have to keep track of all the Zeeman sublevels explicitly, and will be carried out in the near future. Similarly, we have used an approximated value of $\Gamma_{12} \cong 0.35\Gamma_3$, while the maximum possible value of this rate is ~ $0.5\Gamma_3$. The peak value of the gain for the simulation was found to be ~2.4. However, the peak value of the gain observed experimentally was somewhat uncertain due to some imprecision in the measurement of the amplified and unamplified probe power.

8.2 Subluminal Laser

In our proposed system for an SLL, as summarized in Figure 8.15, the gain spectrum consists of two parts: a narrow gain peak added on top of a broad gain spectrum. We use Rb vapor as a specific example of a medium that can be used to realize this. The broad gain is provided by the same mechanism as is used for realizing the conventional DPAL (Diode Pumped Alkali Laser) [96,97,98,99,100,101]. A spectrally broad pump is applied on the D_2 line in a cell filled with a high pressure (~1 atm or more) of Ethane or ^{4}He. Rapid relaxation (induced by the buffer gas) of atoms from the $P_{3/2}$ to the $P_{1/2}$ manifold thus leads to gain on the D_1 line, with a spectral width as much as 5 GHz for a buffer gas pressure of 1 atm, and much larger with higher buffer gas pressures. DPALs with output powers of close to 50 watt [98] have been reported in the literature. The gain peak is provided by adding to the cavity a second Rb cell, without any buffer. An optical pumping beam is applied to this cell to produce a Raman population inversion between the two hyperfine levels in the ground state ($|1\rangle$ and $|2\rangle$ in Figure 8.15.b. A piece of the linearly polarized output of the laser, at

frequency f_1, is rotated in polarization by 90°, and shifted in frequency (by an acousto-optical modulator, AOM-1) by an amount that matches the ground state hyperfine splitting in Rb (~3.034 GHz for ^{85}Rb, for example) to produce the Raman probe beam (at frequency f_2), which is applied to the second cell, by using a polarizing beam splitter (PBS), and then ejected from the lasing cavity by another PBS. Depending on the transition used for the optical pumping, this beam produces either a dip or a peak in the gain spectrum for the lasing field, with a width that can be as narrow as a few hundred KHz. When a gain dip is produced, the system becomes a superluminal laser under a carefully tuned set of parameters that produces $n_g \cong 0$ [20]. When a gain peak is produced, the system becomes an SLL, with the enhancement in stability given by the value of n_g corresponding to the gain peak, which can be as high as 10^5.

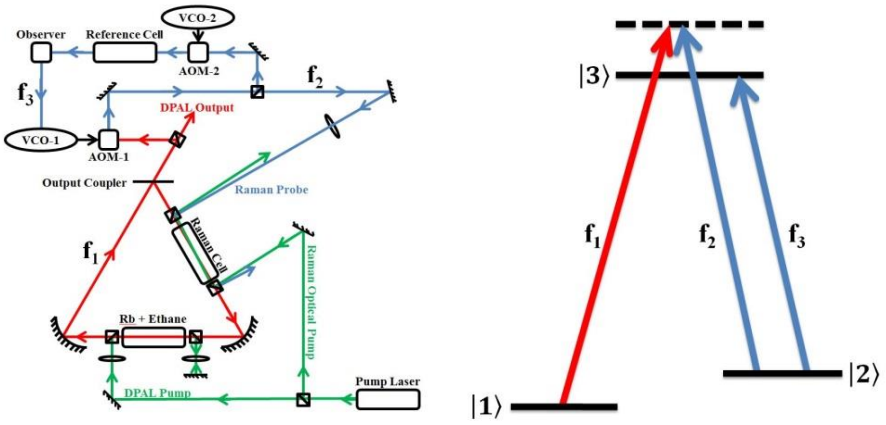

(a) (b)

Figure 8.15 (a) Schematic of the configuration for a subluminal laser and (b) Raman transitions.

It should be noted that in order for the lasing mode to experience a peak (or dip) in the gain, it is necessary for the frequency of the Raman probe beam to remain fixed at an absolute value. To accomplish this, a piece of the Raman probe beam is shifted in frequency by another AOM (AOM-2) to a value (f_3) that becomes resonant with an atomic transition (the $|2\rangle \leftrightarrow |3\rangle$ transition, for example). The beam at frequency f_3 is sent through a reference cell (e.g., a saturated absorption cell), and a feedback generated from the resonance observed in this cell is applied to the voltage controlled oscillator (VCO-1) that determines the frequency of AMO-1. Thus, if the frequency (f_1) of the laser moves (e.g., due to a change in the cavity length), the frequency output of VCO-1 is automatically adjusted to ensure that f_2 remains resonant, and thereby f_1 remains fixed, assuming that the frequency of the VCO (VCO-2) used for AOM-2 remains stable. If a frequency synthesizer is used instead of a VCO for AOM-2, it is possible to keep the frequency of AOM-2 (i.e., (f_2-f_3)) very stable. However, for Rb, Raman probe can be locked to a transition in ^{87}Rb without shifting its frequency, which means that AOM-2 is not necessary in this approach. For example, the short term fractional frequency stability of an oven-controlled crystal oscillator can be $\sim 10^{-12}/\sqrt{\tau}$, where τ is the observation time (in unit of second). Long term stability can be provided by referencing this oscillator to an atomic clock, for example. We should note that a similar scheme can also be employed to increase the stability of a Raman laser, by locking a frequency-shifted piece of the Raman pump to an atomic transition.

We first consider a model of an SLL with idealized gain media, which can be analyzed easily through the semi-classical equation of motion for a single model laser **[**102**]**. Inside the laser cavity, the phase and the amplitude of the field, assumed to be in single mode, are

described by the following equations [102]:

$$\upsilon + \dot{\varphi} = \Omega_c - \frac{\chi'}{2}\upsilon, \tag{8.23}$$

$$\dot{E} = -\frac{\upsilon E}{2Q} - \frac{\chi'' E}{2}\upsilon, \tag{8.24}$$

where υ is the lasing frequency; φ and E are the phase and the amplitude of the lasing field, respectively; Ω_c is the resonant frequency of the cavity without any medium, which is given by $2\pi mc/L$ where L is the cavity length; Q is the quality factor of the cavity; and χ' and χ'' are the real and imaginary part of the susceptibility of the gain medium, respectively. Suppose ν_0 is the frequency around which χ'' is symmetric. We then define as L_0 the length of the cavity for which $\Omega_c = \nu_0$. In this model, while L varies around L_0, Ω_c will derivate from ν_0.

For convenience, we define the parameters: $\Delta \equiv \Omega_c - \upsilon_0, \delta \equiv \upsilon - \upsilon_0$. The derivatives $d\Delta/dL$ and $d\delta/dL$ characterize the resonant frequency shifts produced from a perturbation of L in the empty and filled cavity, respectively. The ratio between the two derivatives, $R \equiv (d\delta/dL)/(d\Delta/dL)$, determines whether the amount of the frequency shift is enhanced ($R>1$) or suppressed ($R<1$) by the intracavity medium. To derive an explicit expression for R, we first solve Eqn.8.23 in steady state. After subtracting ν_0 from both sides, differentiating with respect to L, and applying $dv = d\delta$, we get $d\delta/dL + \chi'/2(d\delta/dL) + v/2(d\chi'/dL) = d\Delta/dL$. By substituting $d\chi'/dL$ by $(d\chi'/d\delta)(d\delta/dL)$, R can be expressed as:

$$R = 1/\left(1 + \frac{\chi'}{2} + \frac{v}{2}\frac{d\chi'}{dv}\right). \tag{8.25}$$

Let us consider the case in which the cavity contains a medium with a narrow absorption as well as a medium with a broad gain. For simplicity we assume that the media overlap each

other, and fill the whole cavity. This configuration creates a net gain profile with a dip in the center. The imaginary part of the susceptibility χ'' can then be written as:

$$\chi'' = -\frac{G_e {\Gamma_e}^2}{2{\Omega_e}^2+{\Gamma_e}^2+4(\nu-\nu_0)^2} - \frac{G_i {\Gamma_i}^2}{2{\Omega_i}^2+{\Gamma_i}^2+4(\nu-\nu_0)^2}, \tag{8.26}$$

where the subscripts *e* and *i* refer to the envelop gain profile and the narrow gain profile, respectively; G_k presents the gain parameter (k=i, e), which is defined as $G_k \equiv \hbar N_k \xi_k/\varepsilon_0$, where N_k is the density of the quantum systems for the medium, ξ_k is defined as $\xi_k \equiv \wp_k^2/(\hbar^2\Gamma_k)$ using the Wigner-Weisskopf model [103] for spontaneous emission, and ε_0 is the permittivity of free space and $\wp_k$ is the dipole momentum. Here, Γ_k presents the linewidth, Ω_k is the Rabi frequency, and ν is the lasing frequency. Then, applying the modified Kramers-Kronig relation [104,105,106], the real part of the susceptibility can be expressed as:

$$\chi' = \frac{2G_e(\nu-\nu_0)\Gamma_e}{2{\Omega_e}^2+{\Gamma_e}^2+4(\nu-\nu_0)^2} + \frac{2G_i(\nu-\nu_0)\Gamma_i}{2{\Omega_i}^2+{\Gamma_i}^2+4(\nu-\nu_0)^2}. \tag{8.27}$$

We fist consider a conventional, homogeneously broadened gain medium, i.e., $G_i = 0$. From Eqn.8.26 and 8.27, χ' and χ'' are then simply related to each other as $\chi'/\chi'' = -2(\nu-\nu_0)/\Gamma_e$. Under steady state lasing condition, $\chi'' = -1/Q$, which leads to $\chi' = -2(\nu-\nu_0)/(Q\Gamma_e)$. As shown in this expression, χ' is a linear function of ν, and antisymmetric around ν_0. Noting that $Q = \nu_0/\Gamma_c$, where Γ_c is the linewidth of the empty cavity, we find that $R = 1/n_g$, where $n_g = 1 + \Gamma_c/\Gamma_e$. Since $n_g > 1$, the sensitivity is suppressed by a conventional gain medium when compared to an empty cavity. In a typical laser, Γ_c/Γ_e is very small, so that this reduction is rather insignificant.

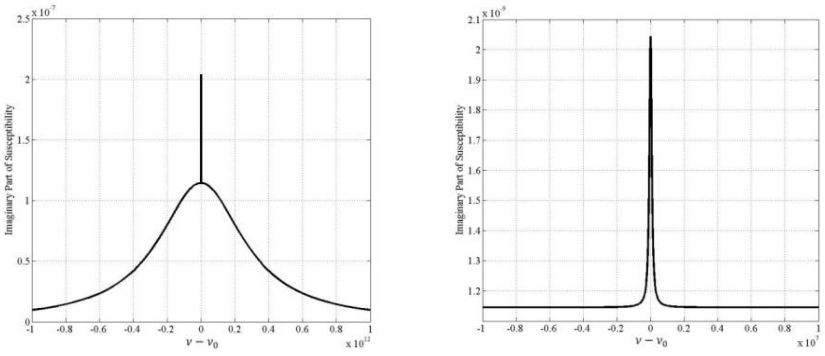

(a) (b)

Figure 8.16 Gain profile based on the analytical model for an idealized SLL: (a) overall gain spectrum and (b) Raman gain.

For the case of a conventional laser medium discussed above, it was easy to determine the value of χ' due to the simple ratio between χ' and χ''. In particular, this ratio does not depend on the laser intensity. However, for the SLL (i.e. $G_i \neq 0$), the two terms in χ'' are highly dissimilar (as shown in Figure 8.16), i.e., the amplitude and the linewidth of the narrow gain peak are significantly different from that of the envelop profile. Therefore, it is no longer possible to find a ratio between χ' and χ'' that is independent of the laser intensity. Thus, in this case, it is necessary to determine first the manner in which the laser intensity depends on all the parameters, including ν. We define $I \equiv |E|^2$ so that ${\Omega_k}^2 \equiv \Gamma_k I \xi_k$. Therefore, Eqn.8.26 and 8.27 become:

$$\chi'' = -\frac{G_e {\Gamma_e}^2}{2\Gamma_e \xi_e I + {\Gamma_e}^2 + 4(\nu-\nu_0)^2} - \frac{G_i {\Gamma_i}^2}{2\Gamma_i \xi_i I + {\Gamma_i}^2 + 4(\nu-\nu_0)^2}, \tag{8.28}$$

$$\chi' = \frac{2G_e(\nu-\nu_0)\Gamma_e}{2\Gamma_e \xi_e I + {\Gamma_e}^2 + 4(\nu-\nu_0)^2} + \frac{2G_i(\nu-\nu_0)\Gamma_i}{2\Gamma_i \xi_i I + {\Gamma_i}^2 + 4(\nu-\nu_0)^2}. \tag{8.29}$$

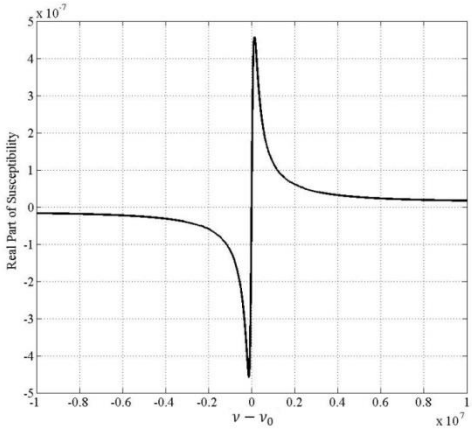

Figure 8.17 Real part of the susceptibility of the model for idealized SLL after lasing.

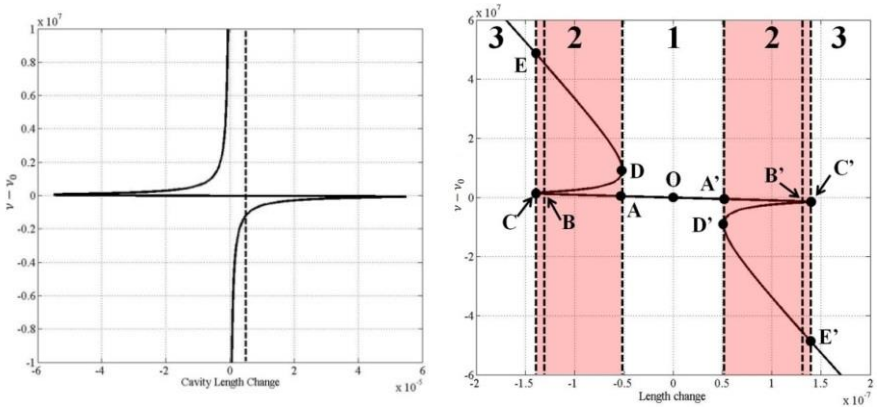

(a) (b)

Figure 8.18 Relationship between cavity length and lasing detuning for the idealized SLL for (a) extremely high stability enhancement and (b) relatively low stability enhancement.

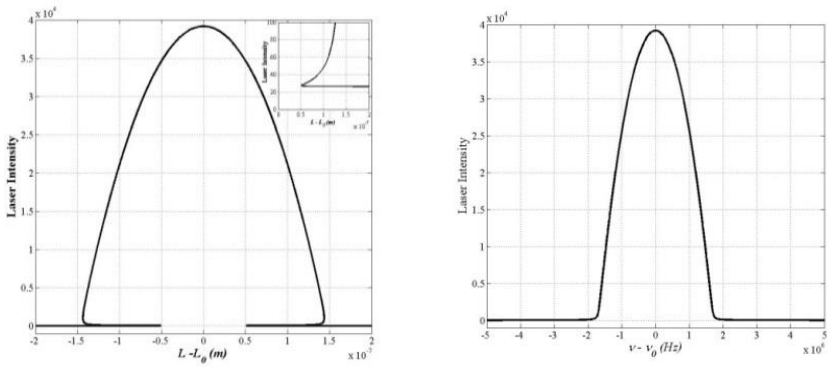

(a) (b)

Figure 8.19 Laser output intensity as a function of (a) length change and (b) laser frequency. The inset in plot (a) shows a blown up view of the multiple values of the intensity over a small vertical range.

Parameters	**Value**
Γ_e	$2\pi \times 5 \times 10^8\ s^{-1}$
Γ_i	$2\pi \times 10^2\ s^{-1}$
v_0	$2\pi \times 3.8 \times 10^{14}\ s^{-1}$
N_e	1×10^6
N_i	1×10^{14}
Q	1.5×10^7
m	1282051
L_0	$0.99999978\ m$
G_e	6.667×10^{-7}
G_i	6.667×10^{-3}

Table 8.1 Parameters used in the analytical model.

By setting Eqn.8.28 equal to −1/Q, we get $aI^2 + bI + c \equiv 0$, where a, b, and c are functions of various parameters. We keep the solution that is positive over the lasing bandwidth: $I = \left(-b + \sqrt{b^2 - 4ac}\right)/(2a)$. Substituting this solution for *I* to evaluate ${\Omega_i}^2$ and ${\Omega_e}^2$ in Eqn.8.29, we get an analytic expression for χ', which is plotted in Figure 8.31. We

note next that the steady state solution of Eqn.8.23 implies that $L = (2\pi mc/v)/(1 + \chi'/2)$. Using this expression, we can thus plot *L* as a function of *v*, as shown in Figure 8.18. All the parameters used for generating Figure 8.16, Figure 8.17, Figure 8.18.a, and Figure 8.19 are listed in Table 8.1.

The condition used in generating Figure 8.18.a corresponds to a group index of $n_g(v = v_0) \sim 2.3 \times 10^5$, as noted earlier the factor by which frequency fluctuation is suppressed in an SLL is given by this value. As such, the conditions used here correspond to a highly stable SLL.

It should be noted, however, that when the cavity length changes sufficiently from its quiescent value of L_0, e.g.: $L - L_0 = 0.5 \times 10^{-5} m$, corresponding to the dashed vertical line in Figure 8.18.a, there are multiple solutions of the laser frequency for a given length. In order to understand what this implies, we consider first a different set of parameters for which n_g is much smaller $\left(n_g(v = v_0) \sim 160\right)$, and the corresponding plot of frequency versus length is shown in Figure 8.18.b. This figure can be divided into three regions. In region 1 and 3, there exists only one solution. But in region 2, the laser equations have two or three solutions, i.e. for a specific cavity length, there are multiple potential lasing frequencies. However, the compound gain medium to be used for realizing the SLL is homogeneously broadened, as discussed in detail later in this paper. As such, mode competition is likely to ensure that only one of these solutions will survive in steady state. A detailed calculation involving nearly-degenerate multiple modes and the gain competition between these modes is needed to determine the exact behavior of the SLL in this region, and will be carried out in the near future, using the practical example we describe in the next section. Nonetheless, we

can understand the behavior of the laser over a limited range of length changes. Assume, for example, that the cavity length is L_0 before the gain is activated. In this case, the SLL will lase at $\upsilon = \upsilon_0$, corresponding to the point O in Figure 8.18.b. If ΔL now stays small enough so that the SLL stays within zone 1, the SLL will move along the line AOA'. If ΔL is large enough, but still smaller than $|OB| = |OB'|$, the SLL will stay on the BAOA'B' line, since the gain in the two other possible modes (within zone 2) will be highly suppressed, given the fact that the SLL is already lasing in the primary mode. Similarly, if ΔL is large enough so that the SLL moves to zone 3, it will jump to the unique frequency corresponding to that zone. The only concern would be when the value of ΔL is such that the SLL reaches point C or C'. In that case, it is not clear whether its frequency will follow the CA line or the CD line when ΔL is reduced. As stated above, this question can only be answered by a study of the temporal dynamics of the cavity field. Thus, if the SLL is operated in such a manner that ΔL remains less than $|OC| = |OC'|$, it will operate in the stable mode, which will experience the enhanced stability in frequency. In what follows, we will refer to this range as the primary mode zone, and the stable mode as the primary mode.

In Figure 8.19.a we plot the output intensity of the laser as a function of the cavity length, for the parameters used in producing Figure 8.18.b. As can be seen, the intensity has a unique value for some ranges of the cavity length, but has multiple possible values over the ranges for which the frequency also has multiple values (see Figure 8.18.b). Again, for our current model, it is not clear as to what the actual value of the intensity would be, and this issue can only be resolved by studying the temporal dynamics, as noted above.

In Figure 8.19.b, we show the output intensity as a function of the laser frequency. This plot

is generated by combining the information presented in Figure 8.18 and Figure 8.19.a. As can be seen, there is a one-to-one correspondence between the intensity and the frequency, for all values of the cavity length. In Figure 8.20.a, we show the laser frequency versus the cavity length for the primary mode, corresponding to the parameters used in Figure 8.18.a. The resulting enhancement in stability is shown in Figure 8.20.b. As can be seen, the stability of the SLL can be $\sim 10^5$ times higher than that of a conventional laser when operating near the center frequency.

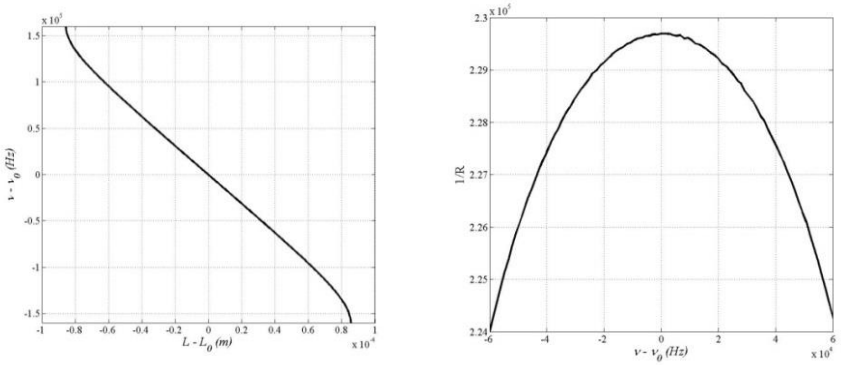

(a) (b)

Figure 8.20 Desired region of operation for the idealized SLL: (a) laser detuning vs. length change and (b) enhanced stability of the SLL.

8.2.1 Theoretical model of an actual SLL

The gain spectrum we have considered so far is, of course, only an ideal one. The behavior of a real system would certainly deviate from such a model. Here, we consider an atomic system that can be tailored to produce a gain spectrum that is very similar to the ideal

one presented above, and determine the expected behavior of an SLL potentially realizable using such a system.

The broad gain profile can be realized using an alkali vapor cell, containing both naturally occurring isotopes of Rb (^{87}Rb and ^{85}Rb), in the presence of a high pressure buffer gas of Ethane. Such a gain medium has recently been used to make the so called DPAL (diode pumped alkali laser). It has also been used recently by us to demonstrate a high-speed optical modulator [107]. The narrow gain profile can be realized using a separate vapor cell, placed in series, containing only ^{85}Rb, configured for Raman gain.

In this case we find the dispersion and absorption of the media by solving the density matrix equations in steady state. Specifically, we employ the Liouville equation, which describes the evolution of the density matrix:

$$\frac{\partial}{\partial t}\tilde{\rho} = -\frac{i}{\hbar}\left[\tilde{\tilde{H}}, \tilde{\rho}\right] + \frac{\partial \tilde{\rho}}{\partial t}_{source} + \frac{\partial \tilde{\rho}}{\partial t}_{dephasing} \tag{8.30}$$

where, $\tilde{\rho}$ is the density matrix in the rotating wave basis, $\tilde{\tilde{H}}$ is the modified time independent Hamiltonian under rotating wave approximations (RWA) augmented by adding complex terms to its diagonal elements in order to represent decays of atomic levels, $\tilde{\rho}_{source}$ represents the influx of atoms into a state due to decay from another state, and $\tilde{\rho}_{dephasing}$ accounts for the dephasing between states induced by the buffer gas [16]. Given the different configuration and parameters used for the two cells, it is necessary to solve the Liouville equation separately for each cell.

For the cell that produces the DPAL-type gain, we use a laser beam tuned to the D2 transition of Rb as the optical pump. The specific parameters, including the frequency of this

pump, are specified later in this section. This pump couples atoms from both hyperfine levels in the $5S_{1/2}$ states to the $5P_{3/2}$ manifold. The presence of a high pressure buffer gas (~0.5 atm of Ethane) causes rapid dephasing of the coherence corresponding to the $5S_{1/2}$, F=1 - $5P_{3/2}$ transition as well as the coherence corresponding to the $5S_{1/2}$, F=2 - $5P_{3/2}$ transition, thus producing a homogeneous broadening of each of these transitions by ~7GHz (for 0.5 atm pressure of Ethane). Furthermore, the buffer gas causes the atom in the $5P_{3/2}$ manifold to decay rapidly to the $5P_{1/2}$ manifold, at a rate that is much faster than the radiative decay rate for the atoms in the $5P_{1/2}$ manifold. As a result, a population inversion is created between the $5P_{1/2}$ manifold and the $5S_{1/2}$ manifold. This inversion provides the broad band gain profile.

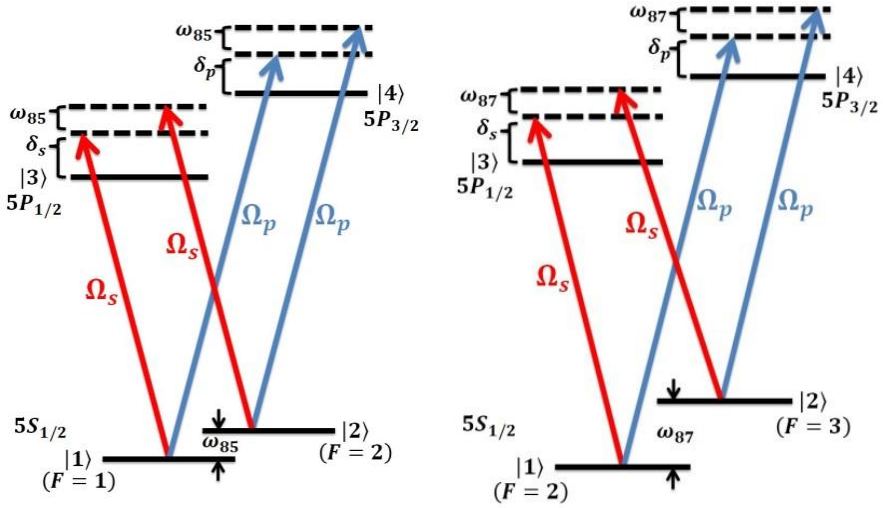

(a) (b)

Figure 8.21 Transitions in the broad gain model for (a) ^{85}Rb and (b) ^{87}Rb.

The homogeneous broadening induced by the buffer gas is significantly larger than the hyperfine splittings within the $5P_{1/2}$ and the $5P_{3/2}$ manifolds. However, it is of the order of the hyperfine splitting in the $5S_{1/2}$ manifold. Thus, we treat the $5P_{1/2}$ and $5P_{3/2}$ manifolds as single

energy levels, but keep track of the two hyperfine levels inside the $5S_{1/2}$ manifolds separately. Therefore, we have a four level system, as shown in Figure 8.21. Plot (a) shows the system for ^{85}Rb. Here $|1\rangle$ is the $5S_{1/2}$, F=2 state, $|2\rangle$ is the $5S_{1/2}$, F=3 state, $|3\rangle$ is the $5P_{1/2}$ manifold, and $|4\rangle$ is the $5P_{3/2}$ manifold. The corresponding system for ^{87}Rb is shown in plot (b), where $|1\rangle$ is the $5S_{1/2}$, F=1 state, $|2\rangle$ is the $5S_{1/2}$, F=2 state, $|3\rangle$ is the $5P_{1/2}$ manifold, and $|4\rangle$ is the $5P_{3/2}$ manifold. In our model, we consider a cell that contains a natural mixture (72.16% of ^{85}Rb, 27.84% of ^{87}Rb) of both stable isotopes of Rubidium. We compute the gain produced by each isotope separately, and add the weighted sum to find the net gain. In doing so, we keep track of the differences in the absolute frequencies of the transitions in these two isotopes. For each isotope of Rb, we assume that the pump beam excites both the $|1\rangle - |4\rangle$ and the $|2\rangle - |4\rangle$ transitions. We assume the transition strengths (i.e. the Rabi frequencies) to be the same, for both transitions, for simplicity.

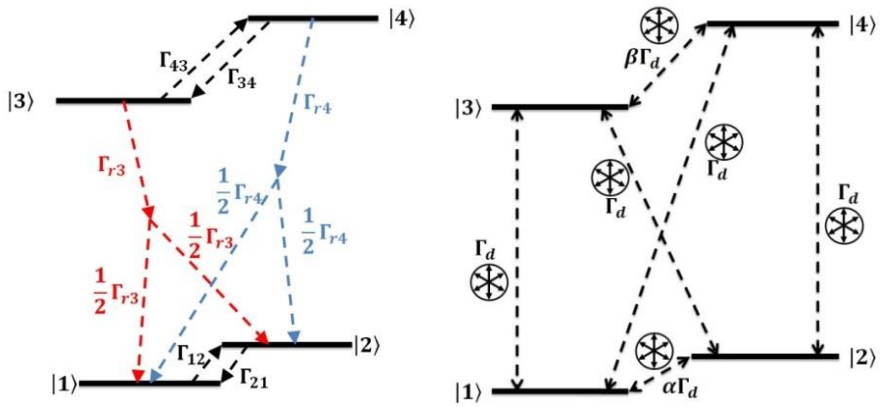

Figure 8.22 In the broad gain model: (a) population decay rates and (b) additional dephasing of coherence due to collisions.

A more accurate calculation would require taking into account the hyperfine levels within the $5P_{3/2}$ manifold, as well as the Zeeman sublevels within each hyperfine states, and the various dipole-moment matrix elements among them [16]. Such a calculation will be carried out and reported in the near future. Similarly, for each isotope of Rb, we assume that the probe beam excites both the $|1\rangle - |3\rangle$ and the $|2\rangle - |3\rangle$ transitions, with equal transition strengths. Other potential issues in a DPAL, such as non-Lorentzian behavior and bleaching of the pump transition are not taken into account in our model. [108,109]

The relevant decay and dephasing rates are illustrated schematically in Figure 8.22. In plot (a), we show only the rates of population decays, due to radiative as well as non-radiative (i.e. collisional) processes. Specifically, Γ_{r3} and Γ_{r4} are the radiative population decay rates which are the inverses of the radiative lifetimes 27.7 ns and 26.24 ns [95,87], respectively. Thus, $\Gamma_{r3} = 36.1 \times 10^6\ sec^{-1}$, and $\Gamma_{r4} = 38.1 \times 10^6\ sec^{-1}$. For simplicity, we again assume that the decay rate of atoms from $|4\rangle$ to $|1\rangle$ is the same as that of atoms from $|4\rangle$ to $|2\rangle$, given by $\Gamma_{r4}/2$. As noted earlier, use of a more accurate branching ratio would require taking into account the dipole-moment matrix elements coupling all the Zeeman sublevels. A detailed calculation of this type would be carried out and reported in the near future. Similarly, we assume that the decay rates to $|1\rangle$ and $|2\rangle$ from state $|3\rangle$ are the same, given by $\Gamma_{r3}/2$. The collisional decay rate, Γ_{43}, at a temperature of ~100 °C, is known to be $\sim 1.41 \times 10^7\ sec^{-1}/Torr$. For a buffer gas pressure of 0.5 atm (~380 Torr) assumed here, we thus have $\Gamma_{43} \simeq 5.36 \times 10^9\ sec^{-1}$. The value of Γ_{34} is determined by assuming thermal equilibrium, obeying the Boltzmann relation. Give that the number of Zeeman sublevels in

the $5P_{3/2}$ manifold is twice as large as the number of Zeeman sublevels in the $5P_{1/2}$ manifold, for both isotopes, we have:

$$\frac{\Gamma_{34}}{\Gamma_{43}} = 2exp\left(-\frac{\Delta E_{43}}{k_B T}\right), \tag{8.31}$$

where ΔE_{43} is the energy difference between states $|4\rangle$ and $|3\rangle$, T is the temperature in Kelvin, and k_B is the Boltzmann constant. Given that ΔE_{43} is approximately the same in both ^{85}Rb and ^{87}Rb, we get that $\Gamma_{34} \simeq 4.27 \times 10^9\ sec^{-1}$. Similarly, the decay rates Γ_{12} and Γ_{21} are related to each other as:

$$\frac{\Gamma_{12}}{\Gamma_{21}} = \frac{5}{3}exp\left(-\frac{\Delta E_{21}}{k_B T}\right), \tag{8.32}$$

where, for both isotopes, the ratio of the number of Zeeman sublevels in levels $|2\rangle$ and $|1\rangle$ is 5/3, and ΔE_{21} is the energy difference between levels $|2\rangle$ and $|1\rangle$. Since $k_B T \gg \Delta E_{21}$ for both isotopes, we get that $\Gamma_{12} \simeq 1.67\Gamma_{21}$. In the absence of buffer gas, the value of $(\Gamma_{21}/2\pi)$ is $\sim 1\ MHz$. The exact effect of the high pressure buffer gas (such as Ethane used to produce DPAL type gain) on this rate has, to the best of our knowledge, not yet been studied, experimentally or theoretically. We assume this effect to be small, and choose $\Gamma_{21} \simeq 2\pi \times 10^6\ sec^{-1}$, so that $\Gamma_{12} \simeq 2\pi \times 1.6 \times 10^6\ sec^{-1}$. These decay terms also contribute to dephasing of the coherence among these states. Specifically, if a state $|i\rangle$ has a net population decay rate of γ_i, and state $|j\rangle$ has a net population decay rate of γ_j, then the $\tilde{\rho}_{ij}$ coherence decays at the rate of $\frac{1}{2}(\gamma_i + \gamma_j)$. As mentioned above, the population decay rates, as well as the dephasing due to these decays, are taken into account by adding a term $-i\hbar\gamma_j/2$ to the *j*-th diagonal element of the Hamiltonian. The influxes of atoms into various states, on the other hand, are taken into account by the second term in Eqn.8.30.

The coherence between two states can undergo additional dephasing due to collisions with the high pressure buffer gas. These buffer-gas-induced (BGI) dephasing rates are illustrated in Figure 8.22.b, and are accounted for by the third term in Eqn.8.30. The BGI dephasing rates of $\tilde{\rho}_{13}$, $\tilde{\rho}_{23}$, $\tilde{\rho}_{14}$, and $\tilde{\rho}_{24}$ are nearly equal to one another, denoted as Γ_d. The value of Γ_d is known [110] to be $\sim 2\pi \times 2 \times 10^7\ sec^{-1}/Torr$, when Ethane is used as a buffer gas. Thus, for a buffer gas pressure of 0.5 atm (~380 Torr) assumed here, we get $\Gamma_d \simeq 2\pi \times 7.6 \times 10^9\ sec^{-1}$. On the other hand, the BGI dephasing rates of $\tilde{\rho}_{34}$ and $\tilde{\rho}_{12}$ for high pressure buffer gases have not been investigated theoretically or experimentally. However, based on the physical processes involved in producing the BGI dephasing of the optical coherences (i.e. $\tilde{\rho}_{13}$, $\tilde{\rho}_{23}$, $\tilde{\rho}_{14}$, and $\tilde{\rho}_{24}$), it is reasonable to assume that these rates are comparable to Γ_d. Specifically, we write the BGI dephasing rate of $\tilde{\rho}_{12}$ ($\tilde{\rho}_{34}$) as $\alpha\Gamma_d$ ($\beta\Gamma_d$), where α and β are parameters with values of the order of unity. Since the amount of $\tilde{\rho}_{12}$ or $\tilde{\rho}_{34}$ coherence produced by the probe is expected to depend very weakly on the actual value of α and β, as we will show later. Based on these findings, we will use $\alpha = \beta \simeq 1$ for our model.

The modified time independent Hamiltonian under RWA augmented by adding complex terms to its diagonal elements of ^{85}Rb and ^{87}Rb can be written as:

$$\frac{2\tilde{\tilde{H}}_k}{\hbar} = (-i\Gamma_{12})|1\rangle\langle 1| + (2\omega_k - i\Gamma_{21})|2\rangle\langle 2| + [-2\delta_s - i(\Gamma_{r3} + \Gamma_{34})]|3\rangle\langle 3| + \big[-2\delta_p - i(\Gamma_{r4} + \Gamma_{43})\big]|4\rangle\langle 4| + \big\{\big[\Omega_s|1\rangle\langle 3| + \Omega_p|1\rangle\langle 4| + \Omega_s|2\rangle\langle 3| + \Omega_p|2\rangle\langle 4|\big] + h.c.\big\}, \quad (8.33)$$

where the subscript k refers to ^{85}Rb or ^{87}Rb; Ω_s and Ω_p are the Rabi frequencies of the signal field and the optical pump field, respectively; δ_s is the detuning of the signal field with respect to the $|1\rangle - |3\rangle$ transition; δ_p is the detuning of the pump field with respect to the $|1\rangle - |4\rangle$ transition; and ω_k is the energy difference between levels $|2\rangle$ and $|1\rangle$ with the different values for the two isotopes. The influx of atoms into various states is:

$$\frac{\partial\tilde{\rho}}{\partial t}_{source} = (\Gamma_{21}\tilde{\rho}_{22} + \Gamma_{r3}\tilde{\rho}_{33}/2 + \Gamma_{r4}\tilde{\rho}_{44}/2)|1\rangle\langle 1| + (\Gamma_{12}\tilde{\rho}_{11} + \Gamma_{r3}\tilde{\rho}_{33}/2 + \Gamma_{r4}\tilde{\rho}_{44}/2)|2\rangle\langle 2| + \Gamma_{43}\tilde{\rho}_{44}|3\rangle\langle 3| + \Gamma_{34}\tilde{\rho}_{33}|4\rangle\langle 4|, \quad (8.34)$$

And the matrix which describes the BGI dephasing is:

$$\frac{\partial\tilde{\rho}}{\partial t}_{dephasing} = -[\alpha\Gamma_d\tilde{\rho}_{12}|1\rangle\langle 2| + \Gamma_d\tilde{\rho}_{13}|1\rangle\langle 3| + \Gamma_d\tilde{\rho}_{14}|1\rangle\langle 4| + \Gamma_d\tilde{\rho}_{23}|2\rangle\langle 3| + \Gamma_d\tilde{\rho}_{24}|2\rangle\langle 4| + \beta\Gamma_d\tilde{\rho}_{24}|3\rangle\langle 4| + h.c.]. \quad (8.35)$$

A typical gain spectrum of the DPAL with ^{85}Rb, ^{87}Rb, and Ethane buffer gas is shown in Figure 8.23. The parameters used in the calculation, such as cell length, temperature, buffer gas pressure, etc., are listed in Table 8.2.

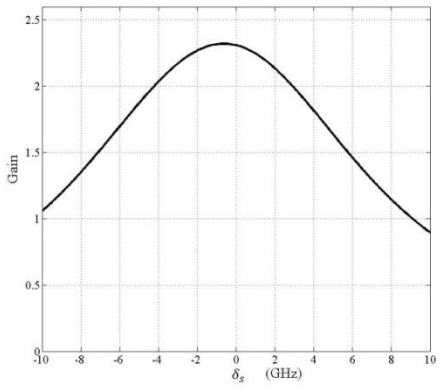

Figure 8.23 A typical spectrum of the gain in the DPAL with Ethane as the buffer gas.

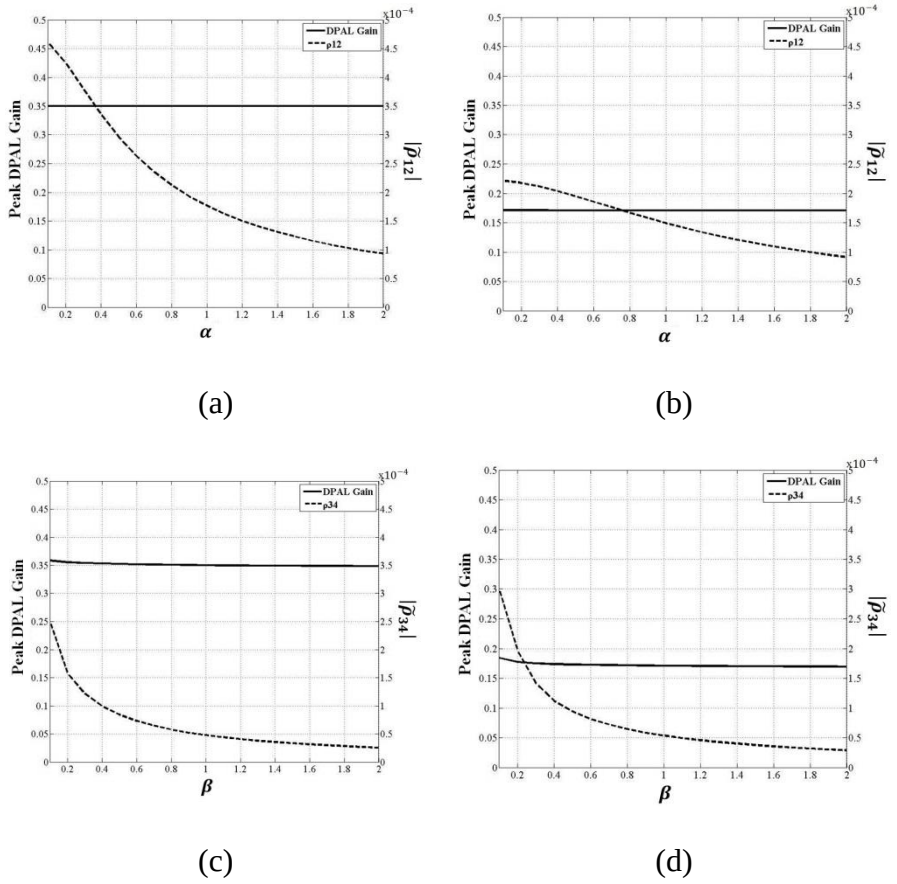

Figure 8.24 (a) The solid line shows the peak value of single-pass amplitude gain (i.e., the peak value of the gain spectrum) through a DPAL cell for a fixed length, as function of α *for* ^{85}*Rb. The dashed line shows the amplitude of the coherence between state* $|1\rangle$ *and* $|2\rangle$*, i.e.,* $|\tilde{\rho}_{12}|$*. (b) Same as figure (a), but for* ^{87}*Rb. (c) The solid line shows the peak value of single-pass amplitude gain as a function of* β *for* ^{85}*Rb. The dashed line shows the amplitude of the coherence between state* $|3\rangle$ *and* $|4\rangle$*, i.e.,* $|\tilde{\rho}_{34}|$*. (d) Same as figure (c), but for* ^{87}*Rb.*

In Figure 8.24, we illustrate how the gain is very weakly dependent on the values of the parameters α and β. Consider first plot (a). Here, the solid line shows the single-pass peak amplitude gain (i.e., the peak value of the gain spectrum as a function of the detuning, as

shown in Figure 8.23) through a DPAL cell with a fixed length, plotted as a function of the parameter α for ^{85}Rb. The dashed line shows the value of $|\tilde{\rho}_{12}|$. As expected, the value of $|\tilde{\rho}_{12}|$ decreases with increasing α. However, it should be noted that even the largest value of $|\tilde{\rho}_{12}|$ is very small, in keeping with our observation made earlier. Finally, we see that the value of the peak gain remains virtually unchanged as a function of α, also in keeping with the observation made earlier. Plot (b) shows the peak gain as a function of α (solid line) and $|\tilde{\rho}_{12}|$ for ^{87}Rb. Here also, we see that the gain remains virtually unchanged as a function of α. Plot (c) and (d) illustrate the corresponding plots as functions of β, for ^{85}Rb and ^{87}Rb, respectively. In these cases also we see that the gain remains virtually unchanged as a function of β. These results justify our use of $\alpha = \beta \simeq 1$ in the model.

Parameters	**Value**
Total cavity length	$0.72\ m$
Gain cell length	$0.1\ m$
Raman cell length	$0.1\ m$
Gain cell temperature	100 ℃
Raman cell temperature	100 ℃
D1 transition wavelength	$795\ nm$
D1 transition life time	$27.7\ nsec$
D2 transition wavelength	$780\ nm$
D2 transition life time	$26.24\ nsec$
Radiative decay rate from $\|2\rangle$ to $\|1\rangle$	$2\pi \times 1 \times 10^6\ sec^{-1}$

Radiative decay rate from $\|1\rangle$ to $\|2\rangle$	$2\pi \times 1.6 \times 10^6\ sec^{-1}$
Effective decay rate from $\|1\rangle$ to $\|2\rangle$	$2\pi \times 1.6 \times 10^7\ sec^{-1}$
Ethane buffer gas pressure	$380\ Torr$ $(0.5\ atm)$
Collisional decay rate from $\|4\rangle$ to $\|3\rangle$	$2\pi \times 8.536 \times 10^8\ sec^{-1}$
Collisional decay rate from $\|3\rangle$ to $\|4\rangle$	$2\pi \times 6.796 \times 10^8\ sec^{-1}$
BGI dephasing rate between $\|1\rangle$ and $\|2\rangle$	$2\pi \times 20 \times 10^6\ (sec \cdot Torr)^{-1}$
BGI dephasing rate between $\|3\rangle$ and $\|4\rangle$	$2\pi \times 20 \times 10^6\ (sec \cdot Torr)^{-1}$
BGI dephasing rate between any other two levels	$2\pi \times 20 \times 10^6\ (sec \cdot Torr)^{-1}$
Frequency difference between $\|1\rangle$ and $\|2\rangle$ (^{85}Rb)	$2\pi \times 3.034 \times 10^9\ sec^{-1}$
Frequency difference between $\|1\rangle$ and $\|2\rangle$ (^{87}Rb)	$2\pi \times 6.835 \times 10^9\ sec^{-1}$
Frequency difference between $\|1\rangle$ of ^{85}Rb and $\|1\rangle$ of ^{87}Rb	$2\pi \times 2.501 \times 10^9\ sec^{-1}$
Rabi frequency of the DPAL pump	$2\pi \times 1.516 \times 10^9\ sec^{-1}$
Rabi frequency of the Raman pump	$2\pi \times 2.873 \times 10^8\ sec^{-1}$
Raman pump detuning	$-2\pi \times 1.6 \times 10^9\ sec^{-1}$
Saturated intensity	$120\ W/m^2$

Table 8.2 Parameters used in the numerical model.

As stated above, the narrow gain profile is realized by inserting a separate vapor cell (Raman cell) inside the cavity to produce Raman Gain. This vapor cell is filled with pure ^{85}Rb without any buffer gas. The basic scheme for this system is shown in Figure 8.25(a). Briefly, an optical pumping beam couples state $|1\rangle$ to state $|4\rangle$. This produces a population inversion among levels $|1\rangle$ and $|2\rangle$. A Raman pump is now applied on the $|2\rangle - |3\rangle$ transition, but detuned significantly above resonance. Under this condition, the probe beam (which is now assumed to excite the $|1\rangle - |3\rangle$ transition only) experiences a narrow-band Raman gain centered around the two photon resonance condition (i.e. the frequency difference between the probe and the Raman pump matches the energy separation between $|1\rangle$ and $|2\rangle$.

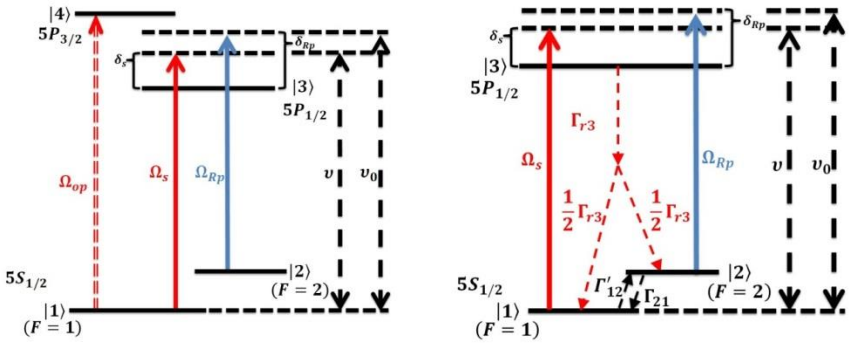

Figure 8.25 In the narrow gain model: (a) transitions, (b) effective 3-level model. Here Ω_{op}, Ω_s, and Ω_{Rp} are the Rabi frequencies for the optical pump, the signal field, and the Raman pump field, respectively. $\delta_s(\delta_{Rp})$ is the detuing of the signal (Raman pump) from the $|1\rangle - |3\rangle$ ($|2\rangle - |3\rangle$) transiton, ν is the frequency of the signal, and ν_0 is defined as the value of the signal frequency corresponding to two photon resonance (i.e. $\delta_s = \delta_{Rp}$).

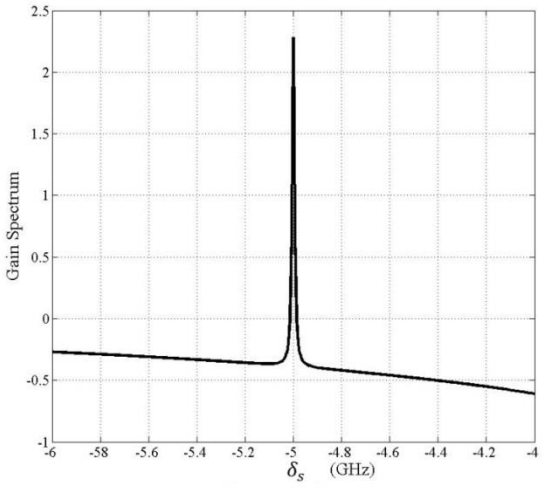

Figure 8.26 A typical gain spectrum produced by the Raman cell.

In Figure 8.25.b, we show the effective 3-level system and the various decay rates relevant to this excitation. For simplicity, we assume that the radiative decay rates from $|3\rangle$ to $|2\rangle$ and that from $|3\rangle$ to $|1\rangle$ are equal ($\Gamma_{r3}/2$). The decay rate from $|2\rangle$ to $|1\rangle$ is Γ_{21}, and that from $|1\rangle$ to $|2\rangle$ is $\Gamma'_{12} = \Gamma_{12} + \Gamma_{op}$. Here, Γ_{12} and Γ_{21} are collisional decay rates that are related to each other by Eqn. 8.32, which in turn implies that $\Gamma_{12} \simeq 1.67\Gamma_{21}$. The additional decay from $|1\rangle$ to $|2\rangle$ at the rate of Γ_{op} accounts for the effect of the optical pumping. The density matrix equation of evolution for this system can now be written as:

$$\frac{\partial}{\partial t}\tilde{\rho} = -\frac{i}{\hbar}\left[\tilde{\tilde{H}}_R, \tilde{\rho}\right] + \frac{\partial \tilde{\rho}}{\partial t}_{source-R}. \tag{8.36}$$

Here,

$$2\tilde{\tilde{H}}_R/\hbar = (-i\Gamma'_{12})|1\rangle\langle 1| + \left(-2\delta_s + 2\delta_{Rp} - i\Gamma_{21}\right)|2\rangle\langle 2| + (-2\delta_s - i\Gamma_{r3})|3\rangle\langle 3| +$$
$$\left(\Omega_s|1\rangle\langle 3| + \Omega_{Rp}|2\rangle\langle 3| + h.c.\right), \tag{8.37}$$

and

$$\frac{\partial\tilde{\rho}}{\partial t}_{source-R} = (\Gamma_{21}\tilde{\rho}_{22} + \Gamma_{r3}\tilde{\rho}_{33}/2)|1\rangle\langle 1| + (\Gamma'_{12}\tilde{\rho}_{11} + \Gamma_{r3}\tilde{\rho}_{33}/2)|2\rangle\langle 2|. \quad (8.38)$$

A typical gain spectrum of the Raman cell is shown in Figure 8.26. The parameters used in the calculation are listed in Table 8.2.

8.2.2 Combined effective susceptibility of the SLL

After solving the density matrix equation of evolution for the two media in steady state, we can calculate the susceptibilities of the two media using the expression:

$$\chi_D = \frac{\hbar c n_D}{\mathcal{I}_{sat}\Omega_s}\left(\frac{\Gamma_{r3}}{2}\right)^2 (\tilde{\rho}_{31} + \tilde{\rho}_{32}), \quad (8.39)$$

$$\chi_R = \frac{\hbar c n_R}{\mathcal{I}_{sat}\Omega_s}\left(\frac{\Gamma_{r3}}{2}\right)^2 \tilde{\rho}_{31}, \quad (8.40)$$

where n_D and n_R are the number density of the atoms in the DPAL and Raman media, respectively, and $\mathcal{I}_{sat}$ (in unit of Watts/m^2) is the saturation intensity which corresponds to a field that produce $\Omega_s = \Omega_{sat} \equiv \Gamma_{r3}/2$. We assume this saturated intensity to be twice as big as that for the strongest transition in the D2 manifold. Then we can write the effective susceptibility of the media in the SLL as:

$$\chi_{eff} = \frac{L_D}{L}(0.72\chi_{D85} + 0.28\chi_{D87}) + \frac{L_R}{L}\chi_R, \quad (8.41)$$

where L is the cavity length, and L_D and L_R are the DPAL cell length and the Raman cell length, respectively. The real and imaginary parts of χ_{eff} must satisfy Eqn.8.23 and 8.24 in steady state. Thus, Eqn.8.31 and the steady state version of Eqn.8.23 and 8.24 have to be solved simultaneously, in a self-consistent manner. This requires the use of an iterative

algorithm to find the value of δ_s and Ω_s (which in turn yields the frequency ν and the field amplitude E) that satisfy these equations; which is described next.

8.2.3 Iterative algorithm for finding the frequency and the amplitude of the SLL

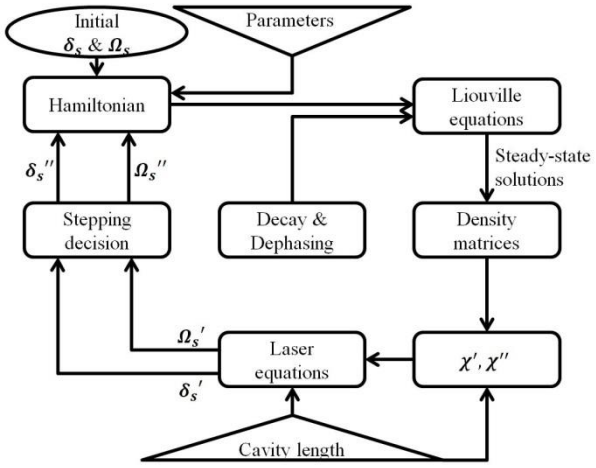

Figure 8.27 Flow-chart of the algorithm for solving the model for an actual SLL.

The flow chart shown in *Figure 8.27* illustrates how the algorithm works. For a certain cavity length, this algorithm is able to find the frequency ν and the intensity $\mathcal{I}$ of the laser field in steady state. The frequency and the intensity of the field can be calculated from δ_s and Ω_s using the following equations:

$$\nu = \nu_0 - \delta_{Rp} + \delta_s, \tag{8.42}$$

$$\mathcal{I} = \mathcal{I}_{sat}\left(\frac{\Omega_s}{\Omega_{sat}}\right)^2, \tag{8.43}$$

where ν_0, δ_{Rp}, δ_s are as defined in Figure 8.25.

The algorithm starts by assuming a pair of values of δ_s and Ω_s. These yield a value of χ_{eff}, by evaluating Eqn.8.41. This value of χ_{eff} (real and imaginary parts) is then fed into the

steady state forms of the laser equations (Eqn.8.23 and 8.24) to find the values of δ_s' and Ω_s'. These values are then compared with the values of δ_s and Ω_s. If the differences $|\delta_s - \delta_s'|$ and $|\Omega_s - \Omega_s'|$ are each below chosen threshold values, the algorithm stops. If not, then either δ_s' or Ω_s' or both are increased of decreased by a suitable step size, and the loop is repeated, until a convergence is found. We note that, under certain conditions, there exist more than one set of solutions (i.e. combination of laser frequency and intensity) for a given set of parameters and cavity length. In these cases, we have found that an alternative form of the algorithm is more convenient to use. In this form, we fix the value of the laser frequency, and then iterate to find the values of the laser intensity and the cavity length that satisfy the relevant equations.

To explore the relationship between the lasing frequency and cavity length variations, we use this algorithm to find the lasing frequency in steady state for different cavity lengths. Then the stability improvement of the SLL can be calculated by comparing the derivative of the frequency shift as a function of the cavity length with that of a conventional laser.

8.2.4 Results

In Figure 8.28.a, we show the output frequency as the cavity length is varied. Here, L_0 is a reference cavity length for which one of the cavity modes matches the value of ν_0 (note that the free spectral range is much larger than the width of the Raman gain). As can be seen, the shift in the laser frequency is small for a significant spread in ΔL. Furthermore, there is a range of cavity lengths for which multiple frequencies satisfy the equations. This is similar to the behavior described in our analytical model earlier. In Figure 8.28.b, we again show a plot of the laser frequency as a function of the cavity length, but for a different set of parameters. As can

be seen, there is a range around $L = L_0$ for which the frequency has a unique value, with a small slope, corresponding to reduced stability. The shaded area corresponds to the range of cavity length for which the laser frequency is not unique, same as what we observed earlier in Figure 8.18.b. As we had noted earlier, a detailed calculation involving nearly-degenerate multiple modes and the gain competition between these modes is needed to determine the exact behavior of the SLL in this region. Such a calculation entails the use of an interaction Hamiltonian that cannot be rendered time independent via rotating wave transformation. As such, many higher orders terms in the solution of the density matrix equations have to be computed, in a manner akin to what is done in Ref.111, although in a different context. This analysis will be carried out and reported in the near future. Outside the shaded area, the frequency is again unique. However, the asymptotic slope is now much larger than that around $L = L_0$, corresponding to the normal sensitivity.

In Figure 8.29.a, we show the laser power as a function of the cavity length, for same parameters we used in producing Figure 8.28.b. As can be seen, the intensity has a unique value for some ranges of the cavity length, but has multiple possible values over the ranges for which the frequency also has multiple values. Again, this behavior is similar to what we presented earlier for the analytical model. In Figure 8.29.b, we show the output intensity as a function of the laser frequency. This plot is generated by combining the information presented in Figure 8.28.b and Figure 8.29.a. As can be seen, there is a one-to-one correspondence between the intensity and the frequency, for all values of the cavity length.

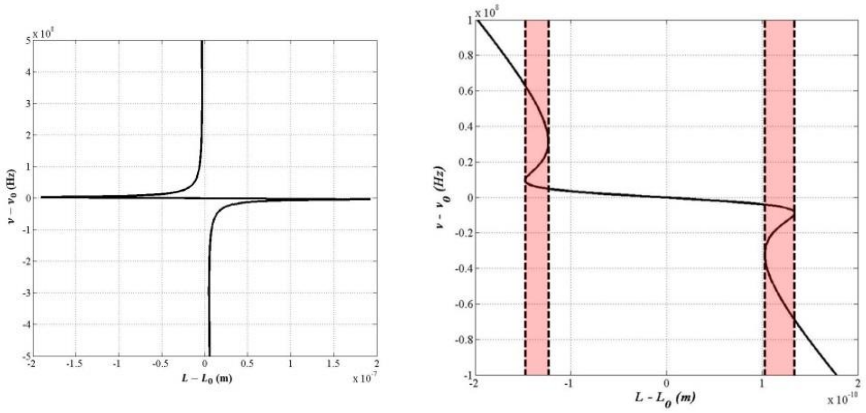

(a) (b)

Figure 8.28 Relationship between cavity length and lasing detuning for the practical SLL for (a) extremely high stability enhancement and (b) relatively low stability enhancement.

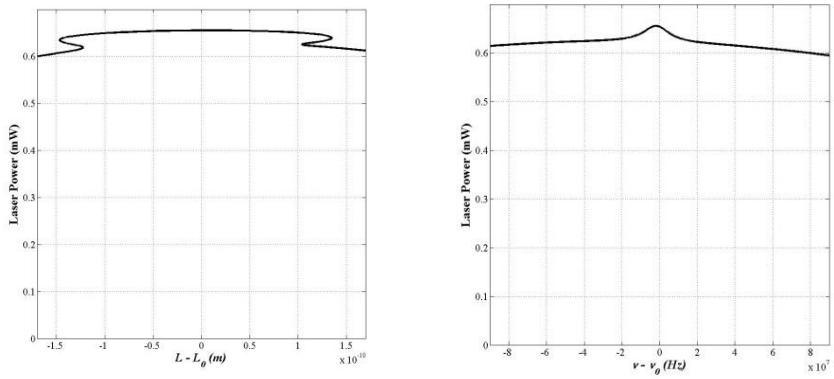

(a) (b)

Figure 8.29 Output power as a function of (a) length change and (b) laser frequency, for the model for a practical SLL.

In Figure 8.30.a, we show the laser frequency as a function of the cavity length, for the primary mode, corresponding to the parameters used in Figure 8.28.a. The resulting enhancement in stability is shown in Figure 8.30.b. The sensitivity of the laser is reduced by a

factor of 10^5 when the lasing frequency is at $\nu = \nu_0$, corresponding to $L = L_0$. Finally, Figure 8.31 shows the real part of the effective dispersion, χ_{eff}, as a function of the laser frequency. As can be seen, the effective dispersion has qualitatively the same shape as that of the analytical approach.

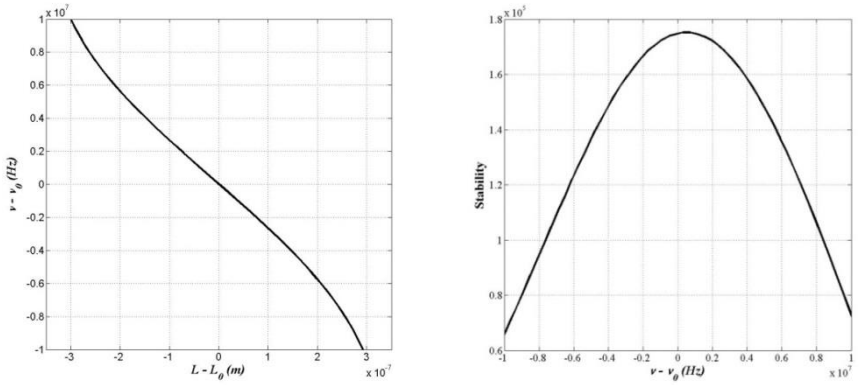

(a) (b)

Figure 8.30 Desired region of operation in the model for a practical SLL: (a) laser frequency as a function of cavity length and (b) stability as a function of laser frequency.

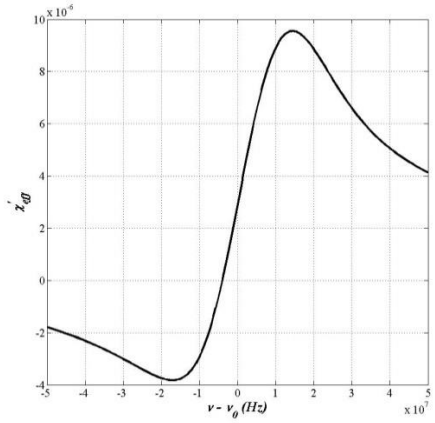

Figure 8.31 Real part of the effective dispersion in steady state of the model for a practical SLL.

8.2.5 Quantum Noise Limited Linewidth of the SLL

As mentioned earlier, an interesting and potentially very important aspect of the SLL is its quantum noise limited linewidth. For a conventional laser with a very flat gain spectrum, the STL can be expressed simply as [112]:

$$\gamma_{STL} = \frac{\hbar\omega}{2P_{out}\tau_c^2}, \tag{8.44}$$

where ω is the laser frequency, P_{out} is the output power, and τ_c is the lifetime of the empty cavity, which can also be expressed simply as the invers of the empty cavity linewidth. In the presence of a non-negligible normal dispersion (but not for anomalous dispersion [113]), this expression is modified significantly [114] as follows:

$$\gamma_{STL} = \frac{\hbar\omega}{2P_{out}(n_g\tau_c)^2}(1 + |\alpha|^2), \tag{8.45}$$

where, n_g is the group index, and $|\alpha| \equiv \left(\frac{\partial n'}{\partial |E|}\right) / \left(\frac{\partial n''}{\partial |E|}\right)$, where n' and n'' are, respectively, the real and imaginary parts of the complex refractive index:

$$n_c \equiv n' + in'' = \sqrt{1+\chi} \approx \left(1 + \frac{1}{2}\chi'\right) + i\frac{1}{2}\chi'', \tag{8.46}$$

with $\chi \equiv \chi' + i\chi''$ being the complex susceptibility of the gain medium, and $|E|$ is the amplitude of the laser field. The measured linewidth, γ_{MEAS}, of a laser depends, of course, on the measurement bandwidth, Γ_M, which is the inverse of the measurement time, τ_M. It has been shown [115,116,117] that the value of γ_{MEAS} is given simply by the geometric mean of γ_{STL} and Γ_M, so that we can write:

$$\gamma_{MEAS} = \sqrt{\gamma_{STL} \cdot \Gamma_M} = \sqrt{\frac{\hbar\omega}{2P_{out}(n_g\tau_c)^2\tau_M}(1 + |\alpha|^2)}, \tag{8.47}$$

which can also be written as:

$$\gamma_{MEAS} = \frac{1}{n_g \tau_c} \cdot \sqrt{\frac{\hbar\omega}{2P_{out}\tau_M}(1+|\alpha|^2)}, \tag{8.48}$$

We consider first the expected value of $|\alpha|$ for the SLL. From the definition of $|\alpha|$ Eqn.8.46, it follows that:

$$|\alpha| = \left(\frac{\partial\chi'}{\partial|E|}\right) / \left(\frac{\partial\chi''}{\partial|E|}\right), \tag{8.49}$$

We recall that in Eqn.8.28 and 8.29, we had defined I as being $|E|^2$. Thus, we can use these equations to determine the numerator and the denominator in Eqn.8.49:

$$\frac{\partial\chi''}{\partial|E|} = \frac{4G_e\xi_e{\Gamma_e}^3|E|}{\left[2\Gamma_e\xi_e|E|^2+{\Gamma_e}^2+4(\nu-\nu_0)^2\right]^2} + \frac{4G_i\xi_i{\Gamma_i}^3|E|}{\left[2\Gamma_i\xi_i|E|^2+{\Gamma_i}^2+4(\nu-\nu_0)^2\right]^2}, \tag{8.50}$$

$$\frac{\partial\chi'}{\partial|E|} = -\frac{8G_e\xi_e{\Gamma_e}^2(\nu-\nu_0)|E|}{\left[2\Gamma_e\xi_e|E|^2+{\Gamma_e}^2+4(\nu-\nu_0)^2\right]^2} - \frac{8G_i\xi_i{\Gamma_i}^2(\nu-\nu_0)|E|}{\left[2\Gamma_i\xi_i|E|^2+{\Gamma_i}^2+4(\nu-\nu_0)^2\right]^2}. \tag{8.51}$$

Since the SLL operates at a frequency that is very close to ν_0, we have $\Gamma_e \gg |\nu-\nu_0|$. Furthermore, since the background gain profile is very broad, compared to the laser Rabi frequency, we can assume $\Gamma_e \gg \xi_e|E|$. Since G_e is much less than unity, we can thus ignore the first terms in both Eqn.8.50 and 8.51. We then get:

$$|\alpha| = \frac{2|\nu-\nu_0|}{\Gamma_i}. \tag{8.52}$$

For a typical range of values of $|\nu-\nu_0|$ within the primary mode zone, $|\alpha| \ll 1$. Thus, this parameter has a negligible effect on the linewidth of the SLL. It should be noted that, in general, the effect of $|\alpha|$ is found to be dominant only in systems where the laser frequency is far away from resonances in the gain media (such as in a semi-conductor laser [114]), and is negligible in a typical gas laser [114,115] where the laser frequency is generally close to the resonance in the gain medium.

Consider next the effect of the group index. As can be seen from Eqn.8.48, the linewidth

decreases with increasing value of n_g. Intuitively, this can be understood as follows. The propagation of a pulse is slowed down by a factor of n_g. Thus, the effective travel time for a pulse as it propagates in the cavity increases by a factor of n_g. Therefore, the effective cavity decay time is $\tau_{c,eff} = n_g \tau_c$.

As we have noted above, Eqn.8.48 is not expected to be valid for a superluminal laser, since the dispersion in that case is anomalous (as noted before Eqn.8.45). The extent to which Eqn.8.48 is valid for a very large value of n_g has not yet been tested experimentally. Realization of an SLL, followed by a careful measurement of γ_{MEAS}, would be a definitive way of answering this question. If Eqn.8.48 turns out to be valid for large values of n_g, then the SLL could also become potentially very useful as a source of radiation with extremely high spectral purity.

8.3 Raman Depletion within Diode Pumped Alkali Laser (DPAL)

In what follows, we make use of the semi-classical equation of motion for an effectively single mode ring laser [118]. First, we consider light in a ring laser cavity which contains a dispersive medium. The phase and amplitude of the field are described by a set of self-consistency equations:

$$\nu + \dot{\varphi} = \Omega - \frac{\chi'(E,\nu)}{2}\nu \qquad (8.53.a)$$

$$\dot{E} = -\frac{\nu E}{2Q}\frac{\chi''(E,\nu)E}{2}\nu \qquad (8.53.b)$$

where φ is the round-trip phase shift, ν is the lasing frequency, and Ω is the resonant frequency of the cavity in the absence of the medium. Ω is given by 2πmc/L where L is the

length of the cavity, c is the vacuum speed of light, and m is the mode number. χ' and χ'' are the real and imaginary part of the susceptibility of the medium, respectively. E is the field amplitude, and Q is the cavity quality factor. ν_0 is the frequency around which χ'' is symmetric. $\Omega = \nu_0$ for a particular length of the cavity: $L = L_0$. In our model, L will be allowed to deviate from L_0, thereby making Ω differ from ν_0. For simplicity, we assume a situation where lasing is unidirectional, made possible by the presence of an optical diode inside the cavity. Any loss induced by the diode is included in Q.

For convenience, we define the parameters, $\Delta = \Omega - V_0$, $\delta = v - v_0$. The derivatives $d\Delta/dL$ and $d\delta/dL$ characterize the resonant frequency shifts under a perturbation of L in the empty and filled cavity, respectively. We consider the ratio, $R \equiv (d\delta/dL)/(d\Delta/dL)$ to determine if the amount of the frequency shift is enhanced (R>1) or diminished (R<1) by the intracavity medium. To derive R, we begin with Eqn.8.53.a. In steady state ($\dot{\varphi} = 0$) subtracting ν0 from both sides, differentiating with respect to L, and applying $dv = d\delta$, we get $d\delta/dL + \chi'/2\,(d\delta\,dL) + v/2\,(d\chi'/dL) = d\Delta/dL$. By substituting $(d\chi'/d\delta)/(d\delta/dL)$ for $d\chi'/dL$, we get:

$$R = 1/[1 + \frac{\chi'}{2} + \frac{v}{2}\frac{d\chi'}{dv}] \qquad (8.54)$$

In order to determine the value of R, it is necessary to know how χ' depends on ν. In case of a passive cavity, this would be determined solely by the response of the medium to a weak probe, and would be related to χ'' by the KK relations. In the case of an active cavity, however, this is no longer true, since χ' depends indirectly on E, which varies as a function of ν, as determined by a self-consistent solution of Eqn.8.53.a. In the later parts of the thesis, we explore this interdependence of χ' and E in detail in order to establish the behavior of the superluminal laser.

We can at this point develop additional insight into the behavior of R by simply assuming that χ' is antisymmetric around $\nu = \nu_0$ (to be validated later). We can then expand χ' around $\nu = \nu_0$, keeping terms up to $\Delta\nu^3$ where $\Delta\nu = \nu - \nu_0$. We get $\chi' = \chi'(v_0) + \Delta v\chi_1' + (\Delta v)^3\chi_3'/6$ where $\chi_n' = \left(\frac{d^n\chi'}{dv^n}\right)|_{v=v_0}$ (n = 1 or 3). Since χ' is assumed to be antisymmetric around $\nu 0$, we have $\left(\frac{d^2\chi'}{dv^2}\right)|_{v=v_0} = 0$. Differentiating χ' with respect to ν, and inserting χ' and the derivative of χ' in Eqn.8.54, we get: $R \cong 1/[1 + \chi'(v_0)/2 + v_0\chi_1'/2 + v_0\chi_3'(\Delta v)^2/4]$. Here, we have dropped terms that are small due to the fact that $|\Delta v| \ll v_0$. Note that if χ' is assumed to be linear, corresponding to keeping only the first two terms in the expansion of χ', the enhancement factor simplifies to: $R \cong 1/[1 + \frac{\chi'(v_0)}{2} + \frac{v_0\chi'}{2}]$.

To illustrate the physical meaning of this result, we note first that the index can be expressed as $n(v) = (1 + \chi')^{\frac{1}{2}} \cong 1 + \chi'(v)/2$. The group index can then be written as $n_g = n_0 + v_0 n_1 = 1 + \chi'(v_0)/2 + \chi_1' v_0/2$, where $n_0 = n(v_0)$ and $n_1 = \left(\frac{dn}{dv}\right)|_{v=v_0}$. Thus, the enhancement factor in this linear limit is given simply as $R \approx 1/n_g$. For normal dispersion ($n_g > 1$), R becomes less than one. Hence, the resonant frequency shift with respect to the length variation decreases compared to the shift in an empty cavity. For anomalous dispersion ($n_g<1$), the frequency shift is amplified to be equal to $1/n_g$ times the amount of the shift in the empty cavity.

In order to determine the actual value of R for an active cavity, we need first to establish the explicit dependence of χ' on the lasing frequency, v. To this end, we first solve Eqn.8.53.b in steady state ($\dot{E} = 0$) so that $\chi''(E, v) = -1/Q$ for $E \neq 0$. Since χ'' is a function of E and v, the solution to the equation yields the saturated electric field E in steady state inside the laser cavity as a function of the lasing frequency v.

Let us consider the case in which the cavity contains a medium with a narrow absorption as well as a medium with a broad gain. This configuration creates a gain profile with a dip in the center. The imaginary part of the susceptibility χ'' can then be written as:

$$\chi'' = -\frac{G_e\Gamma_e^2}{\vartheta_e} + \frac{G_i\Gamma_i^2}{\vartheta_i} \tag{8.55a}$$

where $\vartheta_k = 2\Omega_k^2 + \Gamma_k^2 + 4(v - v_0)^2$, ($k$ = e or i). We use the subscript "e" for the "envelope" gain profile and "i" for the narrower absorption profile.

Using the modified Kramers-Kronig (MKK) relation [105,106] for the saturated susceptibility, we can then express the real part of the susceptibility χ' as:

$$\chi' = \frac{2G_e(v-v_0)\Gamma_e}{\vartheta_e} - \frac{2G_i(v-v_0)\Gamma_i}{\vartheta_i} \tag{8.55b}$$

Here $\Omega_i\,(\Omega_e)$ is the Rabi frequency equal to $\wp_i E/\hbar$ ($\wp_e E/\hbar$) where $\wp_i(\wp_e)$ is the dipole moment associated with the absorbing (amplifying) medium. The gain and the absorption linewidths are denoted by Γ_e and Γ_i, respectively. Using the Wigner–Weisskopf model [103] for spontaneous emission, we can define two parameters: $\xi_i = \wp_i^2/(\hbar^2\Gamma_i)$ and $\xi_e = \wp_e^2/(\hbar^2\Gamma_e)$. In terms of these parameters, the Rabi frequencies can then be expressed as $\Omega_i^2 = \Gamma_i E^2\,\xi_i$ and $\Omega_e^2 = \Gamma_e E^2\,\xi_e$. The gain parameters can then be expressed as $G_i = \hbar N_i\xi_i/\varepsilon_0$ and $G_e = \hbar N_e\xi_e/\varepsilon_0$ where ε_0 is the permittivity of free space, and N_e and N_i represent the density of quantum systems for the absorptive and the amplifying media, respectively.

It is instructive to consider first the case of a conventional gain medium, by setting $G_i = 0$.From Eqn.8.55, χ' and χ'' are then simply related to each other as $\chi'/\chi'' = -2(v - v_0)/\Gamma_e$. From $\chi'' = -1/Q$, it then follows that $\chi' = 2(v - v_0)/(Q\Gamma_e)$. The expression for $\chi'$is linear in v, and antisymmetric around v_0. Note that according to

Eqn.8.53.b, $Q = \nu_0/\Gamma_c$, where Γ_c is the empty cavity linewidth. Therefore, we find from R in the linear limit that$R = 1/n_g$, where $n_g = 1 + \Gamma_c/\Gamma_e$. Since $n_g > 1$, this implies a reduction in sensitivity when compared to an empty cavity. In a typical laser, Γ_c/Γ_e is very small so that this reduction is rather insignificant. The behavior of such a system in the context of the KK relations is discussed in detail in Ref. [104], which also addresses the inadequacies of previous studies.

For the case of a conventional laser medium discussed above, it was easy to determine the value of χ' because of the simple ratio between χ' and χ''. In particular, this ratio does not depend on the laser intensity. However, for the general case (i.e. $G_i \neq 0$), the two terms in χ'' are highly dissimilar. As such, it is no longer possible to find a ratio between χ' and χ'' that is independent of the laser intensity. Thus, in this case, we need to determine first the manner in which the laser intensity depends on all the parameters, including ν. We define $I \equiv |E|^2$ so that $\Omega_i^2 = \Gamma_i I \xi_i$ and $\Omega_e^2 = \Gamma_e I \xi_e$. By setting Eqn.8.55.a equal to $-1/Q$, we get $aI_2 + bI + c = 0$, where a, b, and c are function of various parameters. We keep the solution that is positive over the lasing bandwidth: $I = (-b + \sqrt{b^2 - 4ac}\,/\,(2a)$. Substituting this solution for I to evaluate Ω_i and Ω_e, in Eqn.8.55.b we get an analytic expression for χ'.

The behavior of χ' can be understood by plotting it as a function of ν. For illustration, we consider $\Gamma_e = 2\pi \times 10^9 s^{-1}$, $\Gamma_i = 2\pi \times 10^7 s^{-1}$, $\nu_0 = 2\pi \times 3.8 \times 10^{14}\, s^{-1}$, $N_e = 9 \times 10^6$, and $N_i = 1.2645 \times 10^{11}$. To fulfill the lasing condition in the spectral range of the absorption dip, we consider the gain peak $G_e = 12/Q$ and the absorption depth $G_i = (10 + \epsilon)/Q$ so as to ensure $G_e - G_i > 1/Q$ at $\nu = \nu_0$ where ε is a small fraction.

For a given value of G_e, the choice of ε is critical in determining the optimal behavior of χ'. The particular choice of $\varepsilon = 0.11591$ was arrived at via a simple numerical search through the parameter space. Figure 8.32 shows χ' as a function of ν. Note first that far away from $\nu = \nu_0$, it agrees asymptotically with the linear value of χ' for the case of $G_i = 0$, indicated by the dotted line. The inset figure shows an expanded view of χ'. The steep negative slope of χ' around around $\nu = \nu_0$ is the feature necessary to produce the fast light effect ($n_g \approx 0$).

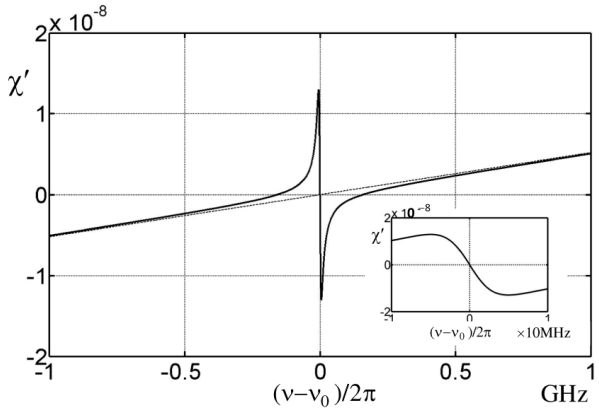

Figure 8.32 Real part of the steady-state susceptibility for the combined absorbing and amplifying media (solid line), and the conventional gain medium (dashed line). The inset shows an expanded view of the solid line in the main figure

We can now evaluate the enhancement factor, R, as expressed in Eqn.8.54. We note first that $d\chi'/d\nu = \partial\chi'/\partial\nu + (\partial\chi'/\partial I)(\partial I/\partial\nu)$, where $\partial I/\partial\nu$ is evaluated from the solution of the quadratic equation for I, and $\partial\chi'/\partial\nu$ and $\partial\chi'/\partial I$ are evaluated from Eqn.8.55. Inserting $\partial\chi'/\partial\nu$ and Eqn.8.55 in 8.54, we find R as a function of ν. This is shown in Figure 8.33 for the parameters mentioned above. The insets (a) and (b) show a view expanded horizontally and a view on a linear vertical scale, respectively. The enhancement

reaches a peak value of ~1.8×10^5 at the center of the gain dip [inset (a)], drops to a minimum (~0.89) and increases to a value close to unity [inset (b)]. These attributes are consistent with the behavior of χ' shown in Figure 8.32. The peak value of R corresponds to the steep negative dispersion. As the dispersion turns around and becomes positive, the value of R drops significantly below unity. Finally, as the dispersion reaches the weak, positive asymptotic value, we recover the behavior expected of a conventional laser, with R being very close to, but less than unity [inset (b)].

The black lines shown in Figure 8.33 correspond to the exact value of R given by Eqn.8.54. It is also instructive to consider the approximate values of R, where we assume χ' to be linear. This is shown by the dotted line in inset (a). Of course, this linear approximation is valid only over a very small range around $\nu = \nu_0$. However, it does show clearly that the peak value of R can be understood simply to be due to the linear, negative dispersion at $\nu = \nu_0$.

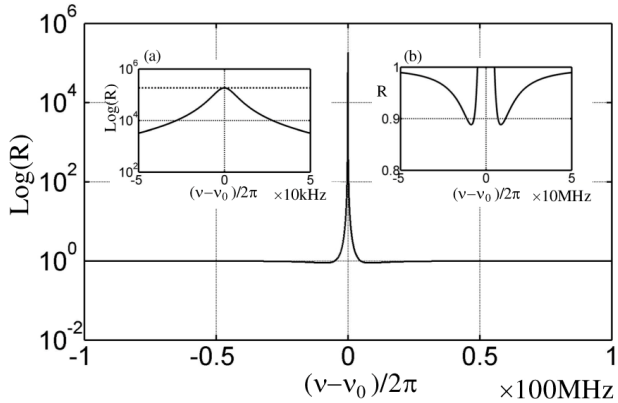

Figure 8.33 Sensitivity enhancement associated with Eqn.8.54. The inset (a) shows R in Eqn.8.54 in an expanded view (solid line), and its value in the linear limit (dotted line). The inset (b) is an expanded view of R with a linear vertical scale.

The enhancement factor *R* indicates how the lasing frequency ν changes when the length of the cavity, *L*, is changed. It is also instructive to view graphically the dependence of ν on *L* explicitly. As discussed earlier, in the empty cavity, we have $\nu_0 = 2\pi mc/L_0$, where ν_0 is the resonance frequency (chosen to coincide with the center of the dispersion profile). For concreteness, we have used $\nu_0 = 2\pi \times 3.8 \times 10^{14}$, corresponding to the D_2 transition in Rubidium atoms. We now choose a particular value of the mode number *m*, so that *L* is close to one meter. Specifically *m* = 1282051 yields L_0 = 0.99999978 meter.

When the dispersive gain medium is present, the lasing frequency will be $\nu = \nu_0$ if *L* is kept at L_0. If *L* deviates from L_0, then ν changes to a different value. Specifically, $L = 2\pi mc/\Omega$, and $\nu = \Omega/(1 + \chi'/2)$ from Eqn.8.53.a in steady state, so that $L = (2\pi mc/\nu)(1 + \chi'/2)$. Using the dependence of χ' on ν as shown in Figure 8.32, we can thus plot L as a function of ν, as shown in Figure 8.34. Even though *L* is plotted on the vertical axis, this plot should be interpreted as showing how ν changes as *L* is varied. For ν far away from ν_0, the variation of ν as a function of *L* is essentially similar to that of an empty cavity, indicated by the dotted line.

Around $\nu = \nu_0$, a small change in *L* corresponds to a very big change in ν as displayed in the inset figure. Specifically, we see that $\Delta L \approx 10^{-13}$ meter produces $f \equiv \Delta\nu/(2\pi) \approx 10^5 Hz$, corresponding to $\Delta f/\Delta L \sim 10^{18}$. In contrast, for a bare cavity, $\Delta L \approx 2 \times 10^{-7}$ produces $\Delta\nu/(2\pi) \approx 8 \times 10^7 Hz$, corresponding to $\Delta f/\Delta L \sim 4 \times 10^{14}$. The value of $\Delta f/\Delta L$ for a conventional laser is also very close to this value, as indicated by the convergence of the dotted and solid lines for ν far away from the superluminal region. Thus the enhancement factor, *R*, is ~2.5×10^3. If we zoom in even more, we will eventually see that as $\Delta L \to 0$,

we have R~1.8×10^{5}, as shown in Figure 8.33.

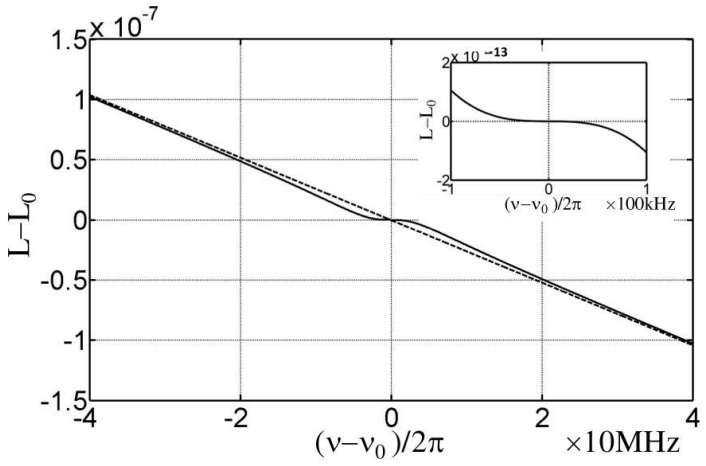

Figure 8.34 Illustration of relation between $L - L_0$ *and* $\nu - \nu_0$ *for* $|\nu - \nu_0|/2\pi < 80MHz$. *Dotted line shows the behavior for an empty cavity. The inset shows an expanded view for* $|\nu - \nu_0|/2\pi < 100kHz$.

The scheme proposed here for a superluminal laser may be realizable in many different ways. For example, the gain profile can be produced by a diode pumped alkali laser [97]. The dip in the gain profile can be produced by inserting a Raman probe, following the technique shown in Ref.119. Figure 8.35 displays the corresponding energy levels, and the experimental configuration to realize a superluminal laser. Figure 8.35(a) illustrates the atomic transitions associated with the process for producing a broadband gain profile. The diode pump, applied from the side along the D2 transition, induces population inversion for the D1 transition in the presence of a buffer gas of ^{4}He. Figure 8.35(b) shows the energy levels within the D1 transition used for producing the Raman depletion. The lasing beam acts as the Raman pump. The Raman probe is produced by sampling a part of the laser output, and shifting it in frequency with an acousto-optic modulator, operating at the frequency that matches the

hyperfine splitting in the ground state [119]. An additional optical pumping beam is applied to produce the population inversion among the metastable hyperfine states necessary for the Raman gain and depletion. Thus, the laser light experiences the Raman dip in the cell B, as illustrated in Figure 8.35(c). Efforts are underway in our laboratory to realize such a scheme.

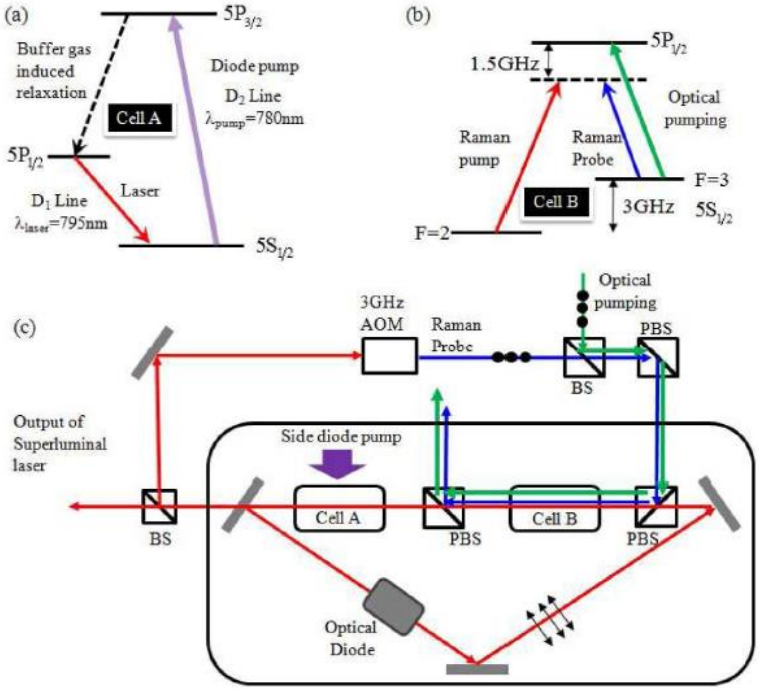

Figure 8.35 Energy levels for (a) 795-nm Rb laser to produce broadband gain, (b) Raman depletion to induce narrowband absorption dip. (c) Schematics of the experimental set-up to realize a superluminal laser: PBS, polarizing beam splitter; BS, beam splitter; AOM, acousto-optic modulator. Note that the superluminal laser is the same as the Raman pump. The scheme shown is for ^{85}Rb atoms. The broadband gain is produced by side-pumping with a diode laser array.

8.4 Future Work: A Double Raman Pumped Superluminal Laser

Figure 8.36 shows the schematic of a double Raman pumped superluminal laser. The

same double Raman system, as introduced in Sec. 8.1., is used here. A ring cavity, composed of two curved mirrors (CM) and one beam splitter (BS), is built around the Rb cell. To calculate the enhancement factor, we need to replace the susceptibility in Eqn.8.53 with the numerical solutions of double Raman pumped gain media shown in Sec. 8.1. Remember the double Raman model contains multiple harmonics and is no more in the same shape as a double Lorentz function, it is not proper to solve the laser equation (Eqn.8.53) analytically, which makes the computation more complex. Figure 8.37 shows the difference between gain profiles in a double Lorentz function (Eqn.8.55) and in a double Raman gain model (Sec. 8.1).

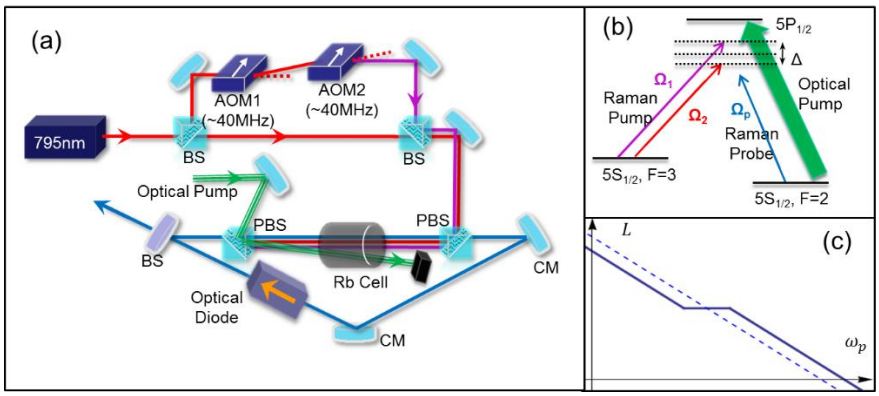

Figure 8.36 Experiment Setup of a superluminal ring laser using double Raman pumped gain.

An algorithm is built to get numerical solution to the laser equation efficiently. Bisection method [120] is used first to scan through the gain profile coarsely and find all the ranges that contains a root. Susceptibility is guaranteed to be monotonically increasing or decreasing. Within each of the ranges, we will call a customized root finding method to find the solution. This method is essentially built on an Illinois method [30] with an additional boundary

constrain. Order of convergence is ~1.442 compared with traditional bisection method whose convergence speed is 1. This algorithm would return all the roots that satisfy the laser equation, which corresponds to all the possible modes exist in the cavity.

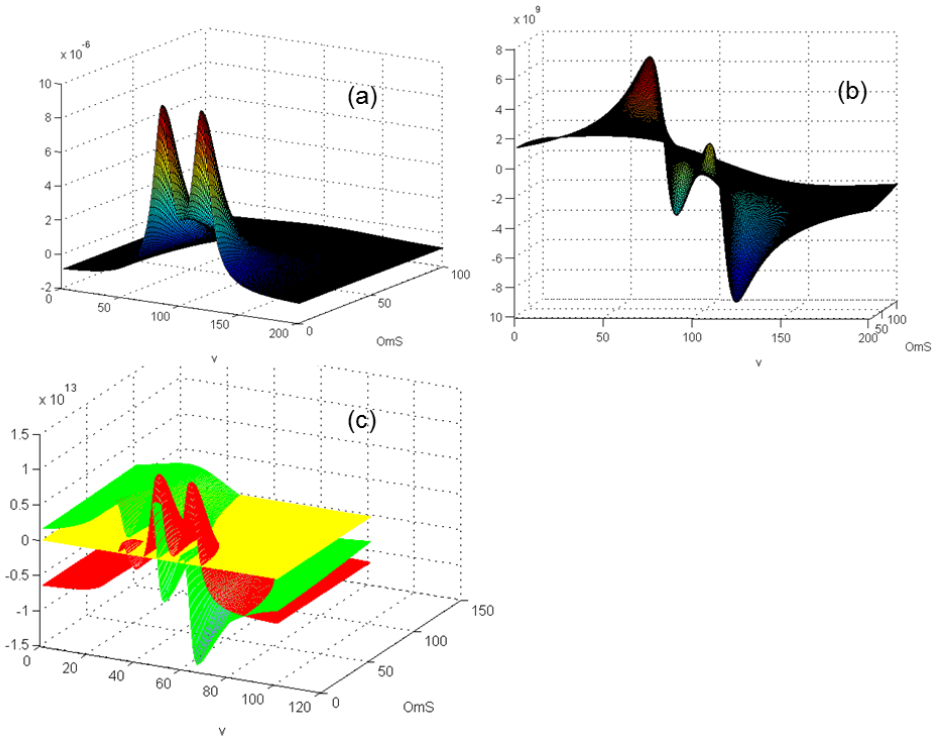

Figure 8.37 Comparison between double peak gain profiles built by double Lorentz function and double Raman gain model. Plot (a) (b) shows the image part and real part of susceptibility calculated by the double Lorentz function as signal Rabi frequency and signal frequency are scanned. Plot(c) shows the corresponding case where susceptibility is calculated by the double Raman gain model. Red and green surfaces represents the χ'' *and* χ' *respectively.*

Figure 8.38 shows the results of using this algorithm to simulate a single Raman laser. The schematic of the system is shown in plot (d). Susceptibility of this Raman gain is shown in plot(d), where signal Rabi frequency and signal frequency are scanned. Decay rate of $5P_{1/2}$

is $\Gamma = 6MHz$, frequency difference between F=2 and F=3 is $3.034 \times 10^9 Hz$, optical pumping rate (OP) is $3MHz$, pump frequency detuning is 1.2GHz, and Rb density is $5 \times 10^{14} m^{-3}$. The reflectivity of the output coupler (BS) in Figure 8.36 is 0.9. Cavity length is 1m. For simplicity, we assume the Rb fills the whole cavity. Numerical solutions are shown in plot (a-c) as pump Rabi frequency is scanned, where a1, b1, c1 show the signal Rabi frequency, signal frequency detuning, and error of one potential mode in the laser. Plot (a2, b2, c2) show the other mode.

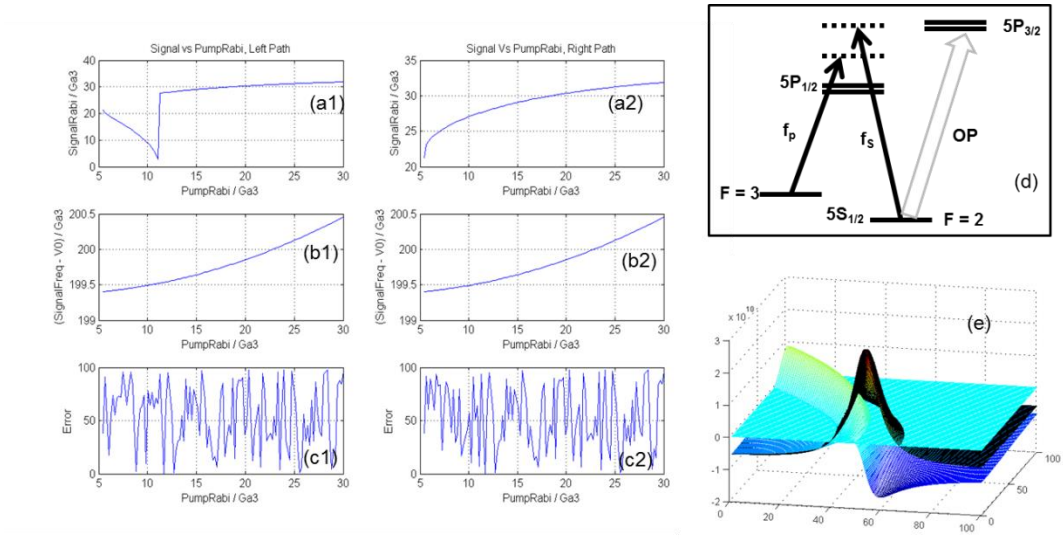

Figure 8.38 An example of using our algorithm to get two set of numerical solutions to a single Raman laser. See text for more details.

CHAPTER 9 SUMMARY

Ultra-low power optical modulation, development of optically controlled waveplate and polarizer for high-speed Stokes-metric imaging, and development of a superluminal ring laser for a range of applications, including ultra-sensitive rotation sensing and vibrometry, are investigated in this thesis both theoretically and experimentally.

Our study on the all-optical modulation and switching has demonstrated an all optical modulator which can operate at a power level much lower than any other technique demonstrated so far. Specifically, a tapered nano fiber (TNF) embedded in Rb vapor has been used to produce ultra-low power modulation.

An N-Level algorithm has been developed in order to develop an accurate model for the interaction of multiphoton laser fields with Rb atoms, This algorithm can be used to generate automatically the density matrix equations of motion for a system with an arbitrary number of energy levels, such as the Zeeman sublevels within the hyperfine energy levels in Rb atoms. It has been used to design, analyze, and optimize many processes of interest using Rb atoms, including the study of ladder transitions, high speed modulation, optically controlled polarizer and waveplate, and double Raman gain for realizing a superluminal laser.

Study of all-optical modulation has been further extended to a Rb cascade system. With the Rb 5S-5P-6S ladder transition, optical modulation is demonstrated at a telecommunication band wavelength. With the use of a high pressure buffer gas, a 100-fold increase in modulation bandwidth has been observed.

An optically controlled polarizer and an optically controlled waveplate have also been

demonstrated using the Rb ladder system. A combination of both can be used for realizing all optical switching and all optical logic gates. These devices can also be used to realize a high-speed Stokes-metric imaging system. The optically controlled polarizer is demonstrated using ^{87}Rb $5S_{1/2}$, F = 1->$5P_{1/2}$, F = 1,2 -> $6S_{1/2}$, F = 1,2 transition, where 795 nm light is used as the control beam and 1323 nm light is used as the probe beam. The optically controlled waveplate is demonstrated using the same transition. Specifically, a differential phase retardance of ~180 degrees between the two circularly polarized components of a linearly polarized signal beam is demonstrated. The optical activity responsible for the phase retardation process is explained in terms of selection rules involving the Zeeman sublevels. Both the optically controlled polarizer and waveplate can be potentially implemented using the TNF in Rb vapor system and be used to realize an ultra-low power all optical switch as well as an all optical logic gate.

I have also investigated the feasibility of realizing a superluminal ring laser (SRL). An SRL contains a gain medium with a tuned negative dispersion, for which the group velocity of light becomes superluminal. For the SRL, the mirror displacement sensitivity is enhanced very significantly. As such, the SRL has many potential applications, including vibrometry and rotation sensing Using a double Raman pumped gain medium within Rb system, the enhancement factor is shown to be as large as 10^7. This system requires two strong pumps that are closely spaced in frequency. Accurate modeling of this system requires taking into account interference between the two pumps. An analysis is presented where we allow for an arbitrary number of harmonics that result from this interference, and investigate the behavior of the gain profile under a wide range of conditions. An experimental study of double-Raman gain in a Rb

vapor cell is also described, which is found to be in close agreement with the theoretical model. Furthermore, a numerical algorithm designed to simulate a double Raman superluminal laser is also presented. As an extension of the study of the SRL, I have also investigated the properties of a subluminal laser (SLL), inside which the group velocity of light is much slower than the vacuum speed of light. It makes use of a composite gain spectrum consisting of a broad background along with a narrow peak. Since the group index can be very high, the frequency of such a laser is highly insensitive to a change in the cavity length, thus making it extremely stable.

CHAPTER 10 APPENDIX

10.7 Appendix A: Matlab Program for Solving the Two Level Problem

```
omeg=5;                 % express rabi freq, normalized to gamma
N=2;                    % number of energy levels
R=401                   % number of points to plot
                        % initialize and set dimensions for all matrices
delta=zeros(1,R);       %detuning array
M=zeros(N^2,N^2);       %M-matrix
rho=zeros(N,N);         %dens mat
Ham=zeros(N,N);         %Hamiltonian with decay
Q=zeros(N,N);           %matrix corresponding to derivative of the density matrix

W=zeros((N^2-1),(N^2-1));       %W-matrix
S=zeros((N^2-1),1);             %S-vector
B=zeros((N^2-1),1);             %B-vector
A=zeros(N^2,R);                 %A-vectors, for all detunings

for m=1:R          %start the overall-loop
 delta(1,m)=(m-(R+1)/2)/2; %define the detuning, normalized to gamma
 Ham=[0 omeg/2; omeg/2 (delta(1,m)+0.5i)*(-1)]; %elements of Hamiltonian

 for n=1:N^2           %start the outer-loop for finding elements of M;
      for p=1:N^2      %start inner-loop for finding elements of M;

            %M(n,p) equals Q(alpha,beta) with only rho(epsilon,        %sigma)=1,    and
other elements of rho set to zero.

                  %determining dummy coefficients alpha and beta
            remain=rem(n,N);
            if remain==0
                  beta=N;
            else beta=remain;
            end
            alpha=(1+(n-beta)/N);

                  %determining dummy coefficients epsilon and sigma
            remain=rem(p,N);
```

```
            if remain==0
                sigma=N;
            else sigma=remain;
            end
            epsilon=(1+(p-sigma)/N);

            rho=zeros(N,N);                    %reset rho to all zeros
            rho(epsilon,sigma)=1;              %pick one element to be unity
            Q=(Ham*rho-rho*conj(Ham))*(0-1i); %find first part of Q matrix
            Q(1,1)=Q(1,1)+rho(2,2);            %add pop source term to Q
                                               %For an N-levl system, add additional
            %source terms as needed
            M(n,p)=Q(alpha,beta);
        end             %end the inner-loop for finding elements of M
    end                 %end of the outer-loop for finding elements of M

        S=M(1:(N^2-1),N^2:N^2);          %find S-vector
        W=M(1:(N^2-1),1:(N^2-1));        %initialize W-matrix

        for d=1:(N-1)
            W(:,((d-1)*N+d))=W(:,((d-1)*N+d))-S; %update W by subtracting
                                                 %from selected columns
        end

        B=(W\S)*(-1);                    %find B-vector: primary solution

        rhonn=1;                         %initialize pop of N-th state
                                 %determine pop of N-th state
        for f=1:(N-1)
            rhonn=rhonn-B(((f-1)*N+f), 1);
        end
                                 %determine the elements of the A vector
        A(1:(N^2-1),m)=B;
        A(N^2,m)=rhonn;

end                 %end of over-all loop
plot(delta,real(A((N^2-0),:)))
```

10.8 Appendix B: Matlab Program for Solving the Three Level Problem

```
oma=1; omb=1;       % express omeg rabi freqs, in units of gamma
dels=0;             % common detuning set to zero
N=3;                % number of energy levels
R=401               % number of points to plot
                    %initialize and set dimensions for all matrices
del=zeros(1,R);     %diff detuning array
M=zeros(N^2,N^2);   %M-matrix
rho=zeros(N,N);     %density matrix
Ham=zeros(N,N);     %Hamiltonian with decay
Q=zeros(N,N);       %matrix representing derivative of density matrix
W=zeros((N^2-1),(N^2-1));   %W-matrix
S=zeros((N^2-1),1);         %S-vector
B=zeros((N^2-1),1);         %B-vector
A=zeros(N^2,R);             %A-vectors, for all detunings

for m=1:R       %start the overall-loop
 del(1,m)=(m-(R+1)/2)/10; %define the detuning
 Ham=[del(1,m)/2 0 oma/2; 0 del(1,m)*(-1)/2 omb/2; ...
      oma/2 omb/2 (dels+0.5i)*(-1)];

 for n=1:N^2        %start the outer-loop for finding elements of M;
     for p=1:N^2    %start inner-loop for finding elements of M;

                    %finding alpha and beta
         remain=rem(n,N);
         if remain==0
             beta=N;
         else beta=remain;
         end
         alpha=(1+(n-beta)/N);

                %finding epsilon and sigma
         remain=rem(p,N);
         if remain==0
             sigma=N;
         else sigma=remain;
         end
         epsilon=(1+(p-sigma)/N);
```

```
            rho=zeros(N,N);                         %reset rho to all zeros
            rho(epsilon,sigma)=1;                   %pick one element to unity
            Q=(Ham*rho-rho*conj(Ham))*(0-1i); %find first part of Q matrix

            Q(1,1)=Q(1,1)+rho(3,3)/2;               %add pop source term to Q
            Q(2,2)=Q(2,2)+rho(3,3)/2;               %add pop source term to Q
                                                        %Modify as needed for general
                %systems
            M(n,p)=Q(alpha,beta);
        end             %end the inner-loop for finding elements of M
    end                 %end of the outer-loop for finding elements of M

        S=M(1:(N^2-1),N^2:N^2);           %find S-vector
        W=M(1:(N^2-1),1:(N^2-1));         %initialize W-matrix

        for d=1:(N-1)
            W(:,((d-1)*N+d))=W(:,((d-1)*N+d))-S; %update W by subtracting
                                                    %from selected columns
        end

        B=(W\S)*(-1);                     %find B-vector: primary solution

        rhonn=1;                            %initialize pop of N-th state
                                %determine pop of N-th state
        for f=1:(N-1)
            rhonn=rhonn-B(((f-1)*N+f), 1);
        end
                                %determine elements of A vector
        A(1:(N^2-1),m)=B;
        A(N^2,m)=rhonn;

end                     %end of over-all loop
plot(del,real( A ( (N^2-0),: ) ) )
```

CHAPTER 11 LIST OF PUBLICATIONS

11.7 Journal Publications

- **Ye Wang**, Zifan Zhou, Joshua Yablon, and Selim Shahriara, “Effect of multiorder harmonics in a double-Raman pumped gain medium for a superluminal laser”, Optical Engineering 54(5), 057106 (May 2015)
- Zifan Zhou, Joshua Yablon, Minchuan Zhou, **Ye Wang**, Alexander Heifetz, M.S. Shahriar, “Modeling and analysis of an ultra-stable subluminal laser”, Optics Communications, (Accepted July 2015)
- S. Krishnamurthy, **Y. Wang**, Y. Tu, S. Tseng, and M. S. Shahriar, “High-speed modulation in ladder transitions in Rb atoms using high-pressure buffer gas”, Optics Express Vol. 23, Issue 9, pp. 11470-11482 (2015)
- S. Krishnamurthy, Y. Tu, **Y. Wang**, S. Tseng, M.S. Shahriar, "Optically controlled waveplate at a telecom wavelength using a ladder transition in Rb atoms for all-optical switching and high speed Stokesmetric imaging”, Optics Express 22 No. 23, 28898-28913 (Nov. 2014)
- M.S. Shahriar, **Ye Wang**, S.Krishnamurthy, Y. Tu , G.S. Pati, and S. Tseng, “Evolution of an N-level system via automated vectorization of the Liouville equations and application to optically controlled polarization rotation” , Volume 61, Issue 4,pp.351-367(February 2014).
- S. Krishnamurthy, **Y. Wang**, S. Tseng, Y. Tu, and M.S. Shahriar, “Optically controlled polarizer using a ladder transition for high speed Stokesmetric Imaging and Quantum

Zeno Effect based optical logic", Optics Express, Vol. 21, Issue21, pp. 24514-24531 (Oct, 2013)

- S. Krishnamurthy, **Y. Wang**, Y. Tu, S. Tseng, and M. S. Shahriar, "High efficiency optical modulation at a telecom wavelength using the quantum Zeno effect in a ladder transition in Rb atoms", Opt.Express (2012)
- K. Salit, M. Salit, S. Krishnamurthy, **Y. Wang**, P. Kumar, and M. S. Shahriar, "Ultra-low power, Quantum Zeno effect based optical modulation in a degenerate V-system with a tapered nano fiber in atomic vapor", Opt. Express (2011)
- H.N. Yum, M. Salit, J. Yablon, K. Salit, **Y. Wang**, and M.S. Shahirar, "Superluminal ring laser for hypersensitive sensing", Optics Express 18, 17658-17665 (2010).

11.8 Conference proceedings and talks

- **Ye Wang**, Zifan Zhou, Joshua Yablon, Shih Tseng, M.S, Shahriar, “Superluninal laser using dual peak Raman gain”, SPIE Photonics West Conference, San Francisco, CA, February, 2014.
- Zifan Zhou, Joshua Yablon, **Ye Wang**, Devin Hilleman, Shih Tseng, M.S. Shahriar, “Theoretical modeling of a DPAL based superluminal laser and comparison with experiment”, SPIE Photonics West Conference, San Francisco, CA, February, 2014.
- **Ye Wang**, Joshua M. Yablon, Zifan Zhou, Shih Tseng, Selam Neda, Yanfei Tu, Tony Abi-Salloum, and Selim Shahriar, “Investigation of a Superluminal Ring Laser using Double-Raman Gain”, OSA Annual Meeting, Orlando, FL, October 2013.
- S. Krishnamurthy, **Y. Wang**, Y. Tu, S. Tseng, and M.S. Shahriar, “Buffer-Gas Assisted High Speed Optical Modulator using Ladder Transitions in Rb”, OSA Annual Meeting, Orlando, FL, Oct. 2013
- Selim M. Shahriar, Joshua Yablon, Zifan Zhou, **Ye Wang**, Shih Tseng, “Superluminal ring laser gyroscopes and accelerometers for hypersensitive and compact inertial measurement units”, SPIE Optics and Photonics conference, San Diego, CA, August, 2013. (Invited).
- **Ye Wang**, Tony Abi-Salloum, Joshua Yablon, Shih Tseng, Yanfei Tu and Selim M. Shahriar, “Double-Raman Gain for Realizing a Superluminal Ring Laser”, Conference on Lasers and Electro-Optics, San Jose, CA, June 2013

- Subramanian Krishnamurthy, **Ye Wang**, Yanfei Tu, Shih Tseng, and M. S. Shahriar, "All-Optical Switch at Telecom Wavelength based on the Quantum Zeno Effect (QZE)", Conference on Lasers and Electro-Optics, San Jose, CA, June 2013
- S. Krishnamurthy, **Y. Wang**, Y. Tu, S. Tseng and M.S. Shahriar, "Optically controlled polarizer and waveplate at telecom wavelength for Quantum Zeno Effect based all-optical switch", APS DAMOP conference, Quebec City, Canada, June 2013
- T.Y. Abi-Salloum, **Y. Wang**, J. Yablon, S. Tseng, Z. Zhu and M.S. Shahriar, "Superluminal Ultrasensitive Optical Gyroscope in an Inverted Double-Raman Lambda System", APS DAMOP conference in Quebec City, Canada, June 2013.
- S. Krishnamurthy, **Y. Wang**, S. Tseng, Y. Tu, and M.S. Shahriar, "Quantum Zeno effect based high speed optical modulator at a telecom wavelength in a ladder transition in Rb atoms", OSA annual meeting, Rochester, NY, Oct. 2012
- J. Yablon, S. Tseng, **Y. Wang**, T. Abi-Salloum, and M.S. Shahriar, "Demonstration of a Tunable Narrowband-Pumped Ring Alkali Laser for Superluminal Applications", presented at the OSA annual meeting, Rochester, NY (2012).
- **Y. Wang**, S. Krishnamurthy, S. Tseng, Y. Tu, and M.S. Shahriar, "Ultra-low Power Optical Modulation within Tapered Nano-fiber using 5S-5P-5D Ladder Transition of Rb Atoms", OSA annual meeting, Rochester, NY, Oct. 2012
- S. Krishnamurthy, **Y. Wang**, S. Tseng, Y. Tu, and M.S. Shahriar, "Optically Controlled Waveplate at a Telecom Wavelength Using a Ladder Transition in Rb Atoms for All-Optical Switching via the Quantum Zeno Effect", OSA annual meeting, San Jose, CA, Oct. 2011

- S. Krishnamurthy, **Y. Wang**, S. Tseng, Y. Tu, and M.S. Shahriar, "High Efficiency, High Speed Optical Modulation at a Telecom Wavelength Using the Quantum Zeno Effect in a Ladder Transition in Rb Atoms", OSA annual meeting, San Jose, CA, Oct. 2011
- H. Yum, J. Yablon, **Y. Wang** and M.S. Shahriar, "Ultra-sensitive Sensing with A Superluminal Ring Laser", presented at the OSA Annual Meeting, Rochester, NY (2010).
- Yum, H., Salit, M., Yablon, J., Salit, K., **Wang, Y**., and Shahriar, M. S., "Ultra-precise Rotation Sensing with a Superluminal Ring Laser", Proceedings of IEEE SENSORS Conference, Hawaii, September 2010 (invited)
- K. Salit, M. Salit, S. Krishnamurthy, **Y. Wang**, P. Kumar, and M.S. Shahriar, "High Bandwidth, Ultra-Low Power All Optical Modulation with a Nano-Fiber Embedded in Rb Vapor", Conference on Lasers and Electro-Optics, San Jose, CA, May 2010
- H. Yum, J. Yablon, **Y. Wang**, P. Hemmer and M. S. Shahriar, "Superluminal Laser: Properties and Applications", SPIE Photonics West, San Francisco, CA, (January 2010).
- M.S. Shahriar, H. Yum, J. Yablon, and **Y. Wang**, "Superluminal Laser for Rotation Sensing and Other Application", presented at the Stanford Photonic Research Center Annual Conference, Stanford, CA, Sept. 2009.
- K. Salit, M. Salit, S. Krishnamurthy, **Y. Wang**, P. Kumar, and M.S. Shahriar, "Atto-Joules, High Bandwidth All Optical Modulation with a Nano-Fiber Embedded in Alkali Vapor", presented at OSA Annual Meeting, San Jose, CA, Oct. 2009.

CHAPTER 12 REFERENCES

1. S. E. Harris and Y. Yamamoto, “Photon switching by quantum interference”, Phys. Rev. Lett. 81(17), 3611–3614 (1998).

2. R. G. Beausoleil, W. J. Munro, D. A. Rodrigues, and T. P. Spiller, “Applications of electromagnetically induced transparency to quantum information processing”, J. Mod. Opt. 51(16-18), 2441–2448 (2004).

3. A. M. C. Dawes, L. Illing, S. M. Clark, and D. J. Gauthier, “All-optical switching in rubidium vapor”, Science 308, 672–674 (2005).

4. Q. Xu and M. Lipson, “All-optical logic based on silicon micro-ring resonators”, Opt. Express 15(3), 924–929 (2007).

5. M. Bajcsy, S. Hofferberth, V. Balic, T. Peyronel, M. Hafezi, A. S. Zibrov, V. Vuletic, and M. D. Lukin, “Efficient all-optical switching using slow light within a hollow fiber”, Phys. Rev. Lett. 102(20), 203902 (2009).

6. V. Venkataraman, P. Londero, A. R. Bhagwat, A. D. Slepkov, and A. L. Gaeta, “All-optical modulation of four-wave mixing in an Rb-filled photonic bandgap fiber”, Opt. Lett. 35(13), 2287–2289 (2010).

7. K. Salit, M. Salit, S. Krishnamurthy, Y. Wang, P. Kumar, and M. S. Shahriar, “Ultra-low power, Zeno effect based optical modulation in a degenerate V-system with a tapered nano fiber in atomic vapor”, Opt.Express 22874, Vol. 19, No. 23 (2011)

8. S. M. Spillane, G. S. Pati, K. Salit, M. Hall, P. Kumar, R. G. Beausoleil, and M. S. Shahriar, “Observation of nonlinear optical interactions of ultralow levels of light in a tapered optical nanofiber embedded in a hot rubidium vapor”, Phys. Rev. Lett. 100(23), 233602 (2008).

9. G. Brambilla, V. Finazzi, and D. J. Richardson, “Ultra-low-loss optical fiber nanotapers”, Opt. Express 12(10), 2258–2263 (2004).

10. S. M. Hendrickson, M. M. Lai, T. B. Pittman, and J. D. Franson, “Observation of two-photon absorption at low power levels using tapered optical fibers in rubidium vapor”, Phys. Rev. Lett. 105(17), 173602 (2010).

11. B. Misra and E. C. G. Sudarshan, “The Zeno’s paradox in quantum theory”, J. Math. Phys. 18(4), 756–763 (1977).

12. W. M. Itano, D. J. Heinzen, J. J. Bollinger, and D. J. Wineland, “Quantum Zeno Effect”, Phys. Rev. A 41(5), 2295–2300 (1990).

13. Y. Huang, J. B. Altepeter, and P. Kumar, “Interaction-free all-optical switching via the quantum Zeno effect”, Phys. Rev. A 82(6), 063826 (2010).

14. S. Ghosh, A. R. Bhagwat, C. K. Renshaw, S. Goh, A. L. Gaeta, and B. J. Kirby, “Low-Light-Level Optical Interactions with Rubidium Vapor in a Photonic Band-Gap Fiber”, Phys. Rev. Lett. 97(2), 023603 (2006).

15. W. Yang, D. B. Conkey, B. Wu, D. Yin, A. R. Hawkins, and H. Schmidt, “Atomic spectroscopy on a chip”, Nat. Photonics 1(6), 331–335 (2007).

16. M.S. Shahriar, Ye Wang, Subramanian Krishnamurthy Y. Tu, G.S. Pati & S. Tseng, “Evolution of an N-level system via automated vectorization of the Liouville equations and application to optically controlled polarization rotation”, Journal of Model Optics, Vol. 61, Issue 4, pages 351-367 (2014)

17. S. Krishnamurthy, Y. Wang, Y. Tu, S. Tseng, and M.S. Shahriar, “Optically controlled polarizer using a ladder transition for high speed Stokesmetric Imaging and Quantum Zeno Effect based optical logic”, Opt. Express, Vol.21, No.21 (2013)

18. S. Krishnamurthy, Y. Wang, Y. Tu, S. Tseng, and M.S. Shahriar, “Optically controlled waveplate at a telecom wavelength using a ladder transition in Rb atoms for all-optical switching and high speed Stokesmetric imaging”, Opt. Express, Vol. 22, No. 23 (2014)

19. Ye Wang, Zifan Zhou, Joshua Yablon, and Selim Shahriar, “Effect of multiorder harmonics in a double-Raman pumped gain medium for a superluminal laser”, Opt. Engineering, 54(5), 057106 (2015)

20. H. N. Yum et al., “Superluminal ring laser for hypersensitive sensing”, Opt. Express 18(17), 17658–17665 (2010).

21. M. S. Shahriar et al., “Ultrahigh enhancement in absolute and relative rotation sensing using fast and slow light”, Phy. Rev. A 75, 053807 (2007).

22. G. S. Pati et al., “Demonstration of displacement-measurement-sensitivity proportional to inverse group index of intra-cavity medium in a ring resonator”, Opt. Commun. 281, 4931–4935 (2008).

23. G. S. Pati et al., “Demonstration of a tunable-bandwidth white light interferometer using anomalous dispersion in atomic vapor”, Phys. Rev. Lett. 99, 133601 (2007).

24. M. S. Shahriar and M. Salit, “Application of fast-light in gravitational wave detection with interferometers and resonators”, J. Mod. Opt. 55, 3133 (2008).

25. D. D. Smith et al., “Dispersion-enhanced laser gyroscope”, Phys. Rev.A 78, 053824 (2008).

26. D. D. Smith et al., “Enhanced sensitivity of a passive optical cavity by an intracavity dispersive medium”, Phys. Rev. A 80, 011809(R) (2009).

27. D. D. Smith et al., “Fast-light enhancement of an optical cavity by polarization mode coupling”, Phys. Rev. A 89, 053804 (2014).

28. O. Kotlicki, J. Scheuer, and M. S. Shahriar, “Theoretical study on Brillouin fiber laser

sensor based on white light cavity", Opt. Express 20(27), 28234 (2012).

29. Dahlquist, Germund; Björck, Åke, Numerical Methods, Dover, pp. 231–232. ISBN 978-0486428079. (2003)

30. Dowell, M., Jarratt, P., "A modified regula falsi method for computing the root of an equation", BIT 11 (2): 168–174, (1971)

31. S. E. Harris, Phys. Today 50, No. 7, 36 (1997).

32. M. D. Lukin, Rev. Mod. Phys.75, 457 (2003).

33. M. C. Dawes et al. , Science 308, 672 (2005).

34. D. A. Braje et al. , Phys. Rev. A 68, 041801(R) (2003).

35. C. J. Hood et al., Phys. Rev. Lett. 80 , 4157 (1998).

36. C. J. Hood et al., Science 287, 1447 (2000).

37. S. M. Spillane et al., Phys. Rev. A 71, 013817 (2005).

38. T. Aoki et al., Nature (London) 443, 671 (2006).

39. K. P. Nayak et al., Opt. Express 15, 5431 (2007).

40. G. Sague et al., Phys. Rev. Lett. 99, 163602 (2007).

41. Tinga, W. R., Voss, W. A. G., Blossey, D. F., "Generalized approach to multiphase dielectric mixture theory". J. Appl. Phys. 44 (9): 3897 (1973)

42. Ramo, Simon, John R. Whinnery, and Theodore van Duzer, Fields and Waves in Communications Electronics, 2 ed., John Wiley and Sons, New York, 1984.

43. http://refractiveindex.info/

44. Sargent M, Scully M O and Lamb W E 1977 Laser Physics (Addison-Wesley)

45. Scully M O and Zubairy M S 1997 Quantum Optics (Cambridge University Press, 1997)

46. Allen L and Eberly J H 1975 *Optical Resonances and Two Level Atoms* (Dover, New

York)

47. Shore B W 1990 The Theory of Coherent Atomic Excitation (Wiley, New York)

48. Metcalf Harold J, Straten Peter van der Laser Cooling and Trapping (Springer) page 4-6 (1999)

49. Shahriar M S, Hemmer P, Katz, D P, Lee A and Prentiss M 1997 Phys. Rev. A. 55 2272.

50. Radmore P M and Knight P L 1982 J.Phys. B 15 561

51. Arimondo E 1996 Prog. Optics 35 259

52. Whitley R M and Stroud, C R Jr. 1976 Phys. Rev. A 14 1498

53. Gray H R, Whitley R M and Stroud C R Jr. 1978 Opt. Letts. 3 218

54. Arimondo E and Orriols G 1976 Nuov. Cim. Letts. 17 333

55. Hemmer P, Shahriar M S, Natoli V and Ezekiel S 1989 J. Opt. Soc. of Am. B 6 1519

56. G. R. White, J. Lough, D. Duncan, J. P. Davis and F. A. Narducci 2009 J. Mod. Optics 56, 2013

57. M.S. Shahriar, Y. Tan, M. Jheeta, J. Morzinksy, P.R. Hemmer and P. Pradhan 2005 J. Opt. Soc. Am. B. 22 1566

58. M. Kasevich and S. Chu 1991 Phys. Rev. Lett. 67 181

59. Itano W M, Heinzen D J, Bollinger J J and Wineland D J 1990 Phys. Rev. A 41 2295

60. J. H. V. Nguyen and B. Odom 2011 Phys. Rev. A 83, 053404

61. Philip M. Morse, Thermal Physics, 1964

62. W.M. Currie, “A Monte Carlo programme for Doppler shift analysis”, Nuclear Instruments and Methods, Vol. 73, Issue 2, Page 173-185, 1969

63. http://www.it.northwestern.edu/research/user-services/quest/index.html

64. H. Sasada, “Wavenumber measurements of sub-Doppler spectral lines of Rb at 1.3 pm and

1.5 pm", IEEE Photonics Technology Letters4, 1307-1309 (1992).

65. H. S. Moon, W. K. Lee, L. Lee, and J. B. Kim, "Double resonance optical pumping spectrum and its application for frequency stabilization of a laser diode", App. Phys. Lett. 85, 3965-3967 (2004).

66. J. E. Bjorkholm, and P. F. Liao, "Line shape and strength of two-photon absorption in an atomic vapor with a resonant or nearly resonant intermediate state", Phys. Rev. A 14, 751-760 (1976).

67. B. V. Zhdanov and R. J. Knize, "Progress in alkali lasers development," Proc. SPIE 6874, 68740F(2008).

68. R. J. Beach, W. F. Krupke, V. K. Kanz, S. A. Payne, M. A. Dubinskii, and L. D. Merkle, "End-pumped continuous-wave alkali vapor lasers: experiment, model, and power scaling," J. Opt. Soc. Am. B 21(12), 2151– 2163 (2004).

69. E. Walentynowicz, R. A. Phaneuf, and L. Krause, "Inelastic collisions between excited alkali atoms and molecules. X. Temperature dependence of cross sections for 2P3/2-2P1/2 mixing in cesium, induced in collisions with deuterated hydrogens, Ethanes, and propanes," Can. J. Phys. 52, 589–591 (1974).

70. S.-Y. Chen and M. Takeo, "Broadening and shift of spectral lines due to the presence of foreign gases," Rev.Mod. Phys. 29(1), 20–73 (1957).

71. M. V. Romalis, E. Miron, and G. D. Cates, "Pressure broadening of Rb D1 and D2 lines by 3He, 4He, N2, and Xe: line cores and near wings," Phys. Rev. A 56(6), 4569–4578 (1997).

72. X. Hu, P. Jiang, C. Ding, H. Yang, and Q. Gong, "Picosecond and low-power all-optical switching based on an organic photonic-bandgap microcavity," Nat. Photonics 2(3), 185–189 (2008).

73. M. S. Shahriar, Y. Wang, Y. Subramanian Krishnamurthy, Y. Tu, G. S. Pati, and S. Tseng, “Evolution of an N level system via automated vectorization of the Liouville equations and application to optically controlled polarization rotation,” J. Mod. Opt. 61(4), 351–367 (2014).

74. F. Nez, F. Biraben, R. Felder, and Y. Millerioux, “Optical frequency determination of the hyperfine components of the 5S1/2-5D3/2 two-photon transitions in rubidium,” Opt. Commun. 102(5-6), 432–438 (1993).

75. F. Nez, F. Biraben, R. Felder, and Y. Millerioux, “Optical frequency determination of the hyperfine components of the 5S1/2-5D3/2 two-photon transitions in rubidium: erratum,” Opt. Commun. 110(5-6), 731 (1994).

76. 31. H. S. Moon and H. R. Noh, “Optical pumping effects in ladder-type electromagnetically induced transparency of 5S1/2–5P3/2–5D3/2 transition of 87Rb atoms,” J. Phys. At. Mol. Opt. Phys. 44(5), 055004 (2011).

77. R. Hamid, M. Cetintas, and M. Celik, “Polarization resonance on S–D two-photon transition of Rb atoms,” Opt. Commun. 224(4-6), 247–253 (2003).

78. R. J. Beach, W. F. Krupke, V. K. Kanz, S. A. Payne, M. A. Dubinskii, and L. D. Merkle, “End-pumped continuous-wave alkali vapor lasers: experiment, model, and power scaling,” J. Opt. Soc. Am. B 21(12), 2151– 2163 (2004).

79. L. Stern, B. Desiatov, I. Goykhman, and U. Levy, “Nanoscale light-matter interactions in atomic cladding waveguides,” Nat. Commun. 4, 1548 (2013).

80. P. Kulatunga, H. C. Busch, L. R. Andrews, and C. I. Sukenik, “Two-color polarization spectroscopy of rubidium,” Opt. Commun. 285(12), 2851–2853 (2012).

81. S. Weilandy, L. Alexander, and L. Gaeta, “Coherent control of the polarization of an optical field”, Phys. Rev. Lett. 81(16), 3359–3362 (1998).

82. M. Xiao, Y. Li, S. Jin, and J. Gea-Banacloche, “Measurement of dispersive properties of electromagnetically induced transparency of Rubidium atoms”, Phys. Rev. Lett. 74(5), 666–669 (1995).

83. P. J. Curran, “Polarized visible light as an aid to vegetation classification”, Remote Sens. Environ. 12(6), 491–499 (1982).

84. M. J. Duggin, “Imaging polarimetry in scene element discrimination”, Proc. SPIE 3754, 108–117 (1999).

85. B. J. DeBoo, J. M. Sasian, and R. A. Chipman, “Depolarization of diffusely reflecting man-made objects”, Appl. Opt. 44(26), 5434–5445 (2005).

86. J. F. de Boer, T. E. Milner, and J. S. Nelson, “Determination of the depth-resolved Stokes parameters of light backscattered from turbid media by use of polarization-sensitive optical coherence tomography”, Opt. Lett. 24(5), 300–302 (1999).

87. D. A. Steck, “Rubidium 87 D line data”, http://steck.us/alkalidata/rubidium87numbers.pdf.

88. D. Stokes, Principles and Practice of Variable Pressure/Environmental Scanning Electron Microscopy (John Wiley & Sons, 2008), Chap. 8.

89. S. Krishnamurthy, Y. Wang, Y. Tu, S. Tseng, and M. S. Shahriar, “High efficiency optical modulation at a telecom wavelength using the quantum Zeno effect in a ladder transition in Rb atoms”, Opt. Express 20(13), 13798–13809 (2012).

90. S. D. Badger, I. G. Hughes, and C. S. Adams, “Hyperfine effects in electromagnetically induced transparency”, J. Phys. B 34(22), L749–L756 (2001).

91. S. Li, B. Wang, X. Yang, Y. Han, H. Wang, M. Xiao, and K. C. Peng, “Controlled polarization rotation of an optical field in multi-Zeeman-sublevel atoms”, Phys. Rev. A 74(3),

033821 (2006).

92. H. S. Moon, “Frequency stabilization of a 1.3 μm laser diode using double resonance optical pumping in the 5P3/2-6S1/2 transition of Rb atoms”, Appl. Opt. 47(8), 1097–1102 (2008).

93. H. D. Do, M. S. Heo, G. Moon, H. R. Noh, and W. Jhe, “Analytic calculation of the lineshapes in polarization spectroscopy of rubidium”, Opt. Commun. 281(15-16), 4042–4047 (2008).

94. H. D. Do, G. Moon, and H. R. Noh, “Polarization spectroscopy of rubidium atoms: theory and experiment”, Phys. Rev. A 77(3), 032513 (2008).

95. Daniel Adam Steck, “Rubidium 85 D Line Data”, http://steck.us/alkalidata/rubidium85numbers.pdf

96. Z. Konefał, “Observation of collision induced processes in rubidium–Ethane vapor”, Opt. Commun. 164(1-3), 95–105 (1999)

97. W. F. Krupke, R. J. Beach, V. K. Kanz, and S. A. Payne, “Resonance transition 795-nm rubidium laser”, Opt. Lett. 28 (23) 2336-2338 (2003)

98. B. V. Zhdanov, T. Ehrenreich, and R. J. Knize, “Highly efficient optically pumped cesium vapor laser”, Opt. Commun. 260(2), 696–698 (2006)

99. A. V. Bogachev, S. G. Garanin, A. M. Dudov, V. A. Yeroshenko, S. M. Kulikov, G. T. Mikaelian, V. A. Panarin, V. O. Pautov, A. V. Rus, and S. A. Sukharev, “Diode-pumped caesium vapour laser with closed-cycle laser-active medium circulation”, Quantum Electronics 42 (2) 95-98 (2012)

100. W. F. Krupke, “Diode Pumped Alkali Lasers (DPALs) – an Overview”, Proc. SPIE 7005, 700521 (2008)

101. B. V. Zhdanov, J. Sell, and R. J. Knize, “Multiple laser diode array pumped Cs laser with 48 W output power”, Electronics Lett. 44(9) 582-583 (2008)

102. M. O. Scully, M. Sargent and W. E. Lamb, Laser Physics, Westview Press, Boulder, Colorado, 1974.

103. M. O. Scully and M. S. Zubairy, Quantum Optics, Cambridge University Press, London, 1997.

104. H. N. Yum and M. S. Shahriar, “Pump-probe model for the Kramers-Kronig relations in a laser”, J. Opt. 12 104018 (2010).

105. H. C. Bolton, and G. J. Troup, “The modification of the Kronig-Kramers relations under saturation conditions”, Philos. Mag. 19 (159) 477-485 (1969).

106. G. J. Troup, and A. Bambini, “The use of the modified Kramers-Kronig relation in the rate equation approach of laser theory”, Phys. Lett. 45A 393 (1973).

107. S. Krishnamurthy, Y. Wang, Y. Tu, S. Tseng, and M.S. Shahriar, “High-speed modulation in ladder transitions in Rb atoms using high-pressure buffer gas”, Optics Express, Vol. 23, Issue 9, pp. 11470-11482 (2015).

108. W. F. Krupke, R. J. Beach, V. K. Kanz, S. A. Payne, and J. T. Early, “New Class of CW High-Power Diode-Pumped Alkali Lasers (DPALs)”, Proc. SPIE 5448, 547954 (2004)

109. G. P. Perram, W. Miller, and E. Hurd, “Diode-pumped alkali laser-bleached wave dynamics”, Proc. SPIE 8547, 854709 (2012)

110. J. T. Verdeyen, Laser Electronics (Prentice Hall, 1995)

111. Y. Wang, Z. Zhou, J. Yablon, and M. S. Shahriar, “Effect of Multi-Order Harmonics in a Double-Raman Pumped Gain Medium For a Superluminal Laser”, to appear in Optical Engineering (2015).

112. C.H. Townes, “Some applications of optical and infrared masers”, in Advances in Quantum Electronics, J.R. Singer., Ed., New York: Columbia Univ. Press, , pp 1-11 (1961).

113. M. A. Biot, “General Theorems on the Equivalence of Group Velocity and Energy Transport”, The Physical Review, Vol. 105, No. 4, 1129-1137, (1957)

114. C. H. Henry, “Theory of the Linewidth of Semiconductor Lasers”, IEEE J. Of Quantum Electronics, Vol. QE-18, No. 2, (1982)

115. W. W. Chow, J. Gea-Banacloche, L. M. Pedrotti, V. E. Sanders, W. Schleich, and M. O. Scully, “The ring laser gyro”, Rev. Mod. Phys. 57, 61 (1985)

116. B. T. King, “Application of superresolution techniques to RLGs: exploring the quantum limit”, Applied Optics 39, 6151 (2000)

117. T.A. Dorschner, H.A. Haus, M. Holz, I.W. Smith, H. Statz, "Laser gyro at quantum limit", IEEE J. Quant. Elect. QE-16, 1376 (1980)

118. M. O. Scully, and W. E. Lamb, Laser Physics, (Westview Press, Boulder, CO, 1974).

119. G. S. Pati, M. Salit, K. Salit, and M. S. Shahriar, “Simultaneous slow and fast light effects using probe gain and pump depletion via Raman gain in atomic vapor”, Opt. Express 17(11), 8775–8780 (2009).

120. S. C. Chapra, R. P. Canale, “Numerical Methods for Engineers”, sixth edition, p124, (2008)